228
4/11/69

756

IDO-17281
March 1969

REACTIVITY ACCIDENT TEST RESULTS AND ANALYSES FOR THE SPERT III E-CORE -- A SMALL, OXIDE-FUELED, PRESSURIZED-WATER REACTOR

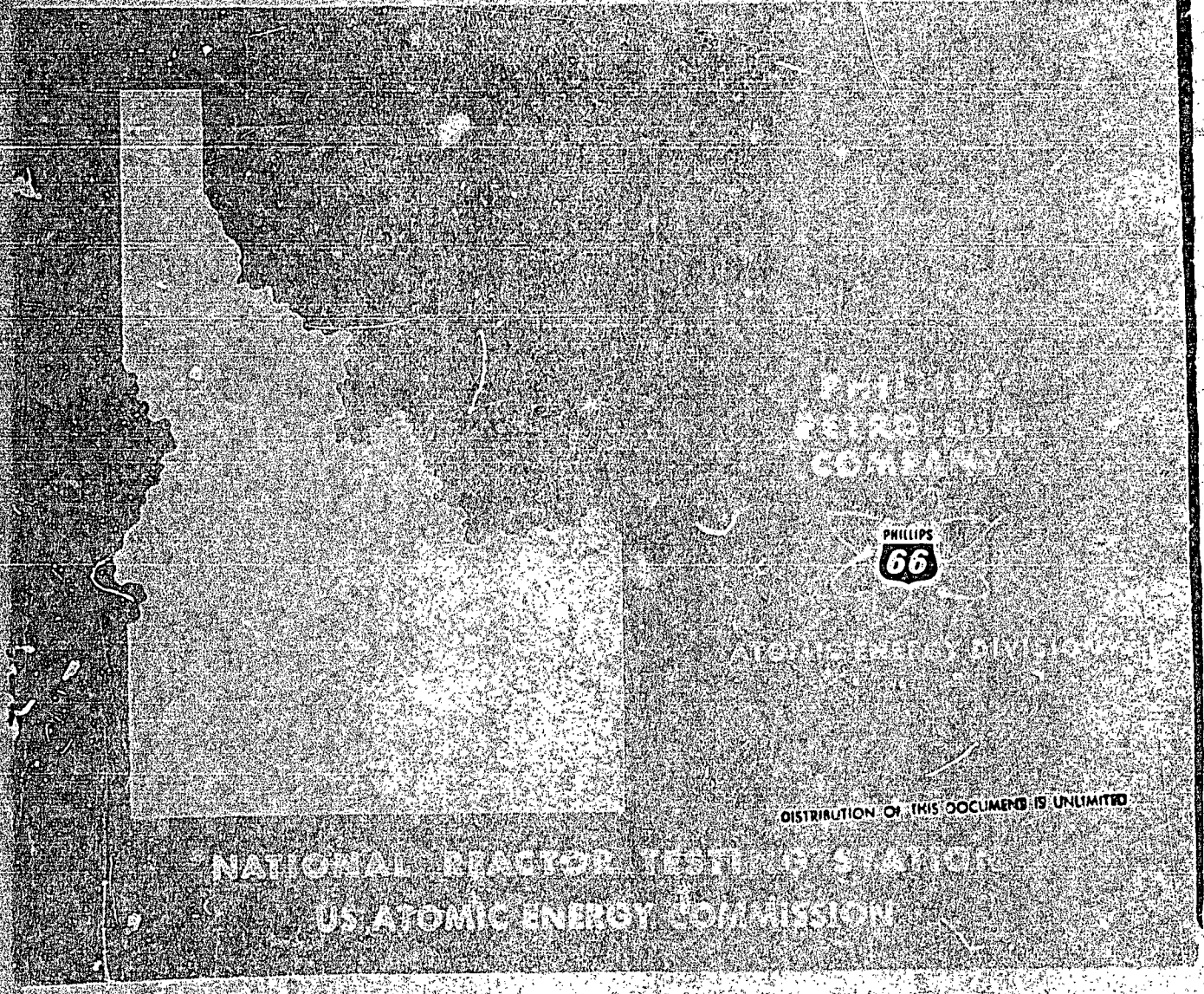

NATIONAL REACTOR TESTING STATION
U.S. ATOMIC ENERGY COMMISSION

Printed in the United States of America
Available from
Clearinghouse for Federal Scientific and Technical Information
National Bureau of Standards, U. S. Department of Commerce
Springfield, Virginia 22151
Price: Printed Copy $3.00; Microfiche $0.65

LEGAL NOTICE

IDO-17281
AEC Research and Development Report
Reactor Technology
TID-4500
Issued: March 1969

REACTIVITY ACCIDENT TEST RESULTS AND ANALYSES FOR THE SPERT III E-CORE -- A SMALL, OXIDE-FUELED, PRESSURIZED-WATER REACTOR

by

R. K. McCardell
D. L. Herborn
J. E. Houghtaling*

* NOW WITH WESTINGHOUSE ELECTRIC CORPORATION, PITTSBURGH, PA.

PHILLIPS
PETROLEUM
COMPANY

Atomic Energy Division
Contract AT(10-1)-205
Idaho Operations Office
U. S. ATOMIC ENERGY COMMISSION

ACKNOWLEDGMENTS

The performance and analysis of the Oxide Core Kinetics Program required the efforts of many people. Special thanks are due to M. Ishikawa, G. A. Mortensen, R. K. Stitt, and M. W. King. Mr. Ishikawa, an exchange scientist on loan from the Japanese Atomic Energy Research Institute, performed many of the PARET calculations and verified that prompt moderator heating was an important E-core feedback mechanism. Dr. Mortensen developed the Doppler feedback model used in the computer codes, and Dr. Stitt performed most of the extrapolative PARET calculations. Both individuals provided much technical advice throughout the program. Mr. King performed the SPORT calculations and prepared the appendix of experimental data plots. The cooperation and efforts of J. P. Campbell, J. F. Scott, and W. A. Eisenbarth, members of the Oxide Core Kinetics Group, are also gratefully acknowledged.

ABSTRACT

A program of reactivity accident tests has been performed with the Spert III E-core -- a small, oxide-fueled, pressurized-water reactor (PWR), which except for size is generally characteristic of an unborated, commercial PWR with essentially no fission product inventory in the core. With this core, 80 nondamaging power excursions were initiated from typical PWR operating conditions, viz, cold-startup, hot-startup, hot-standby, and operating-power initial conditions. The excursions resulted from rapid reactivity insertions ranging from 0.5 to 1.3$. The data obtained provide the only known experimental reactivity accident results for low-enriched oxide cores at initial conditions other than cold-startup. The cold-startup power excursions were essentially limited by Doppler broadening of U-238 resonance absorption cross sections, which provided the majority of the total reactivity compensation. For the other test conditions, reactivity feedback resulting from prompt moderator heating, caused by slowing down of fast neutrons and absorption of prompt gamma rays, became a significant contributor to the total reactivity feedback. The IREKIN and PARET computer codes were evaluated using the experimental data. The IREKIN code, which considers only reactivity feedback from Doppler broadening, provided satisfactory predictions for only the cold-startup tests. The comprehensive PARET code yielded excellent predictions for all accident conditions tested.

SUMMARY

Reactor safety is generally assessed on the basis of calculational models that predict the courses and consequences of postulated reactor accidents. The accuracy of these predictions, however, can be determined only by comparison with experimental data. Reactivity accident tests, which provide data for verification of such calculational models, have been performed in the oxide-fueled, pressurized-water Spert III E-core reactor. The specific objectives of the Spert III E-core program were to (a) obtain reactivity accident data under initial conditions similar to commercial PWR operating conditions, (b) analyze the data to determine the reactor kinetic response, and (c) evaluate computer codes used to predict the reactor kinetic behavior. Except for its small size, this reactor has the characteristics of an unborated, commercial, pressurized-water reactor (PWR) with essentially no fission product inventory in the core. The E-core initial test conditions were representative of cold-startup, hot-startup, hot-standby, and operating-power conditions in PWR's. The tests were initiated with rapid reactivity insertions ranging from 0.5 to 1.3$, which resulted in nondamaging power excursions with reactor periods from about 1000 to 10 msec. These data provide the only known experimental reactivity accident results for low-enriched oxide cores at initial conditions other than cold-startup. Analytical models, used by the nuclear industry to predict the results of reactivity accidents, can now be evaluated for hot-startup, hot-standby, and operating-power conditions.

The kinetic behavior of the E-core was calculated using the PARET and IREKIN digital computer codes, both of which use the point-reactor kinetic equations. The PARET code calculates the coupled thermal, hydrodynamic, and nuclear response of the reactor, and all the known major reactivity feedback mechanisms are accounted for. In the IREKIN code, there are no provisions for coolant flow, and only Doppler reactivity feedback is taken into account. The results of these calculations are typical of reactivity accident analyses performed using current space-independent kinetic techniques.

The E-core experimental and analytical programs were divided into low-initial-power and high-initial-power test phases. Low-initial-power (≈50W)

excursions were performed for cold- and hot-startup conditions. High-initial-power excursions were performed for hot-standby and operating-power conditions. For the E-core, these system conditions are defined as:

Accident Conditions	Coolant Inlet Temperature (°F)	Initial Reactor Power (MW)
Cold Startup	70	5×10^{-5}
Hot Startup	260	5×10^{-5}
	500	5×10^{-5}
Hot Standby	500	1
Operating Power	500	20

With the exception of the cold-startup excursions, the test conditions were generally 1500 psig system pressure and 14 fps coolant flow along the fuel rods. In terms of flow, coolant subcooling, and specific core power, the initial test conditions were characteristic of commercial PWR operating conditions.

Analyses of experimental results from the cold-startup reactivity accident tests demonstrated that these power excursions in the E-core were essentially limited by Doppler broadening of the U-238 resonance absorption cross sections. Over the range of reactor periods considered (1000 to 10 msec) for the cold-startup tests, Doppler broadening provided about 85 to 95% of the total reactivity compensation at the time of peak power. Other oxide cores previously tested at Spert, the Spert I OC and Spert IV CDC, were also Doppler limited during cold-startup excursions. These cores had smaller nonmoderator-to-moderator ratios than did the E-core, and as expected, increasing this ratio increased the Doppler reactivity feedback. Although there were significant differences in Doppler feedback, total mass of UO_2 fuel, and U-235 enrichment among the three cores, the largest variation in peak reactor power or maximum specific energy release at peak power for cold-startup tests initiated by equal reactivity insertions was only a factor of two.

For the 260°F hot-startup tests, the peak reactor powers were about 10 to 35% larger than the values for cold-startup transients initiated with the same reactivity insertions. Peak reactor powers were about 50% larger for 500°F hot-startup tests than for cold-startup transients resulting from the same reactivity insertion. These differences in peak power indicate that Doppler reactivity feedback coefficients decrease with increasing fuel temperature. However, the differences between cold- and 500°F hot-startup peak powers

were not as large as would have been expected if the E-core were solely Doppler limited at hot-startup conditions. Analyses indicated that reactivity feedback resulting from moderator expansion became a significant contributor to the total reactivity feedback at elevated system temperatures. This moderator feedback resulted from prompt moderator heating (PMH) that was caused by the slowing down of fast neutrons and the absorption of prompt gamma rays. During the 500°F hot-startup tests, PMH feedback contributed from 20 to 35% of the total reactivity compensation at the time of peak power.

Analyses of the experimental results from the high-initial-power tests demonstrated that appreciable reactivity feedback occurred during the reactivity insertions, and therefore the power rises for these transients were not pure exponentials. During the high-initial-power tests, the kinetic behavior of the E-core was strongly influenced by the reactivity insertion rate. This is in contrast to the relative unimportance of insertion rate for the low-initial-power tests, where the reactivity insertions were completed before appreciable reactivity feedback occurred, and the transients behaved as if a step reactivity insertion had taken place. Because of the immediate feedback during excursions performed from high-initial-powers, the times required to reach peak power were considerably shorter than those for the low-initial-power tests. The times to peak power for the operating-power tests were about 100 msec regardless of the reactivity insertion. Peak reactor powers were about 40 to 50% larger for the hot-standby transients than for 500°F hot-startup tests initiated with the same reactivity insertions. For superprompt critical, operating-power transients, peak powers were about 2.7 times those for equivalent 500°F hot-startup tests; whereas the subprompt critical, operating-power transients reached peak powers about 10 times those of equivalent 500°F hot-startup tests. High-initial-power test results showed the effect of initial reactor power and further demonstrated the decreasing Doppler coefficient with increasing fuel temperature. During the hot-standby tests, Doppler compensation was still the principal feedback mechanism with PMH reactivity feedback contributing about 35% of the total at the time of peak power. For the operating-power tests, PMH reactivity compensation was the dominating feedback mechanism until about the time of peak power at which time the Doppler feedback became approximately equal to the PMH feedback.

During the hot-startup tests, the effect of coolant flow was investigated for excursions with reactor periods ranging from 250 to 15 msec by varying the coolant flow rate from 2.4 to 24 fps. For long-period transients (reactor period, τ, >40 msec), increasing the coolant flow rate increased the energy release to the time of peak power. This increase in energy release was caused by reduced moderator reactivity feedback at the larger flow rates. The reduction in feedback resulted because considerable heated coolant was transported from the core during the transient. For short-period transients (reactor period, τ. <40 msec), the energy release at the time of peak power was essentially independent of flow rate because little coolant was transported from the core in the short times required to reach peak power. However, for these same short period transients the power levels following the power peak increased with increasing coolant flow rates.

To evaluate the capabilities of calculational models, the E-core kinetic behavior was predicted using the PARET and IREKIN computer codes for the reactivity accident conditions experimentally investigated. IREKIN predictions were up to 30% larger than the experimental results for the cold-startup reactivity tests, but were 40 to 60% larger than experimental values for all the superprompt critical, hot-startup reactivity accident tests. However, the IREKIN code underpredicted the energy release to peak power for the 500°F subprompt critical, hot-startup tests. These inconsistencies in the IREKIN predictions resulted because coolant flow is not considered in the IREKIN code and moderator feedback cannot be satisfactorily taken into account. Because the effects of coolant flow and moderator reactivity feedback are very important at high-initial-power conditions, the limitations in the IREKIN code precluded meaningful calculations for the hot-standby or operating-power reactivity accident tests. PARET predictions were within 30% of the experimental results for all accident conditions tested.

During all the reactivity accident tests, the E-core fuel rods performed satisfactorily and clad integrity was not lost; however, circumferential ridging or clad bambooing occurred along the high flux regions of the fuel rods. Metallurgical investigations indicated that the strength of the cladding was not affected by this bambooing. The maximum fuel rod cladding surface temperature measured during the entire experimental program was about 600°F, and occurred during the operating-power tests. The maximum calculated hot-spot UO_2 fuel

temperature obtained using PARET was about 3800°F. These maximum temperatures are well below the melting temperatures of the stainless steel clad and UO_2 fuel.

Because of the excellent agreement that was obtained between the PARET calculational and experimental results, the PARET code was used to investigate the E-core kinetic behavior for postulated reactivity accidents that were not experimentally investigated. Calculations were performed to determine the effect of positive moderator temperature coefficients at operating-power conditions. These PARET calculations indicate that for a positive moderator temperature coefficient larger than about + 3¢/°F power excursions that are not self-limited by Doppler feedback could occur in the E-core. For these moderator temperature coefficients, E-core power excursions would be limited only by core disassembly.

PARET calculations were performed for postulated E-core reactivity accidents initiated with the maximum available reactivity insertions for the various operating conditions. These reactivity insertions were 4.8$ for the cold-startup and 250°F hot-startup conditions and 3.5$ for the 500°F hot-startup, the hot-standby, and the operating-power conditions. The results of these calculations indicate that the probability of core damage is largest for the cold-startup and operating-power accidents. For the most severe cold-startup reactivity accident considered, fuel melting was calculated to occur in the axial flux peaking region of about 30% of the core. However, during the power burst, the maximum clad surface temperature was calculated to be only about 200°F. For the most severe operating-power reactivity accident, the maximum fuel temperature was calculated to be about 4900°F during the power burst, which would not cause fuel melting. For this case, however, critical clad-water heat transfer conditions (departure from nucleate boiling heat fluxes) were calculated to occur along the axial flux peaking region in about 30% of the core; therefore clad melting could possibly occur.

In summary, analysis of the experimental results indicates that cold-startup power excursions in the E-core are principally limited by reactivity feedback arising from Doppler broadening. For hot-startup and hot-standby power excursions, reactivity feedback from prompt moderator heating becomes important in limiting these excursions. The prompt moderator heating reactivity feedback becomes the principal mechanism in limiting E-core power excursions initiated from operating-power conditions. The IREKIN code, which accounts only

for Doppler feedback, yielded predictions that were within 30% of the experimental results for the cold-startup reactivity accident tests. For all the other test conditions, IREKIN predictions were not satisfactory. Thus, for all reactivity accident conditions except cold-startup, it is concluded that the IREKIN code or codes similar to it are not adequate for predicting reactor kinetic behavior. The comprehensive PARET code, which accounts for all known reactivity feedback mechanisms, yielded predictions that were within 30% or less of experimental results for all accident conditions tested. It is recommended that a code like PARET, which incorporates coolant flow and moderator reactivity feedback, be used for predicting the results of reactivity accidents in small, oxide-fueled PWR's.

CONTENTS

FIGURES

TABLES

REACTIVITY ACCIDENT TEST RESULTS AND ANALYSES FOR THE SPERT III E-CORE -- A SMALL, OXIDE-FUELED, PRESSURIZED-WATER REACTOR

I. INTRODUCTION

Reactor safety is generally assessed from analytical models that predict the courses and consequences of postulated reactor accidents. The accuracy of these predictions, however, can be determined only by comparison with experimental data. An objective of the Special Power Excursion Reactor Test (Spert) Program, which is conducted by Phillips Petroleum Company at the National Reactor Testing Station, is to obtain data for the evaluation of analytical models. Two goals of this program are to determine (a) the mechanical behavior and (b) the nuclear behavior of oxide-fueled reactors for one type of postulated accident, the reactivity accident. The mechanical behavior of UO_2 fuel rods during power excursions is being investigated as part of the Subassembly Test Program[1]. The nuclear behavior of a small, oxide-fueled reactor was investigated during the Oxide Core Kinetics Program, and the results of this investigation are the subject of this report.

Analytical models have been shown to accurately predict the nuclear behavior of oxide-fueled reactors for nondamaging reactivity accident tests initiated from ambient temperature conditions[2-7]. Because experimental data were not available, however, evaluation of these models could not be made for the entire range of temperature, pressure, flow, and power conditions of oxide-fueled reactors. The Oxide Core Kinetics Program was designed to obtain reactivity accident data under initial operating conditions that are similar to commercial, pressurized-water reactor (PWR) operating conditions. The specific objectives of the program were (a) to obtain experimental power excursion data, (b) to analyze these experimental data to determine the important factors that influence reactor kinetic response, and (c) to evaluate analytical models that were used to predict the kinetic behavior of the reactor. The power excursion tests were performed with the Spert III E-core reactor, and the analytical investigations were performed using the PARET[8] and IREKIN[9] digital computer codes.

Typical PWR operating conditions include system pressures in the range from about 1500 to 2250 psig and coolant inlet temperatures in the range

from about 480 to 560°F. While these conditions were well within the capabilities of the Spert III physical plant, the E-core fuel rods were originally designed for the PL-2[10] reactor which had operating conditions of 600 psig system pressure and 489°F coolant inlet temperature. Because of the differences between the fuel rod design and the desired commercial PWR operating conditions, a series of external pressure tests was performed on the E-core fuel rods. Results of these tests and stress analyses indicated that the E-core fuel rods would perform satisfactorily under operating conditions of 30 MW[a] steady state reactor power, 1750 psig system pressure, and 550°F coolant inlet temperature. To allow for a significant safety margin and still satisfy the experimental program objectives, pretest operating limits of 20 MW steady state reactor power, 500°F coolant inlet temperature, and 1500 psig static system pressure were established for the transient tests. Within these limits, a large number of reactivity accident tests could be performed. System conditions representing cold-startup, hot-startup, hot-standby, and operating-power were selected. For the E-core, these initial system conditions are defined as tabulated below:

Accident Conditions	Coolant Inlet Temperature (°F)	System Pressure (psig)	Average Coolant Flow Rate (fps)	Initial Reactor Power (MW)
Cold Startup	70	Atm	0	5×10^{-5}
Hot Startup	260	1500	2.4 to 22	5×10^{-5}
	500	1500	4.8 to 24	5×10^{-5}
Hot Standby	500	1500	14	1
Operating Power	500	1500	14	20

A program limitation was that fuel mechanical damage thresholds would not be exceeded. This limitation was established so that the reactor would not be damaged before all of the accident conditions had been investigated. Therefore, reactivity insertions were limited to about 1.3$, which resulted in reactor

[a] Energy from the heat exchangers in the Spert III plant is vented to the atmosphere. Thus all E-core power levels given in this report are thermal power levels.

periods of about 10 msec. The sequence of reactivity accident testing was from what was considered to be the least to the most severe accident conditions. Therefore, transient testing was begun at cold-startup conditions and was concluded at operating-power conditions.

The acquisition of new experimental power excursion data provided a significant contribution to reactor safety investigations, and the analytical portion of the Spert III E-core program proved equally as important. The analytical effort was essentially fourfold:

(1) The E-core cold-startup experimental data were correlated with data from oxide cores previously tested.

(2) The experimental E-core data for each of the four accident conditions were compared with the data from the other conditions.

(3) The kinetic behavior of the E-core, for each accident condition, was predicted using analytical models and the results of these calculations were compared with experimental data.

(4) Extrapolative calculations using analytical models were performed for reactor conditions that were not experimentally tested.

The oxide-fueled reactors previously tested at Spert had design characteristics that were different from those of the Spert III E-core. Correlation of the E-core cold-startup data with the earlier test data indicated the effects of the different design characteristics on the reactor kinetic behavior. In addition, comparisons of the E-core data from all the reactivity accident conditions considered showed the influence of initial system temperature, reactor power, and coolant flow rate on the E-core kinetic behavior. Comparisons of the experimental and calculational E-core results were performed to evaluate the analytical models. Once verified, these models demonstrated the importance of various reactivity feedback mechanisms and were used for extrapolative calculations.

II. DESCRIPTION OF THE SPERT III FACILITY AND E-CORE

The following subsections contain a brief description of the Spert III facility and the E-core, a discussion of the instrumentation used for transient testing, and a summary of the static nuclear characteristics of the core. For those who desire more detailed plant information, particulars of the reactor and equipment are given in Appendix A of this report, in the Spert III Facility Report -- E-Core Revision[11], the Spert III Facility Report[12], and the Spert III Hazards Summary Report[13]. Results of the static nuclear experiments are discussed in detail in Spert Quarterly Technical Reports[14-17].

1. SPERT III FACILITY AND E-CORE DESCRIPTION

The Spert III reactor facility contains nuclear and hydraulic equipment that characterizes a conventional, pressurized-water reactor in addition to providing a facility for reactor safety experimentation. The reactor vessel and primary coolant system are designed for a steady state pressure up to 2500 psig, transient pressures to 3500 psig, and temperatures up to 700°F. A cutaway view of the Spert III reactor pressure vessel is illustrated in Figure 1. The vessel is a multilayer, welded, Type 304L stainless steel structure. Its inside diameter is 48 inches and its overall length is 23 feet 9 inches. Thermal shields, comprised of concentric cylindrical annuli of stainless steel, minimize the temperature-induced vessel-shell stresses during nuclear operation. The vessel consists of a flanged top head, a cylindrical shell, bottom hemispherical head, and bottom tee. The top head serves as a mount for the control rod drives and is of the bolted full-opening type that permits access to the reactor internal structure. Four 6-inch nozzles located on the top head provide access for instrumentation leads and exits for removable fuel assemblies. The bottom tee bolts to the bottom head and serves as an entrance for the coolant water from the two primary coolant loops. Each of the primary loops consists of two 500 hp, canned-rotor, centrifugal pumps operating in parallel; a heat exchanger; and flow-control and check valves. The total coolant flow rates of both loops can be varied from 400 to 22,000 gpm, which corresponds to velocities in the E-core fuel channels up to about 24 fps. The maximum heat removal capacity of both loops is 60 MW for 30 minutes because of a limitation in the supply

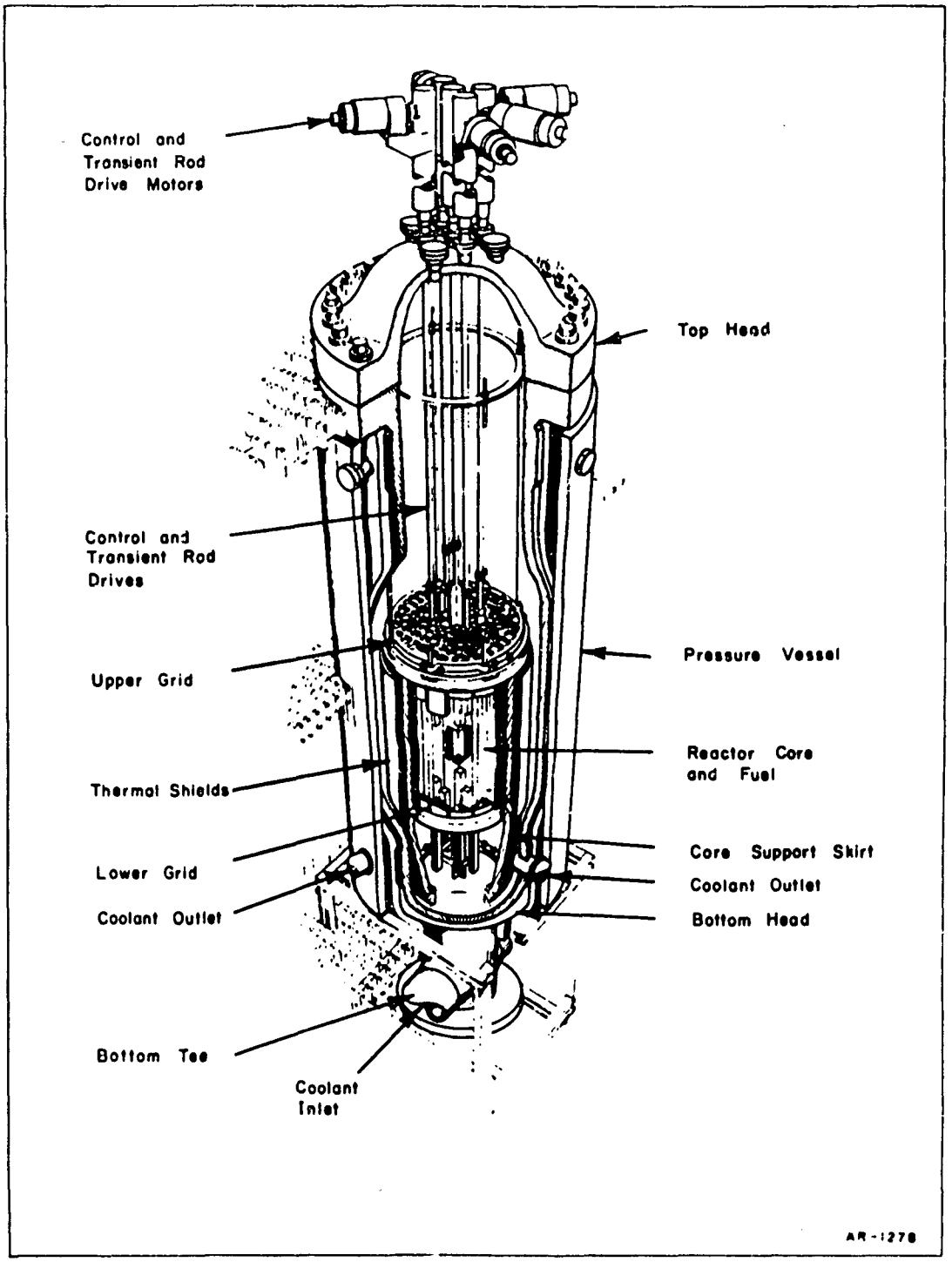

Fig. 1 Reactor vessel assembly.

of secondary coolant water. After entering the vessel bottom tee, the coolant flows upward through the core, reverses direction, and flows downward through the thermal shields leaving the vessel near the bottom.

The reactor core is confined by upper and lower grids and the core skirt. The E-core fuel is comprised of 4.8%-enriched UO_2 fuel rods restrained in stainless steel fuel assembly cans. The maximum number of E-core fuel assemblies that can be loaded in the core is 68. The UO_2 fuel, in the form of 0.42-inch diameter pellets, is contained in 40.8-inch long, 0.466-inch outside diameter Type 348 stainless steel tubes that have a wall thickness of 0.020 inch. There is a 0.003-inch radial, helium-filled gap between the fuel pellets and the cladding. Each of the fuel rods has an active length of 38.3 inches and contains 38.5 grams of U-235. There is a 2.5 inch expansion space at the top of each fuel rod in which a compression spring is positioned to keep the fuel pellets in place.

The cross section and coordinate numbering system for the E-core are illustrated in Figure 2. The fuel assembly locations in the core are designated by the quadrants (N, E, S, and W). The letter "R" indicates that the fuel assembly is removable. The majority of the fuel rods are restrained in 48 3- by 3-inch square assembly cans that contain 25 rods in a 5 by 5 rectangular array with a square pitch of 0.585 inch. The central nine of these 25 rods are removable for inspection. There are 12 smaller 2.5- by 2.5-inch square fuel assembly cans, each containing 16 fuel rods arranged in a 4 by 4 rectangular array with the same pitch as the 25-rod assemblies. Four of the 16-rod assemblies surround the centrally located transient rod guide, and the remaining eight 16-rod assemblies form fuel followers of the eight E-core control rods. The central four fuel rods contained in the assemblies surrounding the transient rod guide are removable for inspection. In addition, the S11 assembly was modified so that the corner fuel rod nearest the transient rod center was removable for instrumentation and inspection because this fuel rod is near the core thermal flux peak.

Figure 2 also indicates the component placement in the E-core. The cruciform-shaped transient rod used for initiating reactor power excursions is located at the core center. The four control rod pairs are indicated by shading. The space between fuel assemblies and the cylindrical core skirt

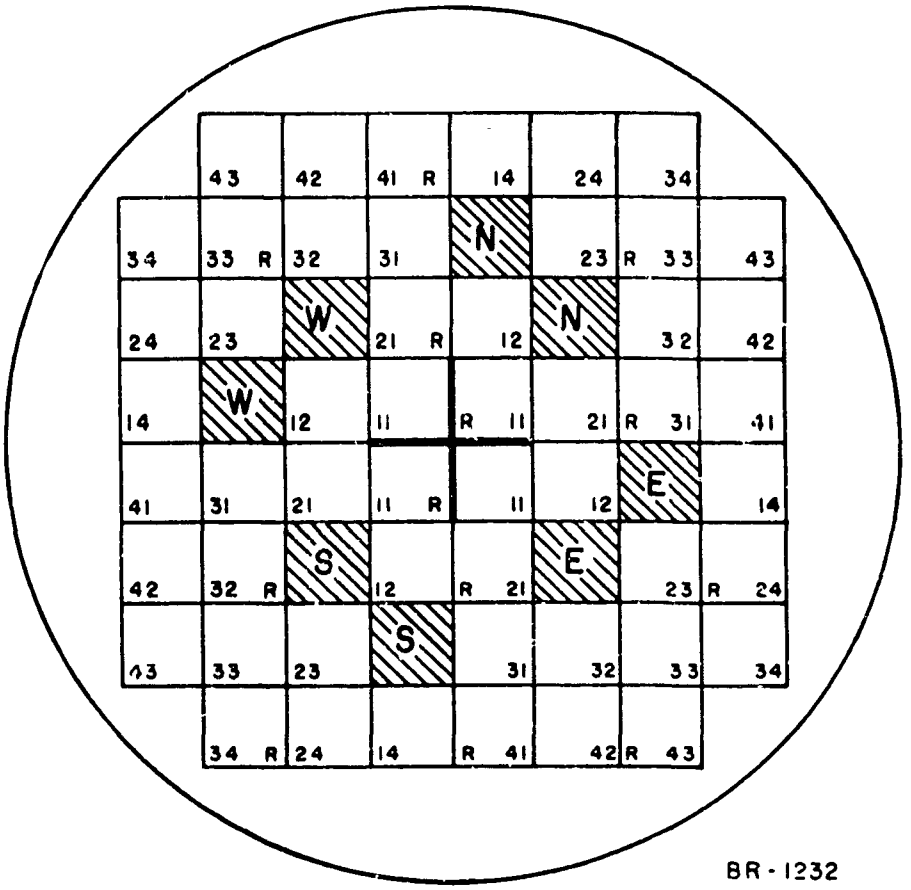

Fig. 2 Spert III E-core lattice.

is occupied by stainless steel filler pieces. A brief summary of the E-core design characteristics is presented in Table I.

2. INSTRUMENTATION FOR TRANSIENT TESTS

The variables for which data were recorded during the Spert III transient tests were reactor power, fuel rod surface temperature, transient pressure, and bulk water temperature. Data were obtained from detectors in the reactor and recorded as analog signals in real time at the control center. The low level signals from the detectors were amplified in the instrument bunker prior to transmission through 3000 feet of coaxial cable to the control center. Time-dependent electrical signals were then recorded on both optical oscillographs and magnetic tape at the control center.

TABLE I

DESIGN CHARACTERISTICS OF THE SPERT III E-CORE

Component	Specification
Vessel and Primary System	
Vessel Type	All-welded multilayer vessel
Vessel Composition	304L stainless steel
Vessel Size	4-ft ID by 23-3/4 ft long
Design Pressure	2500 psig
Design Temperature	700°F
Flow Characteristics	0 to 20,000 gpm upward through core
Heat Removal Capabilities	Up to 60 MW for 1/2-hr duration
Core	
Configuration	Approximately cylindrical, 26-in. diameter
Number and Type of Fuel Assemblies	48 twenty-five-rod assemblies 12 sixteen-rod assemblies
Moderator-Reflector	Light water
Nonmoderator-to-Moderator Ratio	1.03
Fuel	
Type	UO_2 pellets
Length of Fuel Rods	40.8 in.
Active Length	38.3 in.
Pitch	Square, 0.589 in.
Fuel Rod OD	0.466 in.
Clad Thickness	0.020 in.
Enrichment	4.8 percent
UO_2 Density	10.5 g/cm^3
Mass of UO_2 per Fuel Rod	913.5 g
Mass of U-238 per Fuel Rod	766.4 g
Mass of U-235 per Fuel Rod	38.5 g
Cladding	Type 348 stainless steel
Control Rods	
Number and Type	8 total, coupled in units of 2 per quadrant

TABLE I (CONTINUED)

DESIGN CHARACTERISTICS OF THE SPERT III E-CORE

Component	Specification
Composition	Fuel follower and Type 18-8 stainless steel with 1.35 wt% B-10
Dimension of Poison Section	2.496 in. square by 46 in. long
Dimension of Fuel Follower	2.496 in. square by 45-41/64 in. long
Transient Rod	
Type	Cruciform shape
Composition	Upper section: 18-8 stainless steel Poison section: 1.35 wt% B-10 stainless steel
Length	Poison section: 38 in.

Kinetic reactor response was determined primarily from the reactor power data. The principal features of this response included the initial asymptotic power rise, peak power, power burst shape, and runout power. To obtain these features it was sufficient to measure the reactor power rise over six decades. This was done using five uncompensated B-10 lined ion chambers located at different distances from the core. For the low-initial-power transient tests, the reactor power began to deviate from an exponential rise one or two decades below peak power. Since two decades of power rise were desired for the period measurements, four decades of power coverage were required below the expected peak power. In addition, one or two decades of power coverage above the expected peak were required to ensure that the peak power was indeed measured. For the five ion chambers, the current output as a function of the reactor power level was established during static experiments by means of cobalt wire activation measurements at various system temperatures and by primary system heat balance experiments at a temperature of 500°F[17].

Fuel rod cladding surface temperatures were measured throughout the E-core using 38 fine-wire, Chromel-Alumel thermocouples. The ends of the thermocouple wires were slightly flattened and separately attached to the

fuel rod surfaces by resistance welding. The thermocouples were distributed such that a three-dimensional temperature distribution in the core could be obtained. In addition, they were positioned at the suspected core hot spots. All except eight of the thermocouples were stainless steel sheathed (magnesium-oxide insulated) and constructed so that they could withstand large coolant flow rates. Eight faster response, unsheathed (bare junction) thermocouples were installed for the purpose of calibrating the stainless steel sheathed thermocouples during the low-initial-power transient tests. These were located in core positions near the stainless steel sheathed thermocouples.

Moderator temperatures were measured by stainless steel sheathed (magnesium-oxide insulated) thermocouples. There were seven thermocouples located in the bottom tee, and the average of these thermocouples was used to record the moderator inlet temperature. There were four thermocouples located near the upper grid, and the average of these was used to represent the moderator outlet temperature. Thermocouples were also used to measure the moderator temperature at four fuel assembly outlets.

Pressure transducers were mounted near the core to measure transient pressure pulses that could result from moderator and metal expansion during power excursions. Pressure measurements were made using bonded strain gauge, diaphragm-type transducers mounted in protective steel housings. During the cold-startup tests two transducers having a 100 psig full-scale output were mounted over the W33 and the E34 fuel assemblies. A 3000 psig full-scale transducer was mounted at the edge of the core at the axial center line. A 3000 psig full-scale transducer was also mounted in the bottom tee.

3. STATIC NUCLEAR CHARACTERISTICS OF THE CORE

Static nuclear experiments were performed with the E-core prior to the low-initial-power tests. These measurements were required to perform the reactivity accident tests and to analyze the kinetic results. The static nuclear characteristics measured were the critical and operational core loadings, neutron flux distributions, power calibrations of the ion chambers, control rod worths, temperature and void coefficients, and the reduced prompt neutron generation time. With a total mass of 1271.5 kg of UO_2, the core had

an excess reactivity of 14$ at ambient temperature and a 4.7$ excess reactivity at 500°F low power. A summary of selected static nuclear characteristics of the E-core is presented in Table II.

TABLE II

EXPERIMENTAL AND CALCULATED CHARACTERISTICS OF THE SPERT III E-CORE

Coolant Inlet Temperature (°F)	Peak-to-Average Power Density	Moderator Temperature Coefficient of Reactivity (¢/°F)	Uniform Void Coefficient (¢/%void)	Doppler Coefficient of Reactivity (¢/°F)	Reduced Prompt Neutron Generation Time (msec)
70	5.7	-0.4	-50	-0.72[b]	2.15
250	5.2	-2.0	-42[b]	-0.56[b]	2.18[b]
500	3.6	-4.0	-35[b]	-0.37[b]	2.25[b]
500[a]	3.2[b]	-4.1[b]	-37[b]	-0.23[b]	2.25[b]

[a] At 20 MW steady state power.

[b] Calculated values.

III. EXPERIMENTS AND ANALYSIS

The Spert III E-core reactivity accident tests were performed to obtain power excursion data under operating conditions similar to those of commercial PWR's. Operating conditions selected for experimental and analytical investigations included cold-startup, hot-startup, hot-standby, and operating-power conditions.

The sequence of reactivity accident testing was from what was considered to be the least to the most severe, and testing was begun at cold-startup conditions and concluded at operating-power conditions. Prior to the E-core tests, no power excursion data were available for operating conditions other than cold-startup for low-enriched oxide cores. The purposes of the cold-startup tests were to obtain data to correlate with the results of cold-startup tests obtained from other oxide cores and to verify that the analytical models, developed using the results from these other oxide cores, were applicable to the E-core. Verification of the analytical models was expected to form a sound basis for prediction of the E-core kinetic behavior for other accident conditions. The hot-startup tests were performed to obtain experimental information that would extend the available knowledge of the transient behavior of an oxide-fueled reactor to include initial conditions of coolant flow and elevated system temperature and pressure. To determine the effects of system temperature, coolant flow, and reactivity insertion on the kinetic behavior of the E-core, only one parameter was varied for each hot-startup test. An understanding of the E-core kinetic behavior during the hot-startup tests provided a basis for the next sequence of experiments which were performed to investigate the effects of initial steady state power on kinetic behavior. These high-initial-power tests provided experimental power excursion data typical of reactivity accidents initiated from hot-standby and operating-power conditions.

The analytical portion of the Oxide Core Kinetics Program consisted of (a) analyses of experimental data and (b) analyses of calculational results obtained using analytical models. Analyses of the experimental data were made to gain insights into the general kinetic behavior of the E-core for the range of initial accident conditions considered. In these analyses, the power burst shapes, peak reactor powers, and energy releases were investigated.

In addition, comparisons of the experimental results for each accident condition with results from either previously tested oxide-fueled cores or other E-core accident conditions were performed. The analyses performed using calculational models were made to obtain more information about the reactor kinetic behavior than could be observed from the experimental data alone. These investigations were primarily concerned with evaluating the dynamic reactivity feedback mechanisms that limit the reactivity accidents, and determining the transient temperature distributions in the E-core. The most important part of the analytical program was to evaluate the capabilities of the calculational models in predicting the reactor kinetic response; therefore, comparisons were made between the experimental and analytical results for each accident condition.

The experimental data selected for investigation were the reactor power, energy release, reactivity compensation, power burst shape, and fuel rod cladding surface temperature. To aid in the analyses, polynomial curves were least-squares fitted to experimental data for peak power, energy release to peak power, and reactivity compensation at peak power as functions of either reciprocal period or reactivity insertion. A curve calculated using an analytical model can be meaningfully compared with an experimental least-squares fitted curve provided that the confidence in the experimental curve is known. Therefore, 65% confidence bands were determined for the least-squares fitted curves. These confidence bands imply that if a set of experiments was repeated 100 times and a least-squares fitted curve determined for each set of data, then 65 of the fitted curves would lie within the confidence bands. For the 260°F hot-startup tests and the high-initial-power tests, too few experiments were performed to allow the calculation of statistically meaningful confidence bands. For these cases, vertical or horizontal error bars that represent an experimental uncertainty of one standard deviation are given for the experimental data. Comparisons of calculational results with the 260°F hot-startup and high-initial-power experimental data must be made only on a point-wise basis. However, the least-squares fitted curves are also presented as an aid in the general interpretation of the data.

Reactor power excursion behavior for the E-core was calculated using the PARET and IREKIN digital computer codes. The point-reactor kinetics equations are used in both codes. In the IREKIN code, the time-dependent core energy release is calculated and the Doppler reactivity feedback is

determined from a table of core energy release versus feedback that is input to the code. This table of Doppler reactivity feedback is determined from the feedback model developed in Reference 5. No provisions for coolant flow are allowed in the IREKIN code and only Doppler reactivity feedback was considered. The PARET code calculates the coupled thermal, hydrodynamic, and nuclear behavior of the reactor. Continuous reactivity feedback is calculated as the sum of feedbacks from Doppler broadening, moderator expansion, void formation, and fuel rod expansion. In PARET the reactor core can be represented by up to four coolant channel-fuel rod regions. A detailed description of the input parameters used in the PARET code is contained in Appendix B.

1. COLD-STARTUP REACTIVITY ACCIDENT TESTS

The purpose of the cold-startup reactivity accident tests was to obtain experimental E-core power excursion data for correlation with analytical and other experimental results. These correlations were expected to form a sound basis for predictions of E-core behavior for the other accident conditions. Altogether, 40 cold-startup reactivity accident tests were performed with the E-core. The tests were initiated with rapid reactivity insertions ranging from 0.68 to 1.21$. Power excursions with initial reactor periods from 1.9 sec to 10 msec resulted from these insertions.

1.1 Experimental Results

A tabulation of the cold-startup reactivity accident test data is presented in Table III. The listed uncertainties in these data represent one standard deviation. In preparation for test 12 a 0.27$ criticality shift[18] occurred. This criticality shift was caused by a loose flux suppressor in one of the control rod assemblies. The control rod assembly was repaired and transient testing was resumed. A statistical analysis of the cold-startup test data, obtained before and after control rod repair, indicated that the loose flux suppressor caused a slight change in the kinetic behavior of the core. Therefore, results from the first 12 cold-startup tests are not presented in this report. No criticality shifts occurred during the remainder of the cold-startup accident tests.

The significant features of the data presented in Table III will be discussed in the following sections.

TABLE III

DATA SUMMARY FOR COLD-STARTUP ACCIDENT TESTS

Test No.	Reactor Period (msec)	Initial Reactivity Insertion ($)	Initial Primary Coolant Temperature (°F)	Maximum Reactor Power (Mw)	Energy Release to Time of Peak Power (Mw-sec)	Time to Peak Power (sec)	Maximum Measured Fuel Cladding Surface Temperature Rise (°F)	Reactivity Compensation at Peak Power ($)
32	1010 ± 20	0.37 ± 0.03	74 ± 4	2.1 ± 0.3	6.9 ± 1.2	13.7 ± 0.2	93 ± 9	0.26 ± 0.03
15	351 ± 7	0.90 ± 0.01	70 ± 4	4.3 ± 0.6	6.7 ± 1.1	5.3 ± 0.1	99 ± 10	0.23 ± 0.03
13	206 ± 4	0.93 ± 0.01	63 ± 4	5.6 ± 0.8	5.1 ± 0.9	3.2 ± 0.06	127 ± 13	0.19 ± 0.02
14	195 ± 4	0.94 ± 0.01	64 ± 4	5.6 ± 0.8	5.3 ± 0.9	3.2 ± 0.06	104 ± 10	0.20 ± 0.02
37	117 ± 2	0.97 ± 0.01	65 ± 4	8.1 ± 1.2	4.7 ± 0.8	1.77 ± 0.03	143 ± 14	0.17 ± 0.02
33	111 ± 2	0.97 ± 0.01	70 ± 4	7.7 ± 1.2	4.2 ± 0.7	1.61 ± 0.03	131 ± 13	0.16 ± 0.02
16	96.8 ± 1.9	0.98 ± 0.01	75 ± 4	8.2 ± 1.2	3.6 ± 0.6	1.40 ± 0.03	160 ± 16	0.13 ± 0.01
17	96.1 ± 1.9	0.98 ± 0.01	66 ± 4	8.0 ± 1.2	3.4 ± 0.6	1.37 ± 0.02	125 ± 13	0.13 ± 0.01
50	93.7 ± 1.9	0.98 ± 0.01	82 ± 4	9.2 ± 1.4	3.3 ± 0.6	1.47 ± 0.04	150 ± 15	0.11 ± 0.01
12	93.2 ± 1.9	0.98 ± 0.01	77 ± 4	8.3 ± 1.2	3.8 ± 0.6	1.55 ± 0.03	132 ± 13	0.14 ± 0.01
72	91.6 ± 1.8	0.98 ± 0.01	69 ± 4	8.5 ± 1.3	4.0 ± 0.7	1.55 ± 0.06	140 ± 15	0.14 ± 0.02
71	94.0 ± 1.9	0.98 ± 0.01	82 ± 4	7.9 ± 1.2	3.6 ± 0.6	1.54 ± 0.06	145 ± 15	0.14 ± 0.02
11	91.0 ± 1.8	0.99 ± 0.01	66 ± 4	8.6 ± 1.3	3.3 ± 0.6	1.20 ± 0.05	117 ± 12	0.12 ± 0.01
51	89.3 ± 1.8	0.99 ± 0.01	87 ± 4	8.9 ± 1.3	3.1 ± 0.5	1.36 ± 0.04	143 ± 14	0.12 ± 0.01
67	87.0 ± 1.7	0.99 ± 0.01	66 ± 4	9.1 ± 1.4	3.8 ± 0.6	1.36 ± 0.04	187 ± 19	0.11 ± 0.01
73	83.0 ± 1.6	0.99 ± 0.01	67 ± 4	8.8 ± 1.3	3.0 ± 0.5	1.40 ± 0.04	150 ± 15	0.13 ± 0.01
31	78.3 ± 1.6	1.00 ± 0.01	82 ± 4	11 ± 2	2.4 ± 0.4	1.08 ± 0.02	130 ± 13	0.09 ± 0.01
69	83.4 ± 1.1	1.00 ± 0.01	76 ± 4	11 ± 2	2.1 ± 0.4	0.97 ± 0.04	142 ± 14	0.08 ± 0.01
10	89.3 ± 1.8	1.01 ± 0.01	67 ± 4	12 ± 2	2.0 ± 0.3	0.86 ± 0.01	116 ± 12	0.08 ± 0.01
35	55.5 ± 1.1	1.02 ± 0.01	66 ± 4	16 ± 2	2.1 ± 0.4	0.79 ± 0.02	166 ± 17	0.07 ± 0.01
19	44.9 ± 0.5	1.03 ± 0.01	69 ± 4	18 ± 3	1.9 ± 0.3	0.63 ± 0.01	119 ± 12	0.07 ± 0.01
20	35.0 ± 0.7	1.03 ± 0.01	72 ± 4	24 ± 4	2.0 ± 0.3	0.54 ± 0.01	121 ± 12	0.08 ± 0.01
75	33.0 ± 0.7	1.06 ± 0.01	68 ± 4	31 ± 5	2.1 ± 0.4	0.450 ± 0.02	152 ± 15	0.08 ± 0.01
21	28.3 ± 0.6	1.09 ± 0.01	72 ± 4	36 ± 5	2.8 ± 0.5	0.38 ± 0.01	118 ± 12	0.11 ± 0.01
40	22.0 ± 0.4	1.09 ± 0.01	67 ± 4	59 ± 9	2.8 ± 0.5	0.39 ± 0.01	153 ± 16	0.11 ± 0.01
48	21.1 ± 0.4	1.09 ± 0.01	74 ± 4	63 ± 9	2.8 ± 0.5	0.37 ± 0.01	141 ± 14	0.11 ± 0.01
47	19.9 ± 0.4	1.09 ± 0.01	72 ± 4	67 ± 10	3.0 ± 0.5	0.36 ± 0.01	156 ± 16	0.12 ± 0.01
41	15.9 ± 0.3	1.13 ± 0.05	70 ± 4	110 ± 17	3.8 ± 0.6	0.31 ± 0.02	146 ± 15	0.14 ± 0.01
42	12.6 ± 0.3	1.17 ± 0.05	73 ± 4	170 ± 26	4.6 ± 0.8	0.250 ± 0.006	147 ± 15	0.18 ± 0.02
43	10.0 ± 0.2	1.21 ± 0.05	73 ± 4	250 ± 42	6.0 ± 1.0	0.230 ± 0.006	148 ± 15	0.22 ± 0.02

1.11 Reactivity, Energy, and Power Burst Shapes. Reactivity compensation and energy release to the time of peak power as functions of reciprocal period for the cold-startup tests are shown in Figure 3. Least-squares fitted lines to the experimental data and associated 65% confidence bands are also shown. The similarity of the two curves indicates that the reactivity compensation at the time of peak power is directly related to the energy release, and the shape of the compensated reactivity curve is characteristic of most light-water-moderated reactors. The dip in the curve would not be present in reactors which have very long reduced prompt neutron lifetimes ($>10^{-1}$ sec) or which exhibit extremely broad or narrow power bursts[19].

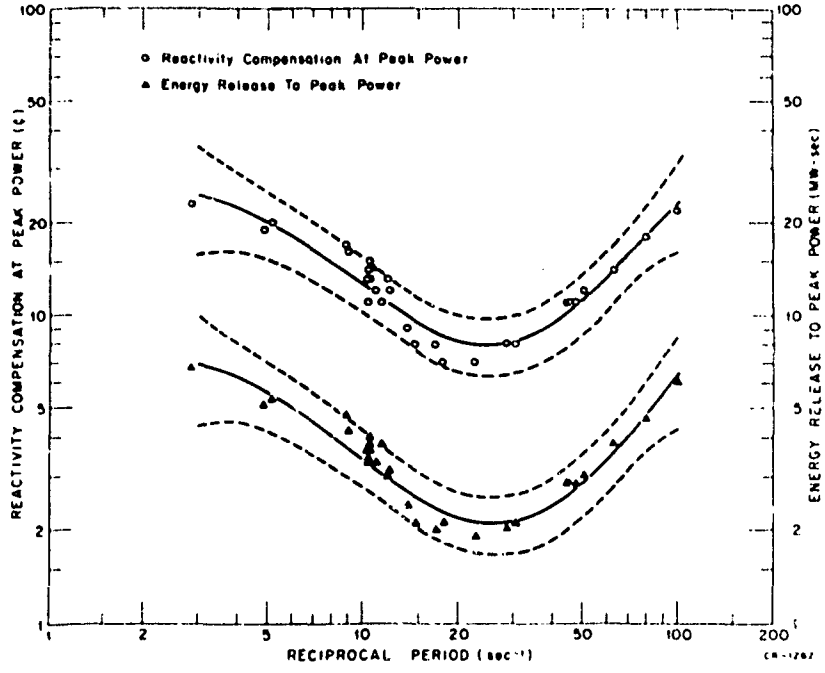

Fig. 3 Experimental energy release to the time of peak power and reactivity compensation at peak power as functions of reciprocal period for the cold-startup tests.

Four power burst shapes are shown in Figure 4. These are for two long-period[a] tests (periods of 206 and 95.7 msec), a test near prompt critical (period of 59.3 msec), and a short-period test (period of 10 msec). For each test, the power is normalized to peak power and the time is normalized to reactor period. In general, the burst shape depends on the reactivity feedback

[a] For the E-core, prompt critical occurs at a period of about 40 msec (reciprocal period, α_o, of 25 sec^{-1}). Long-period transients have periods longer than 40 msec and short-period transients have periods shorter than 40 msec.

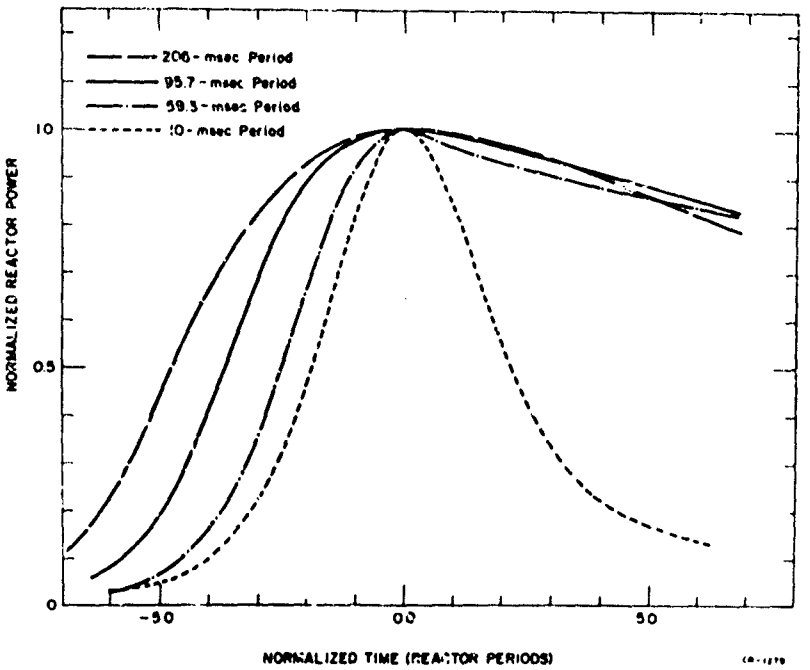

Fig. 4 Experimental power burst shapes for the cold-startup tests.

and the effective neutron lifetime. The reactivity feedback is a function of the energy release, and the effective neutron lifetime depends on delayed neutron contributions. High power levels and large energy releases result from short-period transients, while relatively low power levels and small energy releases result from long-period transients. The 10-msec period burst shape shown in Figure 4 is sharply peaked and almost symmetric because the energy release per unit time is large and the delayed neutron contribution is relatively small during the short transient time. The 206-msec period burst shape is characterized by a relatively broad curve that is asymmetric about its peak. This asymmetry results because the energy release per unit time is small and the time required to reach peak power is long. As a result, the delayed neutrons after peak power are being produced almost as fast as they are being removed from the system, so that a relatively high power level is maintained. Before peak power the system is less dependent on delayed neutron effects than after peak power. However, the burst shape for the 206-msec period test is more dependent on delayed neutron effects before peak power than is the burst shape for the 10-msec period test. The 95.7- and 59.3-msec period power burst shapes demonstrate the trend of more sharply peaked bursts as the reactor period decreases.

1.12 Clad Surface Temperatures. It was necessary to use stainless steel sheathed thermocouples to measure the fuel rod cladding surface temperatures for all tests except the cold-startup and 260°F initial temperature transient tests. Since these stainless steel sheathed thermocouples have slow response times, eight fast-response, unsheathed (bare-junction) thermocouples were used in an attempt to obtain a correction factor. The unsheathed thermocouples were located in core positions near the sheathed thermocouples. Temperature data obtained during the cold-startup and 260°F initial temperature transient tests for both thermocouple types were analyzed, using transfer function approximations, to obtain the correction factor.

For the 260°F initial temperature tests, the sheathed and unsheathed thermocouple responses were about the same. For the cold-startup tests, two unexpected results were observed. The first was that some sheathed thermocouples gave faster response times than the unsheathed thermocouples. The second was that the temperature traces measured by some corresponding sheathed and unsheathed thermocouples crossed during the temperature rise. This unexpected behavior of thermocouple responses could have resulted from differences in the gas gap thicknesses separating the fuel pellets and cladding where the sheathed and unsheathed thermocouples were attached. Because of these unexpected results, no suitable transfer function could be developed for all thermocouple pairs and thus no correction factors were used. The core hot-spot clad surface temperature was measured using a stainless steel sheathed thermocouple located on the corner rod of the S11 fuel assembly. Since no correction factor was obtained, no time-dependent hot-spot clad surface temperatures will be presented in this report.

During cold-startup tests initiated with reactivity insertions larger than about 0.95$, maximum measured fuel rod cladding surface temperatures reached nucleate boiling but did not exceed 260°F during any of these tests. The fuel rod surface temperatures measured near the core hot-spot were characterized by rather smooth, fast rising traces that reached quasi-equilibrium values at the nucleate boiling temperature (≈205°F), or slightly higher. Maximum temperatures were measured during nucleate boiling which began one to two seconds after peak power, depending on the reactor period. The shorter the period the sooner nucleate boiling began. The maximum measured fuel rod cladding

surface temperature rises are listed in Table III for the cold-startup tests. The maximum measured temperature during the entire cold-startup tests was 253°F.

1.2 Comparison with Previous Experimental Results

The Spert I Oxide Core (OC)[3] and the Spert IV Capsule Driver Core (CDC)[6], previously tested under cold-startup accident conditions, differ somewhat from the Spert III E-core. Some characteristics of these three cores at a system temperature of 70°F are listed in Table IV. Assuming that power excursions in these three cores are principally limited by reactivity feedback arising from Doppler broadening of the U-238 resonance absorption cross sections, relative transient behavior of these cores can be estimated using the tabulated characteristics. During an excursion, the peak reactor power and energy release are dependent on the Doppler reactivity feedback, the fuel mass and enrichment, and the reduced prompt neutron generation time. The Doppler feedback is a function of the epithermal neutron flux spectrum,

TABLE IV

CHARACTERISTICS OF THREE OXIDE CORES AT 70°F

	Spert IV CDC	Spert I Oxide Core	Spert III E-Core
Total mass of UO_2 fuel in the core (K_g)	2643	958	1271
Density of UO_2 fuel (g/cm^3)	9.29	9.45	10.5
Percent U-235 Enrichment	3.0	4.0	4.8
Active length of the core (in.)	67	67	38
Control rod bank critical position (in. above bottom of the core)	27.4	26.3	14.6
Peak-to-average thermal neutron flux ratio	3.5	3.1	5.7
Reduced prompt neutron generation time (msec)	4.18	3.57	2.15
Nonmoderator-to-moderator ratio	0.807	0.807	1.0
Available excess reactivity ($)	2.9	3.2	14

which is related to the nonmoderator-to-moderator ratio. The larger this ratio, the more feedback expected. Since the Spert IV CDC and Spert I OC reactors have the same nonmoderator-to-moderator ratio and about the same reduced prompt neutron generation times, the relative peak reactor powers and energy releases can be related by the fuel masses and enrichments. Therefore, the CDC would be expected to yield peak powers and energy releases that are about twice [(2643 kg/958 kg) (3%/4%)] as large as the Spert I OC results for identical reactivity insertions. On this basis, the E-core is estimated to yield peak powers and energy releases that are about 1.6 times [(1271 kg/958 kg) (4.8%/4%)] as large as the Spert I OC results for identical reactivity insertions. However, the E-core has a larger nonmoderator-to-moderator ratio than do the other two cores; therefore, more Doppler feedback per unit power density would be expected and would reduce this difference.

The peak power versus reactivity insertion for the three cores is shown in Figure 5. The curves are results of least-squares fitting the experimental data. For the CDC, the peak powers are about twice those of the Spert I OC for the range of reactivity insertions considered. This result was anticipated

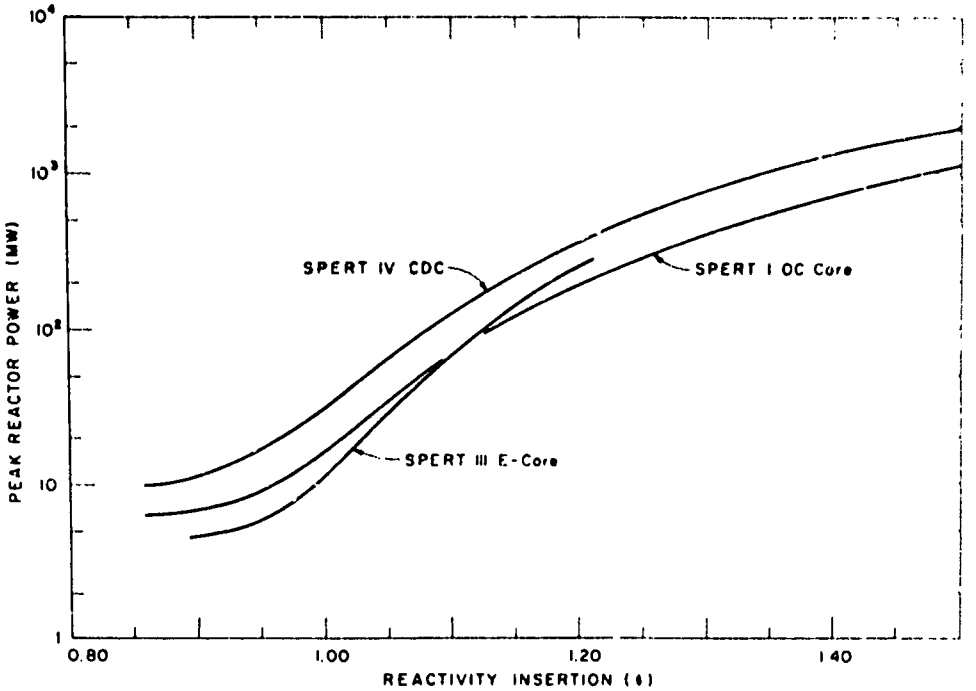

Fig. 5 Experimental peak reactor power as a function of reactivity insertion for the Spert IV CDC, the Spert I OC core, and the Spert III E-core cold-startup tests.

from the ratios of the fuel masses and enrichments. For subprompt critical transients, the E-core peak powers are about 0.7 times the corresponding Spert I OC peak powers. This result indicates the significant difference in Doppler feedback for the two cores caused by the differing nonmoderator-to-moderator ratios. For superprompt critical transients, the E-core peak powers are up to 1.2 times the corresponding Spert I OC peak powers. This result, which differs from that for the subprompt critical case, is not caused by decreased Doppler feedback, but by the smaller reduced prompt neutron generation time of the E-core. In the superprompt critical range, reactor periods are controlled by the reduced prompt neutron generation time. Thus, for a given reactivity insertion, a shorter reactor period results for the E-core than for the Spert I OC. In contrast, reactor periods in the subprompt critical range are controlled by delayed neutron effects, which are about the same for all three cores.

The hot-spot specific energy release at the time of peak power as a function of reactivity insertion is shown in Figure 6. The hot-spot specific energy release in each core was determined by multiplying the experimental

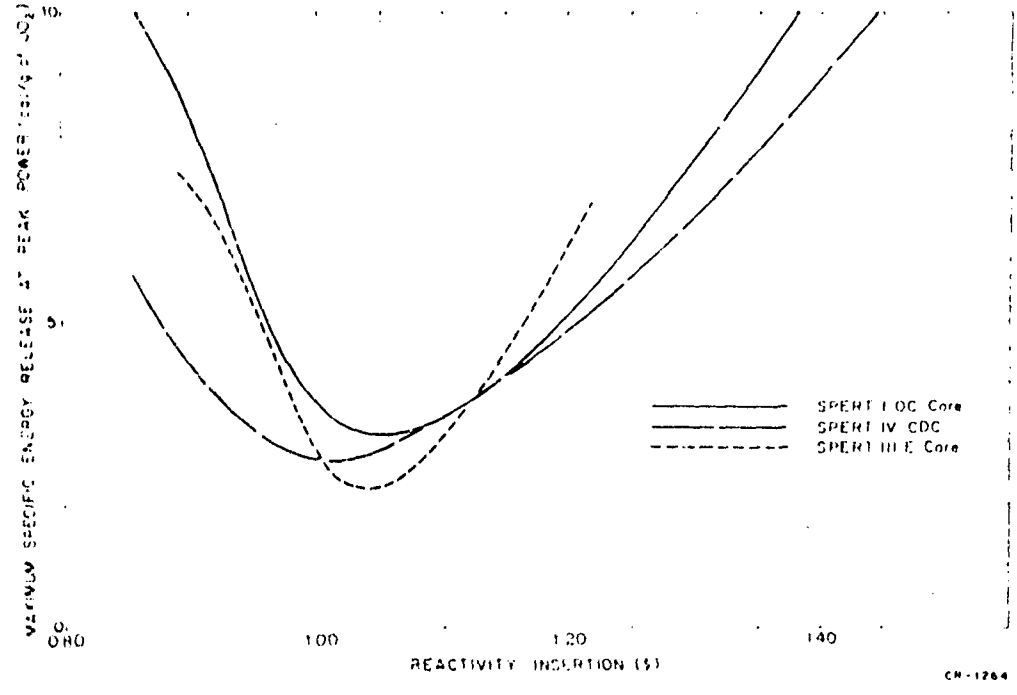

Fig. 6 Maximum specific energy release at the time of peak power as a function of reactivity insertion for the Spert IV COC, the Spert I OC core, and the Spert III E-core cold-startup tests.

least-squares fitted energy release by the peak-to-average thermal flux ratio and dividing by the total mass of fuel in the core. The maximum variation in the hot-spot specific energy release for the three cores is about a factor of 2 for subprompt critical transients and about 1.4 for superprompt critical transients. Because of this small variation for the superprompt critical range, it should be possible to estimate the hot-spot specific energy releases at the time of peak power for reactivity insertions up to 1.2$ in similar oxide-fueled cores using only the reactor characteristics.

1.3 Comparison of Experimental and Calculational Results

One of the objectives of the Spert III E-core Oxide Core Kinetics Program was to evaluate calculational models used to predict the kinetic behavior of the core for reactivity accident tests over a range of reactor conditions. Calculations of the kinetic behavior of the E-core for cold-startup accidents were performed using both the IREKIN and PARET computer codes. Results obtained using the two codes are compared with experimental data in the following paragraphs.

1.31 Peak Reactor Powers. The experimental peak power as a function of reciprocal period is shown in Figure 7, together with PARET- and IREKIN-calculated curves. The experimental curve is a least-squares fitted line to the data, and the associated 65% confidence bands are also shown. The IREKIN curve falls outside of the confidence bands for reciprocal periods between 5 and 90 sec^{-1} (periods between about 200 and 11 msec). The largest disagreement between the experimental and IREKIN curves is only about 30%. The PARET curve falls outside the confidence bands for reciprocal periods between 25 and 90 sec^{-1} (periods between 40 and 11 msec), and the largest disagreement between the experimental and PARET curves is also about 30%. For short-period transients, the PARET and IREKIN curves agree. This agreement was anticipated because the same Doppler reactivity feedback model was used for both codes, and because very little moderator reactivity feedback occurred. The disagreement between the experimental and calculated curves for short-periods indicates that calculated Doppler feedback was probably inaccurate. Errors in the calculated Doppler feedback could result from the Doppler model and/or fuel temperatures used in the Doppler calculations. The radially averaged temperature in the fuel rod was used instead of a temperature near the surface of the fuel rod, even though the latter is probably

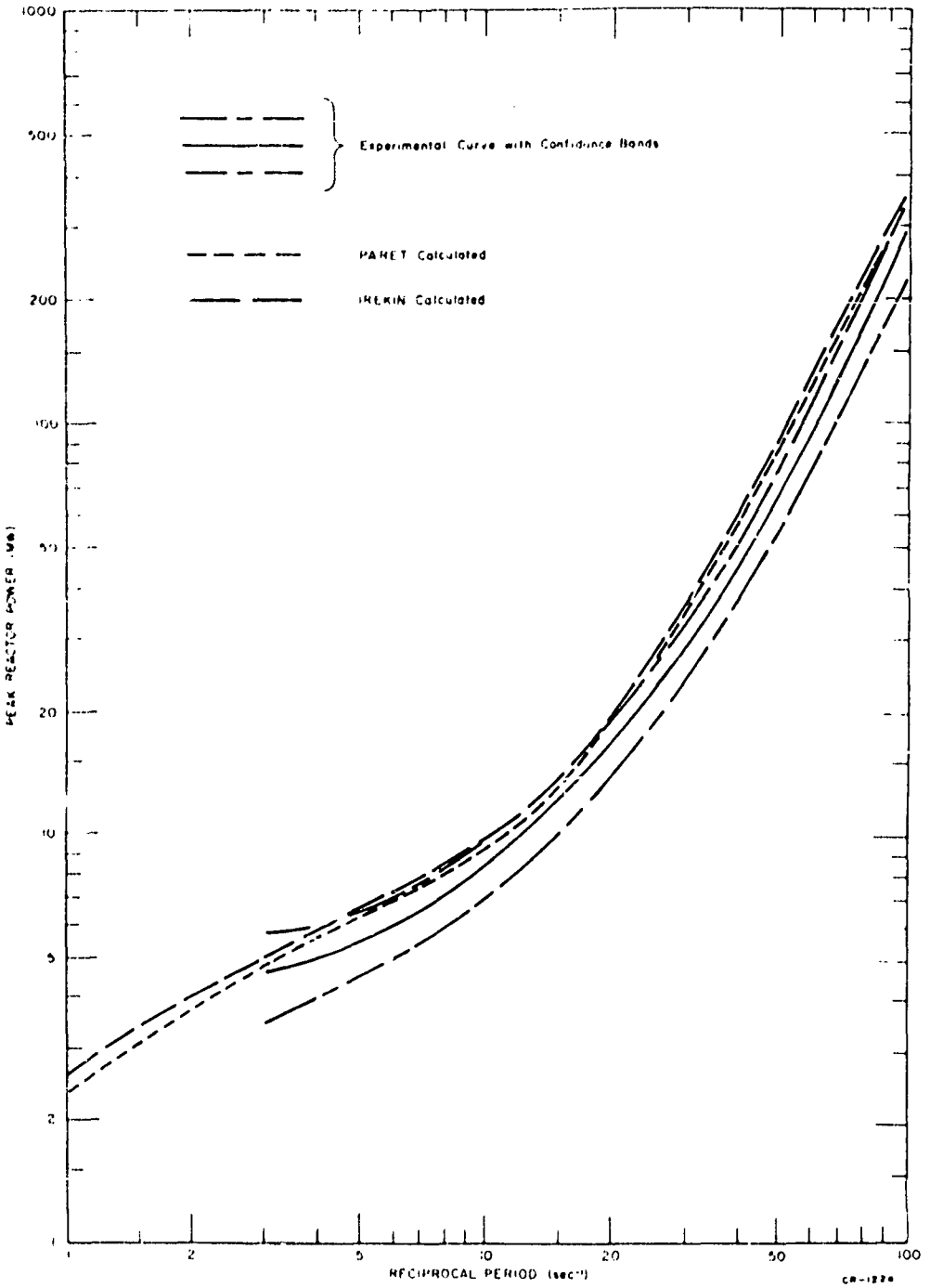

Fig. 7 Experimental, IREKIN, and PARET calculated peak reactor power as functions of reciprocal period for the E-core cold-startup tests.

more realistic. For the long-period tests, the PARET and IREKIN curves disagree because moderator feedback becomes more important and only Doppler feedback is considered in the IREKIN code.

1.32 Energy Release and Reactivity Compensation. The experimental reactivity compensation and energy release to the time of peak power are shown as functions of reciprocal period in Figure 8. The experimental curves are least-squares fitted lines to the data. The two parameters are shown together because reactivity compensation is directly related to the energy release. PARET- and IREKIN-calculated curves are also shown. The calculated reactivity compensation curves fall essentially within the confidence bands; however, both the PARET and IREKIN energy release curves fall outside the confidence bands for reciprocal periods between about 45 and 75 sec^{-1}. In the short-period range, the calculated energy release is up to 30% larger than experimental values. This result is not surprising since the calculated peak reactor powers were also as much as 30% larger than the experimental values in this period range, and the energy releases are obtained by integration of the calculated and experimental power traces.

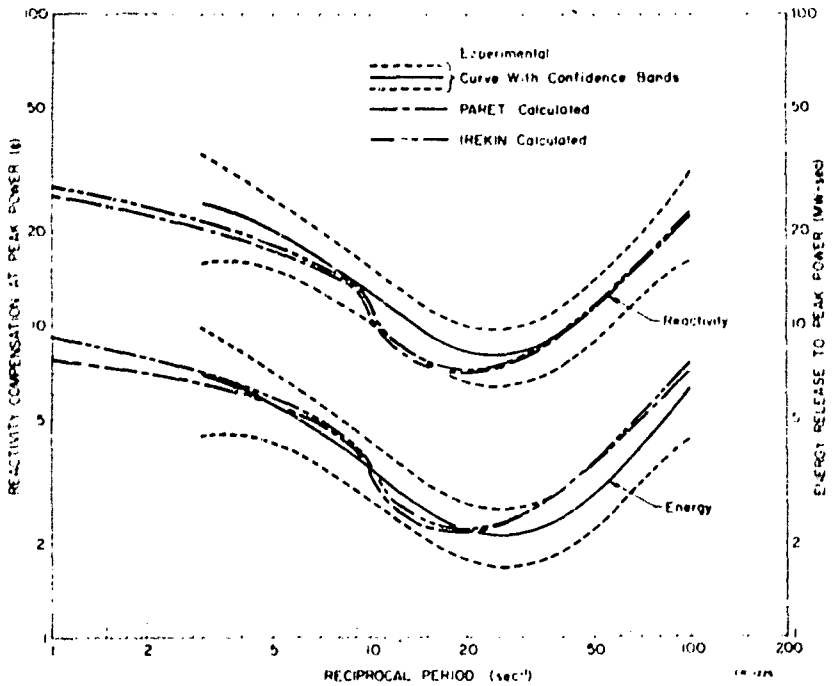

Fig. 8 Experimental, IREKIN, and PARET calculated energy release to the time of peak power and reactivity compensation at peak power as functions of reciprocal period for the cold-startup tests.

1.33 Power Burst Shapes. Time-dependent plots of the reactor power and energy release for 351-msec-period and 12.6-msec-period cold-startup tests are shown in Figures 9 and 10, respectively. For the long-period transient shown in Figure 9, the PARET-calculated peak power is about 7% and the IREKIN-calculated peak power about 15% larger than the experimental value. The power burst shape calculated using the PARET code more closely approximates the experimental burst shape than does the IREKIN curve. This better agreement results because the PARET code accounts for moderator heating reactivity feedback, and the IREKIN code does not. (The reactor scram was not included in the calculations.) For the short-period test shown in Figure 10, both calculated power burst shapes agree quite well with the experimental burst shape even though the magnitude of the calculated peak powers are about 30% larger than the experimental value. The agreement between the calculated and experimental time-dependent energy releases for both tests is essentially the same as the agreement for the reactor powers.

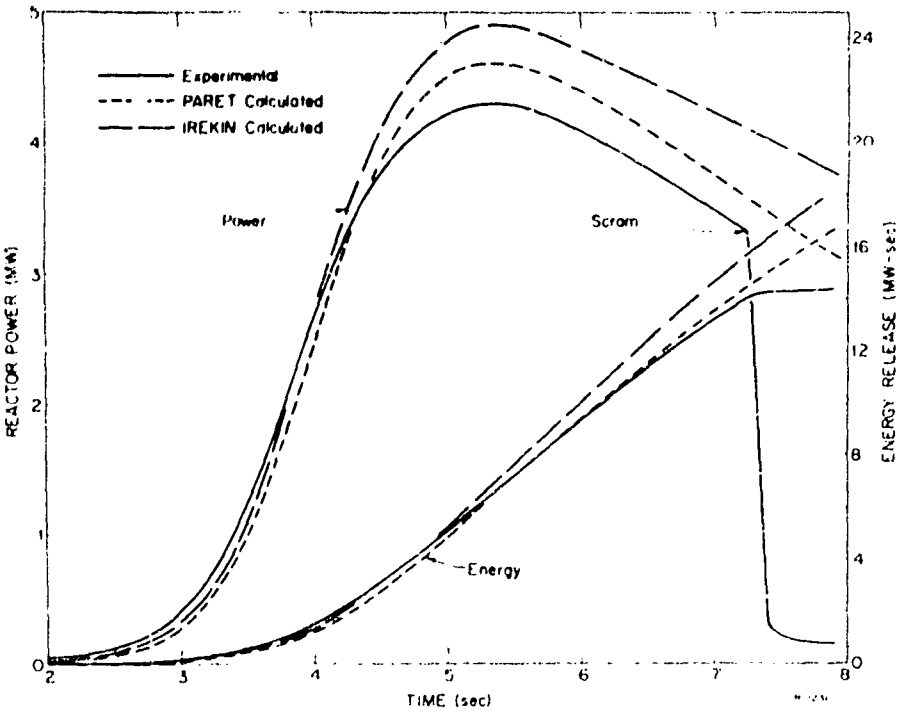

Fig. 9 Experimental, IREKIN, and PARET calculated reactor power and energy release for cold-startup test 18 (351 msec period).

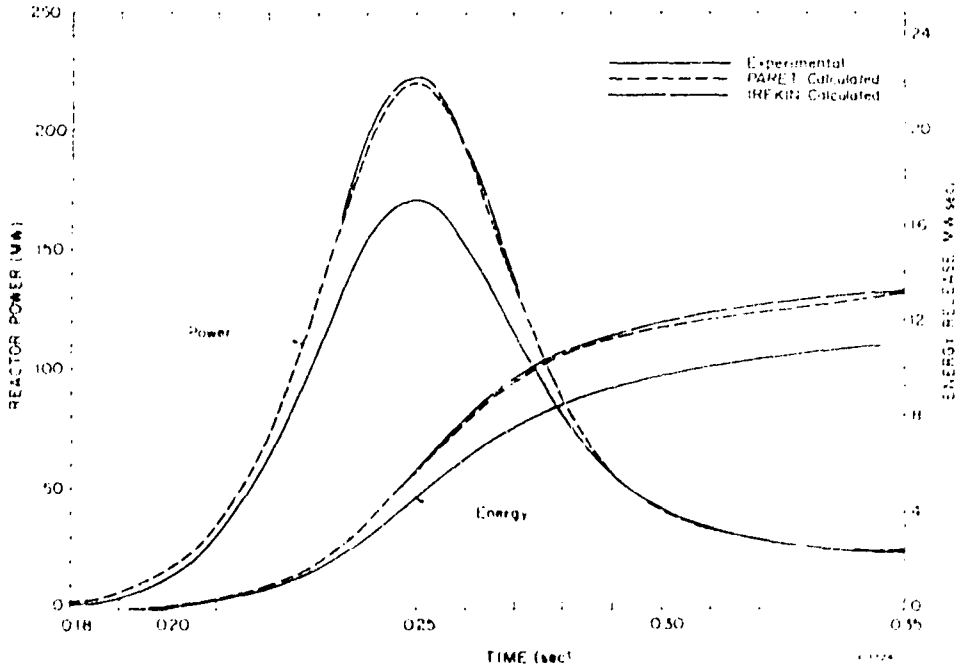

Fig. 10 Experimental, IREKIN, and PARET calculated reactor power and energy release for cold-startup test 42 (12.6 msec period).

1.34 Reactivity Feedback. Time-dependent plots of net system reactivity and total compensated reactivity for the 351- and 12.6-msec-period cold-startup tests discussed above are shown in Figures 11 and 12. The PARET-calculated reactivity feedback resulting from moderator heating and fuel rod expansion is also shown in these figures. For the long- and short-period transients both the IREKIN- and PARET-calculated net system and total compensated reactivity curves are about the same[a]. The largest disagreement between the experimental and calculated curves shown in these figures is 1 ¢ for the 12.6-msec-period test. At the time of peak power, PARET-calculated moderator-compensated reactivity accounts for about 20% of the reactivity compensation for the 351-msec-period transient, but only for about 5% for the 12.6-msec-period transient.

---

[a] For long-period transients, where clad-water heat transfer becomes important, the apparently good agreement between the IREKIN calculations and experimental results arises because the calculations assume that 97% of the energy is retained in the fuel rods. Thus, the Doppler feedback is overestimated because heat transfer would allow a larger percentage of the energy to escape from the fuel.

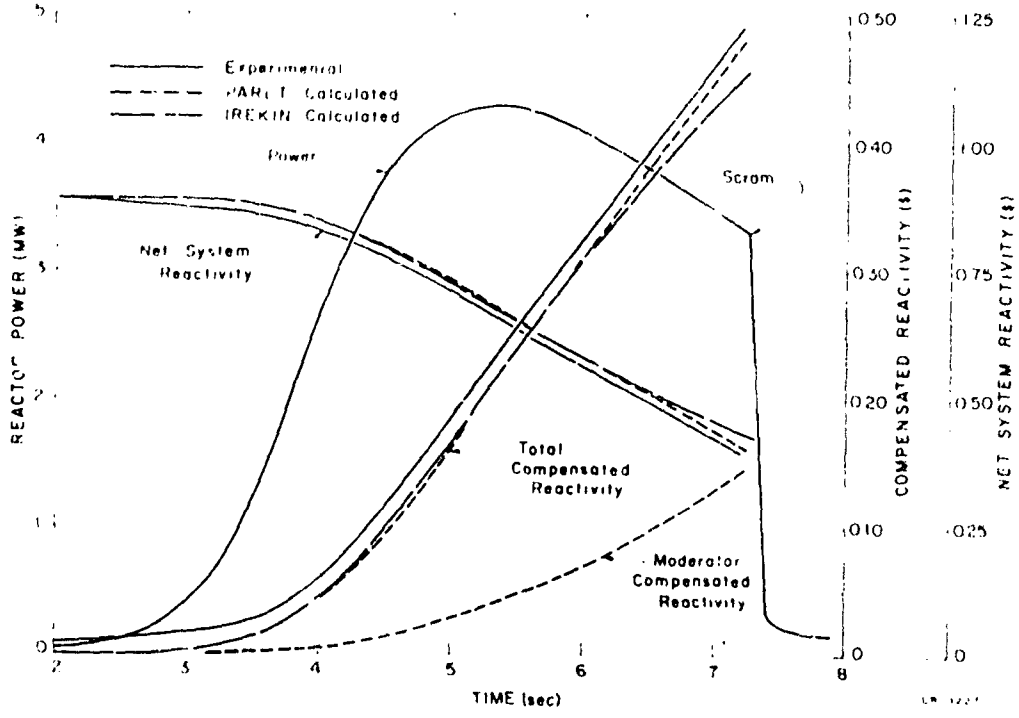

Fig. 11 Experimental, IREKIN, and PARET calculated net system and total compensated reactivity for cold-startup test 18 (351 msec period).

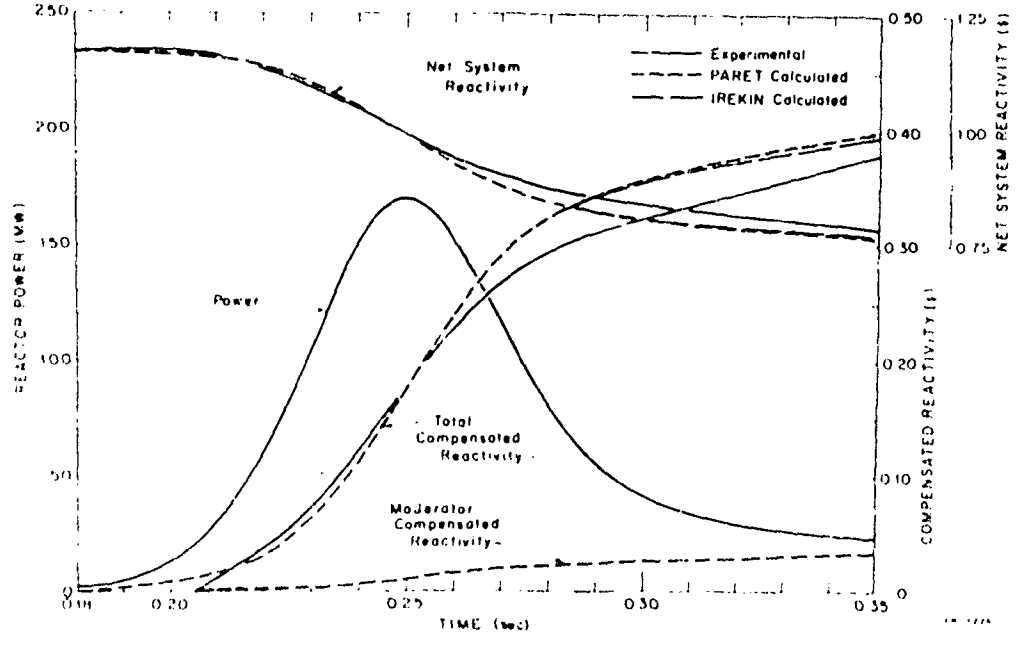

Fig. 12 Experimental, IREKIN, and PARET calculated net system and total compensated reactivity for cold-startup test 12 (12.6 msec period).

1.35 Clad Surface Temperatures. Time-dependent fuel rod cladding surface temperature rises for the 351- and 12.6-msec-period tests are shown in Figures 13 and 14. Experimental clad surface temperatures for core locations N33, N31, and E21 shown in Figure 13 were obtained from unsheathed thermocouples, and the measured temperature for core location S11 was obtained from a stainless steel sheathed thermocouple. For the 351-msec-period test, the clad surface temperature rises calculated using the PARET code agree with the unsheathed thermocouple data to within about 10%. However, the PARET calculated temperature rise is as much as 45% larger than stainless steel sheathed thermocouple data. Since the stainless steel sheathed thermocouple was expected to have a slow response time, the PARET calculated temperature rise at this core location is probably valid.

In Figure 14 experimental clad surface temperatures for core locations E33 and N21 were measured using unsheathed thermocouples, and the measured temperature for core location S11 was obtained using a stainless steel sheathed thermocouple. For this 12.6-msec-period transient, the clad surface temperature

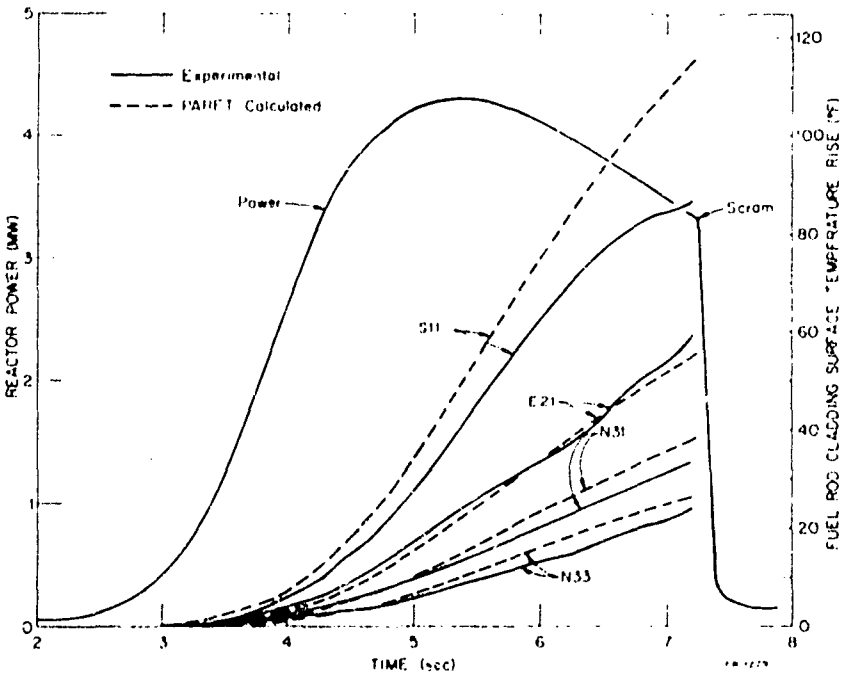

Fig. 13 Experimental and PARET calculated fuel rod cladding surface temperature rises for cold-startup test 18 (351 msec period).

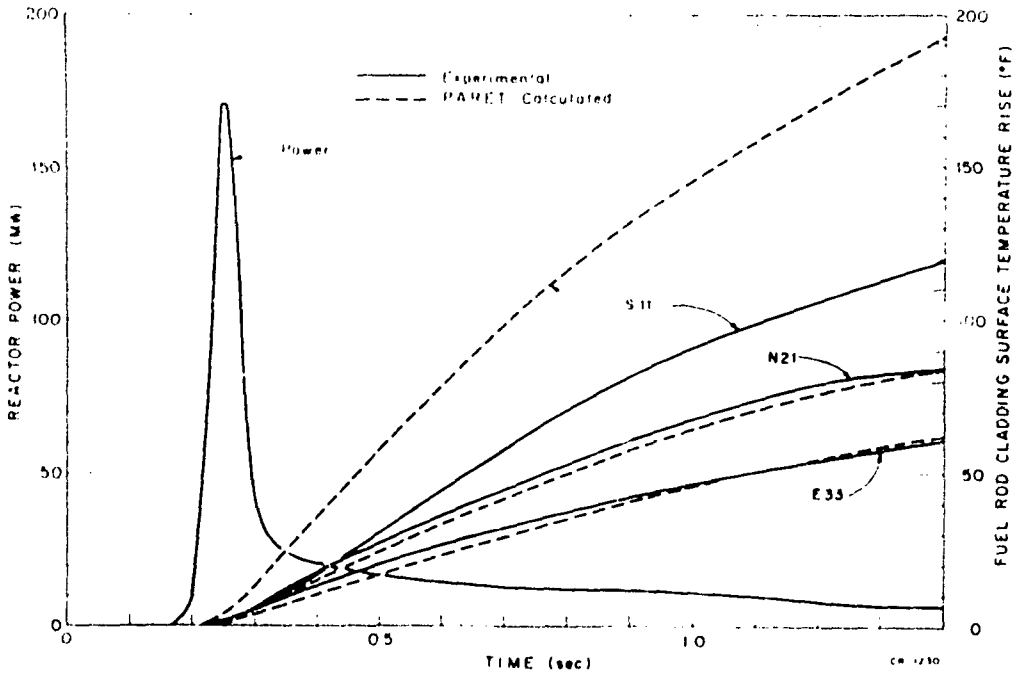

Fig. 14 Experimental and PARET calculated fuel rod cladding surface temperature rises for cold-startup test 42 (12.6 msec period).

rise is considerably faster than was the temperature rise for the 351-msec-period transient. The PARET calculated temperature rise is within about 5% of the experimental values obtained using unsheathed thermocouples. However, the PARET calculated temperature rise is up to 60% larger than the experimental data for the stainless steel sheathed thermocouple.

1.36 Summary. The PARET- and IREKIN-calculated powers and energy releases for the cold-startup reactivity accident tests agree to within 30% or better with the experimental data over the range of reactivity insertions experimentally investigated. Reactivity compensation calculated using the PARET and IREKIN codes are within the uncertainty associated with the experimental data. The PARET calculations indicated that Doppler reactivity feedback accounts for about 80% of the total reactivity feedback at the time of peak power for long-period cold-startup transients and about 95% of the total for short-period cold-startup transients. These results indicate that the Spert III E-core is essentially Doppler limited for cold-startup reactivity accident tests; therefore, computer codes like IREKIN, which consider only Doppler reactivity feedback, will adequately predict the results of cold-startup reactivity accidents in small, low-enriched oxide cores.

2. HOT-STARTUP REACTIVITY ACCIDENT TESTS

Experimental and analytical results obtained from the cold-startup reactivity accident tests demonstrated that the Spert III E-core is essentially Doppler limited for short-period transient tests. The agreement between experimental and calculational results for these cold-startup tests provided confidence in the predictions of the kinetic behavior for the hot-startup reactivity accident tests. The purpose of the hot-startup tests was to obtain experimental information that would extend the available knowledge of the transient behavior of an oxide-fueled reactor to include initial conditions of coolant flow and elevated system temperature and pressure.

Two complete series of hot-startup reactivity accident tests were performed. The first was performed from an initial system temperature of about 260°F and the second was performed from an initial system temperature of about 500°F. Altogether, 33 hot-startup tests were performed. These transient tests were all performed from low initial powers (10 to 50 watts) and an initial system pressure of 1500 psig. The transients were initiated with rapid reactivity insertions ranging from 0.64 to 1.23$. Power excursions with reactor periods from 2.26 sec to 9.7 msec resulted from those insertions. The coolant flow rate for the hot-startup transient tests was varied from 2,000 to 20,000 gpm. Average coolant flow rates through the core were calculated from the measured primary coolant flow and the flow area[20]. The calculated average coolant flow rates corresponding to measured primary coolant flows are as follows:

Measured Coolant Flow (gpm)	Calculated Average Coolant Flow Rate (fps)
2000	2.4
4000	4.8
12000	14
16000	19
18000	22
20000	24

2.1 Experimental Results and Comparison with Previous Experimental Data

A summary of the hot-startup reactivity accident test data for the E-core is presented in Table V. The listed uncertainties in these data represent one standard deviation. Two methods of examining the kinetic behavior during

TABLE V

DATA SUMMARY FOR HOT-STARTUP REACTIVITY ACCIDENT TESTS

Test No.	Reactor Period (msec)	Initial Reactivity Insertion ($)	Primary Coolant Inlet Temperature (°F)	Average Primary Coolant Flow Rate (fps)	Maximum Reactor Power (MW)	Energy Release to Time of Peak Power (MW-sec)	Time to Peak Power (sec)	Maximum Measured Fuel Cladding Surface Temperature Rise (°F)	Reactivity Compensation at Peak Power ($)
24	1140 ± 20	0.75 ± 0.03	259 ± 4	14	3.0 ± 0.5[a]	16 ± 2.7	18.0 ± 0.1	13 ± 1	0.35 ± 0.04
25	1090 ± 20	0.76 ± 0.03	259 ± 4	14	2.8 ± 0.4[a]	6.9 ± 1.5	14.9 ± 0.1	8 ± 1	0.22 ± 0.02
31	249 ± 5	0.92 ± 0.04	259 ± 4	22	6.2 ± 0.9	9.0 ± 1.5	4.5 ± 0.2	21 ± 2	0.25 ± 0.03
26	209 ± 4	0.93 ± 0.04	259 ± 4	14	6.8 ± 1.0	7.6 ± 1.3	3.6 ± 0.1	24 ± 2	0.22 ± 0.02
30	118 ± 2	0.97 ± 0.04	259 ± 4	2.4	7.8 ± 1.2	4.8 ± 0.8	1.98 ± 0.05	46 ± 7	0.19 ± 0.02
37	108 ± 2	0.98 ± 0.04	259 ± 4	19	8.9 ± 1.3	5.7 ± 1.0	1.9 ± 0.1	22 ± 2	0.16 ± 0.02
33	103 ± 2	0.98 ± 0.04	259 ± 4	22	9.4 ± 1.4	5.1 ± 0.9	1.7 ± 0.1	28 ± 3	0.16 ± 0.02
27	102 ± 2	0.98 ± 0.04	259 ± 4	14	9.1 ± 1.4	4.3 ± 0.7	1.6 ± 0.05	26 ± 3	0.14 ± 0.02
35	87.0 ± 1.7	0.99 ± 0.04	259 ± 4	22	9.8 ± 1.5	4.1 ± 0.7	1.4 ± 0.1	28 ± 3	0.14 ± 0.02
34	69.3 ± 1.4	1.00 ± 0.04	259 ± 4	22	11 ± 2	3.2 ± 0.5	1.17 ± 0.03	25 ± 3	0.11 ± 0.01
28	41.6 ± 0.8	1.03 ± 0.04	259 ± 4	14	22 ± 3	2.0 ± 0.3	0.64 ± 0.01	31 ± 3	0.08 ± 0.01
32	39.6 ± 0.8	1.04 ± 0.04	259 ± 4	2.4	23 ± 3	2.0 ± 0.3	0.60 ± 0.02	58 ± 9	0.08 ± 0.01
42	21.8 ± 0.4	1.09 ± 0.04	259 ± 4	2.4	66 ± 10	3.1 ± 0.5	0.39 ± 0.01	103 ± 10	0.11 ± 0.01
29	13.6 ± 0.4	1.13 ± 0.04	259 ± 4	14	78 ± 12	3.2 ± 0.5	0.36 ± 0.01	44 ± 4	0.12 ± 0.01
70	10.3 ± 0.2	1.21 ± 0.03	251 ± 4	14	280 ± 42	6.3 ± 1.1	0.20 ± 0.01	58 ± 6	0.22 ± 0.02
52	2060 ± 50	0.64 ± 0.03	500 ± 4	14	0.14 ± 0.01[a]	0.45 ± 0.06	20 ± 0.1	~0	0.06 ± 0.01
53	1260 ± 20	0.77 ± 0.03	500 ± 4	14	4.0 ± 0.6[a]	14 ± 2	15 ± 0.1	10 ± 1	0.27 ± 0.03
43	592 ± 10	0.84 ± 0.03	501 ± 4	14	5.6 ± 0.6	15 ± 2	9.2 ± 0.2	21 ± 2	0.29 ± 0.03
44	575 ± 10	0.82 ± 0.03	501 ± 4	2.8	4.8 ± 0.5	12 ± 2	8.3 ± 0.2	41 ± 4	0.29 ± 0.03
45	440 ± 9	0.87 ± 0.03	500 ± 4	24	6.6 ± 0.7	13 ± 2	7.0 ± 0.2	13 ± 1	0.22 ± 0.03
54	223 ± 4	0.93 ± 0.04	498 ± 4	14	8.7 ± 0.9	11 ± 1	3.8 ± 0.1	17 ± 2	0.24 ± 0.03
55	70.8 ± 1.4	1.00 ± 0.04	500 ± 4	14	16 ± 2	3.3 ± 0.4	1.00 ± 0.03	19 ± 2	0.08 ± 0.01
56	37.9 ± 0.8	1.04 ± 0.04	501 ± 4	14	35 ± 4	3.1 ± 0.4	0.62 ± 0.007	26 ± 3	0.08 ± 0.01
57	21.7 ± 0.4	1.09 ± 0.04	500 ± 4	17	89 ± 9	4.4 ± 0.6	0.400 ± 0.005	31 ± 3	0.13 ± 0.01
62	20.6 ± 0.4	1.10 ± 0.04	500 ± 4	14	97 ± 10	4.5 ± 0.6	0.370 ± 0.005	30 ± 3	0.12 ± 0.01
61	17.8 ± 0.4	1.12 ± 0.04	500 ± 4	14	120 ± 12	4.9 ± 0.6	0.335 ± 0.005	32 ± 3	0.14 ± 0.02
68	16.0 ± 0.3	1.13 ± 0.05	500 ± 4	14	160 ± 16	5.5 ± 0.7	0.300 ± 0.005	33 ± 3	0.15 ± 0.02
67	15.5 ± 0.3	1.14 ± 0.05	501 ± 4	2.8	170 ± 17	5.6 ± 0.7	0.300 ± 0.005	60 ± 6	0.16 ± 0.02
66	14.3 ± 0.3	1.15 ± 0.05	501 ± 4	24	190 ± 19	5.8 ± 0.8	0.290 ± 0.005	24 ± 2	0.17 ± 0.02
58	14.1 ± 0.3	1.15 ± 0.05	500 ± 4	14	200 ± 20	6.2 ± 0.8	0.285 ± 0.005	36 ± 4	0.17 ± 0.02
59	13.0 ± 0.3	1.17 ± 0.05	500 ± 4	14	230 ± 23	6.5 ± 0.8	0.280 ± 0.005	37 ± 4	0.18 ± 0.02
60	9.73 ± 0.19	1.23 ± 0.05	500 ± 4	14	410 ± 41	8.5 ± 1.1	0.227 ± 0.005	44 ± 4	0.24 ± 0.03

[a] Test was terminated by scram while power was still rising; peak power taken at time of scram.

hot-startup reactivity accident tests are to correlate the experimental data obtained from the 260 and 500°F hot-startup tests with the cold-startup test results and to examine the results from each hot-startup test series. The results of these investigations are discussed in the following sections.

2.11 Peak Reactor Powers. Least-squares fitted curves to the experimental peak power versus reciprocal period data from the E-core cold-startup and hot-startup tests performed with 14 fps coolant flow rates are shown in Figure 15. The 260°F initial temperature peak power values are only about 10% larger than the corresponding 70°F values for short-period transients. Since the Doppler coefficient was calculated to change from -0.72 to -0.56¢/°F as the system temperature increased from 70 to 250°F, the larger peak powers for short-period 260°F tests were anticipated. The apparent greater difference between the 260 and 70°F peak power values for long periods (5 to 15 sec^{-1} reciprocal periods) resulted from the least-squares fitting of the 260°F data. Since only five data points were least-squares fitted to the 260°F peak power curve, the confidence in this line at the ends of the curve is considerably less than the confidence in the 70 and 500°F peak power curves which were fitted to more data points.

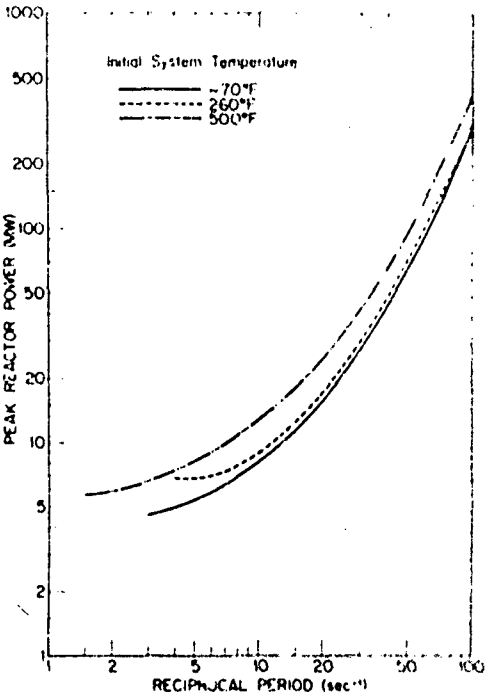

Fig. 15 Experimental peak reactor powers as functions of reciprocal period for the cold- and hot-startup tests.

The 500°F initial temperature peak power values are about 50% larger than corresponding 70°F values over the range of reciprocal periods shown. Peak powers for the short-period 500°F tests were expected to be larger than corresponding peak powers for either the 70 or 260°F tests because the Doppler coefficient was calculated to change from -0.56¢/°F at 250°F to -0.37¢/°F at 500°F.

2.12 Energy Release and Reactivity Compensation. Least-squares fitted curves for the experimental energy release and reactivity compensation at the time of peak power versus reciprocal period for the cold-startup and hot-startup tests performed with 14 lps coolant flow rates are shown in Figure 16[a].

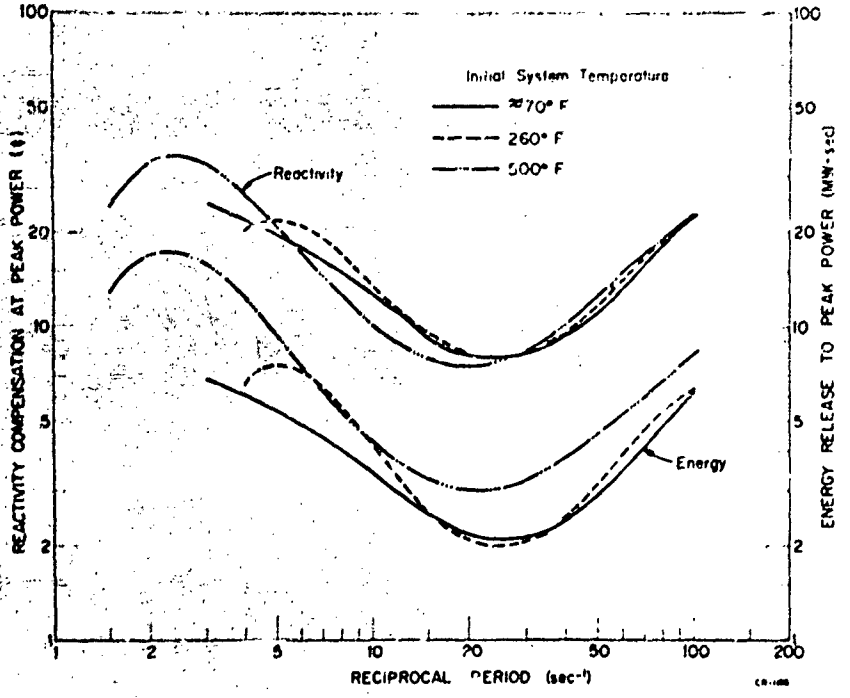

Fig. 16 Experimental energy release to peak power and reactivity compensation at the time of peak power for the cold- and hot-startup tests.

For short-period transients, the 500 and 260°F energy release values are larger than corresponding 70°F values by about the same percentages (50 and 10%, respectively) as were the peak power values. If it is assumed that E-core excursions are essentially Doppler limited for all three initial system temperatures, the above percentage differences for energy release to peak power are not as large as would be expected for short-period transients. For example, since the calculated Doppler coefficient at 500°F is about one-half the 70°F coefficient, the energy to peak power for a 500°F short-period transient would be expected to be about twice as large as the energy release for the corresponding 70°F transient. Instead, the 500°F energy releases are only 1.5 times the

[a] In the long-period region, the hot-startup least-squares fitted curves display an abrupt change in curvature. This behavior is the consequence of fitting few data points in the long-period region to a fourth order polynomial. Actually, the maxima in these curves would occur for reciprocal periods less than 1 sec^{-1}.

2

experimental values. These results imply that the E-core excursions are not solely Doppler limited for all initial system temperatures. Analysis of the results showed that reactivity feedback resulting from prompt moderator heating became an increasingly effective feedback mechanism at elevated temperatures.

The reactivity feedback required to limit the power rise during a transient is relatively insensitive to the initial system temperature. For the three initial system temperatures used for the low-initial-power tests, the maximum variation in reactivity compensation at the time of peak power is about 10% for short-period transients and about 25% for long-period transients. The small variation for short-period transients indicates that the reduced prompt neutron generation time does not change significantly with initial system temperature. This result substantiates the small variations in the calculated reduced prompt neutron generation times listed in Table II.

For the 260°F hot-startup tests, reactivity compensation and energy release to the time of peak power are shown plotted in Figure 17 as functions of reciprocal period. The curves represent least-squares fitted lines to the experimental data from tests performed with 14 fps coolant flow rates. The

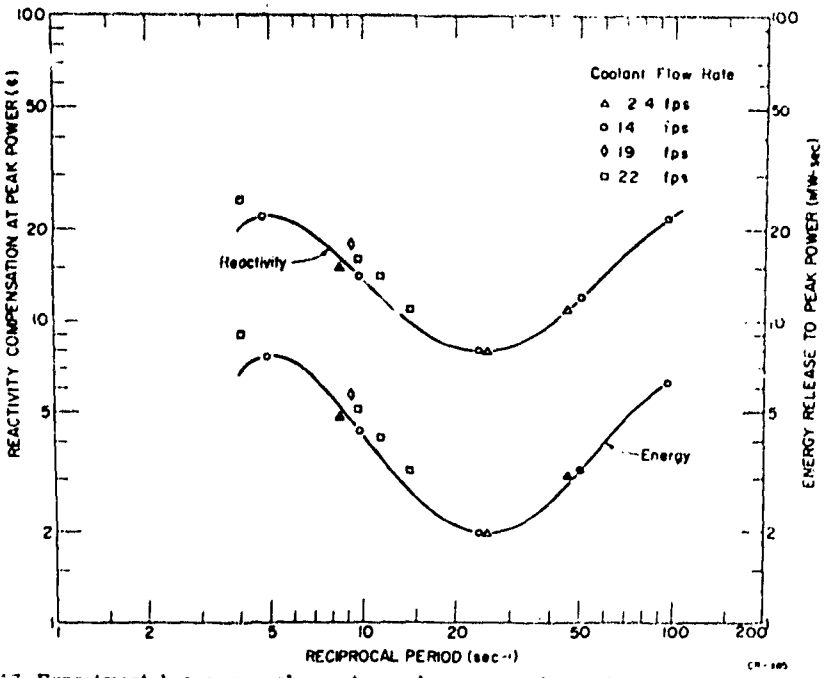

Fig. 17 Experimental energy release to peak power and reactivity compensation at peak power as functions of reciprocal period for the 260°F hot-startup tests.

effects of coolant flow on the E-core kinetic behavior can be determined from this figure. For the long-period transients, the values of energy release and reactivity compensation for flow rates of 19 and 22 fps are consistently larger than the 14 fps values. This behavior was expected for long-period transients. Although heat transfer from the fuel rods to the moderator increases with increasing flow rates, the resulting larger moderator reactivity feedback is more than compensated by a loss of reactivity feedback. The loss results because more heated coolant is continuously swept from the core at larger flow rates. Therefore, for long-period transients and large flow rates, moderator feedback contributes less reactivity compensation at peak power than it does for small flow rates. For short-period transients, the energy release and reactivity compensation at the time of peak power are about the same regardless of coolant flow rate. This behavior results because little coolant is transported from the core during the relatively short times required to reach peak power for short-period transients.

2.13 Power Burst Shapes. Power burst shapes for representative, short-period (≈ 10msec) cold-startup and 500°F hot-startup transients are shown in Figure 18. For each test, the power was normalized to peak power and the

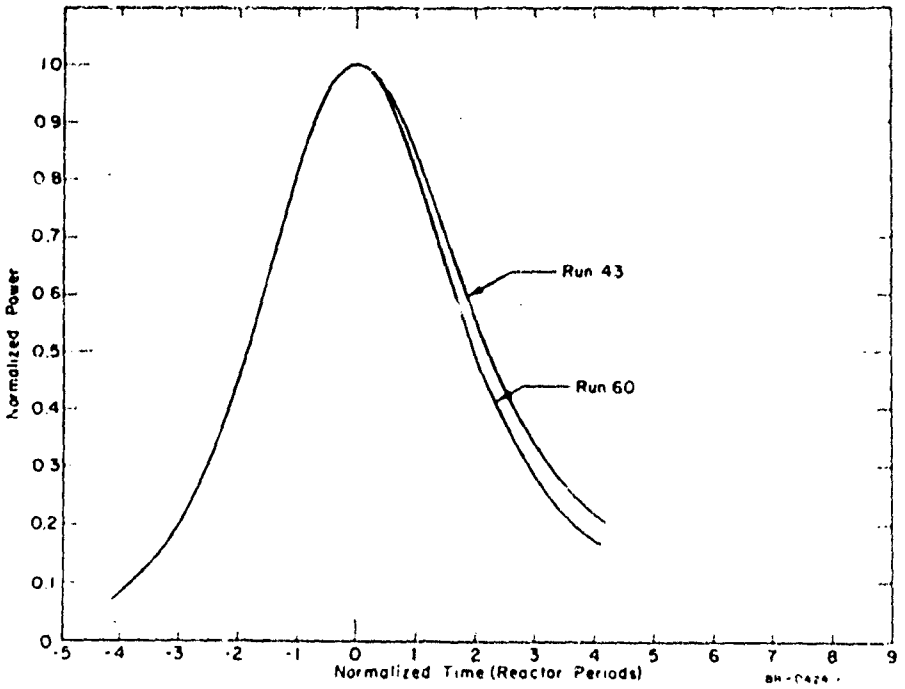

Fig. 18 Experimental power burst shapes for cold-startup test 43 (10 msec period) and 500°F hot-startup test 60 (9.7 msec period).

time was normalized to reactor period. The shapes of the bursts are identical until the time of peak power. After peak power, the 500°F burst decreases more rapidly than the 70°F burst. At a time of two reactor periods after peak power, the difference in burst shape magnitudes is about 15%. Since at this time the experimental uncertainty in each burst shape is about ± 4%, it is very unlikely that this difference in power burst shapes results from experimental uncertainties. Therefore, the differences in burst shapes imply a difference in reactivity feedback mechanisms between the cold-startup and 500°F hot-startup tests. Since the absolute value of the Doppler reactivity feedback coefficient decreases with increasing system temperature, the difference in burst shapes indicates that the moderator reactivity feedback increases or becomes more important at elevated system temperatures.

2.2 Comparison of Experimental and Calculational Results

Calculations of the kinetic behavior of the E-core were performed using both the IREKIN and PARET computer codes for all of the 260 and 500°F hot-startup reactivity accident tests. Results obtained using the two codes are compared with experimental data in the following paragraphs.

2.21 Peak Reactor Powers. The 260°F hot-startup transient data, obtained from tests performed with 14 fps coolant flow, for peak power versus reciprocal period were least-squares fitted; the resulting curve is shown in Figure 19. The PARET- and IREKIN-calculated curves are also shown. The five data points are also plotted with their associated vertical bars representing one standard deviation in peak power. The error bars are shown because the 65% confidence bands for the least-squares fitted curve are extremely broad. In general, neither the PARET- nor IREKIN-calculated curves fall within the experimental uncertainties. The PARET-calculated peak power values are about 25% larger than the experimental values. For short-period transients, the IREKIN-calculated peak powers are 40 to 45% larger than the experimental values. For long-period transients, the IREKIN-calculated values are only 10 to 20% larger than experimental values. This apparently better agreement for IREKIN calculations in the long-period range is not valid. IREKIN does not account for heat transfer out of the fuel; therefore, for long-period tests IREKIN overpredicts the Doppler reactivity feedback and the resulting improved agreement is fortuitous.

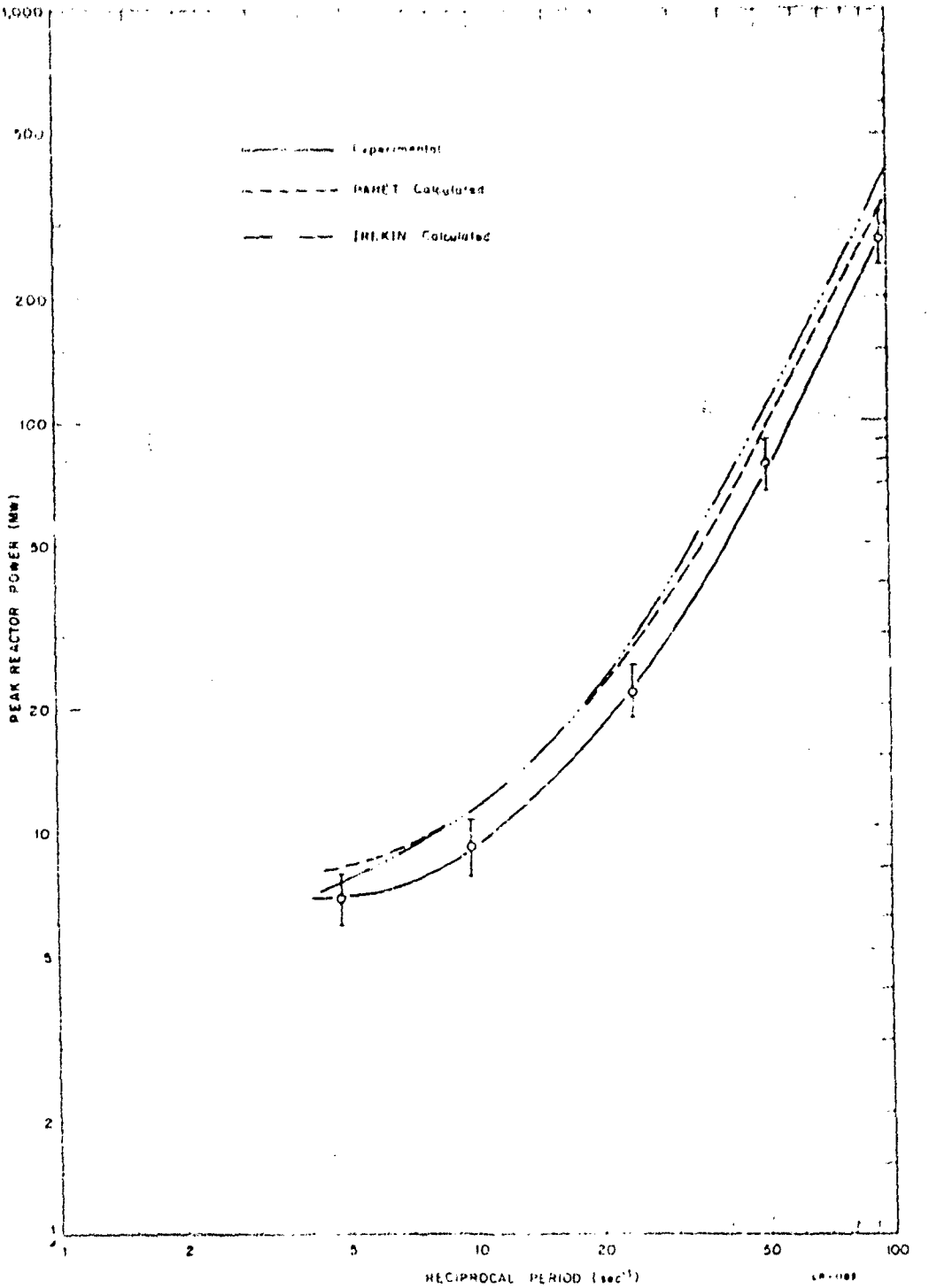

Fig. 19 Experimental, IREKIN, and PARET calculated peak powers as functions of reciprocal period for the 260°F hot-startup tests.

The least-squares fitted line and associated confidence bands for the peak power versus reciprocal period data obtained from the 500°F hot-startup tests at 11 fps flow are shown in Figure 20. For these initial conditions, the PARET calculated curve lies within the confidence bands over almost the entire range of reciprocal periods shown. The IREKIN-calculated curve lies outside of the confidence bands over almost the entire range of reciprocal periods shown. The IREKIN-calculated peak power values are 40 to 60% larger than the experimental values for short-period transients. Again, for long-period transients, the IREKIN calculations appear better because heat transfer is not accounted for in the IREKIN code.

2.22 Energy Release and Reactivity Compensation. Energy release and reactivity compensation at the time of peak power versus reciprocal period data for the 260°F, 14 fps tests were least-squares fitted. This curve is shown in Figure 21 together with PARET- and IREKIN-calculated curves. The experimental data points and vertical error bars (one standard deviation) are also shown. The PARET calculations are essentially within experimental uncertainty for both reactivity compensation and energy release for all the tests. For short-period transients the IREKIN calculations are within experimental uncertainty for reactivity compensation but outside of the experimental uncertainty for energy release. The IREKIN code overpredicts the energy release for these transients because moderator feedback is not taken into account.

The 500°F hot-startup tests performed at 14 fps flow demonstrate the same reactivity compensation and energy release behavior as the 260°F tests. The results are shown in Figure 22. The IREKIN code underpredicts the energy release for long-period transients because coolant flow is not considered. Energy release to peak power calculated using the IREKIN code is about 50% larger than experimental values for short-period transients. The IREKIN-calculated energy release for similar transients at 260°F was about 40% larger than experimental values (Figure 21). Therefore, the larger calculated difference at 500°F indicates that moderator reactivity feedback increases with increasing system temperature.

2.23 Power Burst Shapes and Reactivity Feedback. Time-dependent plots of reactor power and energy release for short-period (≈10msec), 250 and 500°F hot-startup tests are shown in Figures 23 and 24. For both of the tests shown in Figures 23 and 24, the PARET- and IREKIN-calculated burst shapes

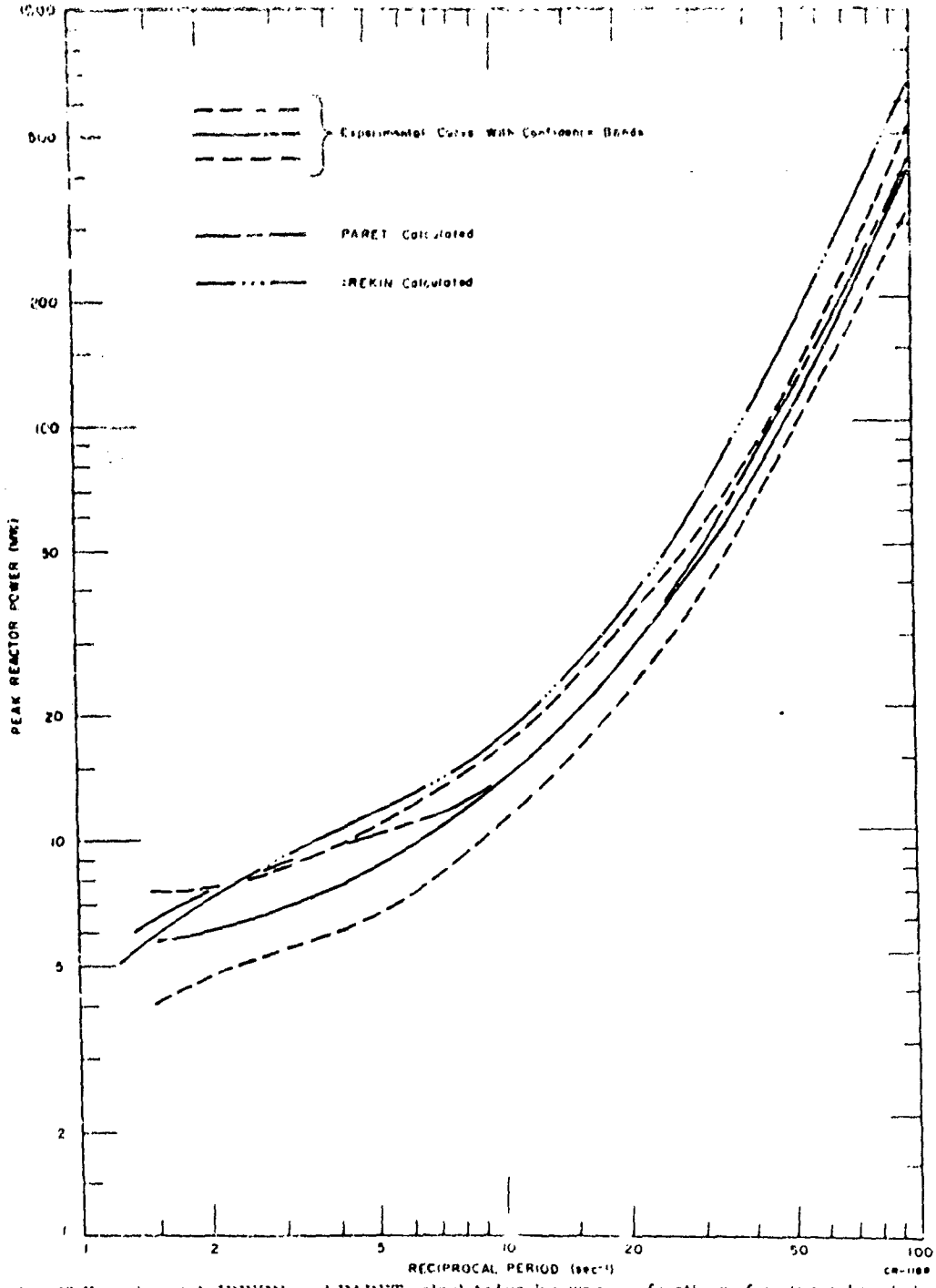

Fig. 20 Experimental, IREKIN, and PARET calculated peak powers as functions of reciprocal period for the 500°F hot-startup tests.

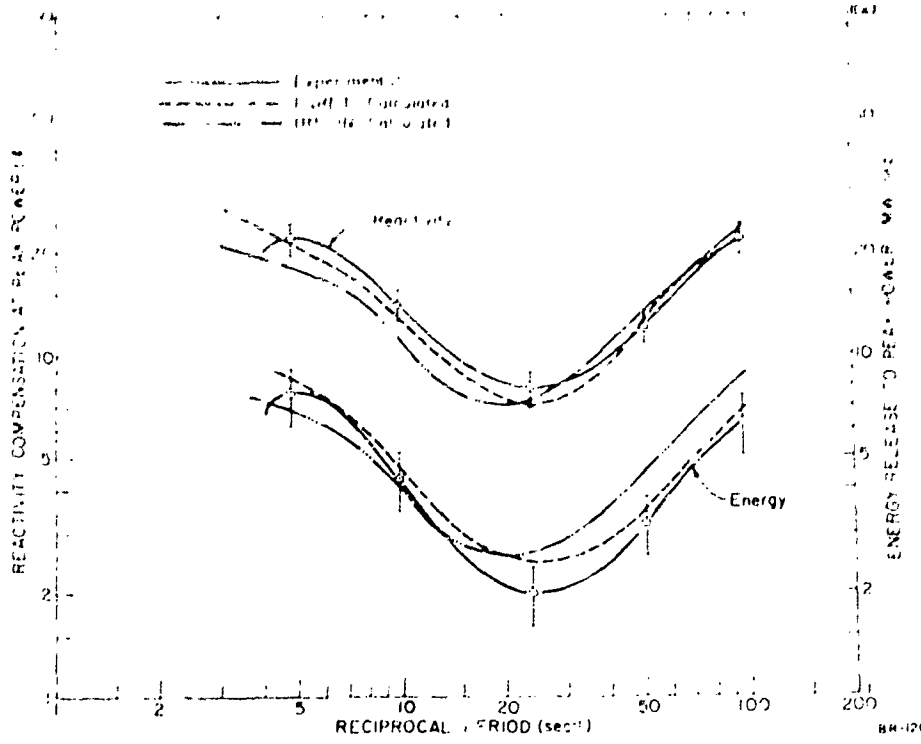

Fig. 21 Experimental, IREKIN, and PARET calculated energy release to the time of peak power and reactivity compensation at peak power for the 260°F hot-startup tests.

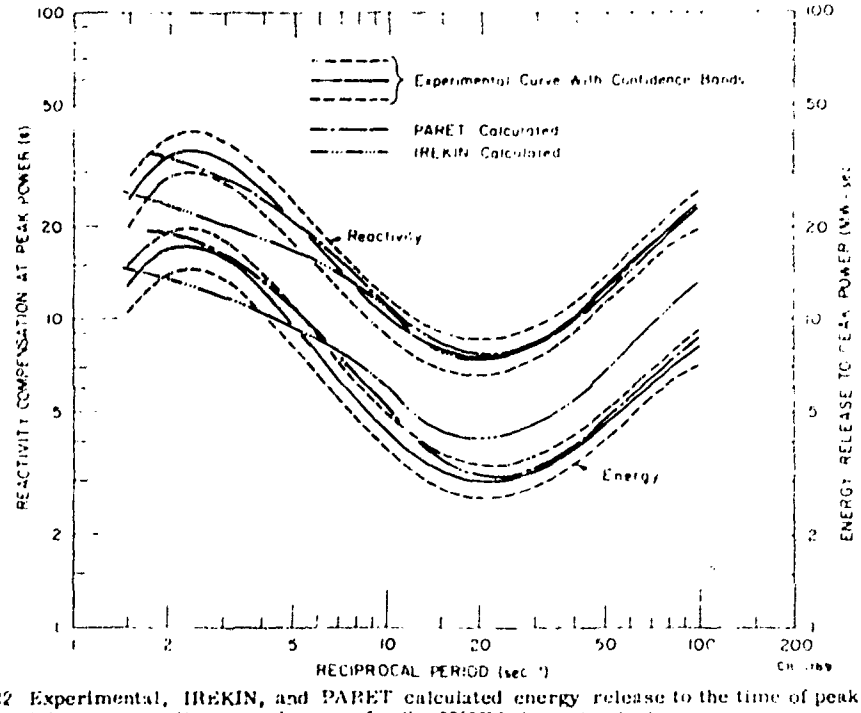

Fig. 22 Experimental, IREKIN, and PARET calculated energy release to the time of peak power and reactivity compensation at peak power for the 500°F hot-startup tests.

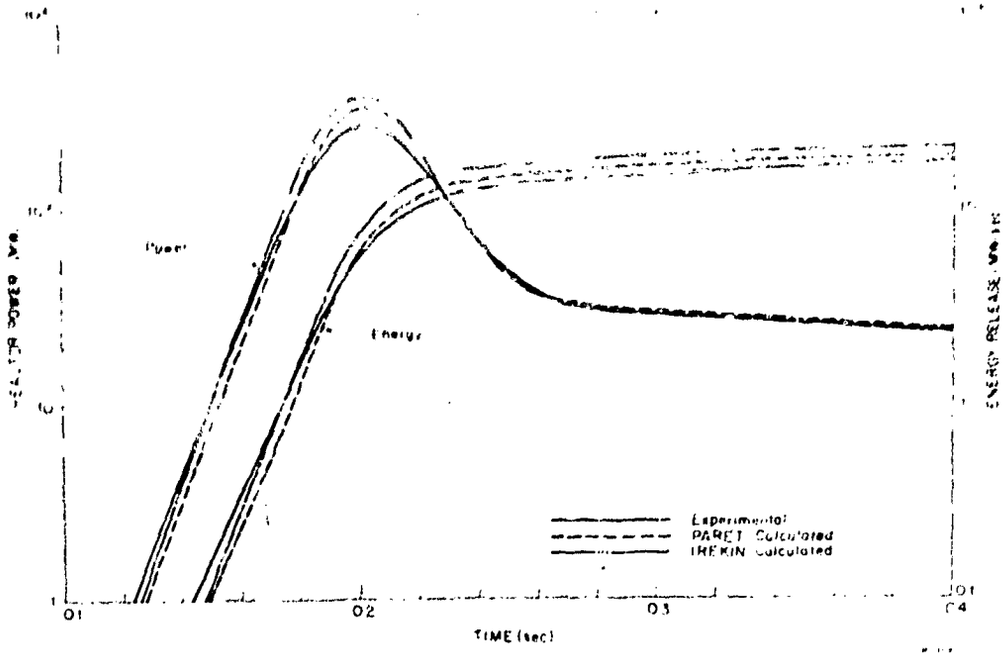

Fig. 23 Experimental, IREKIN, and PARET calculated reactor power and energy release for 250°F hot-startup test 70 (10 msec period).

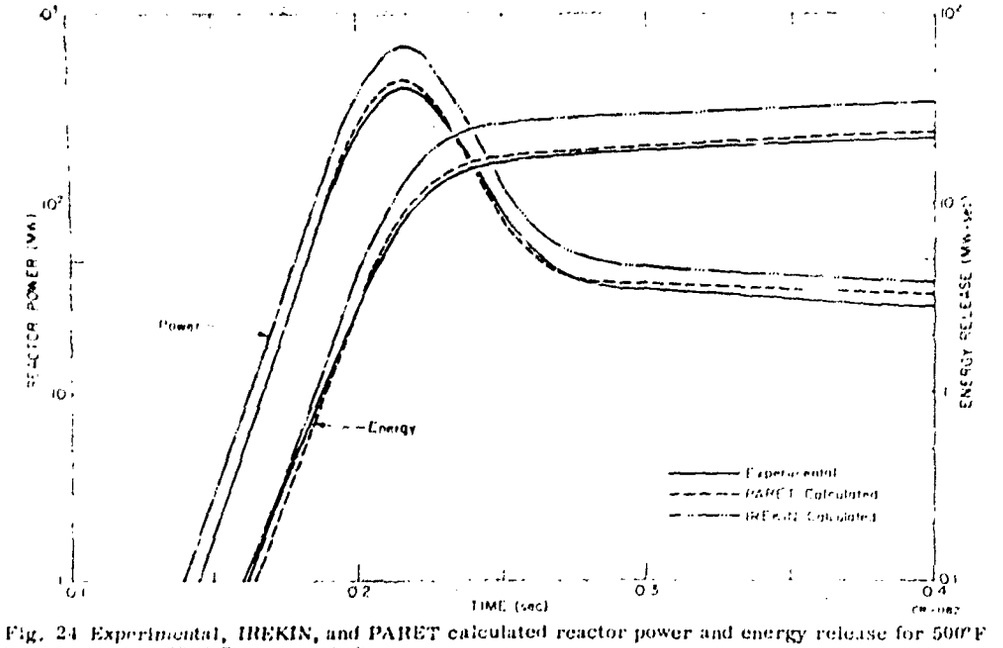

Fig. 24 Experimental, IREKIN, and PARET calculated reactor power and energy release for 500°F hot-startup test 60 (9.7 msec period).

In the experimental [illegible] for the 250°F test, the PARET calculated peak power is about [illegible] larger and the energy release about 10% larger than experimental values. At 500°F, PARET calculated peak power is only 10% larger, and the energy release about 2% larger than experimental values. Thus, in terms of magnitudes and burst shapes, the PARET code yields good results for short-period, hot-startup tests. For the 250°F test, the IREKIN-calculated peak power is about 45% larger and the energy release about 30% larger than experimental values. At 500°F, the IREKIN calculated peak power is about 60% and the energy release about 60% larger than experimental values. Although the IREKIN-calculated burst shapes agree with experimental burst shapes, the code yields conservative results for short-period, hot-startup tests.

For the 250 and 500°F, 10-msec-period tests discussed above, the importance of moderator reactivity feedback is illustrated in Figures 25 and 26. These figures show PARET-calculated, time-dependent reactivity feedback contributions from Doppler, moderator heating, and fuel rod expansion. In these figures, the

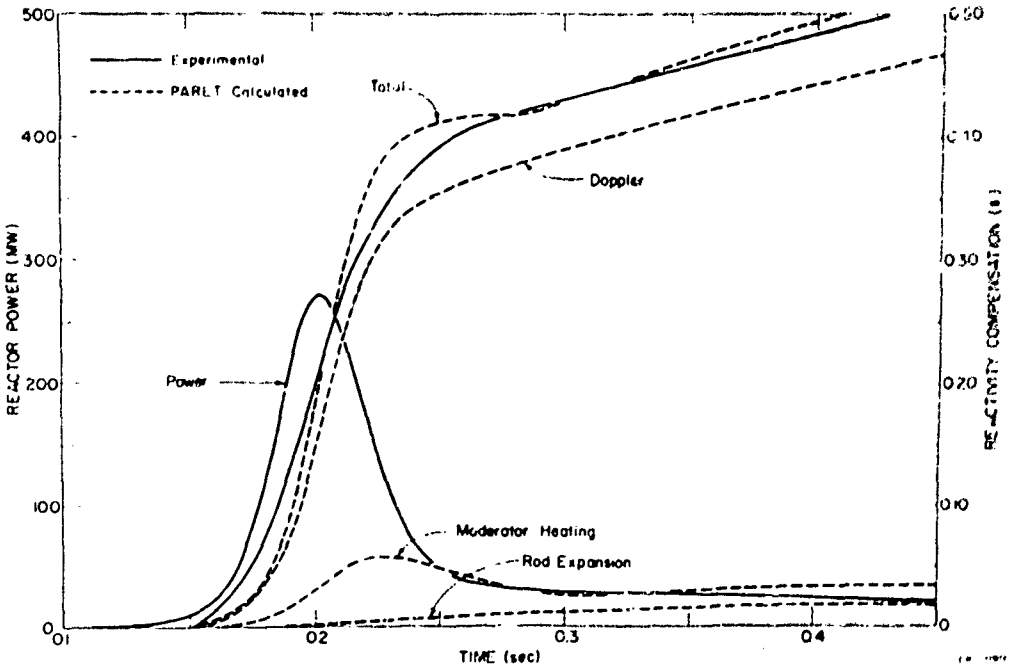

Fig. 25 Experimental and PARET calculated total reactivity compensation for 250°F hot-startup test 70 (10 msec period).

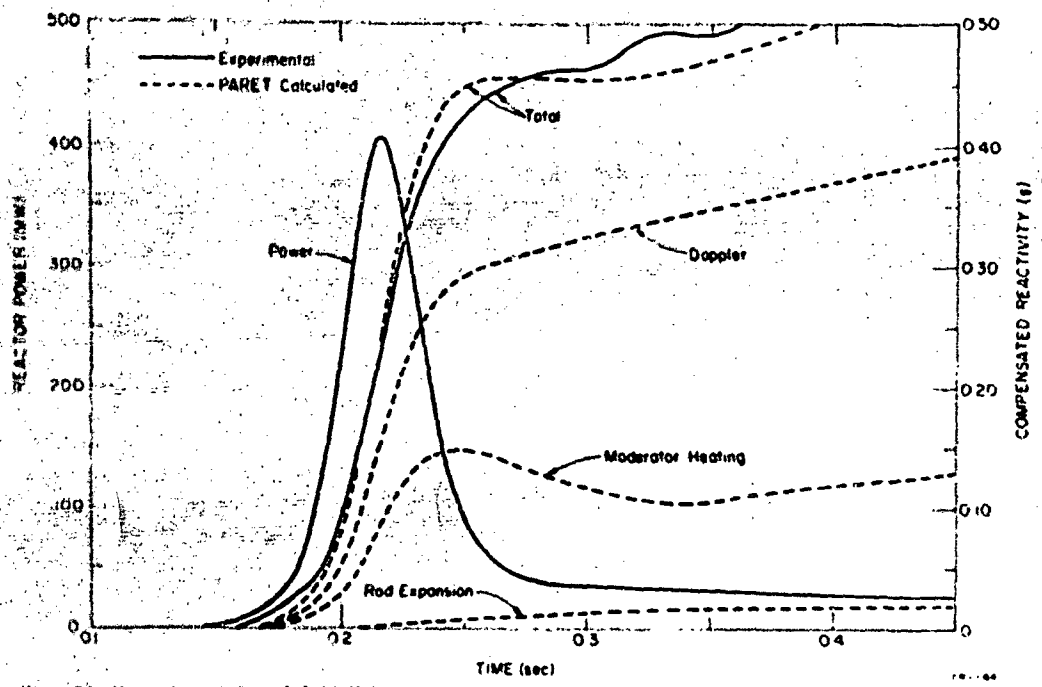

Fig. 26 Experimental and PARET calculated total reactivity compensation for 500°F hot-startup test 60 (9.7 msec period).

experimental power bursts and total reactivity compensations are also shown. Only the total reactivity compensation can be determined from experimental data. The PARET-calculated total reactivity feedback, which is the sum of the three feedback contributions, agrees with the experimental total reactivity feedback within the experimental uncertainty for both tests. For the 250°F test, the PARET-calculated moderator heating reactivity compensation increases during the power rise but decreases after the power burst. The calculated moderator heating feedback again increases at about 0.3 second after peak power. For the 500°F transient, the PARET-calculated moderator reactivity feedback shows a similar time dependency.

During the power bursts shown in Figures 25 and 26, transfer of heat from the fuel rods to the moderator by conduction was small. However, a prompt mechanism for heat transfer to the moderator did exist. This prompt moderator heating (PMH) was caused by the slowing down of fast neutrons and the absorption of prompt gamma rays in the moderator and cladding[21]. As illustrated in Figures 25 and 26, the reactivity feedback caused by PMH increases during the initial power rise and then decreases. The decrease results from heated moderator being continuously transported from core

regions with large importance weighting factors to regions of lesser importance. The total moderator heating feedback again increases at the end of the transient because of conductive transfer of heat from the fuel to the moderator.

For the E-core, PMH reactivity feedback becomes an important feedback mechanism at elevated initial system temperatures as a result of the change in water density with temperature. The negative average temperature coefficient of reactivity of the E-core changes from about -0.4¢/°F at a system temperature of 70°F to about -2¢/°F at a system temperature of 250°F, and becomes about -4¢/°F at a system temperature of 500°F. Over the same temperature range (70 to 500°F), the calculated Doppler coefficient of reactivity changes from -0.72¢/°F to -0.37¢/°F. This combined effect of increasing negative moderator coefficient and decreasing Doppler coefficient with increasing system temperature causes PMH feedback to increase in importance at elevated system temperatures.

A summary of PARET-calculated reactivity feedback contributions at the time of peak power and experimental results is listed in Table VI for representative long- and short-period, cold- and hot-startup reactivity accident tests. For the short-period tests, PMH feedback contributes about 7% of the total reactivity feedback at the time of peak power for the 78°F test, about 17% for the 250°F test, and about 35% for the 500°F test. For both of the hot-startup test conditions, the percentage of moderator feedback at peak power decreases as the reactor period increases. These differences in moderator feedback are caused by heated coolant being transported from the core during the long times required to reach peak power for the long-period transients. For the cold-startup tests, the reactivity feedback contribution from fuel rod expansion shows a marked difference between the long- and short-period tests. This is caused by the poor clad-water heat transfer for the no coolant flow case.

2.24 Effects of Coolant Flow. During equal reactivity insertion, long-period hot-startup tests, the energy release to peak power was increased by increasing the coolant flow. For short-period tests, the energy release to peak power is not measurably affected by the coolant flow rate. For the same short-period tests, however, the power level following the power burst is a function of coolant flow rate. This is illustrated in Figure 27 where experimental and PARET-calculated power burst shapes are shown for two 500°F,

TABLE VI

EXPERIMENTAL AND PARET CALCULATED REACTIVITY COMPENSATION AT PEAK POWER

Experimental Results					PARET Calculated Reactivity Compensation at Peak Power			
Test No.	Primary Coolant Inlet Temperature (°F)	Initial Reactivity Insertion ($)	Reactor Period (msec)	Reactivity Compensation at Peak Power ($)	Total ($)	Doppler (% of total)	Moderator (% of total)	Fuel Rod Expansion (% of total)
13	53 ± 4	0.93 ± 0.04	206 ± 4	0.19 ± 0.02	0.17	85.2	6.6	8.2
43	78 ± 4	1.21 ± 0.05	10.0 ± 0.2	0.22 ± 0.02	0.22	93.6	5.5	0.9
26[a]	259 ± 4	0.93 ± 0.04	209 ± 4	0.22 ± 0.02	0.21	90.4	6.3	3.3
70[a]	251 ± 4	1.21 ± 0.05	10.3 ± 0.2	0.22 ± 0.02	0.21	81.8	17.1	1.1
54[a]	498 ± 4	0.93 ± 0.04	223 ± 4	0.24 ± 0.03	0.22	75.3	21.0	3.7
60[a]	500 ± 4	1.23 ± 0.05	9.70 ± 0.19	0.24 ± 0.03	0.25	63.7	35.3	1.0

[a] For all 4 hot-startup tests, the average primary coolant flow rate was 14 fps and the system pressure was 1500 psig.

short-period (≥15 msec) transients with flow rates of 4.8 and 24 fps. The power burst shapes were normalized to peak power and reactor period. The experimental and calculated results inidicate that the runout power level increases with increasing flow rate. Although the power burst shapes and therefore the energy releases to peak power are not significantly different, the total energy release for long transient times is different. The PMH reactivity feedback is also a function of the coolant flow rate. The effect of coolant flow on the PMH feedback is illustrated by the PARET results shown in Figure 28. Increasing the flow rate decreases PMH feedback because of energy removal. For the large flow rate (50 fps), the PMH feedback has a shape similar to the power burst. For the zero flow case, PMH feedback has a shape similar to the energy release. Because of the short times required to reach peak power for short-period transients, PMH feedback at the time of peak power is not grossly changed by varying the flow rate. For example, in Figure 28 the PMH feedback at peak power changes only about 25% as the flow changes from 0 to 50 fps.

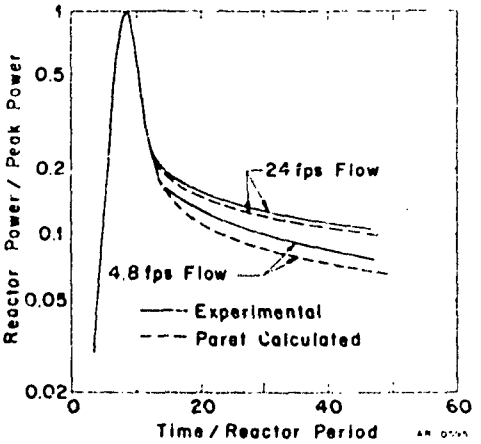

Fig. 27 Experimental and PARET calculated power burst shapes for 500°F hot-startup tests 66 (14.3 msec period, 24 fps flow) and 67 (15.5 msec period, 4.8 fps flow).

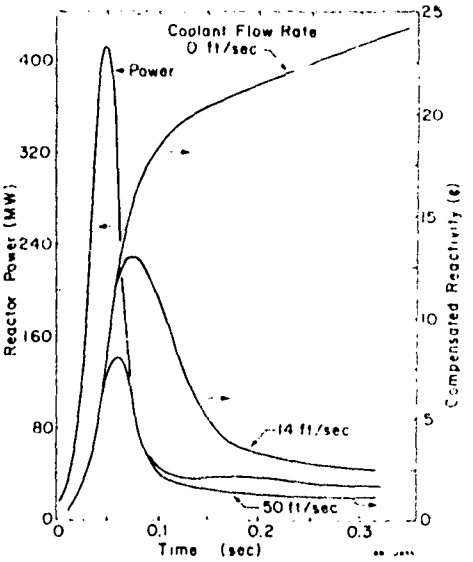

Fig. 28 PARET calculated PMH reactivity feedback as a function of coolant flow rate for 500°F hot-startup test 60 (9.7 msec period). Experimental reactor power for 14 fps flow shown.

2.3 Core Inspection

Upon completion of the low-initial-power reactivity accident tests, the reactor vessel head was removed and a scheduled inspection of the core was begun. The fuel rod cladding surface was found to be discolored, varying from brown to blue hues, as were other stainless steel surfaces in the interior

of the vessel. The discoloration is attributed to oxidation caused by elevated temperatures. During a visual inspection of the fuel rods, circumferential ridges and bowing were observed on a core hot-spot fuel rod and a rod located near the core hot spot. The ridges were in the approximate configuration of bamboo, and therefore the effect has been termed bambooing. A photograph of the ridges on the hot-spot fuel rod cladding is shown in Figure 29. This fuel rod was bowed about 3/16 of an inch. Further core inspection revealed that measurable bambooing had occurred on 11 of 81 fuel rods from 10 removable fuel assemblies in the core, implying that about 15% of the core fuel rods were thus affected. Detailed measurements of the deformed fuel rods showed a definite pattern of circumferential ridges spaced about 3/4 inch apart and continuing 10 to 14 inches above the bottom of the fuel rods, coincident with the highest flux region of the core. The distance between ridges is in agreement with the 0.766 inch design length of the fuel pellets. This deformation of the Spert III E-core fuel rods is discussed in detail in a separate report[22].

Experimental and analytical investigations of these changes in fuel rod conditions were performed. It was determined that the cladding in the bambooed sections had not expanded, but rather had locally collapsed onto the fuel pellet surfaces. Thus it was anticipated that the clad deformation of the bambooed fuel would not exceed that which was observed. With further testing it was believed that the number of core fuel rods affected by bambooing would increase; however, metallurgical investigations indicated that the strength of the cladding was not affected by the bambooing.

During all of the reactor kinetic tests up to the time of the core inspection, the E-core fuel rods performed satisfactorily, and in no case was clad integrity violated. Other than the clad deformations found during this inspection and subsequent investigations, the fuel rods were in good mechanical condition. It was concluded that the clad bambooing would neither affect the experimental results nor preclude the planned high-initial-power experimental program from being performed safely.

2.4 Summary

The Spert III E-core reactivity accident tests initiated at hot-startup conditions were performed to investigate the effects of elevated system temperature and coolant flow rate on the reactor kinetic behavior. Results of these investigations indicate that increasing the system temperature causes the

Fig. 29 Photograph showing bamboo ing (circumferential ridges) on fuel rod from E-core hot-spot.

Doppler reactivity feedback per unit energy generated in the fuel to decrease, as expected. However, as the initial system temperature increased, the magnitudes of the power excursions were not as large as would be expected if the excursions were solely Doppler limited. The additional reactivity compensation that limited the power excursions was caused by feedback that resulted from prompt moderator heating. This PMH feedback contributed up to 35% of the reactivity compensation at the time of peak power for 500°F hot-startup tests.

Investigation of the effects of coolant flow rates on kinetic behavior showed that, for short-period, hot-startup transients, the peak power and energy release to peak power were not affected by flow rate. However, the power level after the power burst was increased by increasing the coolant flow rate because heated coolant that would cause reactivity feedback was removed from the core at faster rates. For long-period transients, increasing the coolant flow rate increased the energy release to peak power because of the loss of moderator reactivity feedback.

Both the IREKIN and PARET codes adequately predicted the experimental results for the reactivity accident tests initiated from cold-startup conditions. These codes were further evaluated for the hot-startup conditions which included coolant flow and elevated system temperature and pressure. IREKIN-calculated peak power and energy release to the time of peak power were 40 to 60% larger than experimental values for all the short-period, hot-startup reactivity accident tests; but, the IREKIN code underpredicted the energy release to peak power for 500°F long-period, hot-startup reactivity accident tests. This inconsistency in the IREKIN predictions resulted because coolant flow is not considered in the IREKIN code and moderator feedback was not accounted for. For the hot-startup reactivity accident condition, the IREKIN code was not adequate for predicting the reactor kinetic behavior, and, as a result, IREKIN calculations were not performed for the high-initial-power reactivity accident tests. For the 260°F hot-startup tests, PARET-calculated peak powers overpredicted the experimental results by about 25%. The PARET-calculated powers and energy releases were within experimental uncertainty for all the 500°F hot-startup tests. The good agreement between PARET-calculated and experimental results indicates that coolant flow and moderator reactivity feedback should be considered in analyses of reactivity accidents at elevated system temperatures.

3. HIGH-INITIAL-POWER REACTIVITY ACCIDENT TESTS

The first phase of the experimental program covered the effects of system environmental conditions on the kinetic behavior of the Spert III E-core during reactivity accidents initiated from low initial powers. This phase provided a significant extension of existing experimental data and kinetic analyses for an oxide-fueled PWR. From these reactivity accident tests the effects of initial system temperature, coolant flow rate, and reactivity insertion upon the reactor kinetic behavior were investigated.

From the analyses of the results of these low-initial-power tests, it was determined that the kinetic behavior of the E-core was understood for the conditions examined. This understanding provided a basis for the next sequence in the experimental program: the investigation of the effects of the initial steady state power on the kinetic behavior of the E-core. The subsequent high-initial-power tests provided experimental data for reactivity accidents initiated from hot-standby and operating-power conditions. No such data were known to exist for oxide-fueled PWR's before these tests.

3.1 Operating Conditions for the High-Initial-Power Tests

For the high-initial-power testing phase, the reactor conditions were considered to be more severe than for the low-initial-power tests because: (a) the steady state fuel temperatures would be nearer the melting point, (b) the reactor core would contain much more stored energy, and (c) the power burst energy release would be considerably larger. The Spert III E-core operating conditions chosen for the high-initial-power reactivity accident tests were 500°F inlet coolant temperature, 1500 psig system pressure, and 12,000 gpm coolant flow. These conditions allowed for a significant safety margin for the experiments and still represented typical commercial PWR levels of coolant subcooling ($\approx$ 100°F) and average coolant velocity along the fuel rods ($\approx$14 fps).

The first series of the high-initial-power tests were performed from a steady state reactor power of about 1 MW. For the E-core, this corresponds to a peak power density of about 30 kW per liter of UO_2 (specific power of 0.8 kW/kg of UO_2), which is representative of hot-standby conditions in commercial PWR's. The second series of tests was performed from an initial reactor power of about 20 MW. This initial power yields a peak power density of about

550 kW per liter of UO_2 (specific power of 16 kW/kg of UO_2) and represents operating-power conditions in commercial PWR's.

To assure a low probability for E-core damage during the high-initial-power tests, the maximum fuel hot-spot enthalpy[a] was limited to 200 cal/g of UO_2. This UO_2 enthalpy is well below the value of about 270 cal/g required to reach UO_2 fuel melting temperatures. For the most severe initial power condition of 20 MW, pretest calculations indicated that the fuel hot-spot enthalpy limit of 200 cal/g of UO_2 would be reached in one second during an excursion initiated with a ramp reactivity insertion of about 1.30$. From the fuel hot-spot energy content consideration, it was decided to limit the reactivity insertions for the high-initial-power test series to about 1.25$, and to terminate the excursions by a control rod scram about one second after the initiation of the transient.

The ramp reactivity insertion rate of high-initial-power conditions was about 15$/sec.

3.2 Experimental Results

A total of five hot-standby and three operating-power reactivity accident tests was performed in the high-initial-power test series. A summary of the experimental results is presented in Table VII. The listed uncertainties in these data represent one standard deviation.

3.21 Power Burst Shapes. Experimental time-dependent power data for the five hot-standby tests and the three operating-power tests are shown in Figures 30 and 31, respectively. The power rise for all of these excursions is not purely exponential for even one decade, and thus these tests did not have stable reactor periods. This nonasymptotic behavior resulted because considerable energy was released immediately after initiation of the transients causing appreciable reactivity feedback during and after the time of reactivity insertion. Therefore, the hot-standby and operating-power reactivity accident tests are classified in Table VII according to initial reactivity insertion instead of reactor period.

Figures 30 and 31 illustrate power burst shapes typifying E-core kinetic behavior during reactivity accidents initiated from high-initial-power conditions. For the superprompt critical excursions, these burst shapes are quite similar

---

[a] The fuel enthalpy is the initial steady state enthalpy plus the enthalpy resulting from the excursion.

TABLE VII

DATA SUMMARY FOR HOT-STANDBY AND OPERATING-POWER REACTIVITY ACCIDENT TESTS

Test No.	Initial Reactivity Insertion ($)	Primary Coolant Inlet Temperature (°F)	Average Primary Coolant Flow Rate (fps)	Initial Reactor Power (Mw)	Maximum Reactor Power (Mw)	Net Energy Release[a] to time of Peak Power (Mw-sec)	Time to Peak Power (sec)	Maximum Measured Fuel Cladding Surface Temperature (°F)	Reactivity[b] Compensation at Peak Power ($)
79	0.86 ± 0.03	513 ± 4	14	1.1 ± 0.1	13 ± 1	6.7 ± 0.9	0.18 ± 0.02	510 ± 10	0.09
80	1.05 ± 0.04	506 ± 4	14	1.3 ± 0.1	120 ± 10	4.5 ± 0.6	0.150 ± 0.003	530 ± 10	0.11
81	1.17 ± 0.04	504 ± 4	14	0.9 ± 0.1	330 ± 30	7.8 ± 1	0.135 ± 0.003	540 ± 10	0.15
83	1.25 ± 0.04	504 ± 4	14	1.1 ± 0.1	620 ± 60	11 ± 1	0.117 ± 0.002	540 ± 10	0.24
82	1.29 ± 0.04	505 ± 4	14	1.2 ± 0.1	880 ± 90	15 ± 2	0.118 ± 0.002	550 ± 10	0.30
84	0.46 ± 0.02	505 ± 4	14	19 ± 1	39 ± 4	4.7 ± 0.6	0.18 ± 0.02	590 ± 10	0.05
85	0.87 ± 0.04	503 ± 4	14	19 ± 1	130 ± 10	14 ± 2	0.155 ± 0.005	590 ± 10	0.04
86	1.17 ± 0.05	502 ± 4	14	19 ± 1	610 ± 60	17 ± 2	0.110 ± 0.005	600 ± 10	0.22

[a] Incremental energy released during burst above that resulting from steady state operation.

[b] Because of uncertainties in initial reactivity insertions and peak power times these values are only approximate.

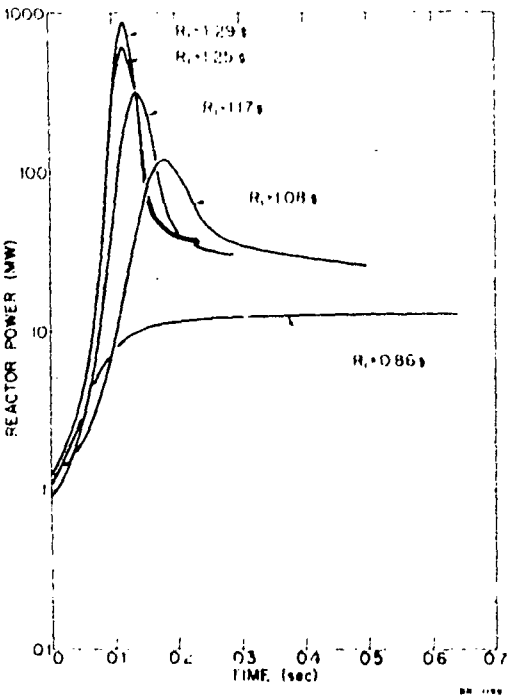

Fig. 30 Experimental power burst shapes as a function of reactivity insertion for the hot-standby tests (initial power ~1 MW).

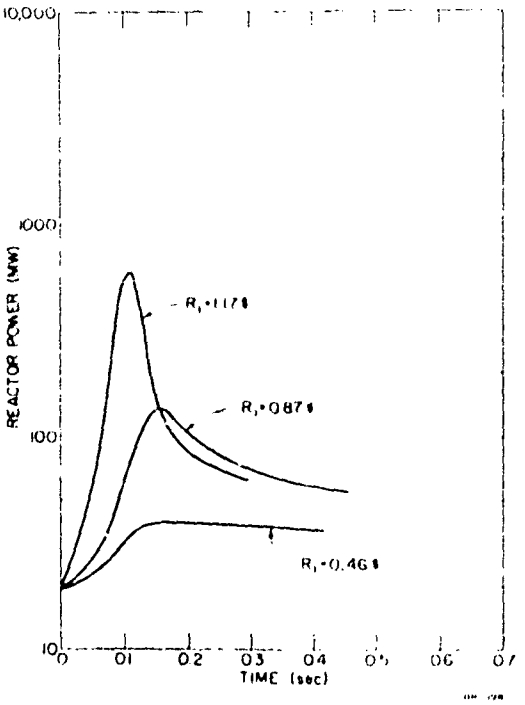

Fig. 31 Experimental power burst shapes as a function of reactivity insertion for the operating-power tests (initial power ~20 MW).

to those obtained during the low-initial-power tests (see Figure 10). Because of the immediate reactivity feedback after transient initiation for the high-initial-power tests, there is a marked difference in burst shapes between these tests and the low-initial-power subprompt critical excursions. For subprompt critical excursions initiated from low initial power, the time to peak power was a few seconds. For the high-initial-power tests, however, this time is only several hundred milliseconds. The immediate feedback and short time to peak power caused the bursts for the 0.86$ test in Figure 30, and the 0.46$ test in Figure 31, to approximate square waves. For these two tests, the reactor core conditions and reactivity insertion rates were such that the nuclear energy generation rate was balanced by the energy removal rate. For the other excursions in the two figures, the energy generation rate exceeded the energy removal rate so that reactivity feedback, which is energy or temperature dependent, was still occurring well after the power rise was terminated.

3.22 Energy Release to Peak Power. The net energy released to the time of peak power as a function of the reactivity insertion, for the 500°F hot-startup, hot-standby, and operating-power tests, is plotted in Figure 32.

The curves, drawn to aid in the general interpretation of the data, were least-squares fitted to the data points. For the hot-startup or low-initial-power tests, the energy to peak power displays a sharp minimum around 1$ reactivity insertion. For subprompt critical reactivity insertions, the energy to peak power decreases as the inserted reactivity increases (reactor period gets shorter). As the reactor period decreases, the time to peak power becomes shorter; thus, a relatively smaller number of delayed neutrons contribute to neutron multiplication. Therefore, less energy is required to terminate the power rise. For superprompt critical reactivity insertions, the reactivity above about 1$ must be compensated to terminate the power rise. For these excursions, as the reactivity insertion increases, larger energy releases are again required for reactivity compensation. For the hot-standby tests, the energy to peak power behavior is similar to that of the low-initial-power case, except that the minimum is not as sharp. This change in behavior again results from differences in the relative times of peak power. Peak power occurs much sooner for the hot-standby tests than for the hot-startup tests for the same reactivity insertion. For the operating-power test data, there is no minimum in the energy to peak power versus reactivity insertion curve. This behavior results because the times to peak power were short for all the operating-power excursions; thus, the delayed neutron contribution to neutron multiplication was small. The number of prompt neutrons that must be removed from the system in order to terminate the power rise increases as the amount of inserted reactivity increases. Therefore, larger energy releases are required for reactivity compensation as the reactivity insertion gets larger.

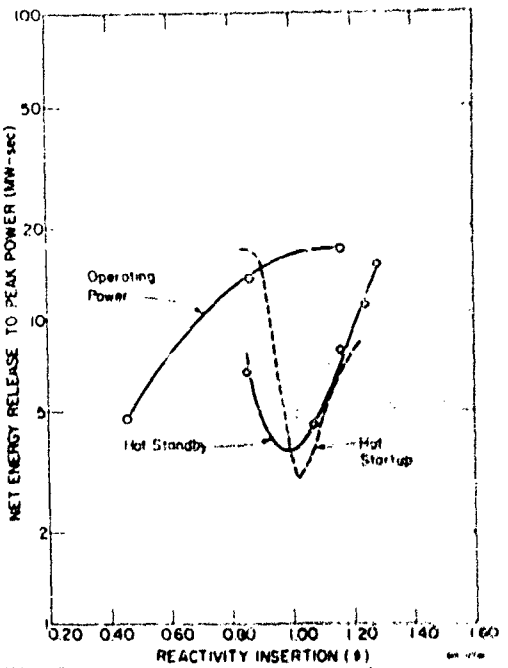

Fig. 32 Experimental net energy release to peak power as functions of reactivity insertion for the 500°F hot-startup, hot-standby, and operating-power tests.

3.3 Comparison of Calculational and Experimental Results

Prior to testing, PARET computer code calculations were performed to predict the kinetic response of the E-core for excursions initiated from high-initial-power conditions. Comparisons of these calculations with the experimental results were made to further evaluate the PARET model. The calculations also provided information that could not be determined by the experimental data alone. Since the PARET model separately accounts for Doppler, moderator heating, void formation, and fuel rod expansion reactivity feedback, the calculational results indicate the influence of initial steady state power on these reactivity feedback mechanisms.

3.31 Peak Reactor Powers. The experimental peak reactor power versus reactivity insertion data for the hot-standby and operating-power reactivity accident tests are plotted in Figure 33 together with the calculated curves obtained using the PARET code. Curves that were least-squares fitted to the data points are also given. Since only a few high-initial-power tests were performed, the confidence bands for the least-squares fitted curves are extremely broad and are not shown. Because of this lack of confidence in the fitted curves, comparisons between the experimental and calculated peak power values are made according to the uncertainties in the experimental data.

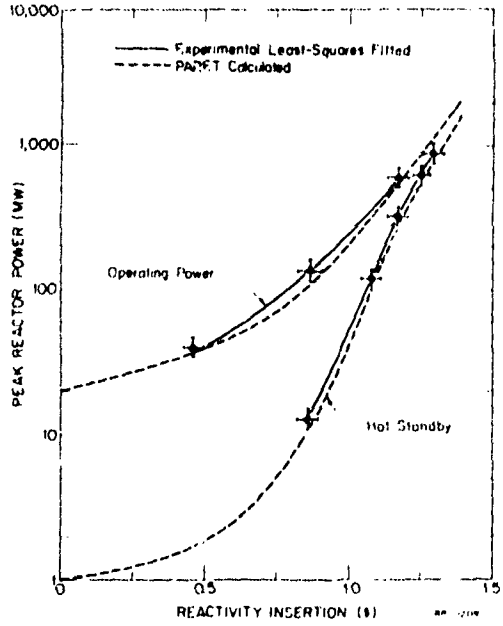

Fig. 33 Experimental and PARET calculated peak reactor powers as functions of reactivity for the hot-standby and operating-power tests.

The uncertainties in the data are represented by vertical and horizontal error bars. The vertical error bars represent an uncertainty of one standard deviation in the experimental peak power, which is about ± 10%. This ± 10% was estimated from the power calibration results[17]. The horizontal error bars represent an uncertainty of one standard deviation in the reactivity insertion. Because there were not stable reactor periods for the high-initial-

power transients, it was not possible to determine the reactivity insertions from the inhour equation. The reactivity insertions were determined as a function of the reactivity worths of the control rods. One standard deviation represents about ±4% uncertainty in the reactivity insertion.

For the entire high-initial-power test series, the PARET-calculated peak power values are 10 to 20% less than the experimental data. For the hot-standby series, the calculated peak power values are in agreement with the experimental results well within the uncertainties in the reactivity insertions. For the operating-power series, the calculated peak power values are in most cases within the uncertainties of the experimental data.

3.32 Power Burst Shapes and Net Energy Release. Time-dependent reactor power and net energy release[a] for two representative high-initial-power tests are shown in Figures 34 and 35. These two tests were initiated with rapid ramp reactivity insertions of about 1.17$. For both tests, the PARET-calculated power and net energy release are in agreement with the experimental results.

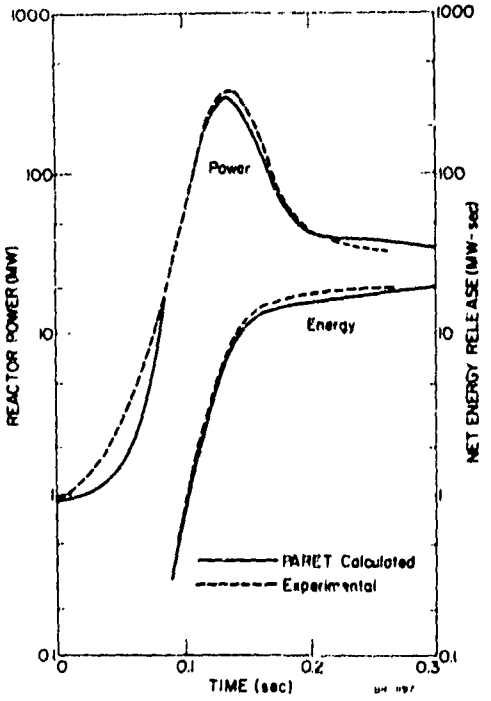

Fig. 34 Experimental and PARET calculated reactor power and net energy release for hot-standby test 81 (1.17$ reactivity insertion).

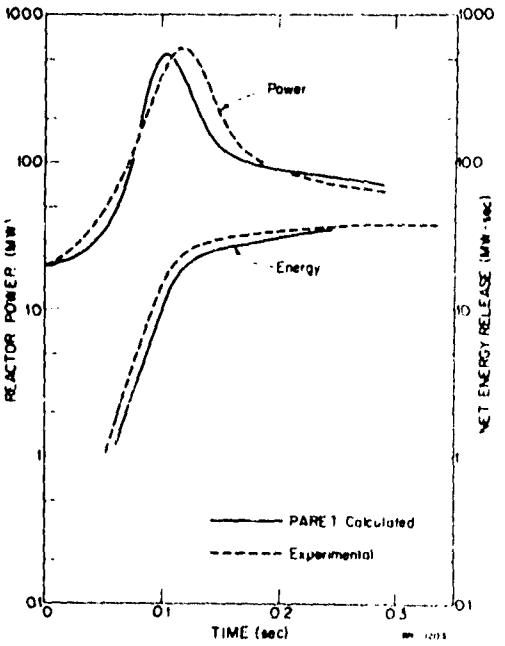

Fig. 35 Experimental and PARET calculated reactor power and net energy release for operating-power test 86 (1.17$ reactivity insertion).

[a] The net energy release is the energy release above that resulting from steady state operation.

The differences in the calculated and experimental burst shapes result in large part from the differences between the experimental reactivity insertion rate and the rate used in the PARET pretest calculations.

3.33 Net System Reactivity and Reactivity Insertion Rate. For the low-initial-power reactivity accident tests, it was possible to compare both the net system and compensated reactivities, determined from experimental power data, with calculational results. The net system reactivity was determined from the experimental power data with the SPORT[23] computer code which uses the point-reactor kinetic equations. During the low-initial-power tests, the net system reactivity was initially assumed to be equal to the total reactivity inserted because stable reactor periods were reached for these tests. Therefore, during these transients the compensated reactivity was determined by subtracting the net system reactivity from the known initially inserted reactivity. However, during high-initial-power tests, appreciable reactivity compensation occurred during the reactivity insertion time; thus the initial net system reactivity could not be assumed to be equal to the total reactivity insertion. Experiments were not performed to determine the precise reactivity insertion rates for transients initiated from high-initial-power levels. For this reason, the compensated reactivity for the high-initial-power tests could not be precisely determined from the experimental data, and only the net system reactivi could be compared with calculational results.

Net system reactivities determined from experimental power data for representative hot-startup and operating-power tests initiated with 1.17$ reactivity insertions are shown in Figures 36 and 37, respectively, together with PARET-calculated results. The largest difference between the experimentally determined and calculated curves shown in these two figures is about 0.10$, or 25% of the experimentally determined value. Since one standard deviation in the net system reactivity derived from experimental data is about 11% at the time of peak power and becomes even larger at post-peak power times (Appendix C), the agreement between the calculated and experimentally determined net system reactivities can be considered good.

The net system reactivities shown in Figures 36 and 37 also indicate the time dependency of reactivity insertion since net system reactivity is the inserted minus the compensated reactivity. If it is assumed that PARET calculations of the reactivity feedback are as good for the high-initial-power

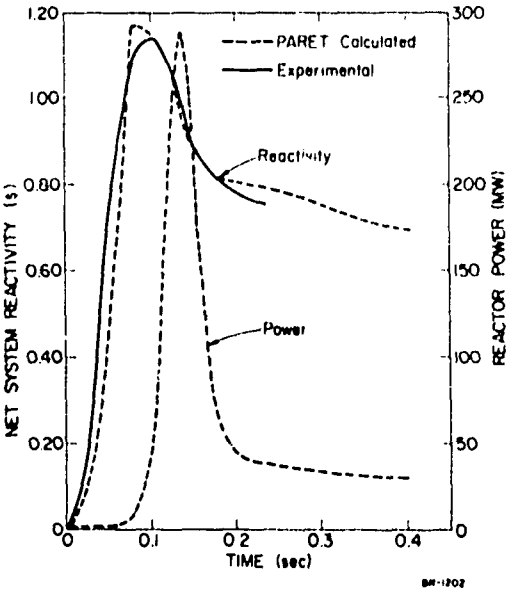

Fig. 36 Experimental and PARET calculated net system reactivity for hot-standby test 81 (1.17$ reactivity insertion).

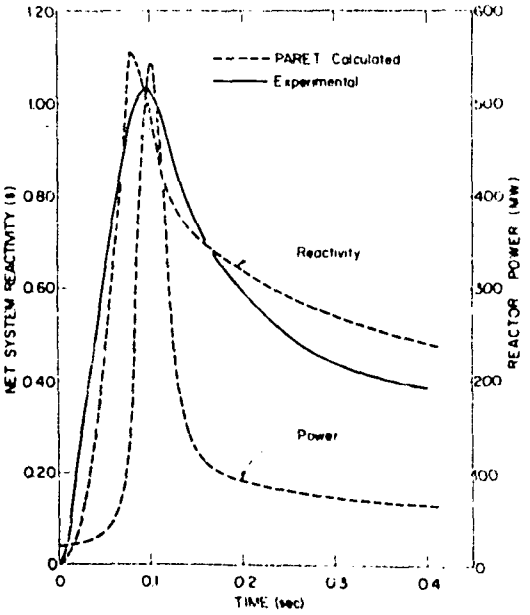

Fig. 37 Experimental and PARET calculated net system reactivity for operating-power test 86 (1.17$ reactivity insertion).

tests as they were for the low-initial-power tests, then a comparison of the calculated and experimentally determined net system reactivities indicates that the reactivity insertion rate was larger at the beginning and smaller at the end of the insertion than the rate used in the PARET calculations. The reactivity insertion rates input to the PARET code were determined from control rod worth measurements and a calculated transient-rod-position versus time curve.

3.34 Fuel and Cladding Surface Temperature. The maximum fuel and cladding temperatures attained during the high-initial-power reactivity accident tests are extremely important in reactor safety investigations. The core hot-spot cladding surface temperature was measured by a stainless steel sheathed thermocouple attached to the corner fuel rod in the S11 fuel assembly. The thermocouple was located 16 inches above the bottom of the fuel rod. Steady state, core hot-spot cladding temperatures were measured to be about 575, 570, and 560°F, respectively, for the three operating-power tests. Differences between these various steady state temperatures are attributed primarily to the differences in the initial power levels and coolant inlet temperatures for the three tests. The steady state, hot-standby, core hot-spot cladding temperatures were measured to be around 500°F for all the tests. PARET-

calculated steady state hot-spot cladding temperatures were 588 and 504°F for the operating-power and hot-standby initial conditions, respectively. The differences between the calculated and experimental steady state cladding surface temperatures were caused by temperature gradients across the thermocouple junctions and heat losses because of flow.

For the two representative hot-standby and operating-power tests initiated with 1.17$ reactivity insertions, the measured maximum transient hot-spot cladding temperatures were about 540 and 600°F, respectively. The PARET-calculated hot-spot cladding temperatures for these two tests are shown in Figure 38. For the hot-standby test, the calculated hot-spot cladding temperature is about 530°F just after the power burst and is calculated to reach about 540°F at the time of automatic control rod scram (1 sec). For the operating-power test, the calculated hot-spot cladding temperature reaches the nucleate boiling temperature of 606°F at 0.14 second and remains at this temperature throughout the duration of the transient. The calculations indicate that this nucleate boiling is confined to a small axial flux peaking region in about 5% of the core. The agreement between the calculated and experimental maximum hot-spot cladding surface temperatures was good.

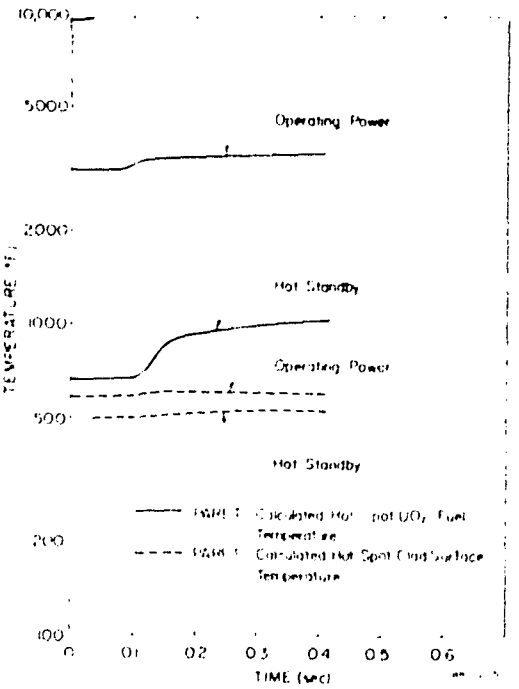

Fig. 38 PARET calculated hot-spot UO_2 fuel and cladding temperatures for hot-standby test 81 and operating-power test 86.

Since the core was not instrumented to measure the UO_2-fuel temperature, this important parameter could only be calculated. The good agreement between the PARET calculated reactor power and net energy release and the experimental results for the two representative high-initial-power excursions shown in Figures 34 and 35 made it reasonable to assume that the PARET model would also adequately estimate the reactor fuel temperature distribution. For the hot-standby test shown in Figure 38, the PARET-

calculated hot-spot UO_2-fuel temperature is about 1050°F just after the power burst and is calculated to become about 1270°F at the time of automatic control rod scram. For the most severe operating-power excursion performed, the post-burst calculated hot-spot fuel temperature is about 3560°F. At the time of automatic control rod scram, the hot-spot fuel temperature is calculated to be about 3800°F. For all of the high-initial-power reactivity accident tests, the PARET-calculated maximum hot-spot fuel temperatures are well below the melting temperature of UO_2.

3.4 Reactivity Feedback Mechanisms

PARET results show the effects of high initial reactor power on the individual dynamic reactivity feedback mechanisms that limit reactivity accidents. The model separately accounts for reactivity feedback arising from fuel rod and moderator heating. Since the largest difference between the experimental and calculated net system reactivities for the high-initial-power tests was about 25%, the calculated total compensated reactivities should be representative of the experimental values. In addition, the consistently good agreement between the calculated and experimental total reactivity compensations for all the low-initial-power tests supports the conclusion that the major reactivity feedback mechanisms are adequately accounted for in the PARET model.

3.41 Fuel and Moderator Heating. The role of fuel and moderator heating as reactivity feedback mechanisms during high-initial-power reactivity accident tests can be estimated from PARET calculations. The feedback resulting from fuel heating is primarily caused by Doppler broadening and fuel rod expansion. Reactivity feedback resulting from moderator heating is caused by moderator expansion and void formation. The calculated fuel and moderator heating reactivity compensations at the time of peak power for several representative 500°F hot-startup, hot-standby, and operating-power tests are listed in Table VIII. The moderator heating reactivity compensation increases from about 30 to 50% of the total compensation as the initial power increases from 50 W to 20 MW. Conversely, the fuel heating compensation decreases from about 70 to 50%. This change in fuel and moderator heating feedback results because with increasing initial power levels (a) the average temperature increases and causes increased moderator reactivity feedback because the moderator temperature coefficient increases with increasing temperature, and (b) the average fuel temperature increases and causes less Doppler reactivity feedback per

TABLE VIII

PARET CALCULATED FUEL AND MODERATOR HEATING REACTIVITY COMPENSATION AT THE TIME OF PEAK POWER

Initial Reactor Power (MW)	Initial Reactivity Insertion ($)	Time to Peak Power (sec)	Fuel Heating Compensation (% of total)	Moderator Heating Compensation (% of total)
5×10^{-5}	0.93	3.46	72	28
5×10^{-5}	1.15	0.269	65	35
1.0	1.07	0.152	66	34
0.9	1.17	0.097	65	35
20.0	0.90	0.097	50	50
19.3	1.17	0.103	51	49

unit energy release because the Doppler coefficient decreases with increasing fuel temperature. There is little difference between moderator heating reactivity feedback contributions for initial powers of 50 W and 1 MW because the moderator temperature coefficients are approximately equal for these cases.

For the low-initial-power tests, where the power rises on a stable period, the moderator heating reactivity feedback is a function of the reactor period or reactivity insertion. In Table VIII, the moderator heating compensation increases from 28 to 35% of the total as the reactivity insertion for the hot-startup tests increases from 0.93 to 1.15$. This behavior of increasing moderator heating compensation with larger reactivity insertions did not occur for the high-initial-power tests. For these tests, the power did not rise on stable periods, and the times to peak power were essentially the same regardless of reactivity insertion.

3.42 Prompt and Delayed Reactivity Feedback. The reactivity feedback can further be broken down into prompt and delayed components. For the fuel heating feedback mechanism, the Doppler compensation is prompt, but the fuel rod expansion compensation caused by heat transfer out of the fuel into the cladding is delayed. For the moderator heating feedback mechanisms, the heating that results from slowing down of fast neutrons and attenuation of prompt gamma rays gives PMH feedback, but the heating caused by heat transfer

out of the fuel into the moderator yields delayed feedback. These various calculated prompt and delayed feedback mechanisms are illustrated in Figures 39 and 40.

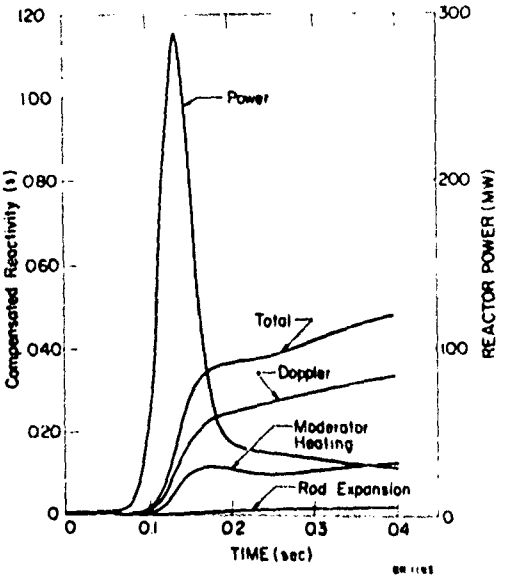

Fig. 39 PARET calculated reactor power and reactivity compensation for hot-standby test 81 (1.17$ reactivity insertion).

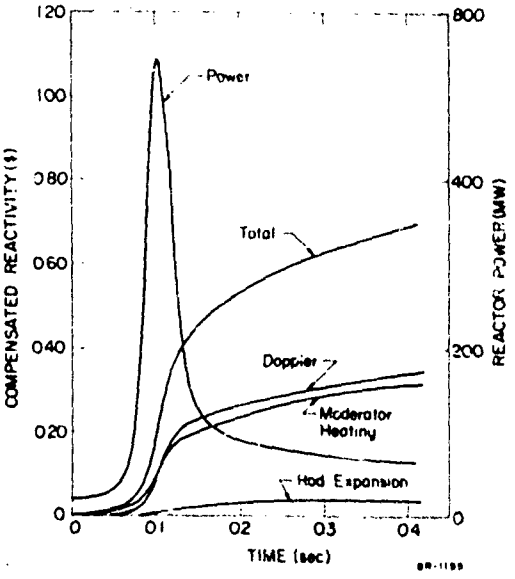

Fig. 40 PARET calculated reactor power and reactivity compensation for operating-power test 86 (1.17$ reactivity insertion).

The PARET-calculated, time-dependent, reactivity compensation for a hot-standby reactivity accident initiated with a reactivity insertion of 1.17$ is shown in Figure 39. The majority of the fuel heating reactivity compensation is due to prompt Doppler feedback, with the delayed fuel rod expansion feedback contributing only around 3% at the time of peak power. Until about 0.2 second, almost all of the moderator heating feedback is due to PMH. This PMH feedback decreases after the power burst. However, the moderator heating feedback is maintained by the delayed heat transfer out of the fuel rods into the moderator. The dip in the moderator heating compensation at about 0.25 second is not as pronounced as was the case for a similar 500°F hot-startup test (Figure 26). The delayed conductive heat transfer from the fuel to the water occurs sooner for the hot-standby than for the hot-startup excursion because the gas gap is smaller and the steady state fuel temperatures are larger. For the E-core hot-standby tests, the reactivity feedback mechanisms which limit the power excursions are principally prompt, with Doppler compensation predominating.

The PARET-calculated, time-dependent, reactivity compensation for an operating-power reactivity accident initiated with a reactivity insertion of 1.17$ is shown in Figure 40. The majority of the fuel heating compensation is again due to prompt Doppler feedback, with the delayed rod expansion feedback contributing around 4% at the time of peak power. Until about 0.15 second, most of the moderator heating feedback is due to PMH. There is no dip in the moderator heating feedback as there was for the hot-standby excursion. The reason for this difference is due to a combination of (a) significant post-burst PMH feedback because of the high runout power level and (b) early conductive heat transfer to the moderator. The clad-water heat transfer occurs sooner because of the very small gas gap and high steady state fuel temperatures at operating-power conditions. For operating-power tests with the E-core, PMH compensation is the dominant feedback mechanism until about the time of peak power, where the Doppler feedback becomes approximately equal to the PMH feedback.

3.5 Summary of the Effects of Initial Reactor Power

To determine the effects of the initial reactor power on the results of reactivity accidents, the initial reactor conditions were uniformly set at 500°F coolant inlet temperature, 1500 psig system pressure, and 14 fps coolant flow. With these initial conditions, reactivity accident tests were initiated by reactivity insertions of 0.46 to 1.29$.

3.51 Time to Peak Power. The time required to reach peak power after initiation of a reactivity accident varies with initial power conditions for identical reactivity insertions. Figure 41 shows the experimental peak power times for a range of reactivity insertions at 500°F hot-startup, hot-standby, and operating-power conditions. For all three test conditions, the reactivity insertion rate was about 15$/sec. For large values of reactivity insertion, the times to peak power for all initial power conditions tend to converge toward a value of roughly 100 msec. For a small value of reactivity insertion such as 0.80$, the time varies from about 13 sec to 160 msec when the initial power changes from 50 W to 20 MW.

3.52 Superprompt Critical Tests. The effects of the initial power on superprompt critical reactivity accident tests are illustrated in Figure 42. In this figure, the time-dependent experimental reactor power and net energy release are given for hot-startup, hot-standby, and operating-power tests, all

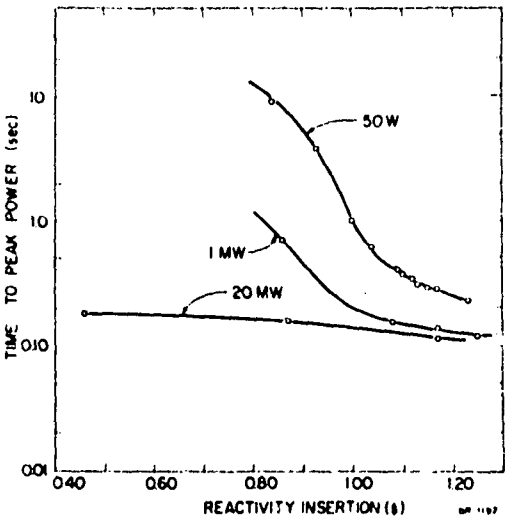

Fig. 41. Experimental times to peak power as functions of initial reactivity insertion and initial reactor power for the 500°F hot-startup, hot-standby, and operating-power tests.

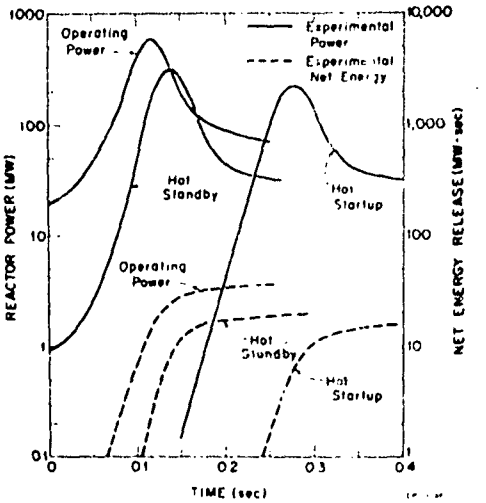

Fig. 42 Experimental powers and net energy releases for 500°F hot-startup test 59, hot-standby test 81, and operating-power test 86, all initiated with 1.17$.

initiated with a ramp reactivity insertion of 1.17$. The power burst shapes are generally similar for all three tests. The power burst magnitude is not strongly dependent on initial power conditions; ie, the hot-standby peak power and runout net energy release are only about 1.4 times the hot-startup values, and the operating-power peak power and runout net energy release are about 2.7 times the hot-startup values. The time to complete the superprompt critical power bursts is also only weakly dependent on the initial power condition. The net energy releases at the time of peak power for the hot-standby and operating-power tests were 1.3 and 2.7 times that for the hot-startup tests. These ratios reflect primarily the effect of the decreasing Doppler reactivity feedback coefficient with increasing initial reactor power and subsequent higher initial fuel temperatures.

3.53 Subprompt Critical Tests. The effects of the initial power on subprompt critical reactivity accident tests are illustrated in Figure 43. The time-dependent experimental reactor power and net energy release are given for hot-startup, hot-standby, and operating-power reactivity accident tests, initiated with ramp reactivity insertions of 0.93, 0.86, and 0.87$, respectively. For these subprompt critical tests there is marked dissimilarity in the power burst shapes. The times to peak power vary considerably, with the hot-startup peak power time about 35 times that of the operating-power tests. In terms

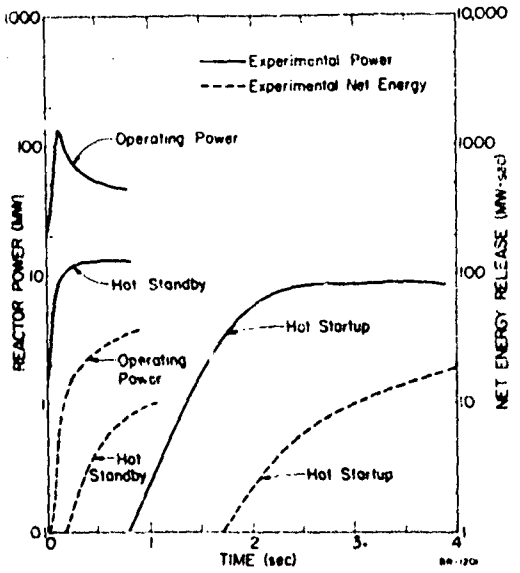

Fig. 43 Experimental powers and net energy releases for 500°F hot-startup test 54 (0.93$ reactivity insertion), hot-standby test 79 (0.86$ reactivity insertion), and operating-power test 85 (0.87$ reactivity insertion).

of the power burst magnitude, the hot-standby and operating-power peak powers are respectively about 1.5 and 10 times the hot-startup peak power. The net energy release at the time of peak power for the hot-standby test is only 0.6 that of the hot-startup value. This energy release relationship, which is opposite to the superprompt critical behavior, is due to the large differences in peak power times and thus the relative number of delayed neutrons contributing to the neutron multiplication. This is demonstrated by the reactivities that had to be compensated in order to terminate the power rises. The compensated reactivities at peak power were 0.25$ for the hot-startup excursion and only 0.09$ for the hot-standby excursion. The net energy release at the time of peak power for the operating-power tests is about twice that of the hot-standby value. The compensated reactivity at peak power was about 0.04$ for the operating-power excursion. Thus, it took twice the energy release at operating-power conditions to compensate about half the reactivity, which demonstrates the effect of the decreasing Doppler reactivity feedback coefficient with increasing initial reactor power.

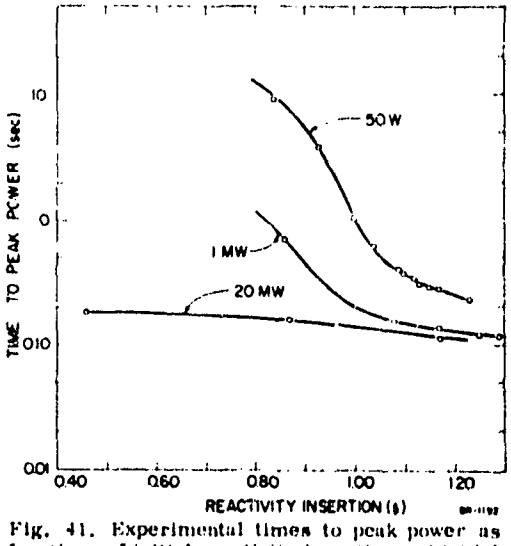

Fig. 41. Experimental times to peak power as functions of initial reactivity insertion and initial reactor power for the 500°F hot-startup, hot-standby, and operating-power tests.

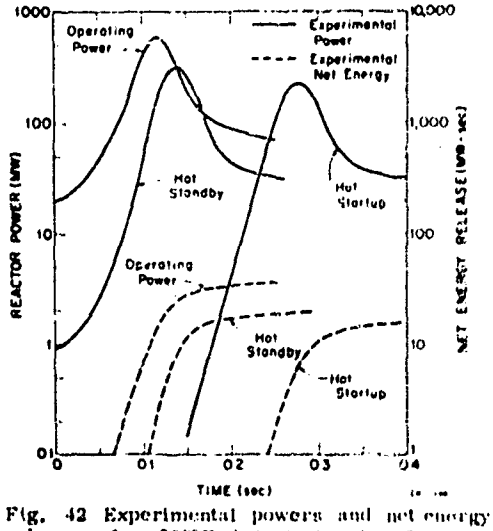

Fig. 42 Experimental powers and net energy releases for 500°F hot-startup test 59, hot-standby test 81, and operating-power test 86, all initiated with 1.17$.

initiated with a ramp reactivity insertion of 1.17$. The power burst shapes are generally similar for all three tests. The power burst magnitude is not strongly dependent on initial power conditions; ie, the hot-standby peak power and runout net energy release are only about 1.4 times the hot-startup values, and the operating-power peak power and runout net energy release are about 2.7 times the hot-startup values. The time to complete the superprompt critical power bursts is also only weakly dependent on the initial power condition. The net energy releases at the time of peak power for the hot-standby and operating-power tests were 1.3 and 2.7 times that for the hot-startup tests. These ratios reflect primarily the effect of the decreasing Doppler reactivity feedback coefficient with increasing initial reactor power and subsequent higher initial fuel temperatures.

3.53 Subprompt Critical Tests. The effects of the initial power on subprompt critical reactivity accident tests are illustrated in Figure 43. The time-dependent experimental reactor power and net energy release are given for hot-startup, hot-standby, and operating-power reactivity accident tests, initiated with ramp reactivity insertions of 0.93, 0.86, and 0.87$, respectively. For these subprompt critical tests there is marked dissimilarity in the power burst shapes. The times to peak power vary considerably, with the hot-startup peak power time about 35 times that of the operating-power tests. In terms

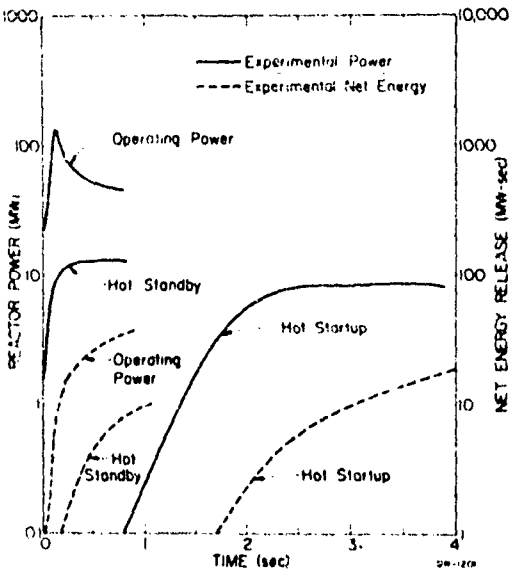

Fig. 43 Experimental powers and net energy releases for 500°F hot-startup test 54 (0.93$ reactivity insertion), hot-standby test 79 (0.86$ reactivity insertion), and operating-power test 85 (0.87$ reactivity insertion).

of the power burst magnitude, the hot-standby and operating-power peak powers are respectively about 1.5 and 10 times the hot-startup peak power. The net energy release at the time of peak power for the hot-standby test is only 0.6 that of the hot-startup value. This energy release relationship, which is opposite to the superprompt critical behavior, is due to the large differences in peak power times and thus the relative number of delayed neutrons contributing to the neutron multiplication. This is demonstrated by the reactivities that had to be compensated in order to terminate the power rises. The compensated reactivities at peak power were 0.25$ for the hot-startup excursion and only 0.09$ for the hot-standby excursion. The net energy release at the time of peak power for the operating-power tests is about twice that of the hot-standby value. The compensated reactivity at peak power was about 0.04$ for the operating-power excursion. Thus, it took twice the energy release at operating-power conditions to compensate about half the reactivity, which demonstrates the effect of the decreasing Doppler reactivity feedback coefficient with increasing initial reactor power.

IV. EXTRAPOLATIVE CALCULATIONS

PARET code calculations were performed as a part of the Spert III E-core program to investigate kinetic behavior for postulated reactivity accidents significantly different from those actually tested. Analytical investigations were made in the areas of (a) the effect of the moderator temperature coefficient of reactivity on an operating-power reactivity accident and (b) the results of reactivity accidents performed with the maximum available E-core excess reactivity inserted at the various initial E-core conditions.

1. POSITIVE MODERATOR TEMPERATURE COEFFICIENT

In Section III-3.4 it was observed that the PMH reactivity feedback contributed about 50% of the total reactivity compensation for E-core operating-power reactivity accident tests. Since the PMH feedback is negative only as long as the moderator temperature coefficient of reactivity is negative, a positive moderator coefficient could cause the PMH feedback to become an inherently unsafe mechanism. For this situation, the PMH feedback would be equivalent to positive reactivity insertion.

At system conditions of 500°F coolant inlet temperature and 1500 psig, the Spert III E-core has a moderator temperature coefficient of about -4¢/°F. This negative value is near the maximum for present operating PWR's. The effect of moderator temperature coefficients on the excursion behavior of the E-core was investigated to verify the strong influence of PMH feedback. PARET calculations were made for operating-power reactivity accidents initiated by a ramp reactivity insertion of 1.22$ with the temperature coefficient arbitrarily varied over the range from -4 to +1.4¢/°F, while all the other E-core parameters were held fixed.

The power bursts for three such PARET-calculated reactivity accidents are illustrated in Figure 44. As the temperature coefficient changes from -4 to +1.4¢/°F, the peak reactor power increases by a factor of about three and the runout power increases by a factor of about two. For these calculations, the net energy releases are shown in Figure 45. For the +1.4¢/°F temperature coefficient, the net energy releases after 250 msec yields an adiabatic hot-spot fuel enthalpy increase of about 58 cal/g of UO_2. When added to the 20 MW steady state energy content, the maximum fuel enthalpy is about 190

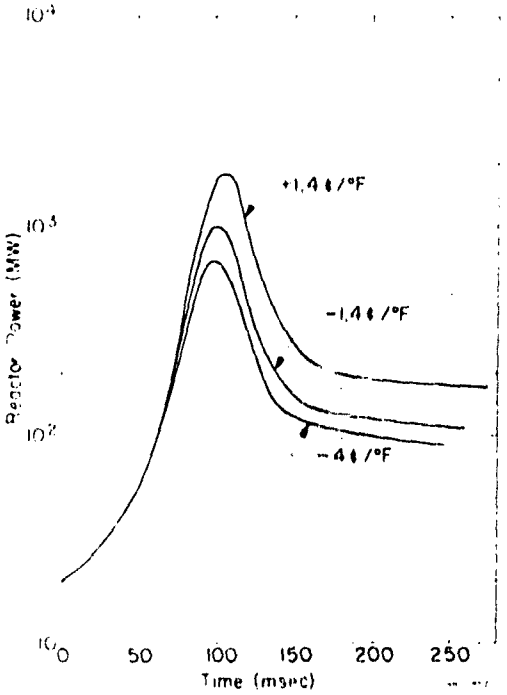

Fig. 44 PARET calculated reactor power for operating-power reactivity accidents initiated with 1.22$ for various moderator temperature coefficients of reactivity.

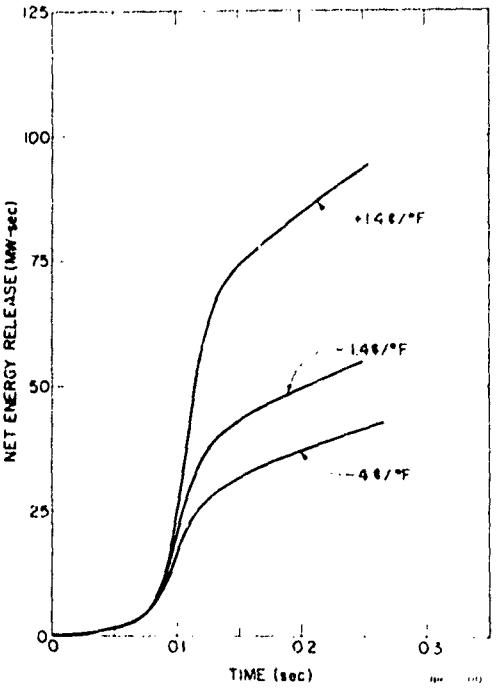

Fig. 45 PARET calculated net energy release for operating-power reactivity accidents initiated with 1.22$ for various moderator temperature coefficients.

cal/g of UO_2 after 250 msec. Thus, no fuel melting should be predicted during the transient time considered.

For these operating-power reactivity accidents, peak power, net energy release to peak power, and hot-spot fuel temperature after 250 msec are shown as functions of the moderator temperature coefficient in Figure 46. The slopes of the power, energy, and fuel temperature curves increase rapidly with increasing values of the moderator temperature coefficient. Extrapolation of these results indicates that power excursions limited only by core damage or disassembly could occur for moderator temperature coefficients greater than about +3¢/°F in the E-core if all the other core parameters were not changed.

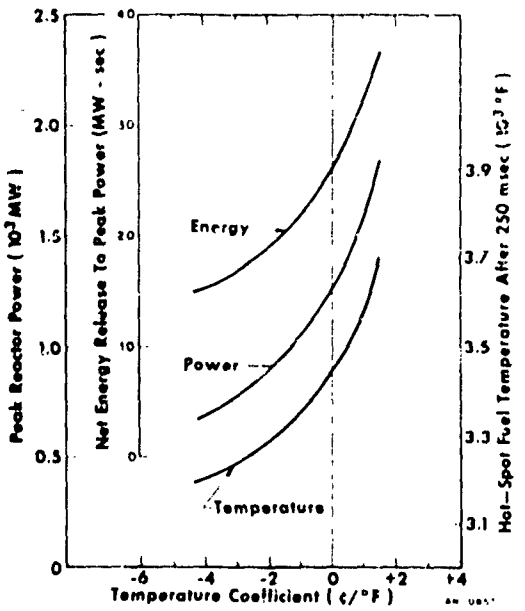

Fig. 46 PARET calculated peak power, net energy release to peak power, and hot-spot fuel temperature as functions of moderator temperature coefficient for 1.22$ operating-power accidents.

2. MAXIMUM SPERT III E-CORE REACTIVITY ACCIDENTS

Because of the excellent agreement between the PARET calculational and Spert III E-core experimental results, it is expected that PARET calculations performed for reactivity accidents significantly more severe than those tested would also yield meaningful results. Therefore, PARET calculations were performed for the maximum available excess reactivity insertions at various initial E-core conditions.

2.1 Accident Conditions

The reactivity accidents that were considered cover a wide range of reactor system temperatures, reactivity insertions, ramp rates, and initial reactor power levels. At ambient system temperature (70°F) the maximum reactivity controlled by the E-core transient rod was about 4.8$. Even though the excess reactivity available at these conditions was larger than 4.8$, the maximum reactivity that could be inserted at 70°F was limited to the transient rod worth. Calculations showed that the maximum transient rod worth did not change appreciably as the reactor temperature increased. As a result, the maximum reactivity that could be inserted at 250°F system temperature was again limited to the transient rod worth of about 4.8$. At a system temperature

of 500°F the excess reactivity available decreased to a value of about 3.5$, and therefore this value was the maximum reactivity that could be inserted at this core condition.

For all of the PARET calculations, the reactivity was inserted according to one of the following three fast ramp rates:

(1) A normal ramp rate was determined from the experimental differential control rod worths and time-dependent transient rod position (calculated assuming the constant design acceleration of the transient rod). This rate is the same as the one used for the PARET calculations in Section III.

(2) The maximum ramp rate that could be achieved within the E-core transient rod design specifications was determined. This ramp rate was about twice the normal ramp rate.

(3) A ramp rate was determined which would represent an excursion initiated with the reactor subcritical. The linear ramp rate for this case was an insertion of 92$/sec.

Calculations were performed for cold-startup, hot-startup, hot-standby, and operating-power conditions. An initial power of one milliwatt was used to represent excursions initiated from subcritical.

2.2 Calculational Results

The results of PARET calculations for the maximum E-core reactivity accidents are listed in Table IX. In the PARET calculations, nonlinear ramp rates were used in most cases, but the reactivity input values listed in the table represent average linear ramp rates. Because the core damage that could occur during the power burst was of primary concern, the calculations were performed for transient times of only 200 msec. By this time all of the reactor runout powers reached quasi-equilibrium values. Since the runout powers were large, fuel melting and critical clad-water heat transfer conditions would be predicted for transient times longer than 200 msec for all of the extrapolative calculations.

For both of the calculations at 70°F system temperature, the reactor power peaked before the end of the reactivity ramp. Considerably more reactivity was inserted at peak power for the excursion initiated from subcritical (92$/sec ramp and one milliwatt initial reactor power) than was the case for

TABLE IX

PARET CALCULATIONAL RESULTS FOR MAXIMUM SPERT III E-CORE REACTIVITY ACCIDENTS

Primary Coolant Inlet Temperature (°F)	Initial Reactor Power (W)	Initial Reactivity Insertion ($)	Reactivity Input Rate ($/sec)	Maximum Reactor Power (MW)	Time to Peak Power (msec)	Maximum UO_2-Fuel Temperature (°F)	Reactivity Inserted to Time of Peak Power ($)	Maximum Net System Reactivity ($)
70	1×10^{-3}	4.8	92	130,000	50	7500[a]	4.62	4.33
70	50	4.8	≈ 25	37,000	102	5100	3.12	2.75
250	1×10^{-3}	4.8	92	115,000	50	6200[a]	4.60	4.20
250	50	4.8	≈ 24	34,000	102	4600	3.12	2.75
500	1×10^{-3}	3.5	≈ 15	46,000	137	3500	3.22	3.14
500	50	3.5	≈ 15	26,000	126	3900	2.85	2.53
500	50	3.5	≈ 30	54,000	73	5700	3.50	3.37
500	1×10^{6}	3.5	≈ 15	9,000	110	2500	2.18	1.75
500	20×10^{6}	3.5	≈ 15	6,000	105	4700	2.01	1.40
500	20×10^{6}	3.5	≈ 30	19,000	60	4900	2.58	1.83

[a] Fictitious value since UO_2 melts at about 5200°F, but indicates that some UO_2 melting is predicted.

the normal 4.8$ excursion. As a result, the peak power for the excursion initiated from subcritical was about four times that calculated for the transient initiated from critical. For the excursion initiated from subcritical, the calculated maximum fuel temperature of 7500°F[a] indicates fuel melting would occur in the high flux regions of the core. The earliest fuel melting at the hot-spot was predicted to occur about 0.2 msec after peak power was reached. At this time the hot-spot cladding surface temperature was calculated to be only 186°F. During the transient time, some fuel melting was also predicted to occur along the axial flux peaking regions in 30% of the core. For the normal ramp at critical, the maximum hot-spot fuel temperature was calculated to be 5100°F. For this case little or no fuel melting is predicted during the transient time.

The 250°F excursions initiated from subcritical and critical yielded results similar to those of the two 70°F excursions. The peak power for the excursion initiated from subcritical was about four times the value of the peak power for the excursion initiated at critical, and much more reactivity was inserted at peak power for the subcritical case. For the subcritical case, fuel melting at the core hot-spot was again predicted to occur, the calculated maximum fuel temperature being 6200°F. This temperature is about 1000°F less than was the case for the 70°F excursion initiated from subcritical. The earliest fuel melting at the hot-spot was predicted to occur about 2 msec after peak power was reached. At this time, the hot-spot cladding surface temperature was calculated to be 418°F. This cladding temperature is about 200°F higher than for the similar cold-startup calculation. This difference is due to the larger initial energy content of the fuel rod at 250°F system temperature. During the transient initiated from subcritical at 250°F, the fuel temperatures along the axial flux peaking regions in 5% of the core were predicted to be above melting. For the normal ramp at critical, the maximum hot-spot fuel temperature was calculated to be 4600°F and no fuel melting was predicted.

---

[a] The PARET code does not consider fuel melting but continues to use the specific heat versus temperature relationship for solid fuel, even though the calculated temperature exceeds the melting point of UO_2. Therefore, any temperature in excess of about 5200°F is fictitious. The real temperature would remain at 5200°F until about 100 cal/g is added for the latent heat of fusion. Thus, in regions where the PARET temperature exceeds the melting point, all the fuel in that region has not necessarily melted.

For the four transient calculations performed for 500°F system temperature and initiated with the normal ramp rate, the power peaked before the end of the input reactivity ramp. The largest peak reactor power was achieved at the lowest initial power level (1×10^{-3} W) because a larger reactivity input was possible before appreciable reactivity feedback occurred. The largest maximum fuel temperature predicted in these four calculations was 4700°F for the operating-power or 20 MW initial power transient. This result reflects the large energy content of the fuel at steady state operating-power conditions. For the operating-power, normal ramp transient, the hot-spot cladding surface temperature at 200 msec was calculated to be 876°F. Although no fuel melting was expected at this time, clad-water heat transfer along the axial flux peaking regions in 30% of the core was predicted to be in the transition boiling regime. The transient calculation performed for 500°F system temperature, 50 W initial reactor power with twice the normal ramp rate indicates that all of the reactivity was inserted before peak power time. The maximum hot-spot fuel temperature reached 3700°F, which was about 800°F higher than the similar normal ramp value. At the end of the transient time the hot-spot cladding surface temperature was predicted to be 718°F and the transition boiling regime occurred along the axial peaking region in 5% of the core. For the 20 MW initial power, double ramp rate case, the maximum hot-spot fuel temperature predicted was 4900°F. This value is only slightly higher than the 4700°F maximum fuel temperature for the normal ramp from 20 MW. The long ramp time of the normal ramp gave rise to a second power peak which increased with hot-spot fuel temperature from 4100 to 4700°F. At the end of the transient time for the 20 MW initial power, double ramp rate calculation, the hot-spot cladding surface temperature was predicted to be 1044°F. The transition boiling regime was again predicted to occur along the axial flux peaking region in 30% of the core.

The results of the extrapolative calculations for the maximum reactivity accidents in the Spert III E-core can be summarized briefly as follows:

(1) For a specified reactor condition and reactivity insertion, the severity of a reactivity accident is predicted to increase with faster ramp rates.

(2) The most fuel melting, with a significant probability of core damage, is predicted to occur with a 70°F initial system temperature for a transient initiated from subcritical.

(3) Some fuel melting in the hotter core regions, with a slight probability of core damage, is predicted to occur at 250°F system temperature conditions for a transient initiated from subcritical.

(4) Although no fuel melting is predicted at 500°F system temperature conditions, critical clad-water heat transfer conditions (departure from nucleate boiling heat fluxes) are predicted in a significant portion of the core for transients initiated from 20 MW initial reactor power or operating-power conditions.

2.3 Maximum UO_2-Fuel Temperature as a Function of Reactivity Insertion and Reactor Operating Condition

In conjunction with the maximum reactivity accident analyses, PARET calculations were performed to determine the E-core maximum fuel temperature behavior for various reactivity accidents initiated from the cold-startup, hot-standby, and operating-power reactor conditions. For these calculations the reactivity was inserted with the normal ramp rate.

The results of the calculations are given in Figure 47. The three lower curves show the maximum hot-spot fuel temperature rise 250 msec after initiation of the excursion. For a reactivity insertion of about 1.2$, the maximum hot-spot fuel temperature rise is the same for all three reactor conditions. For reactivity insertions larger than 2$, the temperature rise is about 40% less for the hot-standby than for the cold-startup accident, and nearly 60% less for the operating-power than for the cold-startup accident. The three upper curves show the maximum hot-spot fuel temperatures predicted during the first 250 msec after initiation of excursions. These temperatures represent the steady state hot-spot fuel temperatures plus the maximum fuel temperature rises. For reactivity insertions larger than about 1.5$, the maximum fuel temperature during a cold-startup accident is about 15% larger than that predicted for a hot-standby accident. For all of the reactivity insertions considered, the maximum fuel temperature predicted during an operating-power accident is larger than that predicted for either the cold-startup or hot-standby accident. For reactivity insertions of about 5$, the cold-startup maximum temperature approaches the values for the operating-power accident.

The E-core maximum hot-spot fuel temperature behavior, illustrated in Figure 47, resulted from the changes in the effective core size and reactivity feedback mechanisms as the reactor operating conditions varied from cold startup to operating power. At a system temperature of 500°F, the control rod withdrawal required for criticality of the E-core was about twice as large as at a system temperature of 70°F. Therefore, the effective fuel mass or core length was larger at 500°F than at 70°F, which resulted in power peaking factors[a] which were 35 and 44% smaller for the hot-standby and operating-power reactor conditions than was the case for the cold-startup condition. The principal feedback mechanisms that limited the excursions were Doppler broadening and prompt moderator heating. The Doppler coefficient of reactivity, which varies as a function of the square root of fuel temperature, decreased as the system temperature increased from 70 to 500°F. The E-core average temperature coefficient of reactivity increased as the system temperature increased from 70 to 500°F. Therefore, PMH feedback became increasingly more important at elevated system temperature. The net effect of decreasing the power peaking factor, decreasing the Doppler coefficient, and increasing the influence of the moderator temperature coefficient was that the maximum fuel temperature rise during a given reactivity-induced excursion became smaller as the initial reactor operating condition changed from cold startup to hot standby to operating power.

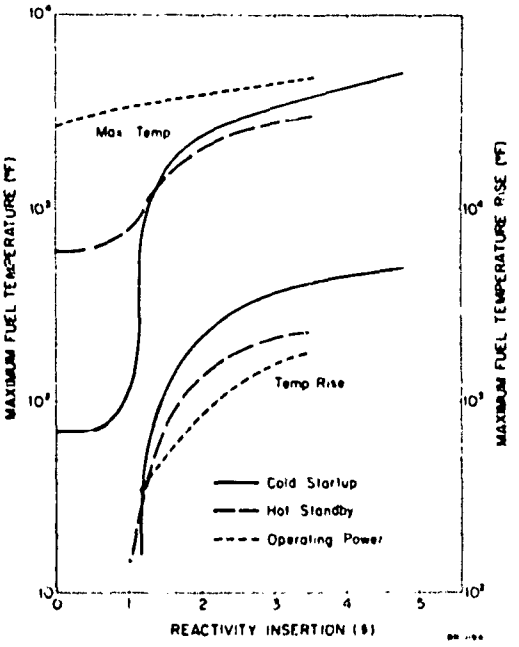

Fig. 47 PARET calculated maximum hot-spot fuel temperature and temperature rise as functions of reactivity insertion and accident condition.

[a] The power peaking factor is defined as the ratio of the hot-spot power density to the average power density.

V. CONCLUSIONS

The Spert III E-core experimental program provided power excursion data for a wide range of reactivity accident conditions in an oxide-fueled PWR. These data include the only known experimental results for reactivity accidents, in low-enriched oxide cores, initiated from typical PWR operating conditions. Analytical models used by the nuclear industry to predict the results of postulated reactivity accidents can now be evaluated for hot-startup, hot-standby, and operating-power conditions using these new data. For the Spert III E-core analytical program, the PARET and IREKIN digital computer codes were used to predict the reactor kinetic behavior for all the reactivity accident tests. Both codes use the point-reactor kinetic equations. PARET is a comprehensive code which considers the coupled thermal, hydrodynamic, and nuclear response of the reactor, and accounts for all the major reactivity feedback mechanisms. IREKIN is a relatively simple code which considers only reactivity feedback from Doppler broadening and has no provisions for heat transfer or coolant flow.

Analyses of the experimental results from the low-initial-power tests demonstrated that the E-core excursions were essentially limited by reactivity feedback from Doppler broadening during cold-startup reactivity accident tests, as were excursions in other oxide cores previously tested at Spert. The nonmoderator-to-moderator ratio of the E-core was larger than those of the other oxide cores, and it was found, as expected, that increasing this ratio does increase the Doppler reactivity feedback. Peak reactor powers were about 50% larger for 500°F hot-startup transients than for equivalent cold-startup transients. These differences in peak power indicate that the Doppler coefficient decreases with increasing fuel temperature. However, the differences between cold- and 500°F hot-startup peak powers were not as large as would have been expected if the E-core excursions were completely Doppler limited at hot-startup conditions. Analyses of the hot-startup test results indicated that prompt moderator heating (PMH) reactivity feedback became a significant contributor to the total reactivity feedback at elevated system temperatures.

The analyses of the experimental and calculational results also showed the effects of coolant flow rate on the E-core kinetic behavior. For long-period, hot-startup transients, increasing the coolant flow rates increased the energy release to peak power. The energy release to peak power was not measurably

affected by coolant flow rate during short period transients; however, the runout power levels increased with increasing flow rate.

Analyses of the experimental results from the high-initial-power tests demonstrated that appreciable reactivity feedback occurred during the reactivity insertions, and therefore, the power rises for these transients were not pure exponentials. Because of the immediate reactivity feedback during the high-initial-power tests, the kinetic behavior of the E-core was influenced strongly by the reactivity insertion rate; whereas, the insertion rate was relatively unimportant for the low-initial-power tests. Peak reactor powers were about 40 to 50% larger for the hot-standby transients than for 500°F hot-startup tests initiated with the same reactivity insertions. For superprompt critical, operating-power transients, peak powers were about 2.7 times those for equivalent 500°F hot-startup tests, while the subprompt critical, operating power transients reached peak powers about 10 times those of equivalent 500°F hot-startup tests. High-initial-power test results show the effect of initial reactor power and further demonstrate the decreasing Doppler coefficient with increasing fuel temperature.

During the hot-standby tests, Doppler compensation was still the principal feedback mechanism, with PMH reactivity feedback contributing about 35% of the total feedback at the time of peak power. For the operating-power tests, PMH reactivity compensation was the dominant feedback mechanism until about the time of peak power, at which time the Doppler feedback became approximately equal to the PMH feedback. Analysis of the PMH reactivity feedback in the E-core indicates that this important feedback mechanism increases with (a) increasing moderator temperature coefficient of reactivity, (b) increasing initial reactor power level, (c) decreasing coolant flow rate, and (d) decreasing reactor period. PMH feedback becomes more important at higher initial reactor powers because the Doppler coefficient of reactivity decreases as a result of the increasing initial fuel temperatures. The coolant flow rate and reactor period determine the amount of heated moderator transported from the core during the power burst. Thus, PMH feedback becomes more important as these parameters decrease because less moderator is transported during the transient time.

During all of the reactivity accident tests, the E-core fuel rods performed satisfactorily and cladding integrity was not lost; however, circumferential ridging, or clad bamboo ing, occurred along the high flux regions of the fuel

rods. Metallurgical investigations indicated that the strength of the cladding was not affected by the bamboozing. The maximum fuel rod cladding surface temperature measured during the entire experimental program was about 600°F and occurred during the tests initiated at 20 MW initial power. The maximum calculated hot-spot UO_2 fuel temperature obtained using PARET was about 3800°F. These maximum temperatures are well below the melting temperatures of the stainless steel cladding and UO_2 fuel.

The capabilities of the IREKIN and PARET codes in predicting the E-core kinetic behavior were evaluated for the reactivity accident test conditions experimentally investigated. The IREKIN code yielded predictions that were within 30% of the experimental results for the cold-startup reactivity accident tests. Because PMH reactivity feedback is a significant feedback mechanism at elevated temperatures, the IREKIN predictions were not satisfactory for tests initiated under hot-startup, hot-standby, and operating-power conditions. The comprehensive PARET code yielded results that were within 30% or less of experimental results for all accident conditions tested.

Because of the excellent agreement that was obtained between the PARET calculational and the experimental results, the PARET code was used to investigate the E-core kinetic behavior for postulated reactivity accidents that were not experimentally investigated. Calculations were performed to determine the effect of positive moderator temperature coefficients on accident results for excursions initiated at 20 MW initial power. PARET calculations indicate that for a positive moderator temperature coefficient larger than about +3¢/°F, power excursions that would be limited only by core damage or disassembly would result in the E-core. PARET calculations were performed for postulated E-core reactivity accidents initiated with the maximum available reactivity insertions for the various operating conditions. These reactivity insertions were 4.8$ for the cold-startup and 250°F hot-startup conditions and 3.5$ for the 500°F hot-startup, the hot-standby, and the operating-power conditions. The results of these calculations indicate that the probability of core damage during the power burst is largest for the cold-startup and operating-power accidents. More fuel melting was predicted to occur during reactivity accidents at cold-startup conditions than for accidents initiated from higher system temperatures. Although no fuel melting was predicted at

operating-power conditions, critical clad-water heat transfer conditions (departure from nucleate boiling heat fluxes) were calculated to occur; therefore, melting of the cladding became highly probable.

Except for size, the Spert III E-core is generally characteristic of an unborated, commercial PWR with essentially no fission product inventory in the core. The experimental program was limited to nondestructive reactivity accident tests, and thus investigations into the mechanical behavior of the fuel were not included. The analytical program provided typical analyses of reactivity transients using current state-of-the-art space-independent kinetics models. These analyses indicated that, for all reactivity accident conditions except cold-startup, the IREKIN code or codes similar to it are not adequate for predicting the reactor kinetic behavior. A code like PARET, which incorporates coolant flow and moderator reactivity feedback, should be used for predicting the results of reactivity accidents in small, oxide-fueled PWR's. Using a comprehensive code like PARET, other investigators should be able to obtain results that agree to within 30% or better with the E-core experimental data.

VI. REFERENCES

1. J. E. Grund et al, Subassembly Test Program Outline for FY-1969 and -1970, IDO-17277 (to be published).

2. A. H. Spano, J. E. Barry, L. A. Stephan, J. C. Young, Self-Limiting Power Excursion Tests of a Water-Moderated Low-Enrichment UO_2 Core in Spert I, IDO-16751 (February 1962).

3. J. E. Grund (ed.), Experimental Results of Potentially Destructive Reactivity Additions to an Oxide Core, IDO-17028 (December 1964).

4. A. H. Spano, "Analysis of Doppler-Limited Power Excursions in a Water-Moderated Oxide Core", Nucl. Sci. Eng., 19 (June 1964) pp 172-186.

5. J. E. Houghtaling, A Model for Analysis of Fast Transient Reactivity Effects in Low-Enriched Oxide-Fueled Reactors, IDO-17224 (January 1967).

6. J. G. Crocker (ed.), Quarterly Technical Report -- Spert Project -- October, November, December, 1965, IDO-17179 (June 1966).

7. J. MacPhee and R. E. Lumb, Pulstar Pulse Tests - II, Western New York Nuclear Research Center, Inc., WYN-020 (February 1965).

8. C. F. Obenchain, PARET -- A Program for the Analysis of Reactor Transients, IDO-17282 (January 1969).

9. R. J. Wagner, IREKIN -- Program for the Numerical Solution of the Reactor Kinetic Equations, IDO-16928 (March 1963).

10. Combustion Engineering, Inc., PL Final Design Report. Volume IV. Reactor Design, CEND-135 (Vol. IV) (June 1961).

11. J. Dugone (ed.), Spert III Reactor Facility: E-Core Revision, IDO-17036 (November 1965).

12. R. E. Heffner and T. R. Wilson, Spert III Reactor Facility, IDO-16721 (October 1961).

13. J. E. Houghtaling, J. A. Norberg, J. C. Haire, Addendum to the Spert III Hazards Summary Report -- Low-Enrichment Oxide Core, IDO-17003, Rev. 2 (October 1965).

14. R. M. Potenza (ed.), Quarterly Technical Report -- Spert Project -- January, February, March, 1966, IDO-17206 (September 1966).

15. T. G. Taxelius and R. M. Potenza (eds.), Quarterly Technical Report -- Spert Project -- April, May, June, 1966, IDO-17207 (January 1967).

16. T. G. Taxelius (ed.), Quarterly Technical Report -- Spert Project -- July, August, September, 1966, IDO-17228 (April 1967).

17. T. G. Taxelius (ed.), Quarterly Technical Report -- Spert Project -- October, November, December, 1967, IDO-17279 (October 1968).

18. T. G. Taxelius (ed.), Quarterly Technical Report -- Spert Project -- October, November, December, 1966, IDO-17245 (October 1967).

19. J. A. Norberg (ed.), Quarterly Progress Report -- January, February, March, 1959, IDO-16539 (November 1959).

20. J. G. Crocker (ed.), Quarterly Technical Report -- Spert Project -- October, November, December, 1964, IDO-17084 (April 1965).

21. T. G. Taxelius (ed.), Quarterly Technical Report -- Spert Project -- January, February, March, 1968, IDO-17287 (November 1968).

22. W. H. Etz, Fuel Rod Deformation in the Spert III Oxide E-Core, IDO-17291 (January 1969).

23. B. J. Power, R. N. Hagen, S. O. Johnson, SPORT -- A System for Processing Reactor Transient Data on the IBM-7040 Computer, IDO-17078 (July 1965).

APPENDIX A

SPERT III E-CORE DESIGN DATA SUMMARY

A summary of the characteristics of the Spert III E-core and major plant equipment is tabulated in this appendix.

1. GENERAL REACTOR DESIGN DATA

Type -- pressurized-water, experimental reactor suitable for boiling or pressurized water experiments

Function -- reactor transient behavior and safety studies

Moderator -- H_2O

Coolant -- H_2O

Neutron energy -- thermal

Core type -- heterogeneous, rod type

Heat removal -- plant, 60 MW (limited to 1/2 hr)

Heat power -- core, 20 MW

Power density (at 20 MW) -- 550 kW/liter of UO_2

Maximum coolant flow rate -- 20,000 gpm

Design pressure and temperature (maximum) -- 2500 psig at 650°F

2. REACTOR-COMPONENT DESIGN DATA

Core (Operational Loading)

Configuration -- approximately cylindrical

Diameter -- ≈ 26 in.

Active height -- 38.3 in.

Volume -- 1.86 ft^3

Composition

Water -- 6.7 wt%

Stainless steel -- 22.5 wt%

UO_2 -- 70.8 wt%

U -- 62.4 wt%

U-235 -- 3.0 wt%

Fuel load, U-235 -- 53.6 Kg

Number of fuel assemblies -- 60

Fuel Assemblies

Type -- rectangular

Number (Operational Loading)

25 rod assembly -- 48

16 rod assembly -- 4

control rod assembly with fuel follower -- 8

Overall dimensions

25 rod assembly -- 2.975 x 2.975 x 52-3/4 in.

16 rod assembly -- 2.476 x 2.476 x 52-3/4 in.

control rod fuel section -- 2.496 x 2.496 x 45-41/64 in.

Fuel content

25 rod assembly -- 962.5 g U-235

16 rod assembly -- 616 g U-235

control rod assembly -- 616 g U-235

Pitch -- 0.585 in. (square)

Flow area (inside)/assembly

25 rod assembly -- 4.29 $in.^2$

16 rod assembly -- 3.16 $in.^2$

control rod assembly -- 2.80 $in.^2$

Heat-transfer area (active fuel length)

25 rod assembly -- 1402 $in.^2$

16 rod assembly -- 897 $in.^2$

control rod assembly -- 897 $in.^2$

Fuel Rods

Type -- cylindrical

Materials

Fuel tube -- stainless steel, Type 348

Pellets -- 4.8% enriched sintered UO_2 (10.5 g/cm^3)

Fuel pellet dimensions

Long pellet -- 0.420 in. OD x 0.766 in.

Short pellet -- 0.420 in. OD x 0.511 in.

Rod dimensions

Diameter -- 0.466 in. OD

Wall thickness -- 0.020 in.

Overall length -- 40.8 in. (excluding end plugs)

Active length -- 38.3 in.

U-235/rod -- 38.5 g

Radial gas gap -- 0.003 in. helium

Control Rods

Type -- rectangular: upper section is absorber material; lower section is a fuel subassembly

Number -- 8

Composition

Absorber section -- 1.35 wt% boron-10 in Type 18-8 stainless steel; 0.186-in.-thick hollow square box

Fuel section -- see fuel assembly section on the preceding page

Overall dimensions

Absorber section -- 2.496 x 2.496 x 45-31/32 in.

Fuel section -- 2.496 x 2.496 x 45-41/64 in.

Travel -- 45 in. maximum

Average scram time -- 0.350 sec (to completion)

Withdrawal rates

Fast -- 17.4 in./min

Intermediate -- 11.5 in./min

Slow -- 5.64 in./min

Transient Rod

Type -- cruciform: lower-section absorber material, upper-section AISI Type 347 stainless steel

Number -- 1

Composition (absorber section) -- 1.35 wt% boron-10 in 18-8 stainless steel

Dimensions

Thickness of blades -- 3/16 in.

Blade width -- 5.125 in.

Absorber section length -- 38 in.

Travel -- 45 in. maximum

Average drop time -- 0.2 sec (to completion)

Control Rod Drives

Type -- Acme nut and screw: air pressure maintains rod in contact with screw and scrams rods

Number -- 5

Motor type -- 480 V, 3Ø, 3 speed, constant torque

Motor rating -- 1 hp

Reactor Vessel

Construction

Shell -- layer type

Top head -- forged, full-opening, flanged, hemispherical

Bottom head -- layer type

Inside diameter -- 48 in.

Shell thickness (including clad) -- 3.25 in.

Head thickness -- 3.5 in.

Materials

Outer shellplate -- carbon steel plates 1/4 in. thick

Inner shellplate -- magnesium-vandium steel (ASTM A225 GrB) with a 1/8-in.-thick 304L stainless steel clad

Top head -- carbon steel manually clad with Type 309 stainless steel

Design pressure

Working pressure -- 2500 psig

Estimated maximum transient pressure -- 3500 psig

Design temperature -- 700°F

Overall length (includes head) -- 19 ft 11-1/8 in.

Maximum diameter of head flange -- 5 ft 7 in.

Number of thermal shields -- 5 (including reactor flow skirt)

Total thickness of shields -- 5.75 in.

Average length of shields -- 45.5 in.

Inside diameter of inner shield -- 32 in.

Weight of vessel

Shell	55,784 lb
Head	10,606 lb
Bottom tee	5,580 lb
Shield	11,430 lb
Total	83,400 lb

Insulation -- 4 in. of foamglass

3. CORE THERMAL DESIGN DATA

Coolant -- deionized water

Heat power (maximum) -- 20 MW

Coolant flow (maximum) -- 20,000 gpm

Coolant passes through core -- one

Velocity in core (maximum flow) -- 24 ft/sec

Heat transfer area -- 541.9 ft^2

Average heat flux (core) -- 1.10×10^5 Btu/hr/ft^2 at 20 MW

4. PRIMARY-COOLANT SYSTEM DESIGN DATA

Primary Pumps

Type -- single stage, single suction, double volute, canned rotor

Number -- 4

Capacity, each -- 5000 gpm

Net differential head -- 328 ft of H_2O at 650°F, 2500 psig

Motor

Rating -- 500 hp

Type -- 480 V, 3Ø, 60 cycle

rpm -- 3550

Weight, each -- 8500 lb

Material -- stainless steel, Type 304L

Heat Exchangers

Type -- U-tube, evaporative

Number -- 2

Heat transfer capacity, each -- 30 MW

Tube side fluid -- primary coolant, deionized H_2O

Shell side fluid -- deionized H_2O

Design pressure

Tube side -- 2500 psig

Shell side -- 75 psig

Design temperature

Tube side -- 668°F

Shell side -- 320°F

Heat-transfer surface -- 1940 ft^2

Number of tubes -- 367 U's

Tube size -- 5/8-in. OD, 0.065-in. wall thickness

Tube straight length -- 191 in.

Tube pitch -- triangular

Pressure drop -- 10 psi

Materials

Tubes -- stainless steel, Type 304L

Tube sheet -- carbon steel (ASTM A266, CL2), clad with stainless steel, Type 304L

Channel -- carbon steel (ASTM A266, CL2), clad with stainless steel, Type 304L

Channel cover -- carbon steel (ASTM A266, CL2), clad with stainless steel, Type 304L

Shell -- carbon-silicon steel (ASTM A-212, Gr3)

Weight

Full -- 43,200 lb

Empty -- 23,400 lb

Tube bundle -- 11,600 lb

Pressurizer Vessel

Number -- 1

Design -- Section VIII ASME Boiler and Pressure Vessel Code

Design Pressure -- 2750 psig

Design Temperature -- 700°F

Dimensions

Overall height -- 15 ft 2-11/16 in.

Overall diameter -- 3 ft 3.3 in.

Volume -- ≈ 83 ft^3

Shell thickness -- 3.15 in.

Head thickness -- 2.9 in.

Materials

Backing -- carbon-silicon steel (ASTM A212, Gr B)

Clad -- nickel 200 (ASTM B-162), 0.100 in.

Heaters -- electric immersion, 480 V, 3Ø

Number -- 16

Capacity, each -- 12 kW

Total capacity -- 192 kW

Weight (empty) -- ≈26,000 lb

Primary System Piping

Type -- centrifugally cast stainless steel (ASTM A 362-52T, modified)

Wall thickness

10 to 16 in. -- schedule 160

8 in. -- schedule 140

Material -- stainless steel, Type 304L

Insulation -- 3 in. of 85% Magnesia

5. POISON SHUTDOWN SYSTEM

Poison -- boric acid solution

Addition method -- reactor primary system makeup pump

Reactivity compensated by poison addition -- 17.8$

Boric acid concentration required -- 4.97 g/ℓ

Time for total addition -- 107 minutes

APPENDIX B

APPLICATION OF THE PARET CODE

The PARET code, a Program for the Analysis of REactor Transients, computes the coupled thermal, hydrodynamic, and nuclear behavior of the core during a transient. The PARET model represents the reactor core by up to four fuel elements and associated coolant channels. Each of the channels is assumed to represent the average behavior of some selected region of the core. The channels can be subdivided into a maximum of 20 axial sections, and the radial dimension of the fuel element can be described by up to 50 radial sections. The power behavior of the reactor is determined through a solution of the point-reactor kinetics equations, in which continuous reactivity feedback from the known major feedback mechanisms is accounted for. Detailed heat transfer and hydrodynamic calculational models are contained in the code.

This appendix is specifically concerned with the application of the PARET code to the Spert III E-core reactor. The material is presented in the same order as it appears in the PARET input data instructions[B-1]. In most cases, the same nomenclature is used as that used in the PARET report.

1. GEOMETRIC CORE MODEL

The Spert III E-core was divided into four PARET regions or channels, which are shown in Figure B-1. The type and number of fuel assemblies in each of the channels can be determined from the E-core lattice description given in Section II-1. The fraction of core fuel rods in each channel is given in the following tabulation.

PARET Channel	Fuel Assemblies	Fuel Rods	Fraction of Core Fuel Rods
1	20	500	0.3968
2	20	500	0.3968
3	12	288	0.2286
4	1	61	0.0484

The fraction of core fuel rods in each region was used as a reactivity feedback weighting factor.

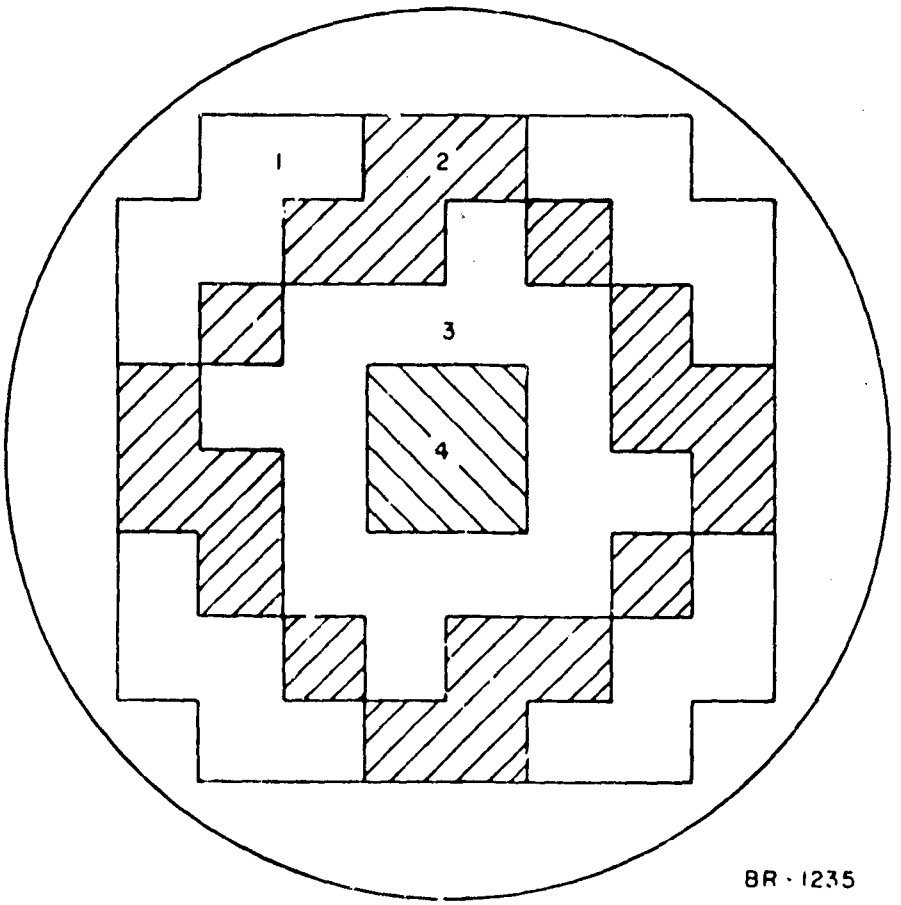

Fig. B-1 Four-channel PARET representation of the Spert III E-core.

2. REACTIVITY FEEDBACK CALCULATIONS

The following subjects are specifically described in this section: (a) the methods used to obtain the flux profiles from which the reactivity feedback importance weighting factors are determined; (b) the calculation of the source,

moderator, and Doppler importance weighting factors; (c) the Doppler reactivity feedback model; and (d) single average-channel PARET model transient calculations.

2.1 Real and Adjoint Flux Profiles

The axial and radial, real and adjoint flux distributions in the core, that were used to determine importance weighting factors, were computed using one- and two-dimensional diffusion theory computer codes. The one-dimensional flux distributions were required as input for the calculation of these importance weighting factors. A number of two-dimensional computations were performed to assure that consistent results were obtained by the axial and radial, one-dimensional models. The procedure used to obtain the radial and axial, one-dimensional flux profiles was as follows:

(1) Radial and axial one-dimensional flux profiles were obtained for the control rods either fully inserted (rods-in) or completely withdrawn (rods-out) from the co e.

(2) An iteration technique for the radial and axial bucklings was used for each control rod configuration to assure consistent radial and axial leakages for the two one-dimensional models.

(3) Radial and axial one-dimensional flux profiles for a specified control rod position in the core were then calculated using the rods-in and rods-out leakages obtained from the iteration calculations.

The real and adjoint flux shapes for the perturbed core condition were used for all reactivity feedback calculations. This means that the transient rod poison section was consi ered .o be out of the core and that the control rods were at a specified position corresponding to a predetermined reactivity insertion.

In the diffusion theory computations, the following fo ir energy groups were used:

Group 1 -- 10 MeV to 0.82 MeV
Group 2 -- 0.82 MeV to 5.5 keV
Group 3 -- 5.5 keV to 0.532 eV
Group 4 -- 0.532 eV to 0.0 eV.

The Group 4 constants were obtained using a combination of the TOPIC[B-2] S_n transport theory code and the TEMPEST[B-3] thermal spectrum code. Constants for groups 1, 2, and 3 were obtained using the PHROG code (a modification of the GAM-1[B-4] code) together with the RAVEN[B-5] code. The RAVEN code was used to obtain the U-238 resonance energy cross sections.

Two-dimensional (x-y geometry) real and adjoint flux profiles were first calculated using the PDQ-4[B-6] diffusion theory code. The fluxes were calculated for the control rods fully inserted (rods-in) and the control rods completely withdrawn (rods-out) core configurations. For both of these cases, the geometry used in the PDQ-4 code represented the reactor core as it actually existed in the x-y plane (Figure B-2a). Different diffusion theory constants were input for each material in the core. The core axial dimension, for both control rod positions, was represented by the geometric or energy independent bucklings.

One-dimensional (radial geometry) real and adjoint flux profiles were next calculated for the rods-in and rods-out cases using the CORA[B-7] diffusion theory code. The one-dimensional cylindrical geometry model was an approximation of the explicit geometry in the PDQ-4 model. The transient rod follower, control rods, fuel, and water in the core were represented as cylindrical areas (Figure B-2b). The diffusion theory constants used were the same as those used in the PDQ-4 calculations. The core axial dimension was again described by the geometric bucklings. The eigenvalues and flux profiles calculated with the CORA code were compared with the PDQ-4 values. If the one-dimensional radial model values did not agree with the PDQ-4 results, the cylindrical areas in the CORA model were adjusted until the values did agree.

One-dimensional (axial geometry) real and adjoint flux profiles were then calculated for the rods-in and rods-out cases using the CORA code. In this slab geometry model, the axial dimensions represented the actual core dimensions (Figure B-2c). The homogenized, fuel region and water region diffusion theory constants used were the same as those used in the PDQ-4 and the radial CORA codes. The core radial dimensions were represented by the radial material or energy dependent bucklings that were calculated using the CORA one-dimensional, cylindrical geometry model. Whether the axial slab geometry model represented the control rods-in or -out configuration depended only upon the radial material bucklings used. Using the rods-out radial material bucklings

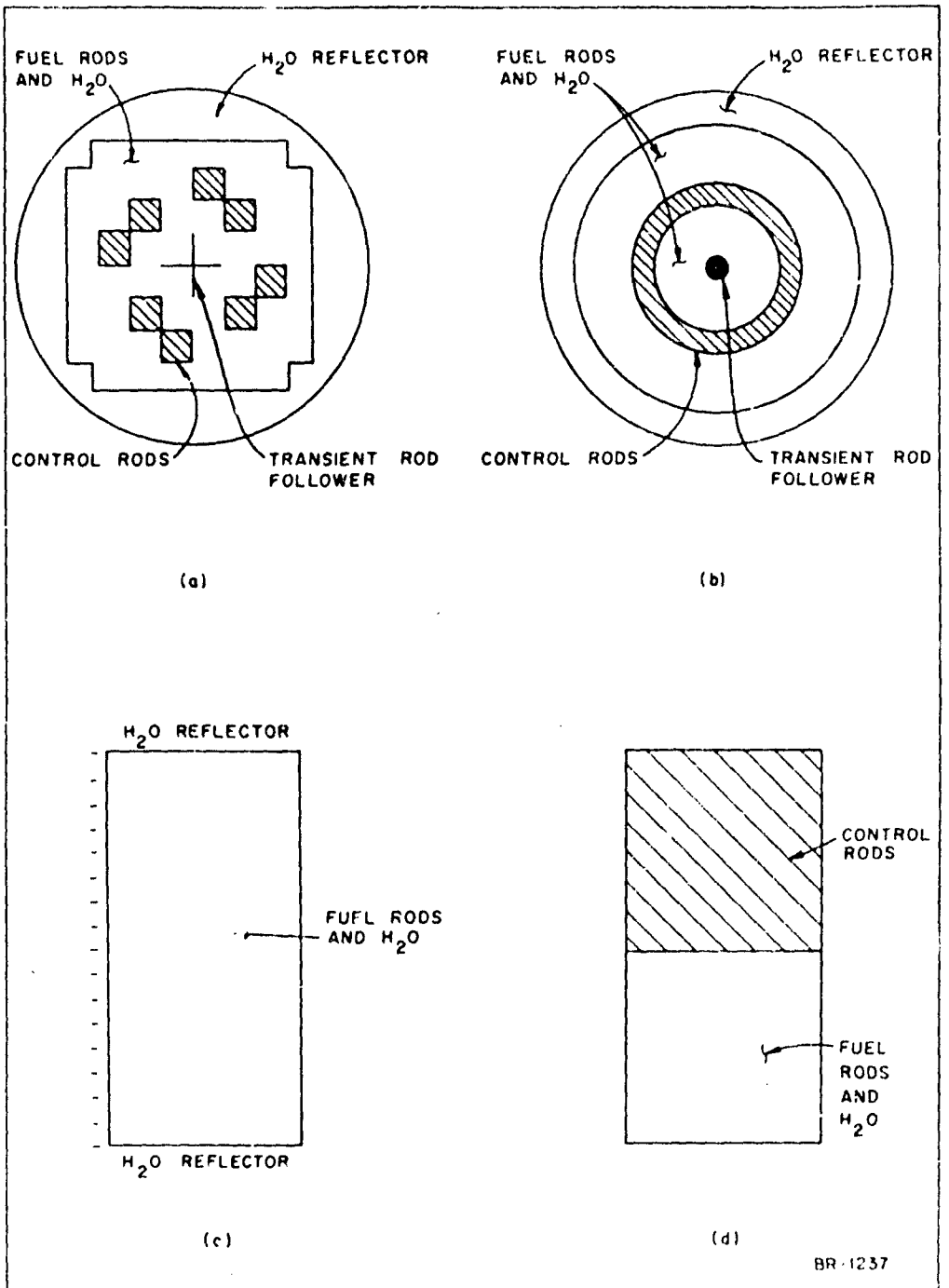

Fig. B-2 Geometric representations of the Spert III E-core for diffusion theory code calculations.

gave the rods-out axial slab geometry CORA model, and using the rods-in material bucklings gave the rods-in axial slab geometry CORA model.

The one-dimensional, cylindrical geometry CORA calculations were repeated exactly as previously performed, with the exception that the core axial dimension was represented this time by the axial material bucklings calculated from the slab geometry CORA model. The rods-in axial material bucklings were used in the rods-in radial CORA calculations, and the rods-out axial material bucklings were used in the rods-out radial CORA calculations. The radial geometry-axial geometry iteration technique was continued until the eigenvalues and four energy group, radial and axial material bucklings converged. At this point axial and radial, real and adjoint flux distributions were known for the two cases of control rods either fully inserted or completely withdrawn.

One-dimensional (axial geometry) CORA calculations were made for a given control rod withdrawal position that would represent the excess reactivity necessary to initiate a transient of a specific stable period. The core was represented axially by rods-in and rods-out regions (Figure B-2d). For this calculation, the same diffusion theory constants were used as were used in the PDQ-4 rods-in and rods-out calculations. In the rods-in region, the radial dimension was represented by the material bucklings calculated from the converged, rods-in, cylindrical geometry CORA model. In the rods-out region, the radial dimension was represented by the material bucklings calculated from the converged, rods-out, cylindrical geometry CORA model. From this calculation, the axial real and adjoint flux profiles pertaining to a given reactor period[a] were obtained, and these values were used to determine the importance weighting. The radial real and adjoint flux profiles that were used for importance weighting were those that resulted from the converged, cylindrical geometry CORA calculations for the control rods completely withdrawn[b].

---

[a] The flux profiles represented a control rod withdrawal position that would result in a 10-msec-period transient. These profiles were also valid for 1- to 100-msec-period transients, since little additional control rod movement was required.

[b] Most of the reactivity feedback occurred in the high flux regions of the E-core. Thus, the radial real and adjoint flux profiles used for importance weighting of reactivity feedback were those calculated for the control rods-out model. (With the control rods fully withdrawn, the fuel in the lower section of the control rods would be in the core. For the PARET calculations, the total fuel volume included the fuel in the control rods and was 4.27445 ft^3.)

2.2 Source Importance Weighting Factors

The UO_2 temperature distribution in the core was computed in the PARET code by solving the heat conduction equation, which contains a volumetric heat source term defined as

$$S(r,z,t) = P_f\ \phi(t)\ Q_M(r)\ W_S(m,n) \qquad \text{B-1}$$

where

$\phi(t)$ = average reactor power

P_f = factor to convert average reactor power to power per unit fuel volume

$Q_M(r)$ = radial source description in fuel rod obtained from TOPIC transport theory code calculations

$W_S(m,n)$ = source importance weighting factor for region (m,n).

The source importance weighting factors, $W_S(m,n)$[a], were computed using a computer code which solves the equation

$$W_S(m,n) = \frac{\frac{1}{\Delta V_{mn}} \int_{\text{PARET radial region m}} 2\pi r\,dr \int_{\text{PARET axial region n}} dz \sum_i^4 \Sigma_{fi}\ \phi_i(r)\ \phi_i(z)\ N_{zi}}{\frac{1}{V} \int_{\text{all fuel regions}} 2\pi r\,dr \int_{\text{all fuel regions}} dz \sum_i^4 \nu\Sigma_{fi}\ \phi_i(r)\ \phi_i(z)\ N_{zi}} \qquad \text{B-2}$$

where

ΔV_{mn} = volume of UO_2 in region (m,n)

V = total volume of UO_2 in core

$\phi_i(r)$ = real flux for energy group i at space point r obtained from radial CORA calculations

$\phi_i(z)$ = real flux for energy group i at space point z obtained from axial CORA calculations

ν = number of neutrons liberated for every fission

Σ_{fi} = macroscopic fission cross section for energy group i

$$N_{zi} = \frac{\int dz\ \phi_4(z)}{\int dz\ \phi_i(z)} = \text{normalization factor.}$$

[a] In the PARET code, the core can be represented by up to four radial flow channels and up to 20 axial sections, ie, m = 1,2,3,4 and n = 1,2,3 . . . 20.

The radial and axial, real flux profiles were those computed with the CORA code, as described in Section 2.1 of this appendix. The calculated source importance weighting factors were input to the PARET code as the axial source description.

2.3 Moderator Importance Weighting Factors

In the PARET code, the total reactivity feedback due to moderator density changes during a time step t is computed from the equation

$$R^M(t) = \frac{1}{V^M} \sum_m G_m \sum_n \Delta V^M_{mn} \; W_M(m,n) \; C \; \Delta\rho_{mn}(t) \qquad \text{(B-3)}$$

where

ΔV^M_{mn} = volume of moderator associated with fuel rod in region (m,n)

V^M = total volume of moderator in core

G_m = fraction of core in channel m or number of fuel rods in channel m

$W_M(m,n)$ = moderator importance weighting factor for region (m,n)

C = overall void volume coefficient of reactivity

$\Delta\rho_{mn}(t) = \dfrac{\bar{\rho}_{ref} - \bar{\rho}_{mn}(t)}{\bar{\rho}_{ref}}$ = fractional change in moderator volume for region (m,n).

The moderator importance weighting factors, $W_M(m,n)$, were computed using a computer code which solves the equation

$$W_M(m,n) = \frac{\dfrac{1}{\Delta V_{mn}} \displaystyle\int_{\substack{\text{PARET}\\\text{radial}\\\text{region m}}} 2\pi r\,dr \int_{\substack{\text{PARET}\\\text{axial}\\\text{region n}}} dz \; \phi_4(r)\,\phi_4(z)\,\phi_4^*(r)\,\phi_4^*(z)}{\dfrac{1}{V} \displaystyle\int_{\substack{\text{all fuel}\\\text{regions}}} 2\pi r\,dr \int_{\substack{\text{all fuel}\\\text{regions}}} dz \; \phi_4(r)\,\phi_4(z)\,\phi_4^*(r)\,\phi_4^*(z)} \qquad \text{(B-4)}$$

where

$\phi^*_i(r)$ = adjoint flux for energy group i at space point r obtained from radial CORA calculations

$\phi^*_i(z)$ = adjoint flux for energy group i at space point z obtained from axial CORA calculations

$$N^{*}_{zi} = \frac{\int dz\ \phi^{*}_{4}(z)}{\int dz\ \phi^{*}_{i}(z)} = \text{normalization factor}$$

$$N_{z4} = N^{*}_{z4} = 1.0.$$

The radial and axial, real and adjoint, group 4 flux profiles were computed with the CORA code. The calculated moderator importance weighting factors were input to the PARET code as the axial void volume weights.

2.4 Doppler Reactivity Feedback and Doppler Importance Weighting Factors

The Doppler reactivity feedback was calculated as a function of the change in the group 3 macroscopic absorption cross section, $\delta\Sigma_{a3}$, with temperature. The change in Σ_{a3} was calculated as a function of the UO_2 temperature in a unit cell using the PHROG and RAVEN codes. The water and clad temperatures were held at the base temperature of the system, T_o. From the PHROG-RAVEN output, the resonance integral temperature coefficient, γ, was computed by the least-squares fitting of $\delta\Sigma_{a3}$ to the equation[B-8]

$$\delta\Sigma_{a3} = \gamma[\Sigma_{ao}(\sqrt{T} - \sqrt{T_o})] \tag{B-5}$$

where

Σ_{ao} = macroscopic group 3 cross section at the base temperature, T_o

T = UO_2 temperature, °K.

The general equation used to compute Doppler reactivity feedback, $R^{D}(t)$, was

$$R^{D}(t) = \frac{\int_{\substack{\text{all fuel}\\\text{regions}}} 2\pi r dr \int_{\substack{\text{all fuel}\\\text{regions}}} dz\ \delta\Sigma_{a3}\ \phi_3(r)\ \phi_3(z)\ \phi^{*}_3(r)\ \phi^{*}_3(z)\ N_{z3} N^{*}_{z3}}{\beta_{eff} \int_{\substack{\text{all fuel}\\\text{regions}}} 2\pi r dr \int_{\substack{\text{all fuel}\\\text{regions}}} dz \sum_{i,j}^{4} \nu\Sigma_{fi}\ \phi_i(r)\ \phi_i(z)\ \chi_j\ \phi^{*}_j(r)\ \phi^{*}_j(z)\ N_{zi}\ N^{*}_{zj}} \tag{B-6}$$

where

χ_j = fraction of fission neutrons born in energy group j

$$\sum_{j=1}^{4} \chi_j = 1$$

β_{eff} = effective delayed neutron fraction.

For convenience, we defined

$$2\pi F = \int_{\substack{\text{all}\\\text{fuel}\\\text{regions}}} 2\pi r dr \int_{\substack{\text{all}\\\text{fuel}\\\text{regions}}} dz \sum_{i,j}^{4} \nu\Sigma_{fi}\phi_i(r)\phi_i(z)\chi_j\phi_j^*(r)\phi_j^*(z)N_{zi}N_{zj}^* \quad . \tag{B-7}$$

Substituting Equations (B-5) and (B-7) into (B-6) yields

$$R^D(t) = \frac{\gamma\Sigma_{ao}}{\beta_{eff}2\pi F} \int_{\substack{\text{all}\\\text{fuel}\\\text{regions}}} 2\pi r dr \int_{\substack{\text{all}\\\text{fuel}\\\text{regions}}} dz \; (\sqrt{T} - \sqrt{T_o})\phi_3(r)\phi_3(z)\phi_3^*(r)\phi_3^*(z)N_{z3}N_{z3}^* \quad . \tag{B-8}$$

In the PARET code, the Doppler reactivity feedback for each small region in a fuel rod, ΔV_{mn}, is given by

$$R^D_{mn}(t) = W_D(m,n) \; [\gamma_o + \gamma_1 T_{mn} + \gamma_2 (T_{mn})^2 + \gamma_3 (T_{mn})^k] \tag{B-9}$$

where

$W_D(m,n)$ = Doppler importance weighting factor for region (m,n)

$T_{mn} = \bar{U}_{mn}(t) + \gamma_4$

$\bar{U}_{mn}(t)$ = mean UO_2 temperature in region (m,n), °R

k = arbitrary power to which T_{mn} is raised

γ_i = polynomial coefficients.

The total Doppler reactivity feedback for time step t is computed from

$$R^D(t) = \frac{1}{V}\sum_m G_m \sum_n \Delta V_{mn} \; R^D_{mn}(t) \quad . \tag{B-10}$$

Substituting Equation (B-9) into (B-10) yields

$$R^D(t) = \frac{1}{V}\sum_m G_m \sum_n \Delta V_{mn} \; W_D(m,n) \; [\gamma_o + \gamma_1 T_{mn} + \gamma_2 (T_{mn})^2 + \gamma_3 (T_{mn})^k] \tag{B-11}$$

To determine the various coefficients appearing in Equation (B-11) and the proper Doppler importance weighting factors, Equations (B-8) and (B-11) are compared. These equations correspond to each other if

$$\gamma_1 = \gamma_2 = \gamma_4 = 0$$

$$k = 0.5$$

$$\gamma_3 = \frac{\gamma \Sigma_{ao} V}{\beta_{eff} 2\pi F} \qquad \text{(B-12)}$$

$$\gamma_o = - \gamma_3 \sqrt{T_o} \qquad \text{(B-13)}$$

$$W_D(m,n) = \frac{1}{\Delta V_{mn}} \int_{\substack{\text{PARET} \\ \text{radial} \\ \text{region m}}}^{2\pi r dr} \int_{\substack{\text{PARET} \\ \text{axial} \\ \text{region n}}}^{dz} \phi_3(r)\, \phi_3(z)\, \phi_3^*(r)\, \phi_3^*(z)\, N_{z3}\, N_{z3}^* \qquad \text{(B-14)}$$

The coefficients γ_o and γ_3 that were input to the PARET code were calculated using values of β_{eff} and F obtained from the DOPP-3B[B-9] computer code. The Doppler importance weighting factors, $W_D(m,n)$, were calculated from Equation (B-14) using the radial and axial, real and adjoint flux profiles computed by the CORA code.

2.5 Average-Channel PARET Model Transient Calculations

In all of the previous PARET code calculations in this report, the standard model of four flow channels represented the reactor core. Investigations were made to determine if a single-channel PARET model could yield transient results comparable to the four-channel PARET calculations. For this model, a single flow channel represented the reactor core average channel.

2.51 Importance Weighting Factors. For the single average-channel PARET model, the source, moderator, and Doppler importance weighting factors were generated using the axial, real and adjoint flux profiles. The radial importance weightings were assumed to be unity. Since the radial, real and adjoint flux profiles were not used, the normalization factors, N_{z1} and N_{z1}^*, were not required. Source importance weighting factors for the average-channel PARET calculations were computed from the equation

$$W_S(n) = \frac{\frac{1}{\Delta V_n}\int_{\substack{\text{PARET}\\ \text{axial}\\ \text{region n}}} dz \sum_i^4 \nu\Sigma_{fi}\ \phi_i(z)}{\frac{1}{V_n}\int_{\substack{\text{all fuel}\\ \text{regions}}} dz \sum_i^4 \nu\Sigma_{fi}\ \phi_i(z)} \qquad \text{(B-15)}$$

where

ΔV_n = volume of UO_2 in fuel rod in axial region (n)

$$V_n = \sum_n \Delta V_n .$$

Moderator importance weighting factors for the average-channel PARET calculations were obtained from the equation

$$W_M(n) = \frac{\frac{1}{\Delta V_n}\int_{\substack{\text{PARET}\\ \text{axial}\\ \text{region n}}} dz\ \phi_4(z)\ \phi_4^*(z)}{\frac{1}{V_n}\int_{\substack{\text{all fuel}\\ \text{regions}}} dz\ \phi_4(z)\ \phi_4^*(z)} \qquad \text{(B-16)}$$

Doppler importance weighting factors for the average-channel PARET calculations were computed from the equation

$$W_D(n) = \frac{1}{\Delta V_n}\int_{\substack{\text{PARET}\\ \text{axial}\\ \text{region n}}} dz\ \phi_3(z)\ \phi_3^*(z) \ . \qquad \text{(B-17)}$$

The quantity $2\pi F$ used to compute γ_0 and γ_3 was obtained from the equation

$$2\pi F = \int_{\substack{\text{all fuel}\\ \text{regions}}} dz \sum_{i,j}^4 \nu\Sigma_{fi}\ \phi_i(z)\ \chi_j\ \phi_j^*(z) \ . \qquad \text{(B-18)}$$

The fuel volume used to calculate γ_0 and γ_3 was V_n.

3

GENERATION TIME CALCULATIONS, AND DELAYED NEUTRON PARAMETERS

The effective delayed neutron fraction, β_{eff}, and the prompt neutron generation time, Λ, were computed using the DOPP-3C[B-9] computer code. This code used the converged, axial and radial, real and adjoint flux profiles calculated with the CORA code. Delayed neutron parameters for the E-core were calculated using published delayed neutron data for U-235 and U-238[B-10] which were weighted by a fast fission factor.

3.1 Effective Delayed Neutron Fraction

The DOPP-3C code calculates this parameter by solving the following equation derived by Henry[B-11]:

$$\beta_{eff} = \frac{\beta_a \int_{\text{all core regions}} 2\pi r dr \int_{\text{all core regions}} dz \sum_{i,j}^{4} \nu\Sigma_{fi}\, \phi_i(r)\phi_i(z)\chi_j^{\beta}\, \phi_j^*(r)\phi_j^*(z)\, N_{zi}N_{zj}^*}{\int_{\text{all core regions}} 2\pi r dr \int_{\text{all core regions}} dz \sum_{i,j}^{4} \nu\Sigma_{fi}\, \phi_i(r)\phi_i(z)\, \chi_j\, \phi_j^*(\,)\phi_j^*(z)\, N_{zi}N_{zj}^*} \qquad \text{(B-19)}$$

where

χ_j^{β} = fraction of delayed neutrons produced in energy group j

χ_j = fraction of prompt neutrons produced in energy group j

β_a = actual delayed neutron fraction for a mixture of U-238 and U-235.

The actual delayed neutron fraction is calculated from the equation

$$\beta_a = \frac{1}{\varepsilon'}\beta^{235} + \frac{\varepsilon'-1}{\varepsilon'}\beta^{238} \qquad \text{(B-20)}$$

where

β^{235} = U-235 total delayed neutron fraction

β^{238} = U-238 total delayed neutron fraction

ε' = a fast fission factor.

This fast fission factor, ε', was defined as the ratio of the total neutrons produced to the neutrons produced by U-235 fissions[a] and was calculated from the equation

[a] The fast fission factor, ε, is defined as the ratio of total neutrons produced to the neutrons produced by thermal fissions.

$$\beta_{eff} = \frac{\beta}{1 - \beta^{238}} \qquad \text{(B-21)}$$

where

β^{238} = fraction of all neutrons produced by fissioning of U-238 (obtained from CORA diffusion theory code calculations).

3.2 Prompt Neutron Generation Time

The DOPP-3C code calculates this parameter by solving the following equation derived by Henry:

$$\Lambda = \sum_{j=1}^{k} \left\{ \frac{\int_{\text{all core regions}} 2\pi r dr \int_{\text{all core regions}} dz \left(\frac{1}{v_j}\right) \phi_j(r)\, \phi_j^*(r)\, \phi_j(z)\, \phi_j^*(z)\, N_{zj}\, N_{zj}^*}{\int_{\text{all core regions}} 2\pi r dr \int_{\text{all core regions}} dz \sum_{i,j}^{k} \nu\Sigma_{fi}\, \phi_i(r)\, \phi_i(z)\, \chi_j\, \phi_j^*(r)\, \phi_j^*(z)\, N_{zi}\, N_{zj}^*} \right\} \qquad \text{(B-22)}$$

where

v_j = average neutron velocity in energy group j.

3.3 Calculated Results

The calculated values of β_{eff} and Λ for various E-core system temperatures are tabulated below:

Coolant Inlet Temperature (°F)	Effective Delayed Neutron Fraction	Prompt Neutron Generation Time (usec)
70	0.00718	15.55
250	0.00724	15.78
500	0.00725	16.31

In the Spert III E-core PARET calculations, six delayed neutron groups were used. The delayed neutron parameters for these six groups at a system temperature of 500°F are tabulated[B-12] on the next page:

Delayed Group	Delayed Neutron Fraction	Delayed Neutron Decay Constant (sec^{-1})
1	0.0352	0.0127
2	0.2014	0.0317
3	0.1685	0.1167
4	0.4006	0.3142
5	0.1437	1.4007
6	0.0333	3.3803

4. HYDRODYNAMIC CALCULATIONS

For the hydrodynamic calculations, the time-dependent moderator inlet mass flow rate was specified for the coldest PARET coolant channel-fuel rod region (channel 1). The time-dependent pressure drop across channel 1, which is calculated by the code, was then specified for the other three channels. This scheme allows for flow reversal in the three hotter channels, which can occur during excursions resulting from large reactivity insertions. In order to calculate the pressure drop across the core (as well as point-wise pressures, fluid enthalpies, and mass flow rates along the length of each channel) certain hydraulic items were required as input. These were the physical dimensions and geometry of the reactor system and the pressure loss coefficients. Those hydraulic items which cannot be readily obtained from either Appendix A or the reactor facility description[B-13] will be presented in this section.

The PARET channels represented complex fuel rod assemblies, each consisting of fuel rods, fuel can, two intermediate grids, upper and lower fuel grids, and upper and lower end-box adaptors. In the PARET code the total pressure drop across these complex channels is calculated as the sum of the cumulative pressure losses due to (a) inlet and exit area enlargements or contractions, (b) the inlet and exit plenums, (c) the inlet and exit nonfueled portions of the fuel rods, and (d) the fuel rods. In the E-core, the hydraulic parameters of a 16-rod fuel assembly are represented by those of PARET channel 4 and the parameters of a 25-rod fuel assembly are represented by those of PARET channels 1, 2, and 3. The following hydraulic parameters were used in the PARET calculations performed for this report.

Active fuel length -- 3.19166 ft

Inlet nonfueled length -- 0.06511 ft

Outlet nonfueled length -- 0.212625 ft

Inlet plenum length -- 0.495 ft

Outlet plenum length -- 0.4325 ft

Inlet plenum equivalent diameter -- 0.17667 ft

Outlet plenum equivalent diameter -- 0.0805 ft

	PARET Channels 1, 2, and 3	PARET Channel 4
Inlet loss coefficient	3.19	4.44
Inlet area ratio	1.22	1.31
Outlet loss coefficient	3.59	6.09
Outlet area ratio	1.62	1.98

The steady state E-core pressure drops calculated with the PARET code at various reactor conditions are compared with experimental results, obtained from hydraulic tests, in the following tabulation:

Core Pressure Drop at Various Flow Rates

Flow Rate (gpm)	PARET Calculated Pressure Drop (psi)	Experimental Pressure Drop (psi)
	1500 psig and 250°F	1700 psig and 250°F
12,000	14.6	13.5
16,000	24	24
18,000	30	30
	1500 psig and 500°F	1700 psig and 500°F
12,000	12	11

This good agreement between the calculated and experimental core pressure drops indicates that the PARET code accurately represents the steady state hydrodynamic behavior of the E-core.

The PARET program calculates continuous heat transfer for both moderator boiling and nonboiling conditions. The details of the PARET heat transfer calculations are contained in Reference B-1. In addition, a heat transfer model for gas gap conductance was developed for the Spert III E-core calculations.

In the PARET code the thermal conductivity of the helium gap separating the UO_2 fuel pellets from the stainless steel cladding is described as a function of the gap temperature. An expression for the gap conductance that would be valid for all transient conditions and would take into account varying gap temperatures and widths was desired. Anderson and Lechliter[B-14] developed such an expression, based on the work done by Ross and Stoute[B-15] on UO_2 and Zircaloy-2 surfaces in contact. Since the width of the gas gap for each E-core fuel pellet can vary about its nominal 3-mil value, these variations in the spacing between the UO_2 and cladding approximately satisfy the UO_2-cladding contact conditions considered by Ross and Stoute. Anderson and Lechliter's expression for the conductivity of the gas gap when applied to the E-core fuel becomes

$$k_g = \frac{6.43 + 7.43 \times 10^{-3}T - 1.07 \times 10^{-6}T^2}{(22.56 + 2.54 \times 10^{4}\Delta)} \qquad \text{(B-25)}$$

where

k_g = thermal conductivity of gas gap, Btu/hr-ft-°F
T = average gap temperature, °F
Δ = gap width, inches.

In the equation it is necessary to specify a constant gap width, Δ. It was assumed that the gap thickness at the time of peak power represented the gap distance for the entire transient. The following tabulation gives the gap widths used in the PARET calculations for the various reactor conditions.

Coolant Inlet Temperature (°F)	Initial Reactor Power (MW)	Gap Width (in.)
70	50×10^{-6}	0.0030
250	50×10^{-6}	0.0025
500	50×10^{-6}	0.0020
500	1	0.0015
500	20	0

represented in Equation (B-23). Since the gap conductance could not be directly measured, the applicability of the model was determined by comparing the PARET-calculated and experimental cladding surface temperatures and reactor powers. For both long- and short-period cold-startup tests, the model gave good agreement between the experimental and calculational results[B-16].

6. RADIAL HEAT SOURCE DESCRIPTION CALCULATIONS

In addition to the axial source importance weighting factors derived from the reactor physics calculations, radial source descriptions in the fuel, cladding and moderator must be provided as input into the PARET code. The cladding and moderator sources must be described in terms of fixed fractions of fission heat deposited directly in the clad and coolant. The radial distribution of fission energy generated in the fuel pellets is specified as a time-independent function of the radial dimension. The radial source description calculations will be presented in this section.

6.1 Moderator and Cladding Heat Sources

These heat sources were estimated using the data for the prompt energy release from fission of U-235 published by Keepin[B-10]. It was assumed that all fission neutron energy was deposited in the moderator, all fission fragment energy was deposited in the fuel, and the gamma energy was deposited in proportion to the mass ratio of the materials in the E-core unit cell. Calculations based upon these assumptions yielded values of 0.032 and 0.004 as the fractions of the total energy released directly in the moderator and clad, respectively.

The radial source description for a region R was calculated from the equation

$$Q_R(r) = F_R \frac{\phi_R(r)}{\bar{\phi}_R} \frac{V_M}{V_R} \qquad \text{(B-24)}$$

where

F_R = fraction of total energy release in region R

$\phi_R(r)$ = power in region R at radial point r

$\bar{\phi}_R$ = radial average of $\phi_R(r)$ across region R

V_M = volume of [illegible]

V_R = volume of region R

Assuming the heat generated in the moderator and cladding from gamma and neutron energy is not radially dependent, then $\phi_R(r)/\bar{\phi}_R$ is equal to unity. Taking into account the relative volumes of fuel, moderator, and cladding in a unit cell, the values of the radial source descriptions are 0.026 and 0.02 for the moderator and cladding, respectively.

6.2 Fuel Heat Source

The fraction of the prompt energy release from fission that remains in the fuel was calculated to be 0.964. This fraction was separated into radially weighted and nonweighted portions. The fraction of the heat generation in the fuel due to gamma ray attenuation was assumed to be nonweighted and amounted to 0.027. The fraction of the heat generation in the fuel due to fission fragments was calculated to be 0.937 and was radially weighted by the fission density in the rod. In terms of Equation (B-24), the radial source description for the fuel becomes

$$Q_M(r) = 0.937 \frac{\nu\Sigma_f\phi(r)}{\overline{\nu\Sigma_f\phi}} + 0.027 \qquad \text{(B-25)}$$

where

$\nu\Sigma_f\phi(r)$ = fission density at radial point r

$\overline{\nu\Sigma_f\phi}$ = average fission density in fuel.

The fission density at each point and the average fission density in the fuel rod were calculated for four energy groups using the TOPIC transport theory code. The solutions for the radial source description in the fuel at the various E-core system temperature conditions are presented in Figure B-3. At a system temperature of 500 F, the radial source description varied little as the initial reactor power increased from 50 W to 20 MW.

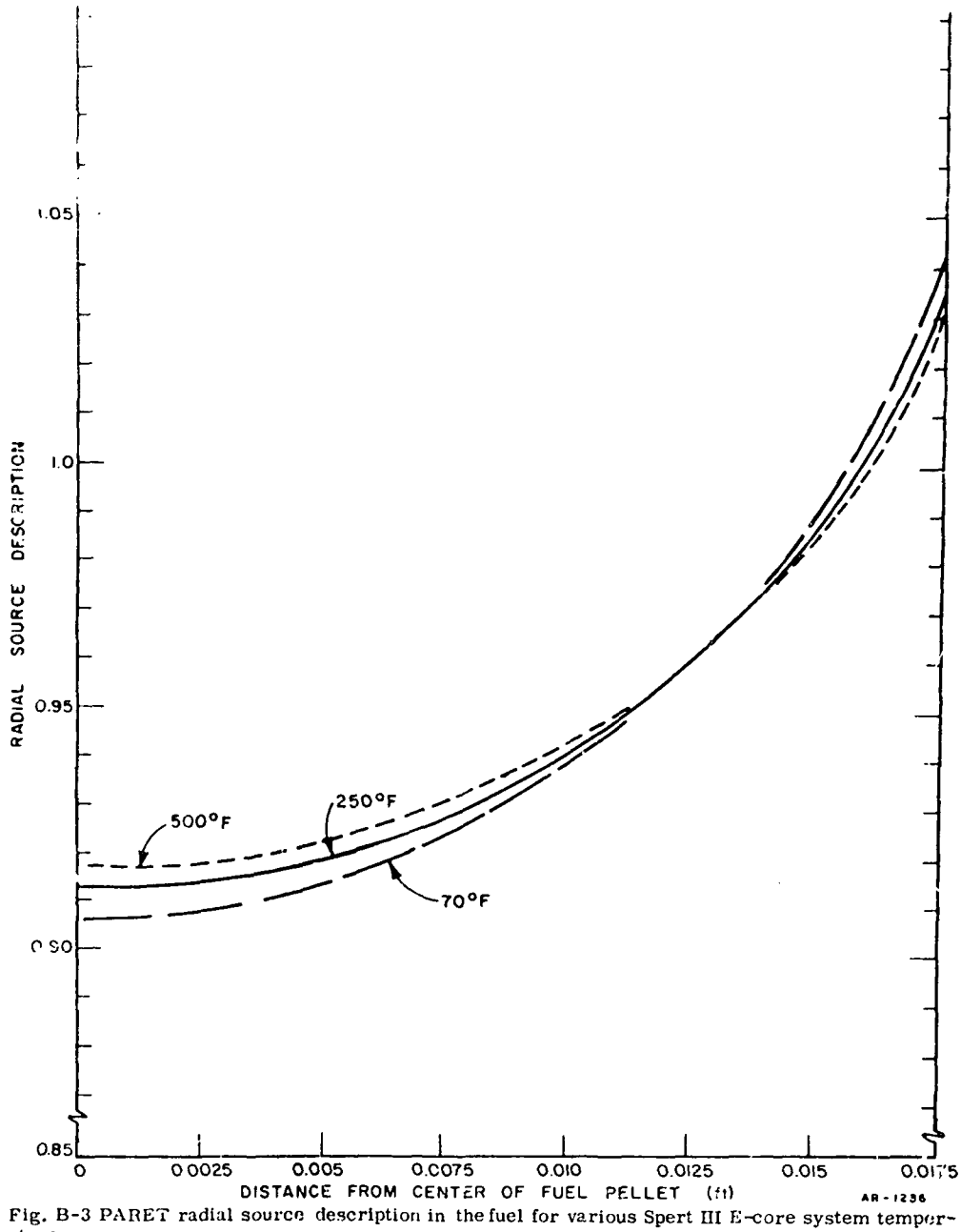

Fig. B-3 PARET radial source description in the fuel for various Spert III E-core system temperatures.

7. OVERALL VOID VOLUME COEFFICIENT

To determine the reactivity feedback from moderator heating and void formation in the PARET code, an overall void volume coefficient must be specified. For the E-core cold-startup conditions this coefficient was obtained directly from the experimental uniform void coefficient of -0.50$/% void[B-17]. The overall void volume coefficient used in the PARET code is given by the equation

$$C = \alpha_V \beta_{eff} \tag{B-26}$$

where

C = overall void volume coefficient, $\frac{\delta k}{k}$/% void

α_V = uniform void coefficient, $/% void

β_{eff} = effective delayed neutron fraction.

Since β_{eff} was 0.00718 at ambient temperature, the overall void volume coefficient for 70°F system temperature was $3.59 \times 10^{-3} \frac{\delta k}{k}$ /% void.

Since the uniform void coefficient was measured only at ambient temperature, another method was used to obtain the overall void volume coefficients at the other reactor system temperatures. The coefficients were calculated using the experimental temperature coefficients measured during the control rod worth experiments[B-12]. The overall void volume coefficients were calculated using the equation

$$C = \frac{\alpha_T \beta_{eff}}{-\left[\frac{\Delta v}{\Delta T} / v(t)\right] 100} \tag{B-27}$$

where

α_T = temperature coefficient, $/°F

v = specific volume, ft^3/lb

T = moderator temperature, °F

$-\left[\frac{\Delta v}{\Delta T}/v(t)\right]100$ = % void/°F.

The values of the overall void volume coefficients calculated from the various system temperature coefficients are listed in the following tabulation:

System Temperature (°F)	Initial Reactor Power (MW)	Temperature Coefficient ($/°F)	Effective Delayed Neutron Fraction	Overall Void Volume Coefficent ($\frac{\delta k}{k}$/% void)
250	50×10^{-6}	- 0.0197	0.00724	3.02×10^{-3}
500	50×10^{-6}	- 0.0399	0.00725	2.56×10^{-3}
500	1	- 0.0399	0.00725	2.56×10^{-3}
512.5	20	- 0.0413	0.00725	2.69×10^{-3}

8. REACTIVITY INSERTION RATES

In preparation for an excursion, the control rods are withdrawn to a predetermined position and the reactor is maintained at criticality by inserting the poison section of the transient rod into the lower part of the core. The excursions are initiated by ejecting the transient rod poison section from the core. The reactivity insertion rates input to the PARET code were determined from differential control rod worth measurements and a calculated transient rod position versus time curve. The differential control rod worth curve was based upon experimental data from the static and low-initial-power transient tests. The static data were required because no low-initial-power transient tests were performed in the control rod withdrawal position range that represented the 20 MW initial reactor power conditions. Plots of transient rod worth versus position for three system temperatures are given in Figure B-4. Since no data were available for transient rod insertions larger than nine inches, it was assumed that the slopes of the curves could be extrapolated for larger insertions. Smooth curves were fitted such that the reactivity controlled by the transient rod was zero at the bottom of the core fuel.

The transient rod displacement was calculated on the basis of a design transient rod acceleration of 2000 in./sec^2. By use of a transient rod position versus time curve based on this constant acceleration, and the values of worth per unit length from Figure B-4, the reactivity insertion rates were determined. These reactivity insertion rates are shown in Figure B-5. Since the differential transient rod worth was constant over most of the rod travel, constant values of worth/in. were used in determining the reactivity insertion

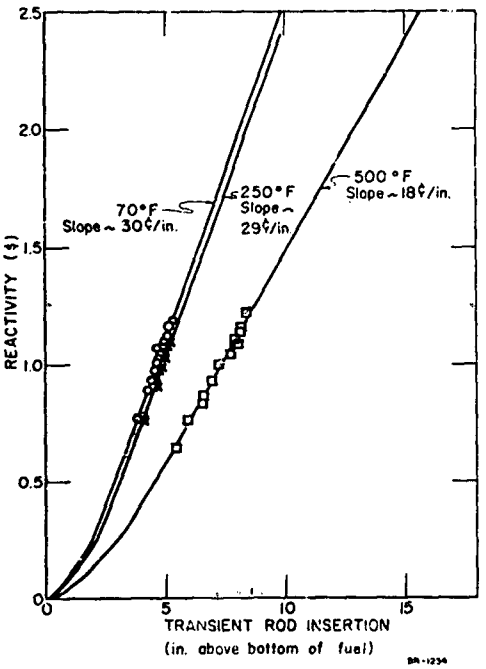

Fig. B-4 Experimental transient rod worths for various Spert III E-core system temperatures.

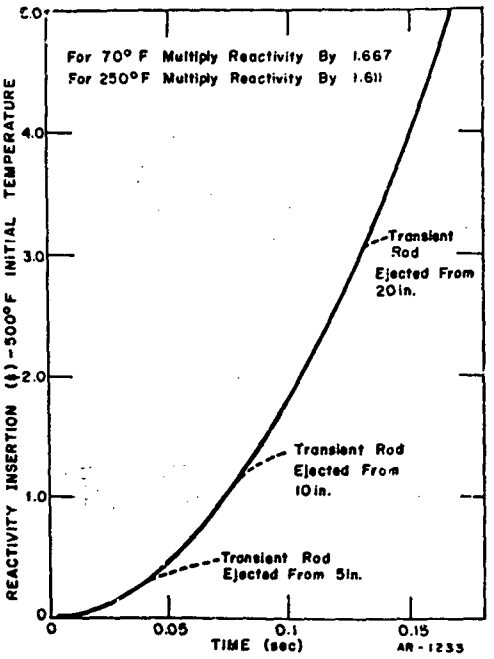

Fig. B-5 Calculated reactivity insertion rates for various Spert III E-core system temperatures.

rates, represented by the solid line in Figure B-5. An error in the insertion rate was introduced for the last few cents of any ramp insertion since the rod worth decreased at the bottom of the core. The dashed lines on Figure B-5 were calculated using the fitted lines rather than a constant slope and show this error for three initial transient rod positions. For small transient rod insertions, the shape of the insertion rate curve and the time required to insert the total reactivity are quite different from the values determined from the constant worth/in. calculations. For large transient rod insertions, however, the transient rod traverses the bottom region at high speed and the differences between the curves are small.

For low-initial-power excursions, the reactivity insertions were completed before appreciable reactivity feedback occurred and the excursions behave essentially as if a step reactivity insertion had taken place. Thus, for the PARET calculations of the low-initial-power excursions, a linear ramp rate of 15$/sec was used for all the transients. During the high-initial-power excursions, the kinetic behavior of the E-core was strongly influenced by the reactivity insertion

rate because appreciable reactivity feedback occurred during the reactivity insertion.

9. AVERAGE-CHANNEL PARET CALCULATIONS

Single average-channel PARET calculations were made for several representative Spert III E-core reactivity accidents. These transients were initiated with reactivity insertions of 1.23 and 1.17$ at initial reactor power levels of 50 W, 1 MW, and 20 MW, respectively. The reactor operating conditions were 500°F inlet coolant temperature, 1500 psig system pressure, and 12,000 gpm coolant flow. The calculated peak reactor powers for these transients, along with those obtained from four-channel PARET calculations, are listed in the following tabulation:

Initial Reactor Power	50 W	1 MW	20 MW
Reactivity Insertion ($)	1.23	1.17	1.17
Four-Channel PARET Calculated Peak Power (MW)	447	287	543
Average-Channel PARET Calculated Peak Power (MW)	470	306	592
Experimental Peak Power (MW)	410 ± 40	330 ± 30	610 ± 60

The average-channel calculations yielded peak powers that were within 10% of those obtained from the four-channel calculations. The average-channel peak powers were slightly conservative, or they overestimated the values calculated by the four-channel model.

The average-channel PARET calculations yielded peak power results comparable to those from the four-channel PARET model for the small Spert III E-core reactor because this reactor had perturbed radial peak-to-average thermal and resonance flux ratios that were small (less than 2). However, for reactors where the perturbed radial flux peaking factors are large, the four-channel PARET model should yield more accurate results than the single average-channel model.

10. REFERENCES

B-1 C. F. Obenchain, PARET -- A Program for the Analysis of Reactor Transients, IDO-17282 (January 1969).

B-2 G. E. Putnam, TOPIC -- A Fortran Program for Calculating Transport of Particles in Cylinders, IDO-16968 (April 1964).

B-3 R. H. Shudde and J. Dyer, TEMPEST II -- A Neutron Thermalization Code, TID-18284 (June 1962).

B-4 G. D. Joanou and J. S. Dudek, GAM-1: A Consistent P1 Multigroup Code for the Calculation of Fast Neutron Spectra and Multigroup Constants, GA-1850 (June 1961).

B-5 F. J. Wheeler, RAVEN -- A Computer Package for Evaluating Resolved and Unresolved Resonance Absorption Including Pin Shadowing, IDO-17212 (February 1967).

B-6 W. R. Cadwell, PDQ-4 -- A Program for the Solution of the Neutron-Diffusion Equations in Two Dimensions on the Philco-2000, WAPD-TM-230 (June 1961).

B-7 E. C. Anderson and G. E. Putnam, CORA -- A Code for One-Dimensional Reactor Analysis, IDO-17199 (to be published).

B-8 J. E. Houghtaling, A Model for Analysis of Fast Transient Reactivity Effects in Low-Enriched Oxide-Fueled Reactors, IDO-17224 (January 1967).

B-9 G. A. Mortensen, Phillips Petroleum Company, Private Communication (January 1967).

B-10 G. R. Keepin, Physics of Nuclear Kinetics, Reading, Massachusetts: Addison-Wesley Publishing Co., Inc., 1965, p 13.

B-11 A. F. Henry, Computation of Parameters Appearing in the Reactor Kinetics Equations, WAPD-142 (December 1955).

B-12 T. G. Taxelius (ed.), Quarterly Technical Report -- Spert Project -- July, August, September, 1966, IDO-17228 (April 1967).

B-13 J. Dugone (ed.), Spert III Reactor Facility: E-Core Revision, IDO-17036 (November 1965).

B-14 W. K. Anderson and G. L. Lechliter, "Some Input Functions for Computer Description of Fuel Properties", ANS Trans., 9 n 2 (October 30 - November 3, 1966) pp 375-376.

B-15 A. M. Ross and R. L. Stoute, Heat Transfer Coefficient Between UO_2 and Zircaloy-2, CRFD-1075 (June 1962).

B-16 T. G. Taxelius (ed.), Quarterly Technical Report -- Spert Project -- January, February, March, 1967, IDO-17260 (February 1968).

B-17 T. G. Taxelius and R. M. Potenza (eds.), Quarterly Technical Report -- Spert Project -- April, May, June, 1966, IDO-17207 (January 1967).

APPENDIX C

UNCERTAINTIES IN THE EXPERIMENTAL RESULTS

To evaluate properly the results of an experimental program, it is necessary to determine the uncertainties in the experimental data. These uncertainties arise from systematic and random errors. A systematic error equally influences all measurements of a particular quantity; for example, an instrument calibration can introduce systematic errors. Random errors result when repeated measurements of the same quantity give rise to differing values, and these errors could depend, for example, upon instrument reproducibility.

For the Spert III E-core test program, experimental uncertainties resulting from instrument calibrations and data repeatability were determined. These experimental uncertainties are presented in this report in terms of standard deviations and least-squares fitted curves with their associated confidence bands. The standard deviation is a measure of the spread or scatter of experimental data. The method of least-squares was used to obtain curves from the experimental data since this method is almost universally accepted as yielding fitted curves that come as close as possible to each data point.

The E-core experimental data were used to evaluate calculational models, and thus, the experimental uncertainties were of particular significance to the overall program objectives. Comparison of a data point with a calculated result can be made if the standard deviation or scatter in that data point is known. A curve calculated using an analytical model can be compared meaningfully with an experimental least-squares fitted curve provided that the confidence in the experimental curve is known. The confidence in the least-squares fitted curves is given in terms of confidence bands in this report.

1. STANDARD DEVIATION OF THE EXPERIMENTAL DATA

The standard deviation is a rigorous measure of the accuracy of experimental data. For a normal distribution, about 68% of repeated experimental measurements lie within one standard deviation of the average value. The standard deviation can be determined by one of the three following methods:

(1) If an experimental measurement is repeated a number of times, the standard deviation is given by the root mean square of the deviations from the average of the measurements. However, during the Oxide Core Kinetics Program it was generally not practicable to determine standard deviations in experimental measurements by repeated experiments.

(2) If an experimental quantity is measured over a range of conditions (as opposed to repeated measurements at one condition), the standard deviation for a predicted point can be determined from the variance of the data about a least-squares fitted curve[C-1].

(3) If a parameter cannot be experimentally measured, but can be calculated from an equation, then the standard deviation in that parameter can be determined if the standard deviations in the independent variables in the equation are known[C-2].

In the Oxide Core Kinetics Program, if the standard deviation of a quantity could not be determined by any of the three methods discussed above, then the standard deviation was estimated on the basis of experience.

One standard deviation in the reactor peak power, energy release to the time of peak power, maximum measured fuel rod cladding surface temperature, reactor period, reactivity insertion, and reactivity compensation at the time of peak power were determined by one of the above methods. The standard deviations obtained for the various parameters are discussed in the following paragraphs.

1.1 Peak Power and Energy Release to Peak Power

In order to obtain the standard deviation in peak reactor power, the accuracy of the neutron detector constants, that were calculated from the results of power calibration experiments, had to be determined. The neutron detector constants were calculated from the results of flux wire activation experiments for system temperatures of 70, 250, 400, and 500°F. In addition to flux wire experiments, low- and high-power, primary system heat balance experiments were performed at a system temperature of 500°F.

The standard deviation in the neutron detector constants measured by flux wire activation was determined by combining the standard deviations of the independent variables in the equation used to calculate reactor power from flux wire activation data. Combining this standard deviation (which is discussed in detail in Reference C-3) with the estimated standard deviation resulting from random errors or data repeatability yielded a deviation of ± 15% in reactor power. This standard deviation of 15% coupled with the estimated uncertainty in the time of peak power leads to a standard deviation ± 17% in energy release to the time of peak power. Thus, for transient tests performed from initial system temperatures of 70, 250, and 400°F the standard deviation in reactor power was ± 15% and the standard deviation in energy to peak power was ±17%.

Several low- and high-power primary system heat balance experiments were performed at a system temperature of 500°F; therefore, the root mean square method was used to obtain the standard deviation in detector constants for this temperature. Standard deviations of ± 10% in reactor power and ± 13% in energy release to the time of peak power were obtained for a system temperature of 500°F[C-3].

1.2 Fuel Rod Surface Temperature

Maximum measured fuel rod cladding surface temperatures in the E-core were all obtained from stainless steel sheathed thermocouples attached to the corner fuel rod in assembly S11. A correction factor for the stainless steel sheathed thermocouples could not be obtained by a transfer function approximation with the faster-response unsheathed thermocouples. Therefore, time-dependent fuel rod cladding temperatures are not shown in this report. Maximum measured fuel rod cladding surface temperature rises are estimated to have standard deviations of about ± 10%, but the maximum fuel rod surface temperatures are more accurate than ± 10%. For example, the standard deviation in maximum fuel rod surface temperature is about 8 to 9% at a system temperature of 70°F and about 2% at a system temperature of 500°F.

1.3 Reactor Period and Reactivity Insertion

The reactor period for a given transient was calculated from the power data assuming an initial exponential power rise. Past experience indicated that the calculated reactor period obtained from different neutron detectors for a given transient test did not vary by more than about ± 2%. In addition, the systematic

error in the analog-to-digital conversion system, which is used to reduce the power data recorded on magnetic tape to digital form, is less than ± 2%. Therefore, the standard deviation in the reactor period was estimated to be ± 2%.

For the low-initial-power reactivity accident tests, the reactivity insertion for a given transient test was determined from the inhour equation. The standard deviation in reactivity insertion, as determined from the inhour equation, is a function of standard deviations in the reactor period, reduced prompt neutron generation time, and delayed neutron parameters. The standard deviations in these independent variables were ± 2, ± 2.5, and ± 7 to 15%, respectively, which led to a standard deviation in reactivity insertion of about ± 4% [C-4].

Asymptotic reactor periods were not attained during the high-initial-power tests; thus the inhour equation could not be used to determine the reactivity insertion. For these tests, the control rod worth curve had to be used to obtain the reactivity insertions. The standard deviation in the reactivity insertion for a given high-initial-power transient, as determined from the control rod worth curve, was calculated from the variance of the control rod worth data about a least-squares fitted curve [C-4]. This standard deviation was also about ± 4%.

1.4 Reactivity Compensation at Peak Power

The time-dependent reactivity compensation was determined from the point-reactor kinetic equations. These equations are functions of the reactor power, reduced prompt neutron generation time, reactor period, and delayed neutron parameters. The standard deviation in the time-dependent reactivity compensation was calculated from the previously mentioned standard deviations in the independent variables. The time-dependence of the standard deviation in the compensated reactivity is illustrated in Figure C-1 for a 10-msec-period cold-startup test. The irregularities in the standard deviation were caused by low-level noise in the reactor power data. At the time of peak power about 0.22$ of the 1.21$ initial reactivity insertion was compensated. At that time, the standard deviation in compensated reactivity was about 0.025$ or about 11%. Calculations were performed for other transient tests with reactor periods ranging up to about one second. Results were similar to those shown in Figure C-1 and it was concluded that the uncertainty in the reactivity compensation is only weakly dependent on the amount of reactivity compensation. Thus one standard deviation in the reactivity compensation at the time of peak power is about ± 11% for the range of reactivity accidents tested in the E-core.

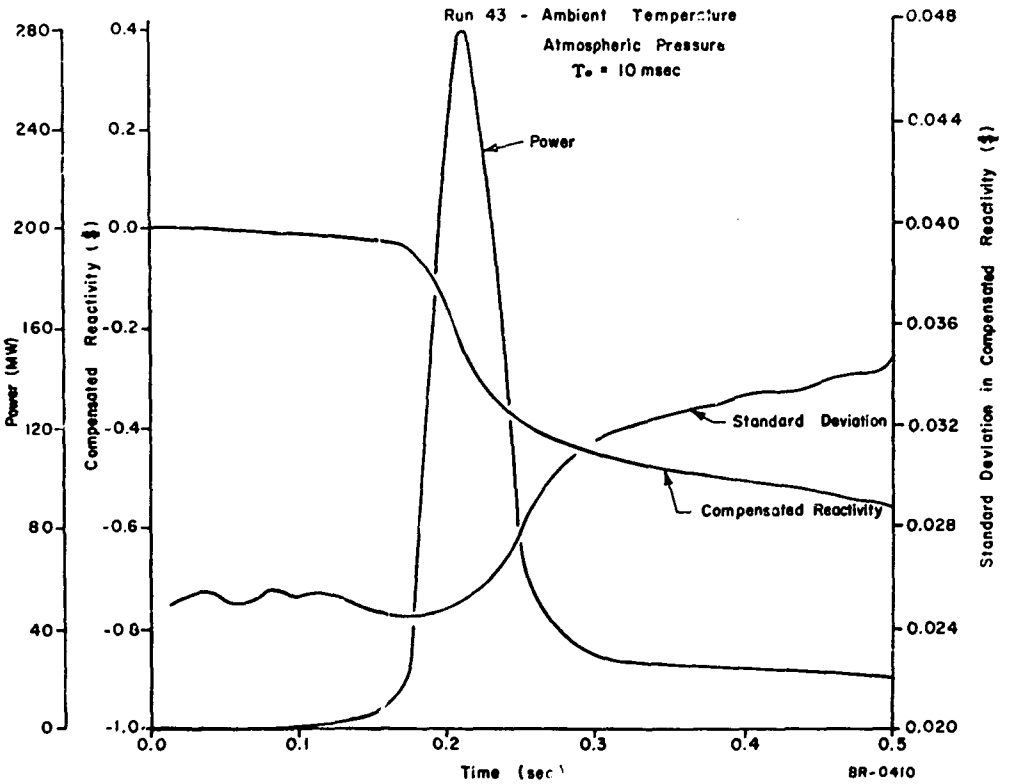

Fig. C-1 Calculated compensated reactivity and standard deviation in compensated reactivity for cold-startup test 43 (10 msec period).

2. LEAST-SQUARES FITTED CURVES

Correlation of the Spert III E-core experimental data and comparisons of these data with calculational results was accomplished using curves that were least-squares fitted to the experimental data. Before discussing the statistical method by which the confidence in these fitted curves was determined, the principle of least squares will be briefly reviewed. The least-squares principle is that the best fit of a curve to data points results when the sum of the squares of the deviations between the data points and the curve is a minimum. This principle is given by the equation

$$\sum_{i=1}^{n} (Y_i - Y_i')^2 = \text{Minimum} \qquad \text{C-1}$$

n = number of data points

Y_i = value of data point

Y_i' = value obtained from fitted curve.

As a simple example of least-squares fitting, consider the second order polynomial

$$Y_i' = a_o + a_1 X_i + a_2 X_i^2 \qquad \text{C-2}$$

where the coefficients a_o, a_1, and a_2 are to be determined by the least-squares method. The expression for Y_i' given in Equation (C-2) is substituted into Equation (C-1). The partial derivative of Equation (C-1) is then taken with respect to each of the three coefficients and the resulting three expressions are set equal to zero. This procedure yields three equations, called the normal equations, from which the three coefficients are determined. Written in matrix form, the normal equations are

$$\begin{bmatrix} n & \Sigma X_i & \Sigma X_i^2 \\ \Sigma X_i & \Sigma X_i^2 & \Sigma X_i^3 \\ \Sigma X_i^2 & \Sigma X_i^3 & \Sigma X_i^4 \end{bmatrix} \begin{bmatrix} a_o \\ a_1 \\ a_2 \end{bmatrix} = \begin{bmatrix} \Sigma Y_i \\ \Sigma X_i Y_i \\ \Sigma X_i^2 Y \end{bmatrix} \qquad \text{C-3}$$

$$\begin{bmatrix} a_o \\ a_1 \\ a_2 \end{bmatrix} = \begin{bmatrix} n & \Sigma X_i & \Sigma X_i^2 \\ \Sigma X_i & \Sigma X_i^2 & \Sigma X_i^3 \\ \Sigma X_i^2 & \Sigma X_i^3 & \Sigma X_i^4 \end{bmatrix}^{-1} \begin{bmatrix} \Sigma Y_i \\ \Sigma X_i Y_i \\ \Sigma X_i^2 Y_i \end{bmatrix} = \begin{bmatrix} C_{00} & C_{01} & C_{02} \\ C_{10} & C_{11} & C_{12} \\ C_{20} & C_{21} & C_{22} \end{bmatrix} \begin{bmatrix} \Sigma Y_i \\ \Sigma X_i Y_i \\ \Sigma X_i^2 Y_i \end{bmatrix}$$

where C_{ij} is the ij^{th} element of the inverse matrix.

There are three types of confidence bands that can be determined for a least-squares fitted curve. These are confidence bands for a point on the fitted curve, confidence bands for a new predicted experimental value using the fitted curve, and confidence bands for the curve as a whole. Confidence bands for the least-squares fitted curve as a whole are used for comparison with a

calculated curve. The width of a confidence band at a given value of X (at x = h) on the curve is given by the equation[C-1]

$$W_h = 2\sqrt{2F_{1-\alpha}(k,n-k)} \quad S_y \left\{ \sum_{i=o}^{k-1} \sum_{j=o}^{k-1} X_h^i X_h^j C_{ij} \right\}^{1/2} \qquad C\text{-}4$$

where

W_h = total width of confidence band

n = number of data points

k = number of coefficients of the fitted polynomial

C_{ij} = ij^{th} element of the inverse matrix of the normal equations

$1-\alpha$ = desired confidence level

$F_{1-\alpha}(k,n-k)$ = value from an F-distribution table (See Reference C-1)

S_y = standard deviation of the data about the fitted curve.

Since the inverse matrix is symmetric, Equation (C-5) becomes

$$W_h = 2\sqrt{2F_{1-\alpha}(k,n-k)} \quad S_y \left[C_{00} + 2X_h C_{01} + X_h^2(2C_{02} + C_{11}) + 2X_h^3 C_{12} + X_h^4 C_{22}\right]^{1/2} \qquad C\text{-}5$$

for a second order polynomial.

In the determination of confidence bands for the least-squares fitted curves presented in this report, a confidence level of 0.95 was used. However, these 95% confidence bands did not account for systematic errors such as the uncertainty in the absolute reactor power. Combining these systematic uncertainties with the 95% confidence bands led to the 65% confidence bands that are presented in the figures and tables of this report. These confidence bands imply that if a set of experiments were repeated 100 times and a least-squares fitted curve determined for each set of data, then 65 of the fitted curves would lie within the confidence bands.

Polynomial curves were least-squares fitted to experimental peak power, energy to peak power, and reactivity compensation at peak power data as functions of either reciprocal period or reactivity insertions. For the cold-startup tests and the hot-startup tests performed from 500°F system temperature, 65% confidence bands were determined for the least-squares fitted curves. For the

hot-startup tests performed from about 260°F and for the high-initial-power tests, too few transients were performed to allow the calculation of meaningful confidence bands; therefore, the least-squares fitted curves serve only as an aid in the general interpretation of data. The values for the least-squares fitted curves are listed in Tables C-I through C-XIII. In addition, values for the least-squares fitted curves of peak power and energy to peak power versus reciprocal period data for the Spert I OC core and the Spert IV CDC are given in Tables C-XIV through C-XVII.

TABLE C-I

LEAST-SQUARES FITTED CURVE FOR COLD-STARTUP PEAK POWER VERSUS RECIPROCAL PERIOD DATA

Reciprocal Period (sec^{-1})	Peak Power (MW)	Upper 65% Confidence Band (MW)	Lower 65% Confidence Band (MW)
3	4.57	5.80	3.42
4	4.93	5.98	3.92
5	5.36	6.38	4.37
6	5.85	6.91	4.81
7	6.39	7.51	5.28
8	6.96	8.15	5.79
9	7.57	8.83	6.31
10	8.21	9.57	6.87
15	11.9	13.8	10.1
20	16.5	19.3	13.7
30	28.6	33.7	23.5
40	45.2	53.5	37.1
50	67.2	79.5	55.1
60	95.5	114	78.2
70	131	156	106
80	175	213	140
90	228	282	178
100	293	370	221

TABLE C-II

LEAST-SQUARES FITTED CURVE FOR COLD-STARTUP ENERGY RELEASE TO PEAK POWER VERSUS RECIPROCAL PERIOD DATA

Reciprocal Period (sec^{-1})	Energy to Peak Power (MW-sec)	Upper 65% Confidence Band (MW-sec)	Lower 65% Confidence Band (MW-sec)
3	6.83	9.82	4.37
4	6.22	8.18	4.46
5	5.55	7.02	4.18
6	5.00	6.21	3.84
7	4.47	5.51	3.48
8	4.07	4.98	3.20
9	3.75	4.56	2.97
10	3.47	4.22	2.76
15	2.52	3.04	2.02
20	2.19	2.68	1.71
30	2.14	2.61	1.69
40	2.42	3.00	1.87
50	2.86	3.58	2.19
60	3.42	4.28	2.61
70	4.05	5.06	3.11
80	4.76	5.97	3.62
90	5.50	7.23	3.95
100	6.27	8.58	4.27

TABLE C-III

LEAST-SQUARES FITTED CURVE FOR COLD-STARTUP REACTIVITY COMPENSATION AT PEAK POWER VERSUS RECIPROCAL PERIOD DATA

Reciprocal Period (sec^{-1})	Reactivity Compensation at Peak Power ($)	Upper 65% Confidence Band ($)	Lower 65% Confidence Band ($)
3	0.244	0.351	0.156
4	0.222	0.290	0.161
5	0.199	0.251	0.151
6	0.179	0.222	0.139
7	0.162	0.199	0.127
8	0.148	0.180	0.118
9	0.137	0.166	0.110
10	0.128	0.154	0.103
15	0.0931	0.111	0.0757
20	0.0814	0.0991	0.0646
30	0.0818	0.0986	0.0656
40	0.0942	0.115	0.0739
50	0.112	0.139	0.0873
60	0.134	0.166	0.104
70	0.158	0.195	0.123
80	0.182	0.226	0.141
90	0.206	0.268	0.150
100	0.229	0.310	0.159

TABLE C-IV

LEAST-SQUARES FITTED CURVE FOR 260°F HOT-STARTUP PEAK POWER VERSUS RECIPROCAL PERIOD DATA[a]

Reciprocal Period (sec^{-1})	Peak Power (MW)
4	6.87
5	6.86
6	7.08
7	7.45
8	7.92
9	8.47
10	9.07
15	12.9
20	17.8
30	31.2
40	49.6
50	72.6
60	104
70	141
80	186
90	239
100	301

[a] Coolant flow rate of 14 fps.

TABLE C-V

LEAST-SQUARES FITTED CURVE FOR 260°F HOT-STARTUP ENERGY TO PEAK POWER VERSUS RECIPROCAL PERIOD DATA[a]

Reciprocal Period (sec^{-1})	Energy to Peak Power (MW-sec)
4	6.64
5	7.66
6	7.28
7	6.43
8	5.56
9	4.80
10	4.19
15	2.59
20	2.10
30	2.07
40	2.49
50	3.13
60	3.88
70	4.67
80	5.39
90	5.98
100	6.40

[a] Coolant flow rate of 14 fps.

TABLE C-VI

LEAST-SQUARES FITTED CURVE FOR 260°F HOT-STARTUP REACTIVITY COMPENSATION AT PEAK POWER VERSUS RECIPROCAL PERIOD DATA[a]

Reciprocal Period (sec^{-1})	Reactivity Compensation at Peak Power ($)
3	0.126
4	0.202
5	0.221
6	0.210
7	0.191
8	0.170
9	0.152
10	0.137
15	0.0959
20	0.0825
30	0.0829
40	0.972
50	0.118
60	0.141
70	0.166
80	0.189
90	0.209
100	0.224

[a] Coolant flow rate of 14 fps.

TABLE C-VII

LEAST-SQUARES FITTED CURVE FOR 500°F HOT-STARTUP PEAK POWER VERSUS RECIPROCAL PERIOD DATA[a]

Reciprocal Period (sec^{-1})	Peak Power (MW)	Upper 65% Confidence Band (MW)	Lower 65% Confidence Band (MW)
1.5	5.64	7.62	4.02
2	5.99	7.50	4.64
3	6.72	8.35	5.25
4	7.50	9.45	5.77
5	8.32	10.5	6.39
6	9.19	11.5	7.08
7	10.1	12.7	7.81
8	11.0	13.8	8.61
9	12.0	14.9	9.46
10	13.1	16.1	10.3
15	18.9	22.7	15.3
20	25.8	31.8	21.2
30	43.8	51.9	36.2
40	67.9	79.7	56.7
50	99.3	115	84.0
60	139	161	119
70	189	218	161
80	250	294	209
90	324	390	263
100	412	512	322

[a] Coolant flow rate of 14 fps.

TABLE C-VIII

LEAST-SQUARES FITTED CURVE FOR 500°F HOT-STARTUP ENERGY TO PEAK POWER VERSUS RECIPROCAL PERIOD DATA[a]

Reciprocal Period (sec^{-1})	Energy to Peak Power (MW-sec)	Upper 65% Confidence Bands (MW-sec)	Lower 65% Confidence Bands (MW-sec)
1.5	12.8	15.1	10.7
2	17.0	19.3	14.8
3	15.9	18.3	13.6
4	12.4	14.3	10.5
5	9.61	11.0	8.29
6	7.71	8.76	6.69
7	6.40	7.26	5.57
8	5.49	6.21	4.79
9	4.84	5.48	4.22
10	4.36	4.94	3.80
15	3.27	3.70	[illegible]
20	3.01	3.39	2.64
30	3.23	3.59	2.86
40	3.81	4.21	3.40
50	4.54	5.01	4.07
60	5.34	5.89	4.79
70	6.15	6.77	5.53
80	6.91	7.63	6.20
90	7.60	8.49	6.75
100	8.19	9.29	7.12

[a] Coolant flow of 14 fps.

TABLE C-IX

LEAST-SQUARES FITTED CURVE FOR 500°F HOT-STARTUP REACTIVITY COMPENSATION AT PEAK POWER VERSUS RECIPROCAL PERIOD DATA[a]

Reciprocal Period (sec^{-1})	Reactivity Compensation at Peak Power ($)	Upper 65% Confidence Band ($)	Lower 65% Confidence Band ($)
1.5	0.243	0.291	0.199
2	0.337	0.388	0.288
3	0.332	0.387	0.280
4	0.267	0.311	0.223
5	0.212	0.245	0.180
6	0.173	0.198	0.148
7	0.146	0.166	0.126
8	0.126	0.145	0.109
9	0.113	0.129	0.097
10	0.103	0.117	0.0886
15	0.0798	0.0912	0.0689
20	0.0756	0.0859	0.0657
30	0.0842	0.0942	0.0744
40	0.102	0.113	0.0907
50	0.124	0.137	0.110
60	0.147	0.163	0.132
70	0.171	0.189	0.153
80	0.193	0.215	0.172
90	0.213	0.240	0.187
100	0.230	0.263	0.198

[a] Coolant flow rate of 14 fps.

TABLE C-X

LEAST-SQUARES FITTED CURVE FOR HOT STANDBY PEAK POWER VERSUS REACTIVITY INSERTION DATA

Reactivity Insertion ($)	Peak Power (MW)
0.85	12.0
0.90	19.9
0.95	29.7
1.00	50.1
1.05	87.3
1.10	152
1.15	260
1.20	427
1.25	656
1.30	914

TABLE C-XI

LEAST-SQUARES FITTED CURVE FOR HOT-STANDBY ENERGY TO PEAK POWER VERSUS REACTIVITY INSERTION DATA

Reactivity Insertion ($)	Energy to Peak Power (MW-sec)
0.85	7.42
0.90	4.84
0.95	3.90
1.00	3.74
1.05	4.12
1.10	5.03
1.15	6.56
1.20	8.82
1.25	11.8
1.30	15.2

TABLE C-XII

LEAST-SQUARES FITTED CURVE FOR OPERATING-POWER PEAK POWER VERSUS REACTIVITY INSERTION DATA

Reactivity Insertion ($)	Peak Power (MW)
0.1	20.6
0.2	22.8
0.3	26.5
0.4	32.1
0.5	40.5
0.6	53.5
0.7	73.7
0.8	106
0.9	159
1.0	249
1.1	408
1.2	697
1.3	1240

TABLE C-XIII

LEAST-SQUARES FITTED CURVE FOR OPERATING-POWER ENERGY TO PEAK POWER VERSUS REACTIVITY INSERTION DATA

Reactivity Insertion ($)	Energy to Peak Power (MW-sec)
0.1	0.821
0.2	1.44
0.3	2.37
0.4	3.70
0.5	5.42
0.6	7.60
0.7	10.0
0.8	12.4
0.9	14.6
1.0	16.2
1.1	17.0
1.2	16.9
1.3	15.8

TABLE C-XIV

LEAST-SQUARES FITTED CURVE OF SPERT I OC CORE PEAK POWER VERSUS RECIPROCAL PERIOD DATA

Reciprocal Period (sec^{-1})	Peak Power (MW)	Upper 65% Confidence Band (MW)	Lower 65% Confidence Band (MW)
2	6.28	8.34	4.38
3	6.67	8.46	5.05
4	7.45	9.15	5.79
5	8.41	10.3	6.61
6	9.51	11.6	7.48
7	10.7	13.0	8.39
8	12.0	14.6	9.40
9	13.4	16.3	10.5
10	14.9	18.1	11.7
15	23.6	28.6	18.6
20	34.4	41.7	27.2
30	62.8	75.9	49.9
40	101	122	79.9
50	149	180	118
60	208	252	165
70	279	338	221
80	363	439	287
90	459	557	363
100	569	690	447
150	1350	1640	1070
200	2570	3140	2010
300	6630	8320	5020
400	13300	17400	9600

TABLE C-XV

LEAST-SQUARES FITTED CURVE OF SPERT I OC CORE ENERGY TO PEAK POWER VERSUS RECIPROCAL PERIOD DATA

Reciprocal Period (sec^{-1})	Energy to Peak Power (MW-sec)
2	12.9
3	10.7
4	8.83
5	7.52
6	6.60
7	5.94
8	5.46
9	5.10
10	4.83
15	4.16
20	4.04
30	4.35
40	5.00
50	5.84
60	6.83
70	7.94
80	9.17
90	10.5
100	11.9
150	20.2
200	29.8
300	49.8
400	67.7

TABLE C-XVI

LEAST-SQUARES FITTED CURVE OF SPERT IV CDC PEAK POWER VERSUS RECIPROCAL PERIOD DATA

Reciprocal Period (sec^{-1})	Peak Power (MW)	Upper 65% Confidence Bands (MW)	Lower 65% Confidence Bands (MW)
2	10.0	14.1	6.48
3	11.6	15.3	8.19
4	13.5	17.5	9.70
5	15.7	20.4	11.4
6	18.2	23.5	13.3
7	21.0	27.1	15.2
8	24.0	30.9	17.5
9	27.2	35.0	19.8
10	30.6	39.3	22.4
15	51.1	64.8	38.0
20	77.1	96.6	58.4
30	147	181	114
40	242	294	192
50	364	441	289
60	515	621	411
70	697	840	555
80	910	1100	726
90	1160	1390	930
100	1440	1740	1140
150	3420	4130	2730
200	6460	7780	5160
300	16300	20000	12700

TABLE C-XVII

LEAST-SQUARES FITTED CURVE
OF SPERT IV CDC ENERGY
TO PEAK POWER VERSUS
RECIPROCAL PERIOD DATA

Reciprocal Period (sec^{-1})	Energy to Peak Power (MW-sec)
2	17.8
3	13.3
4	11.3
5	10.2
6	9.56
7	9.17
8	8.94
9	8.80
10	8.73
15	8.93
20	9.53
30	11.2
40	13.3
50	15.5
60	17.9
70	20.5
80	23.2
90	26.1
100	29.2
150	46.1
200	67.2
300	119

3. REFERENCES

C-1 M. G. Natrella, Experimental Statistics. (NBS Handbook 91) Washington, D. C.: U. S. Government Printing Office, 1963.

C-2 A. G. Worthing and J. Geffner, Treatment of Experimental Data, New York: John Wiley & Sons, Inc., 1950, p 213.

C-3 T. G. Taxelius (ed.), Quarterly Technical Report -- Spert Project -- October, November, December, 1967, IDO-17279 (October 1968).

C-4 T. G. Taxelius (ed.), Quarterly Technical Report -- Spert Project -- July, August, September, 1966, IDO-17228 (April 1967).

APPENDIX D

EXPERIMENTAL DATA PLOTS

A summary of transient test data of reactor power, energy, and system reactivity from the Spert III E-core test series is presented in graphical form in this appendix.

1. SPERT DATA PROCESSING SYSTEM

The Spert III E-core test data obtained from the reactor instrumentation system was recorded in two forms (a) frequency modulated and multiplexed magnetic tape and (b) light-sensitive oscillograph paper. The magnetic tape was the primary data source, with the oscillograph records used for verification and backup.

1.1 Magnetic Tape Data

Reduction of the magnetic tape data was accomplished by an analog-to-digital conversion system. This system provided time-dependent plots, digital magnetic tapes, and input for a PDP-5 digital computer. Detailed descriptions of the analog-to-digital conversion system and the PDP-5 computer are contained in Reference D-1. The inherent error in the conversion system, including plots and output tapes, is less than 2%.

A processing program for the PDP-5 computer performs the following operations:

(1) Normalizes and converts data to convenient engineering units

(2) Scales and plots all time-dependent reactor parameters

(3) Calculates and plots time-dependent transient energy release

(4) Calculates peak power, time to peak power, energy release to time of peak power, and total energy release

(5) Calculates initial reactor period.

1.2 Oscillograph Records

The oscillograph records were analyzed using either a metal ruler and appropriate calibration number, or using a manually operated curve follower

and digitizer. The estimated error in curve following and digitizing is less than 5%. A record of oscillograph results was maintained as a continuous check of magnetic tape data.

1.3 Data Processing on the IBM 7044 Computer

Further processing of E-core data was accomplished using the SPORT computer program[D-2] on the IBM 7044 computer. The code uses as its input the digital tape generated by the analog-to-digital conversion system or punched cards from the oscillograph records. The SPORT program includes a least-squares data smoothing subroutine to minimize electronic noise in the data. The program computes the system and compensated reactivities using the point-reactor kinetics equations. The output of SPORT includes, in addition to the reactivity, the reactor power and energy as functions of time.

2. EXPERIMENTAL POWER, ENERGY, AND REACTIVITY PLOTS

The experimental, time-dependent power, energy, and system reactivity for all of the Spert III E-core transient tests are presented in the following figures. These graphs were plotted by the SPORT processing system. Each figure is labeled according to the following symbols:

Θi = initial inlet coolant temperature
Flow = average coolant flow rate through the core
P_i = initial system pressure
τ = asymptotic reactor period
ρo = total reactivity inserted
Φi = initial reactor power.

The time scale for each graph was chosen to clearly illustrate the burst shape. For all of the tests except 79, 80, 84, 85, and 86, zero on the time scale represents the time of transient initiation. For these five tests, the recorded timing channel was started manually, and the times shown are not referenced to the start of the transients.

Either the inverse asymptotic period or initial concentrations of the delayed neutron precursors must be specified for SPORT code calculations. In processing the E-core test data using the SPORT program, the inverse asymptotic reactor

periods were specified. For the low-initial-power tests, the inverse asymptotic periods were calculated from the power data using the PDP-5 computer. For these tests the reactivity insertions were completed before appreciable reactivity feedback occurred, and the transients behaved as if a step reactivity insertion had taken place. Thus for these tests (Figures D-1 through -62), the initial system reactivity was equal to the total reactivity inserted. However, during the high-initial-power tests, appreciable reactivity compensation occurred during the reactivity insertion, and thus asymptotic periods were not attained. For these tests (Figures D-63 through -70), an initial steady state condition or inverse reactor period of zero was specified in the SPORT Program. Consequently, the system reactivity has an initial value of zero in these figures and increases to a maximum value during the transient.

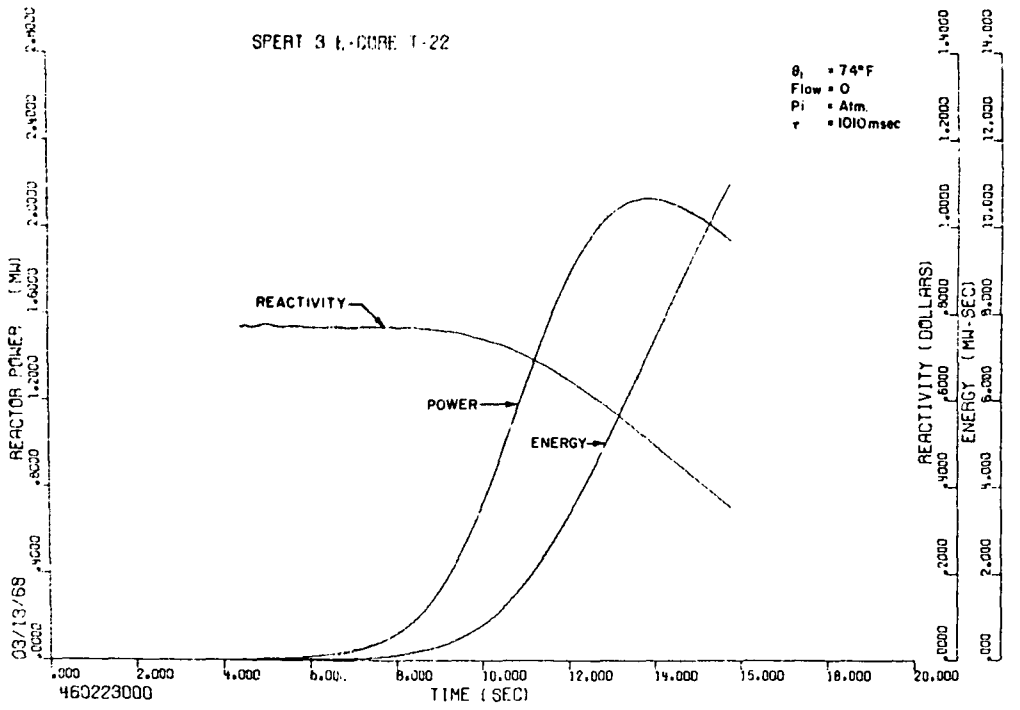

Fig. D-1 Experimental power, energy, and system reactivity for cold-startup test 22 (1010 msec, 0.77$ reactivity insertion).

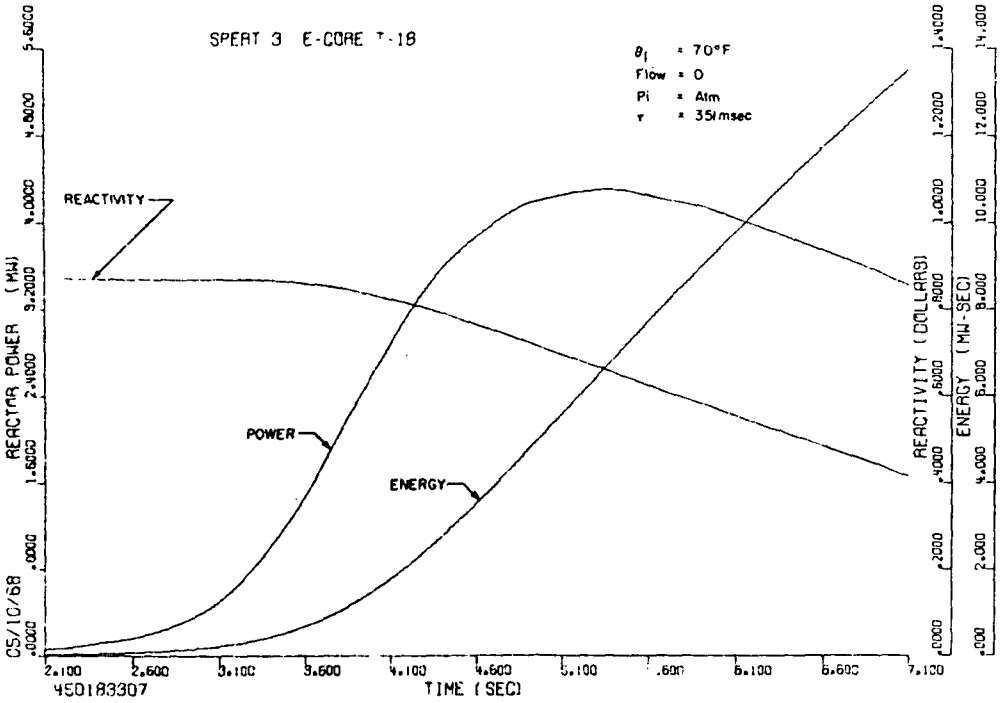

Fig. D-2 Experimental power, energy, and system reactivity for cold-startup test 18 (351 msec period, 0.90$ reactivity insertion).

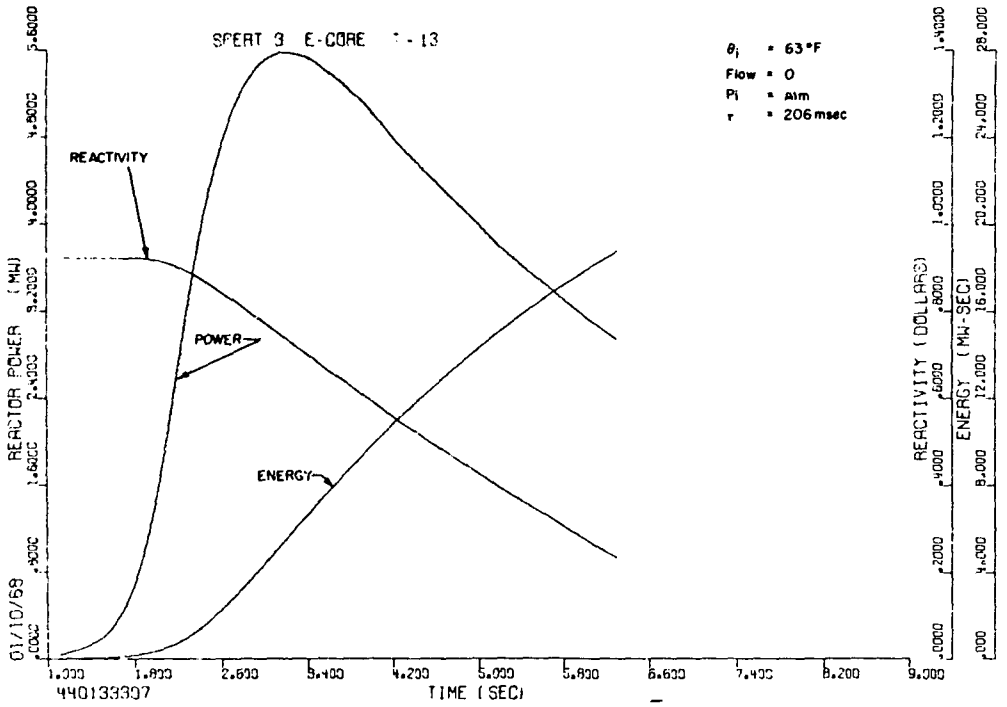

Fig. D-3 Experimental power, energy, and system reactivity for cold-startup test 13 (206 msec period, 0.93$ reactivity insertion).

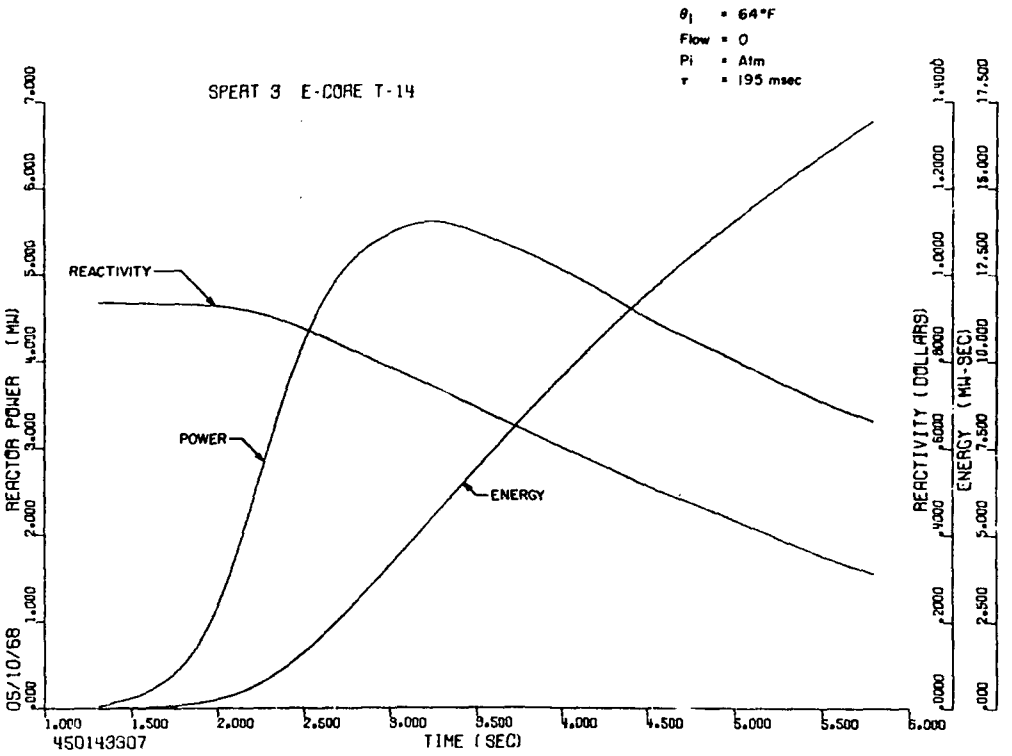

Fig. D-4 Experimental power, energy, and system reactivity for cold-startup test 14 (195 msec period, 0.94$ reactivity insertion).

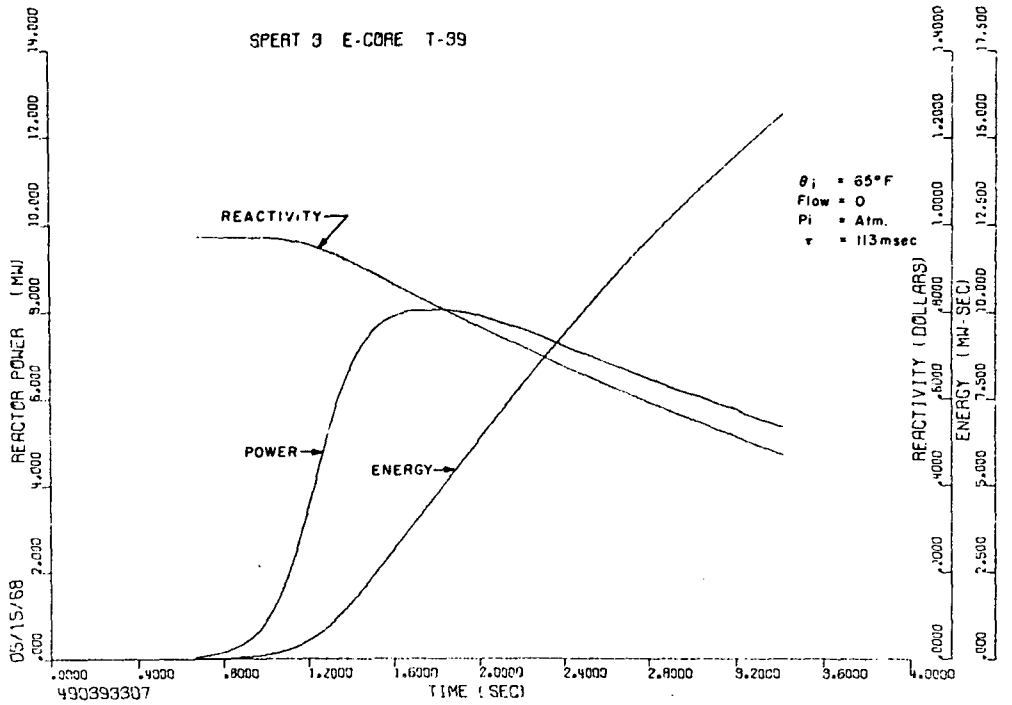

Fig. D-5 Experimental power, energy, and system reactivity for cold-startup test 39 (113 msec period, 0.97$ reactivity insertion).

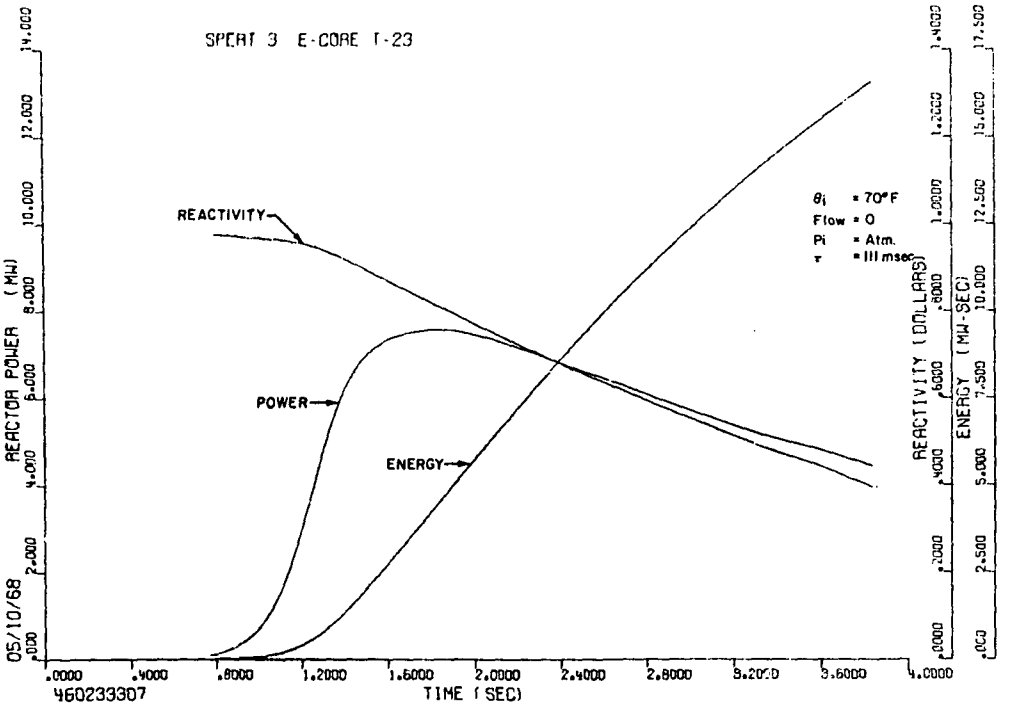

Fig. D-6 Experimental power, energy, and system reactivity for cold-startup test 23 (111 msec period, 0.97$ reactivity insertion).

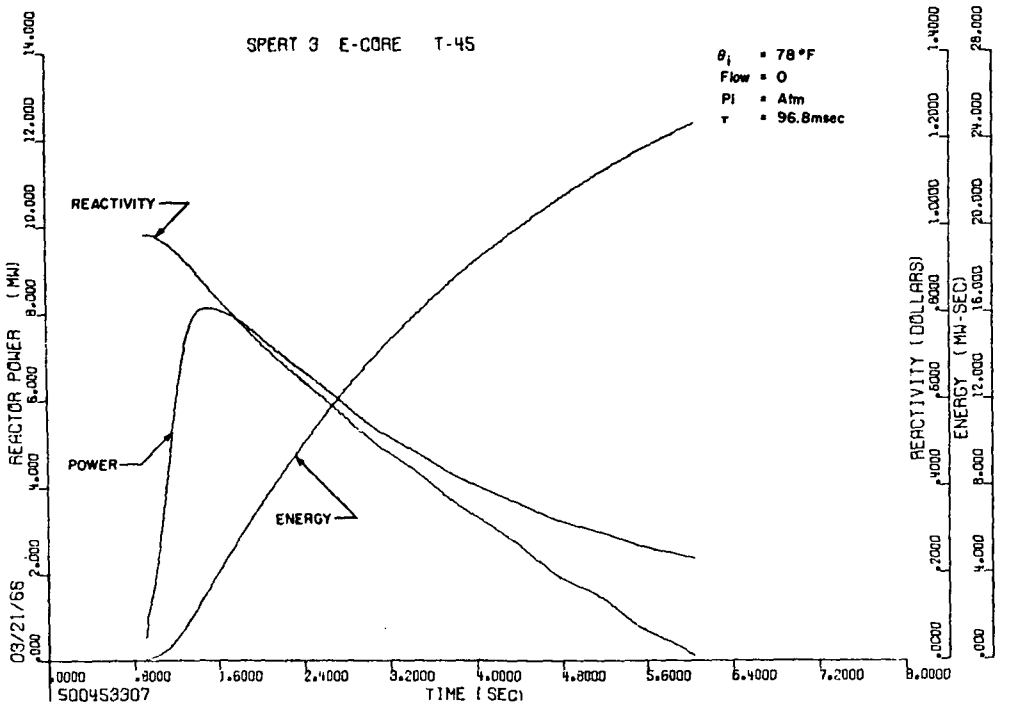

Fig. D-7 Experimental power, energy, and system reactivity for cold-startup test 45 (96.8 msec period, 0.98$ reactivity insertion).

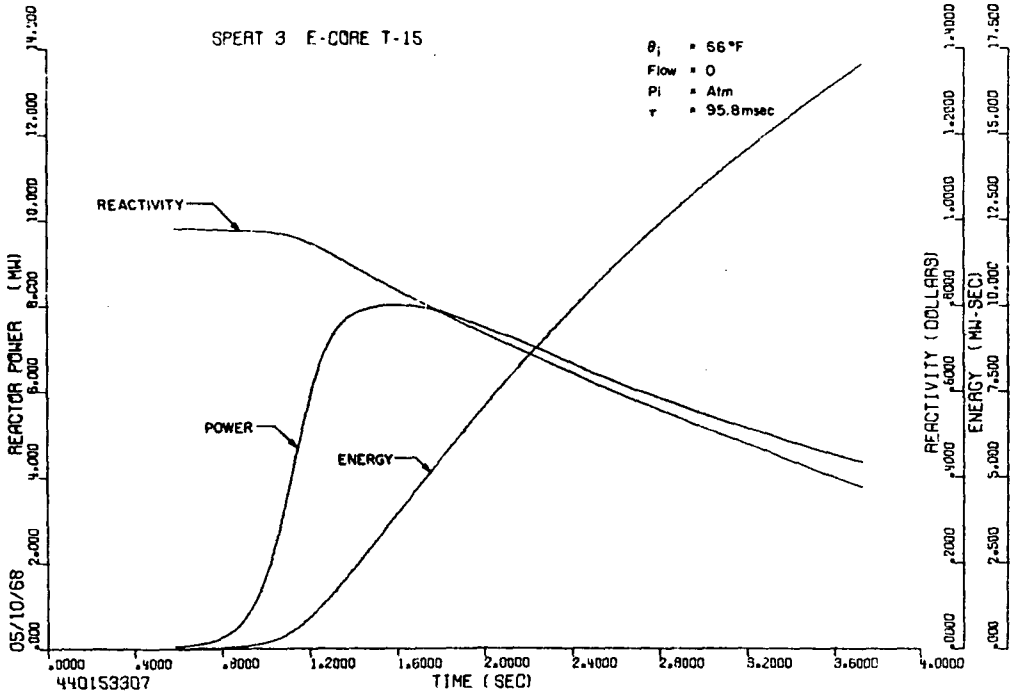

Fig. D-8 Experimental power, energy, and system reactivity for cold-startup test 15 (95.8 msec period, 0.99$ reactivity insertion).

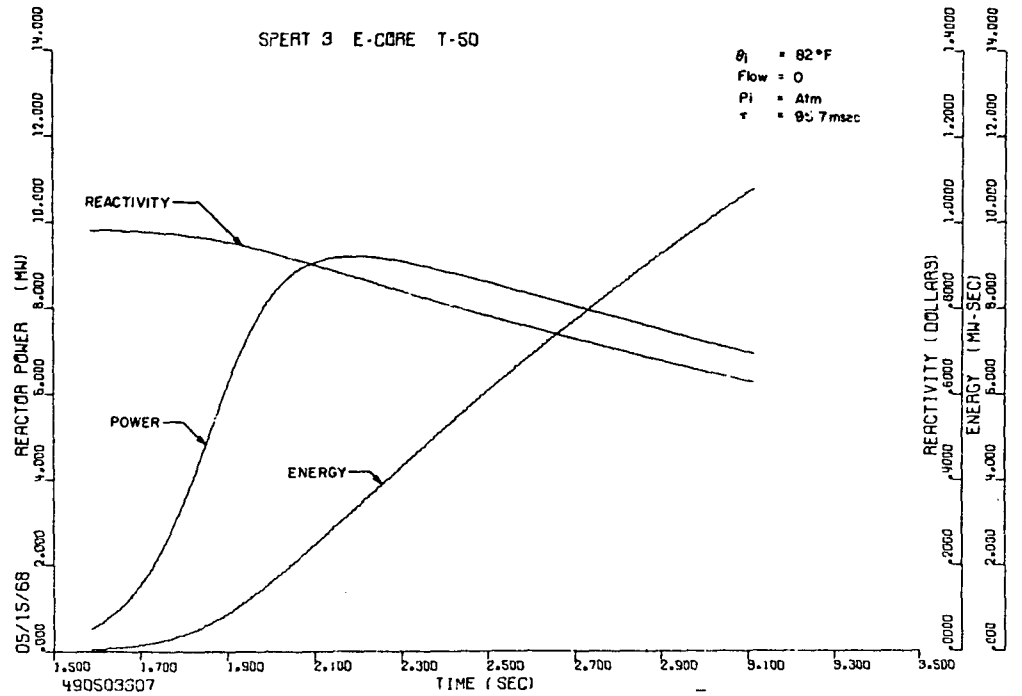

Fig. D-9 Experimental power, energy, and system reactivity for cold-startup test 50 (95.7 msec period, 0.98$ reactivity insertion).

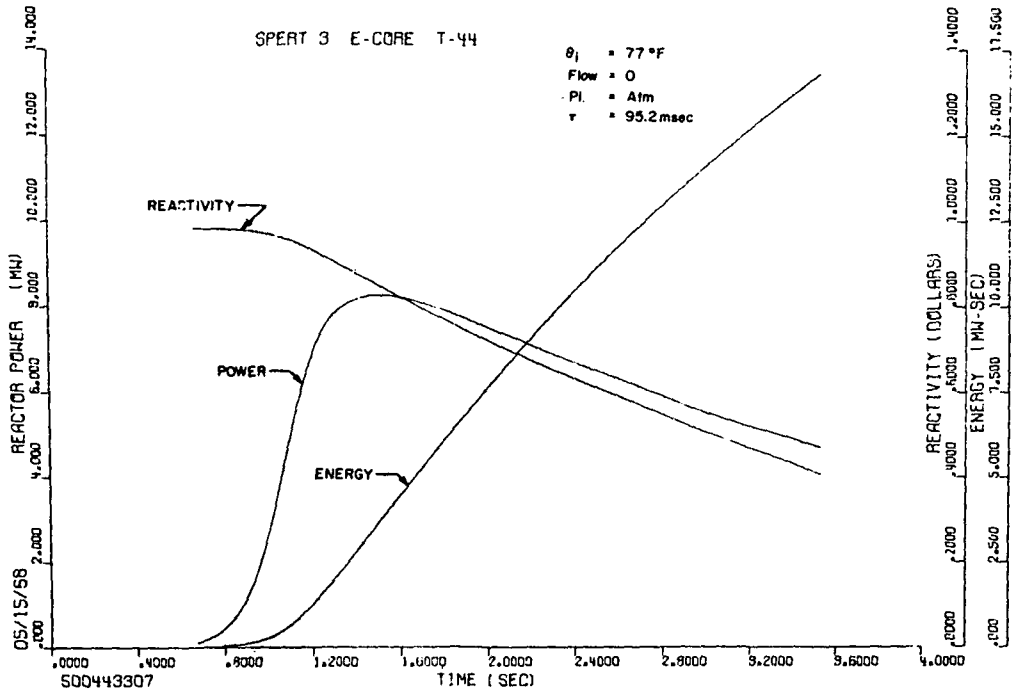

Fig. D-10 Experimental power, energy, and system reactivity for cold-startup test 44 (95.2 msec period, 0.98$ reactivity insertion).

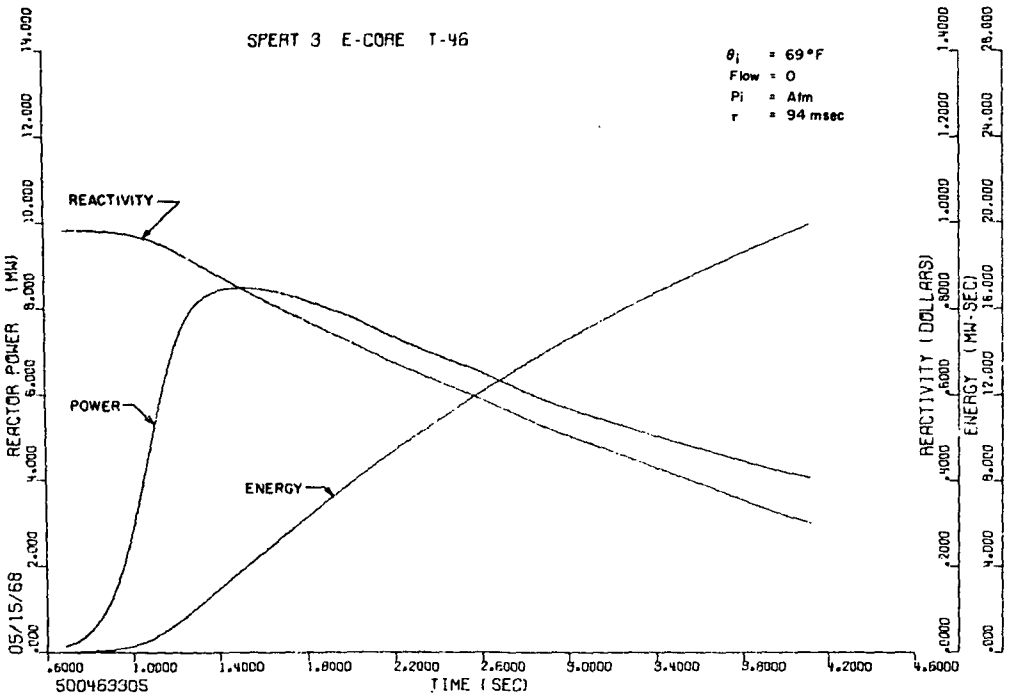

Fig. D-11 Experimental power, energy, and system reactivity for cold-startup test 46 (94 msec period, 0.98$ reactivity insertion).

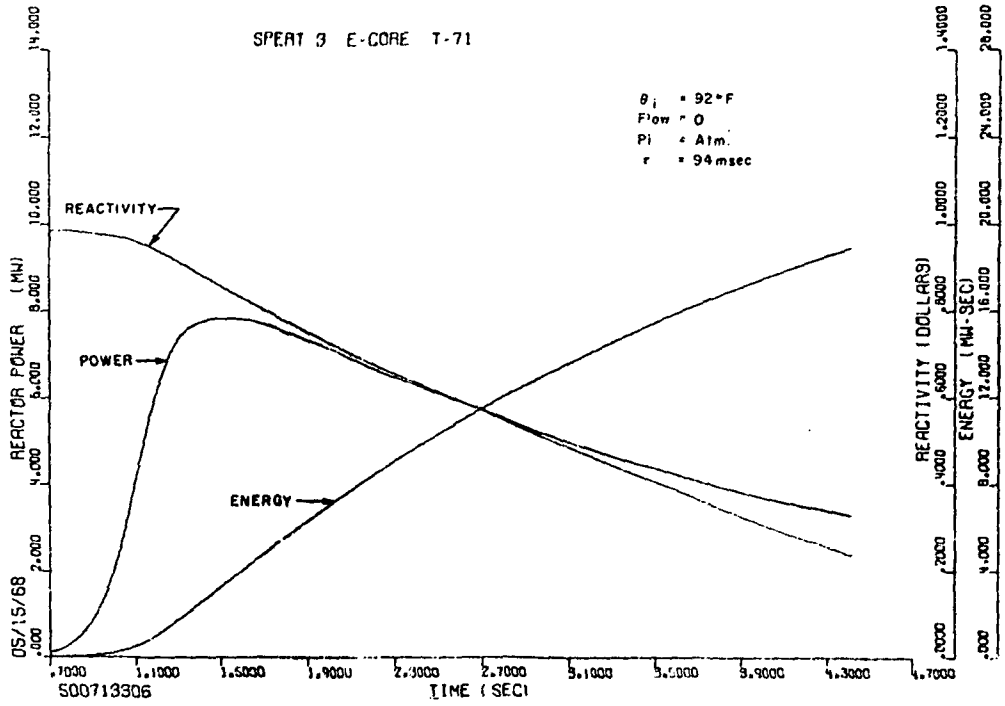

Fig. D-12 Experimental power, energy, and system reactivity for cold-startup test 71 (94 msec period, 0.98$ reactivity insertion).

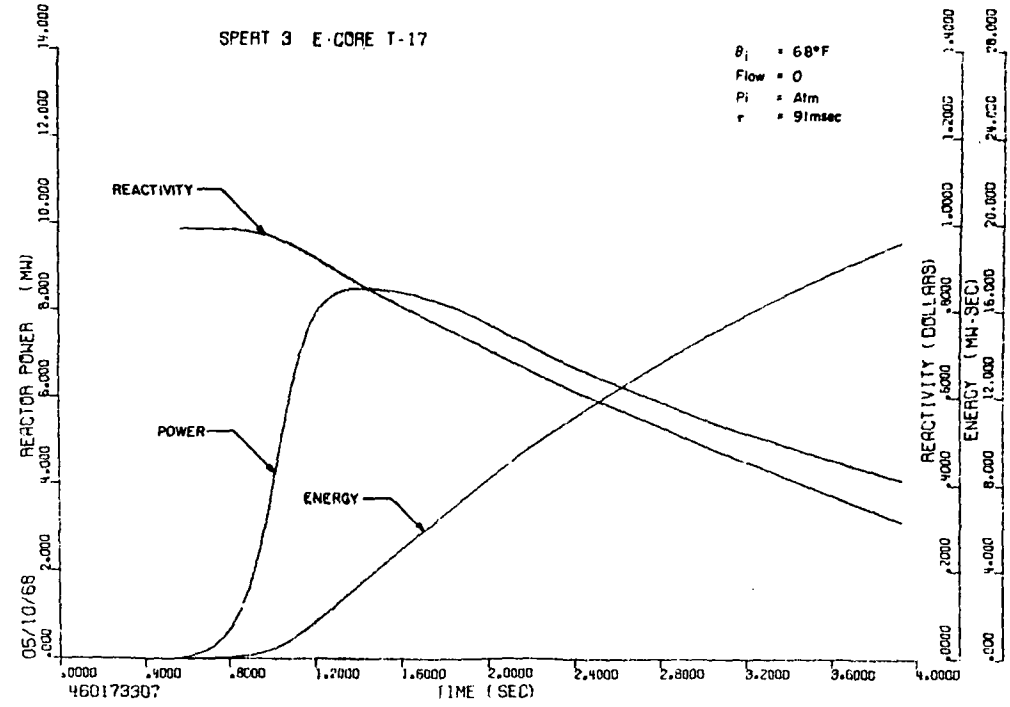

Fig. D-13 Experimental power, energy, and system reactivity for cold-startup test 17 (91 msec period, 0.99$ reactivity insertion).

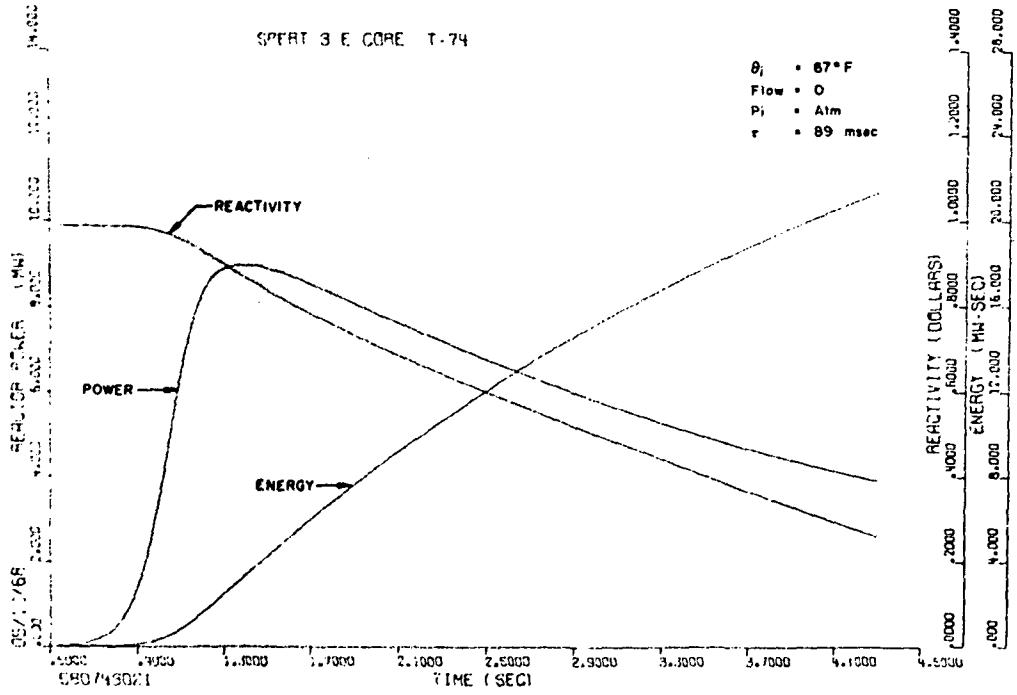

Fig. D-14 Experimental power, energy, and system reactivity for cold-startup test 74 (89 msec period, 0.99$ reactivity insertion).

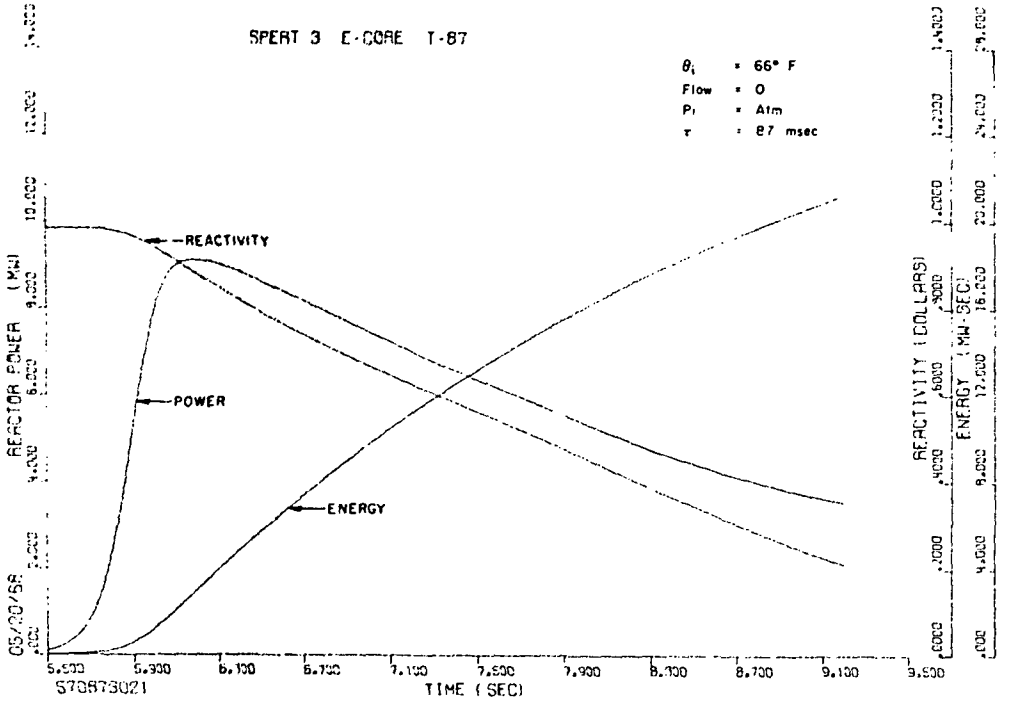

Fig. D-15 Experimental power, energy, and system reactivity for cold-startup test 87 (87 msec period, 0.99$ reactivity insertion).

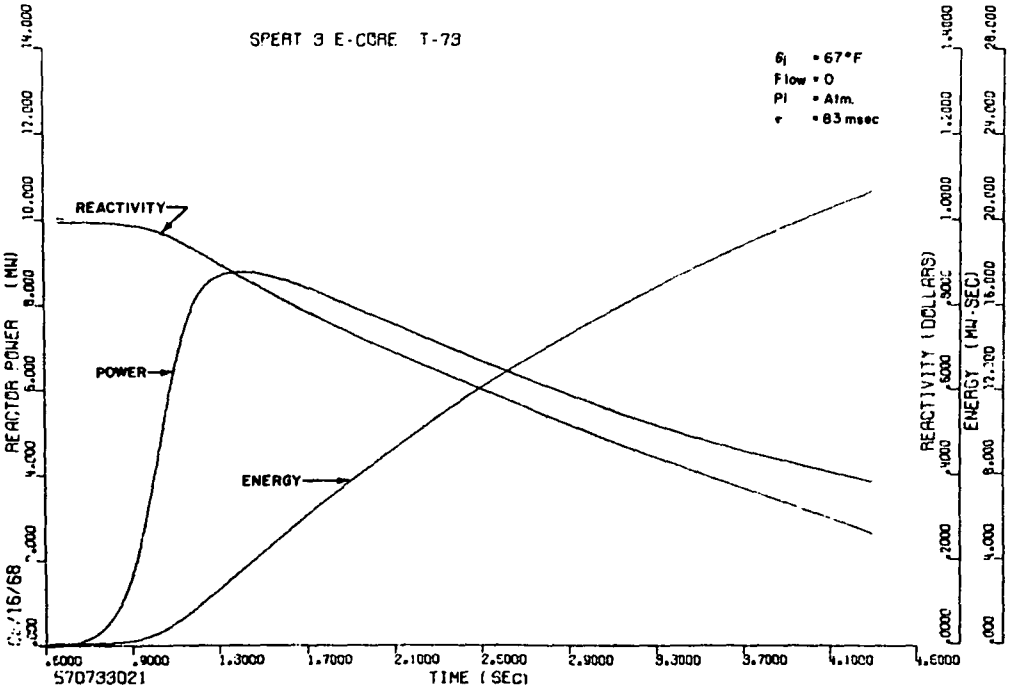

Fig. D-16 Experimental power, energy, and system reactivity for cold-startup test 73 (83 msec period, 0.99$ reactivity insertion).

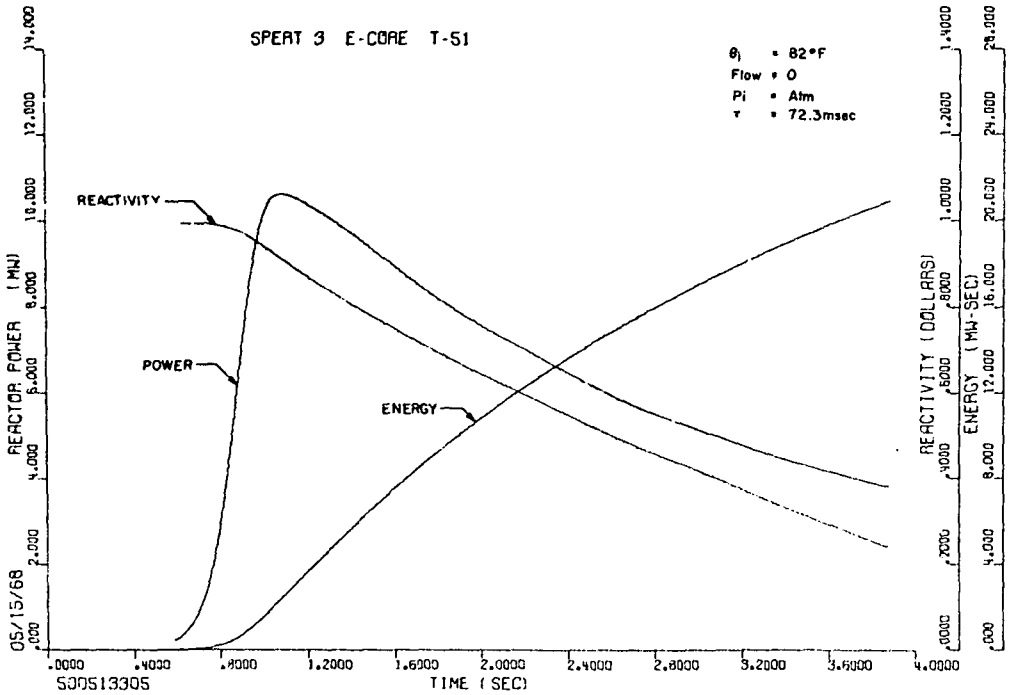

Fig. D-17 Experimental power, energy, and system reactivity for cold-startup test 51 (72.3 msec period, 1.00$ reactivity insertion).

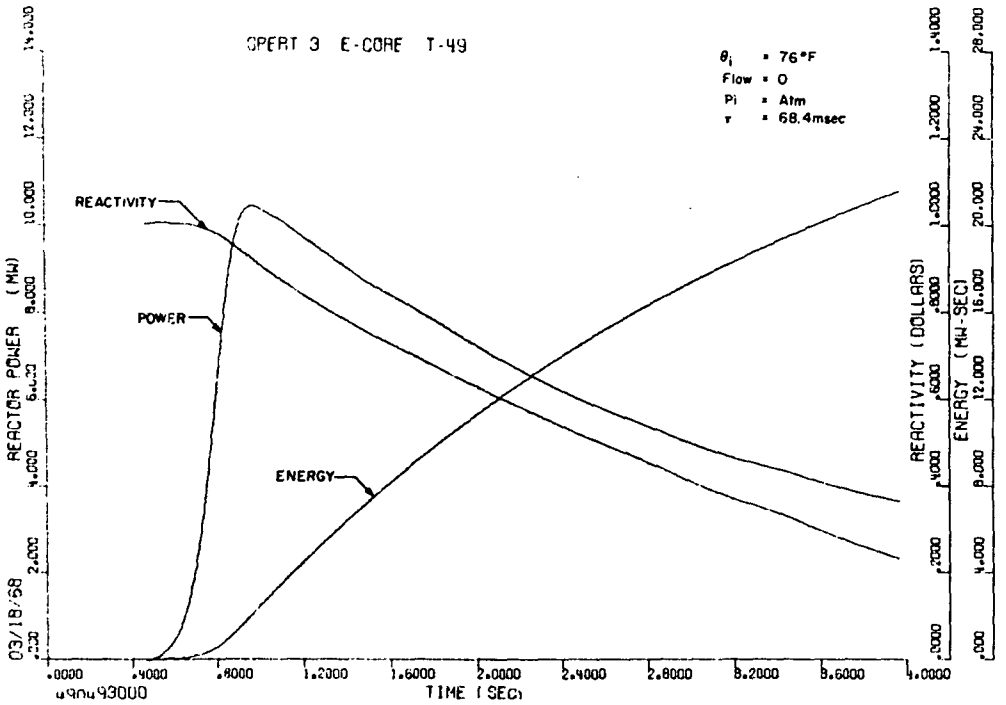

Fig. D-18 Experimental power, energy, and system reactivity for cold-startup test 49 (68.4 msec period, 1.00$ reactivity insertion).

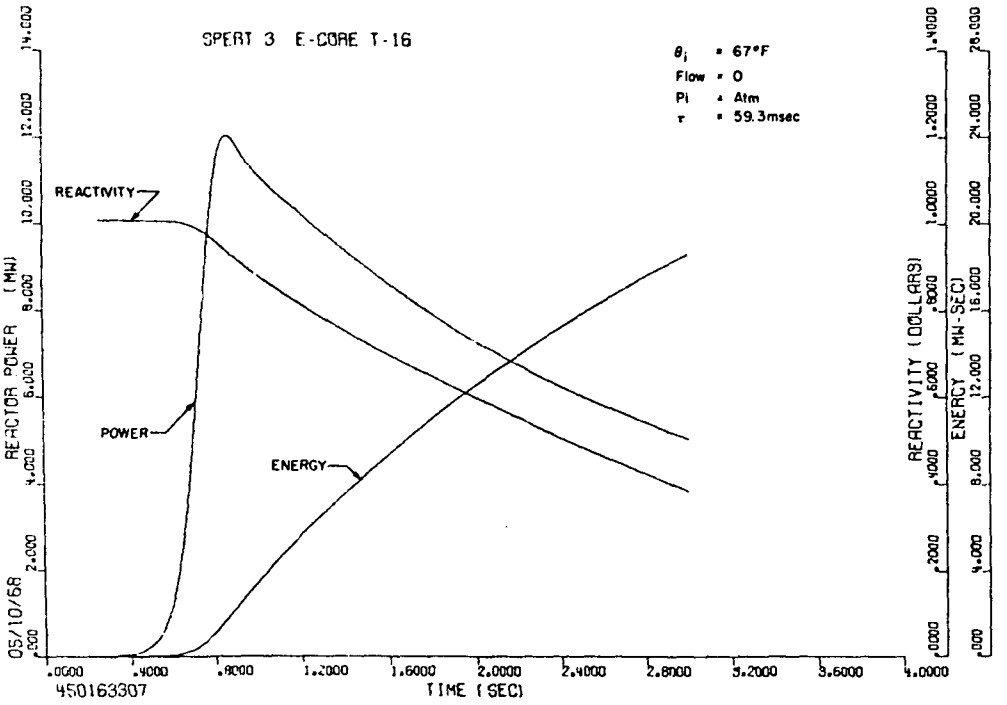

Fig. D-19 Experimental power, energy, and system reactivity for cold-startup test 16 (59.3 msec period, 1.01$ reactivity insertion).

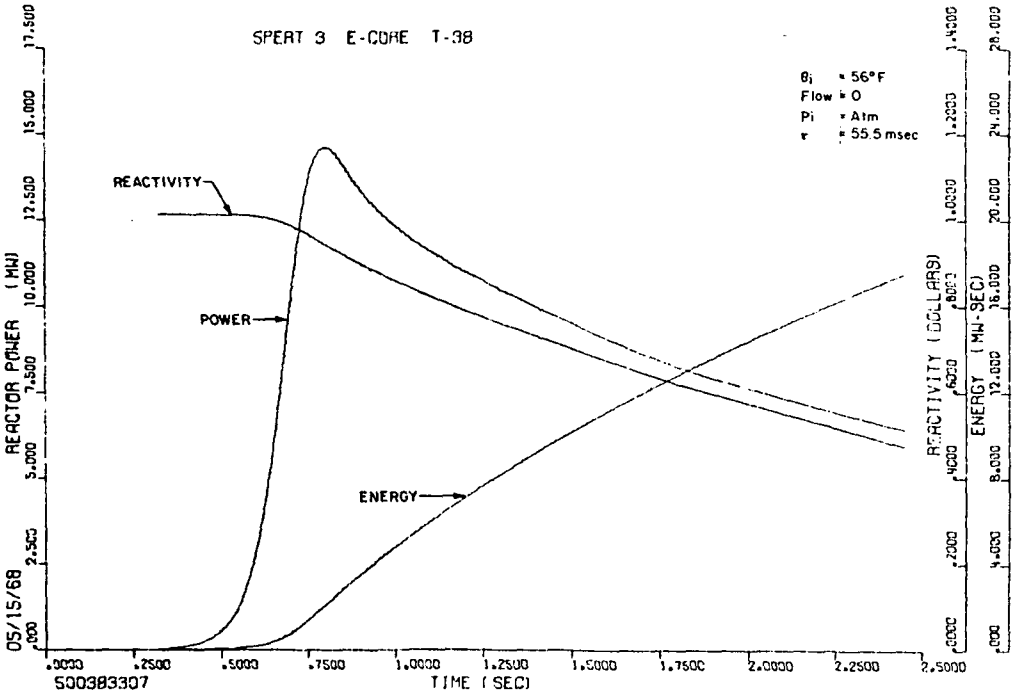

Fig. D-20 Experimental power, energy, and system reactivity for cold-startup test 38 (55.5 msec period, 1.02$ reactivity insertion).

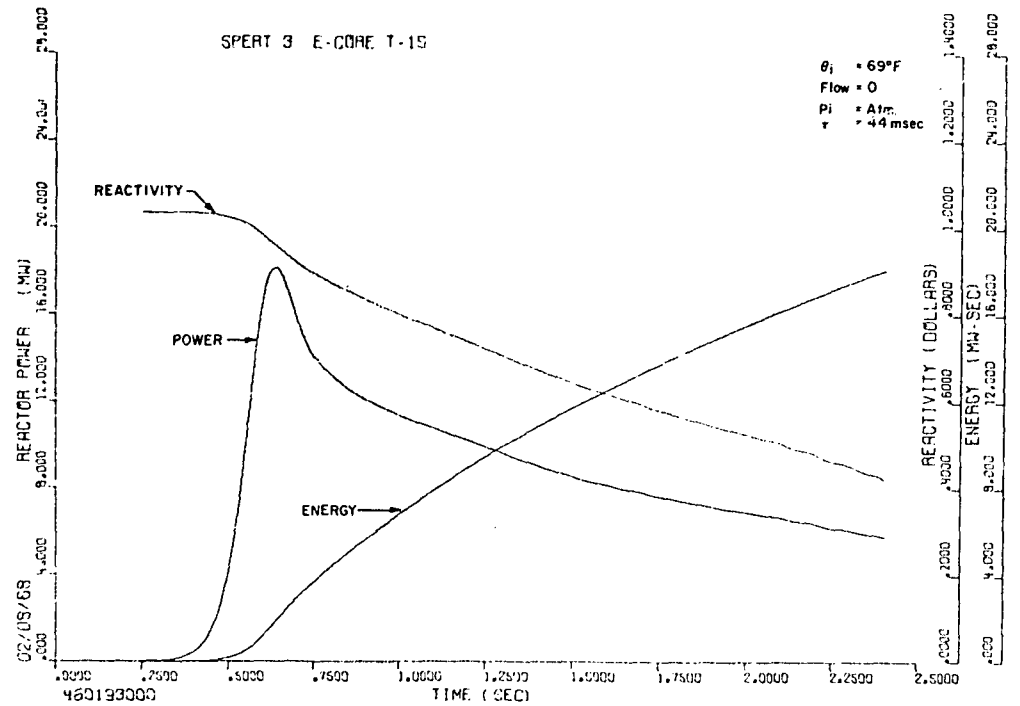

Fig. D-21 Experimental power, energy, and system reactivity for cold-startup test 19 (44 msec period, 1.03$ reactivity insertion).

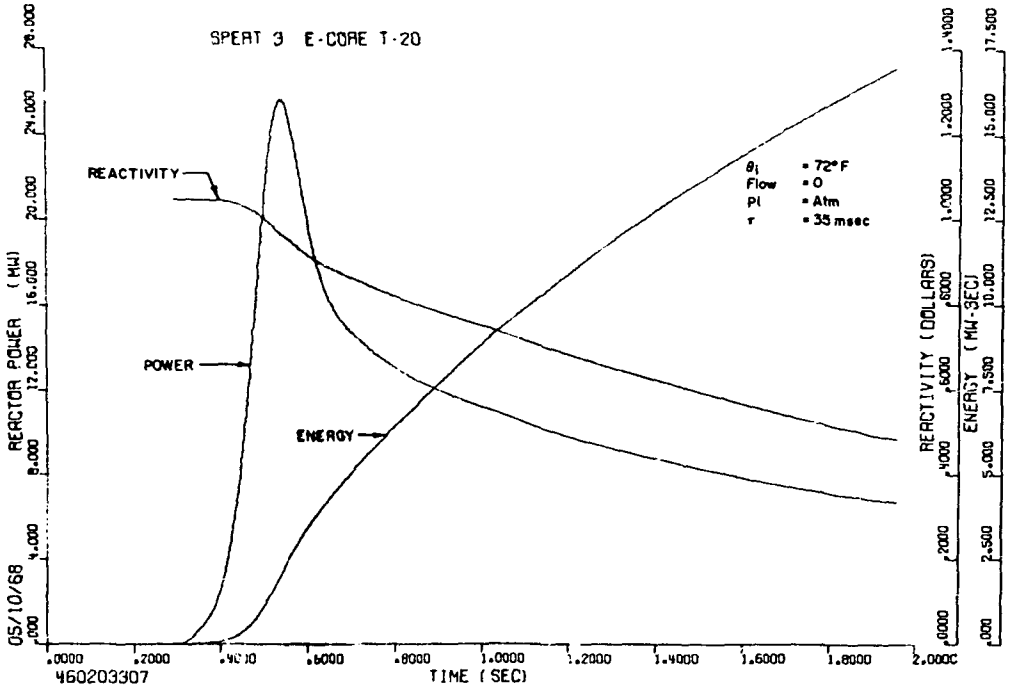

Fig. D-22 Experimental power, energy, and system reactivity for cold-startup test 20 (35 msec period. 1.03$ reactivity insertion).

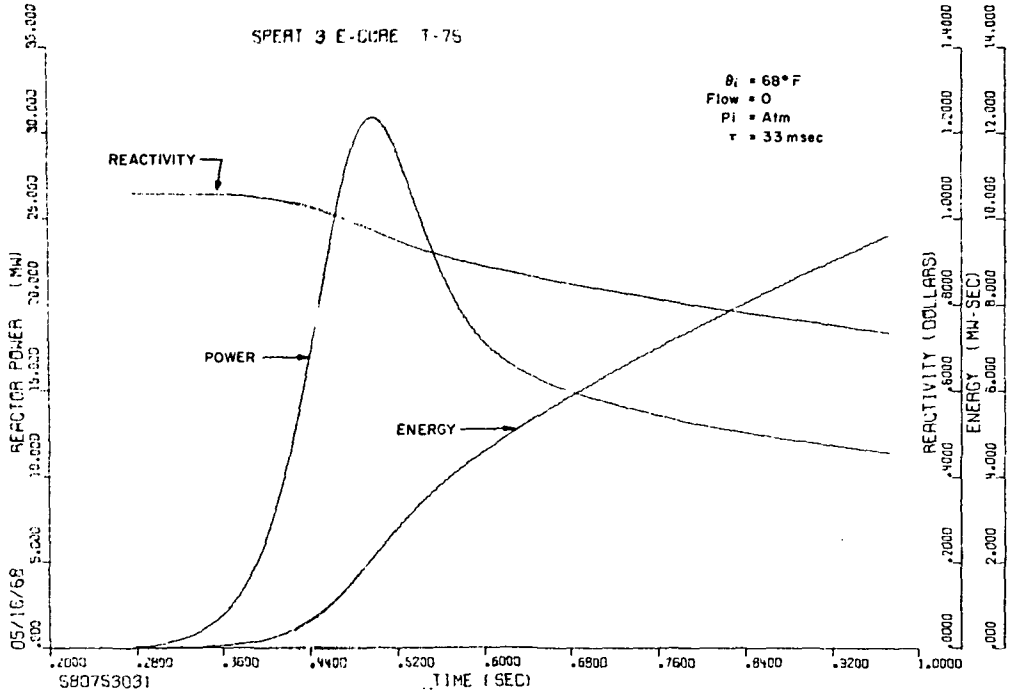

Fig. D-23 Experimental power, energy, and system reactivity for cold-startup test 75 (33 msec period, 1.05$ reactivity insertion).

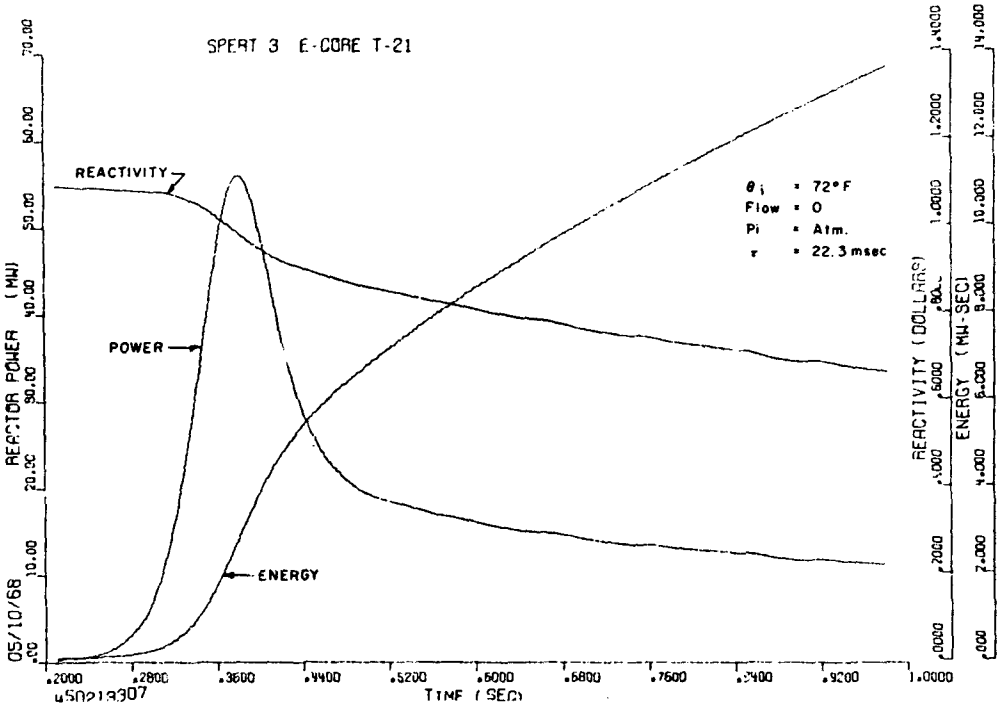

Fig. D-24 Experimental power, energy, and system reactivity for cold-startup test 21 (22.3 msec period, 1.09$ reactivity insertion).

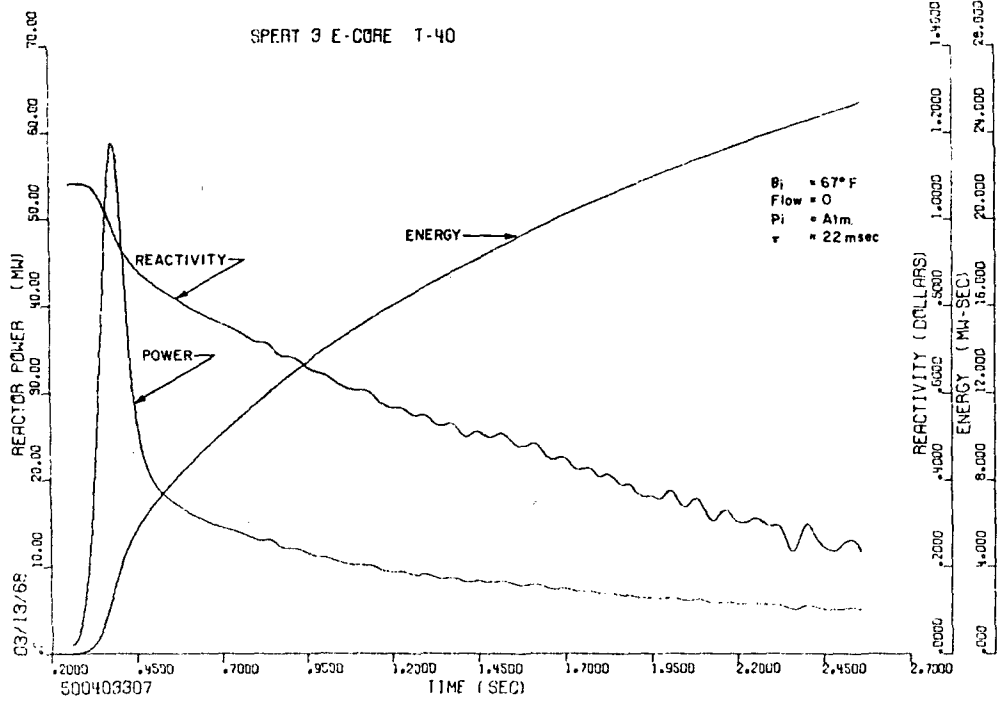

Fig. D-25 Experimental power, energy, and system reactivity for cold-startup test 40 (22 msec period, 1.09$ reactivity insertion).

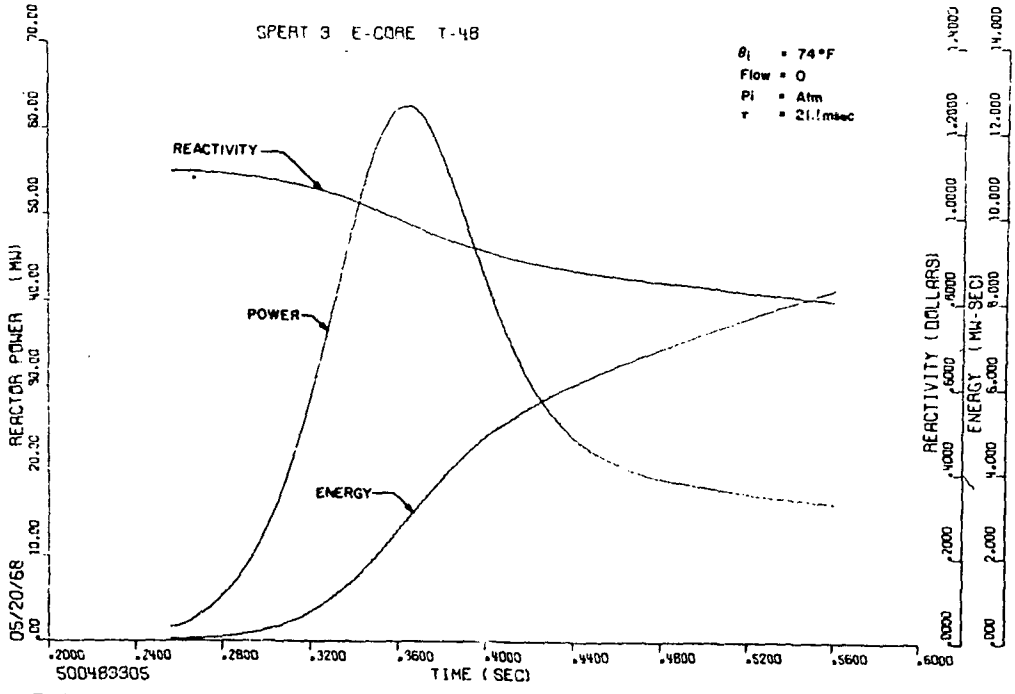

Fig. D-26 Experimental power, energy, and system reactivity for cold-startup test 48 (21.1 msec period, 1.09$ reactivity insertion).

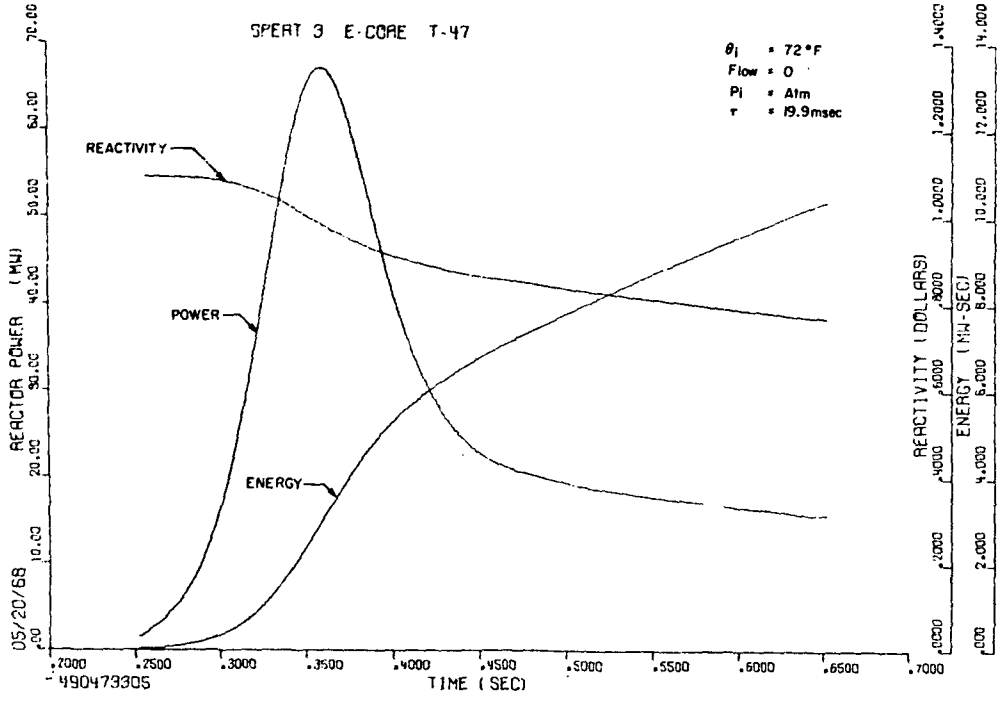

Fig. D-27 Experimental power, energy, and system reactivity for cold-startup test 47 (19.9 msec period, 1.09$ reactivity insertion).

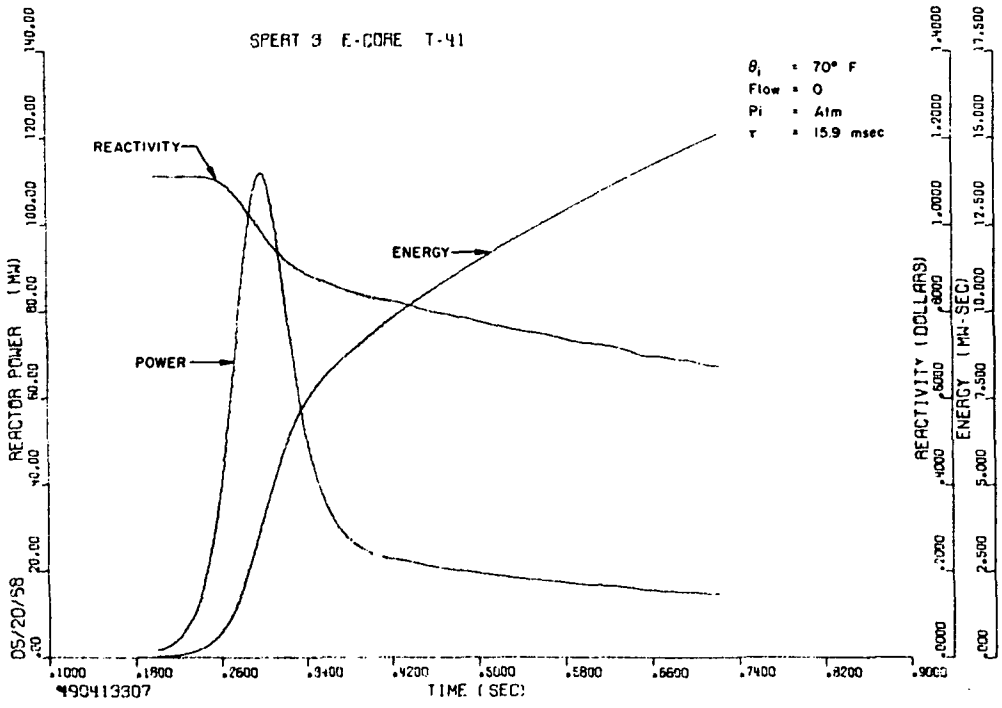

Fig. D-28 Experimental power, energy, and system reactivity for cold-startup test 41 (15.9 msec period, 1.13$ reactivity insertion).

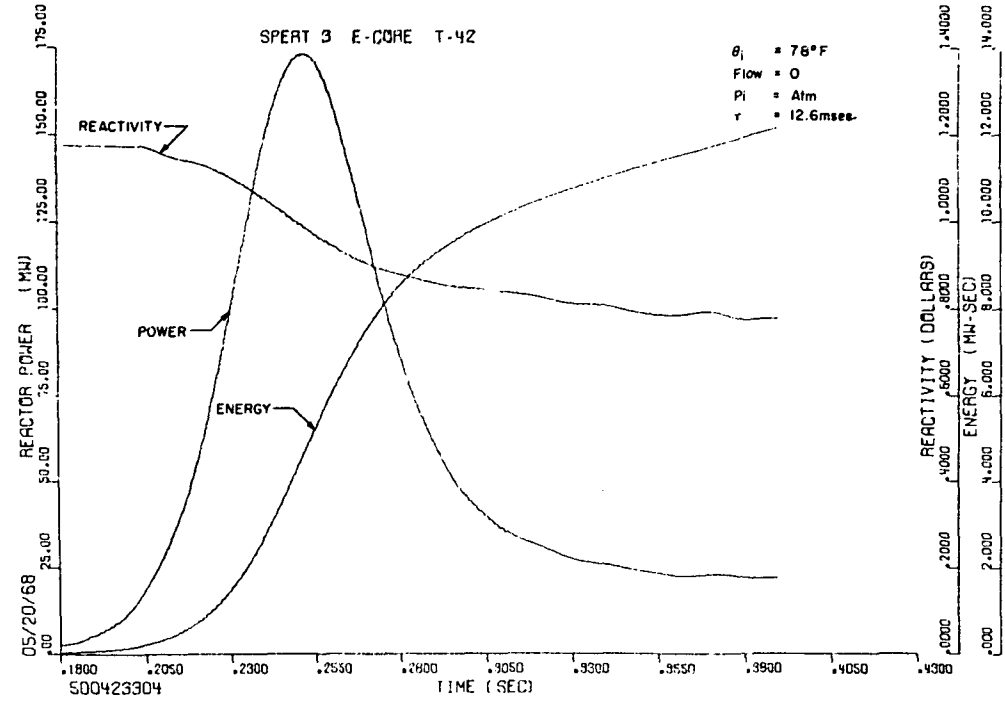

Fig. D-29 Experimental power, energy, and system reactivity for cold-startup test 42 (12.6 msec period, 1.17$ reactivity insertion).

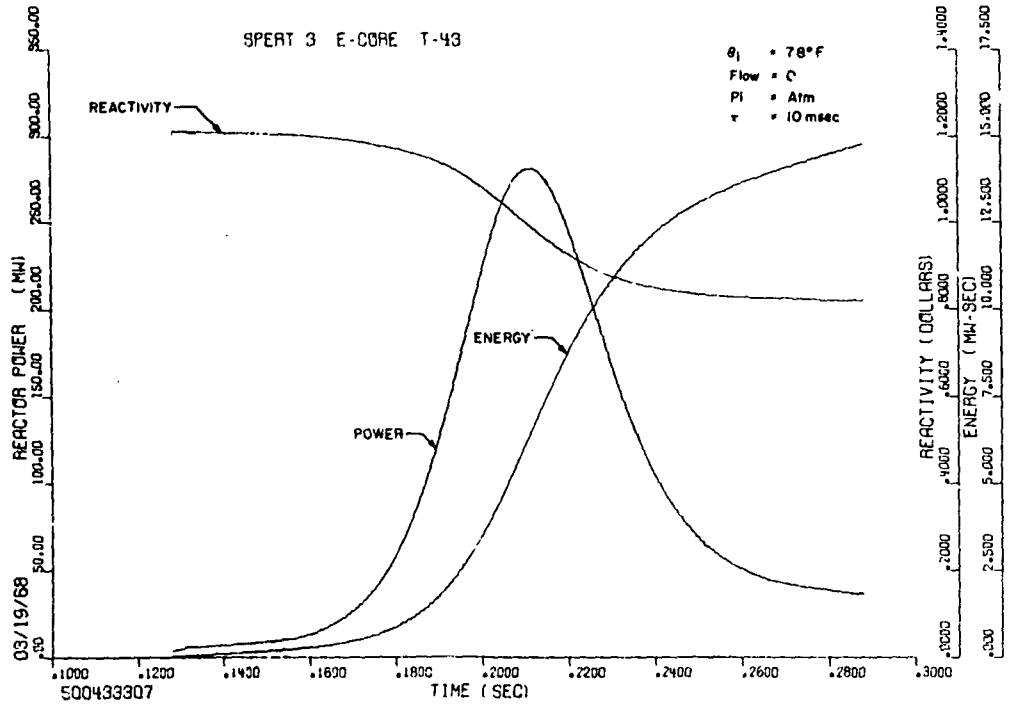

Fig. D-30 Experimental power, energy, and system reactivity for cold-startup test 43 (10 msec period, 1.21$ reactivity insertion).

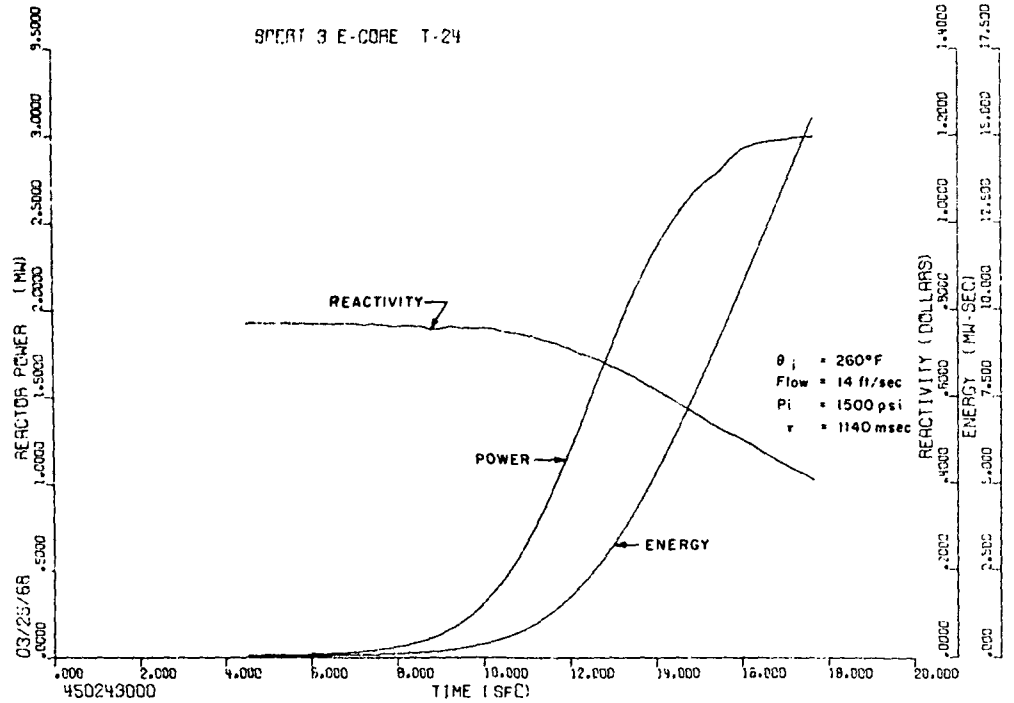

Fig. D-31 Experimental power, energy, and system reactivity for 260°F hot-startup test 24 (1140 msec period, 0.75$ reactivity insertion).

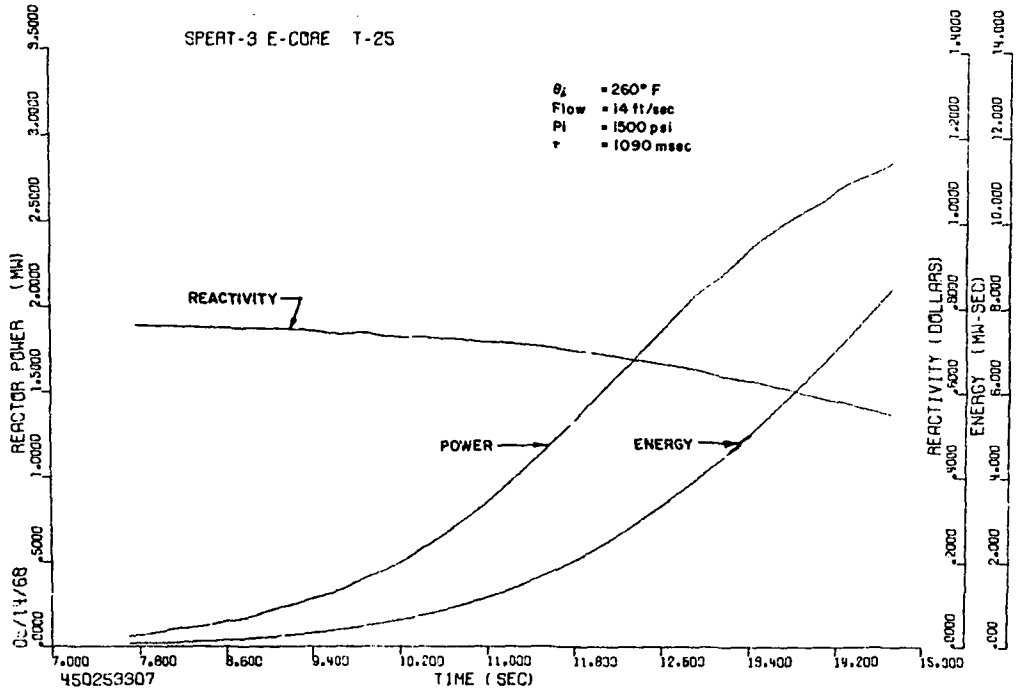

Fig. D-32 Experimental power, energy, and system reactivity for 260°F hot-startup test 25 (1090 msec period, 0.76$ reactivity insertion).

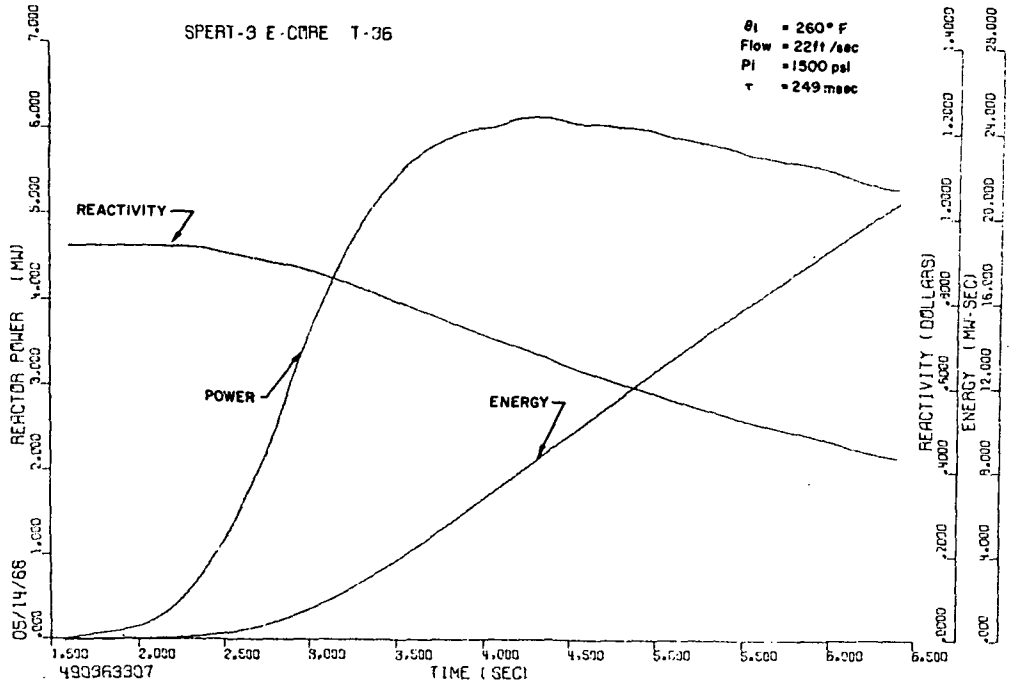

Fig. D-33 Experimental power, energy, and system reactivity for 260°F hot-startup test 36 (249 msec period, 0.92$ reactivity insertion).

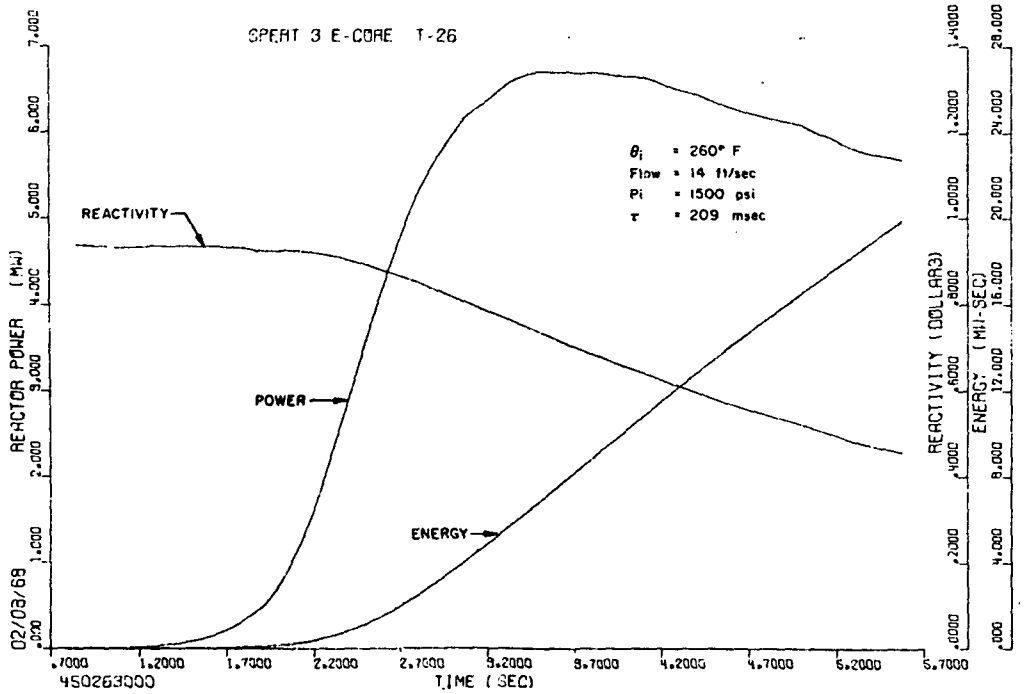

Fig. D-34 Experimental power, energy, and system reactivity for 260°F hot-startup test 26 (209 msec period, 0.93$ reactivity insertion).

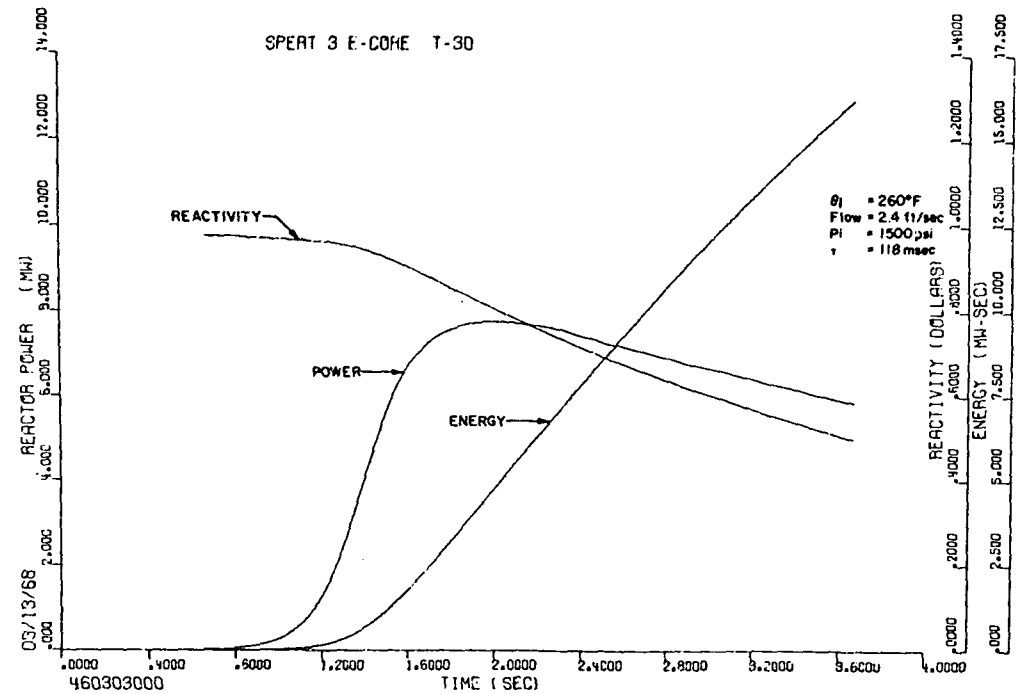

Fig. D-35 Experimental power, energy, and system reactivity for 260°F hot-startup test 30 (118 msec period, 0.97$ reactivity insertion).

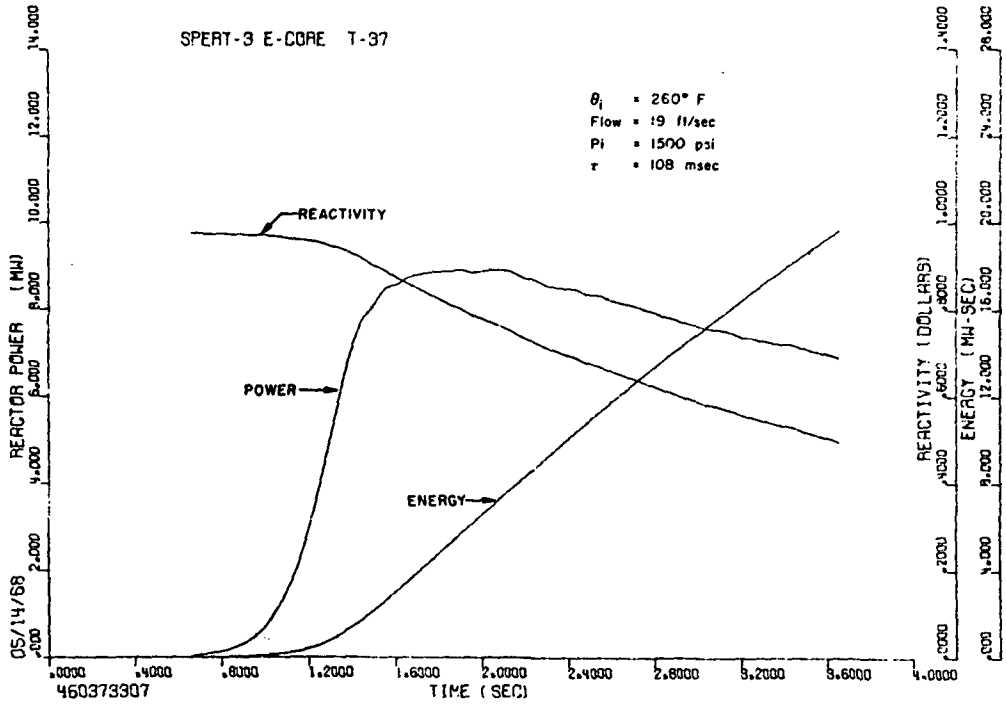

Fig. D-36 Experimental power, energy, and system reactivity for 260°F hot-startup test 37 (108 msec period, 0.98$ reactivity insertion).

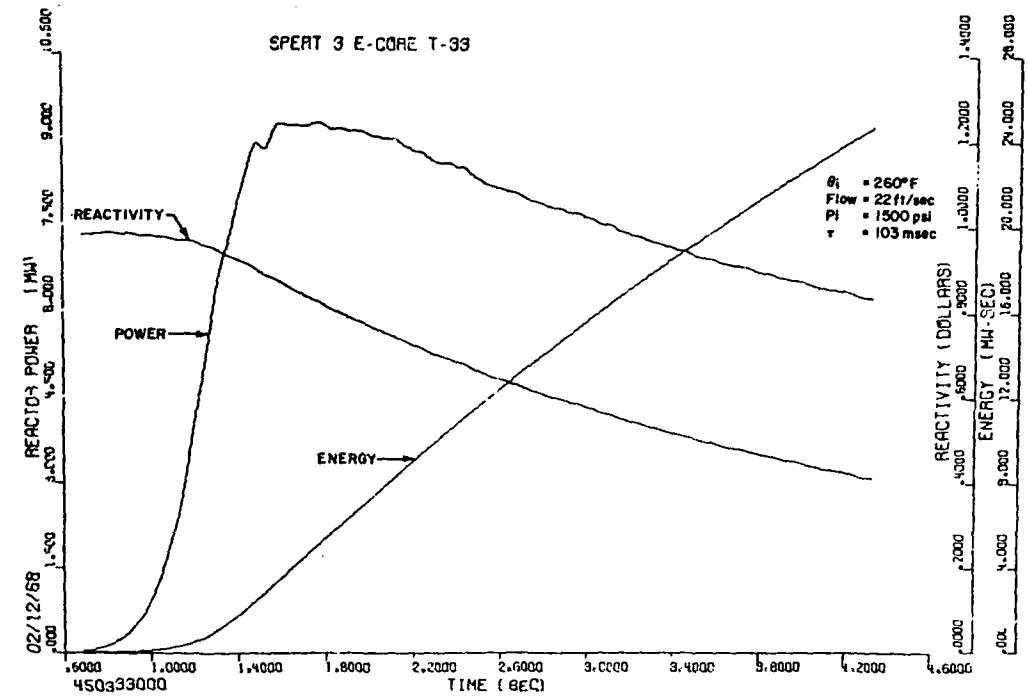

Fig. D-37 Experimental power, energy, and system reactivity for 260°F hot-startup test 33 (103 msec period, 0.98$ reactivity insertion).

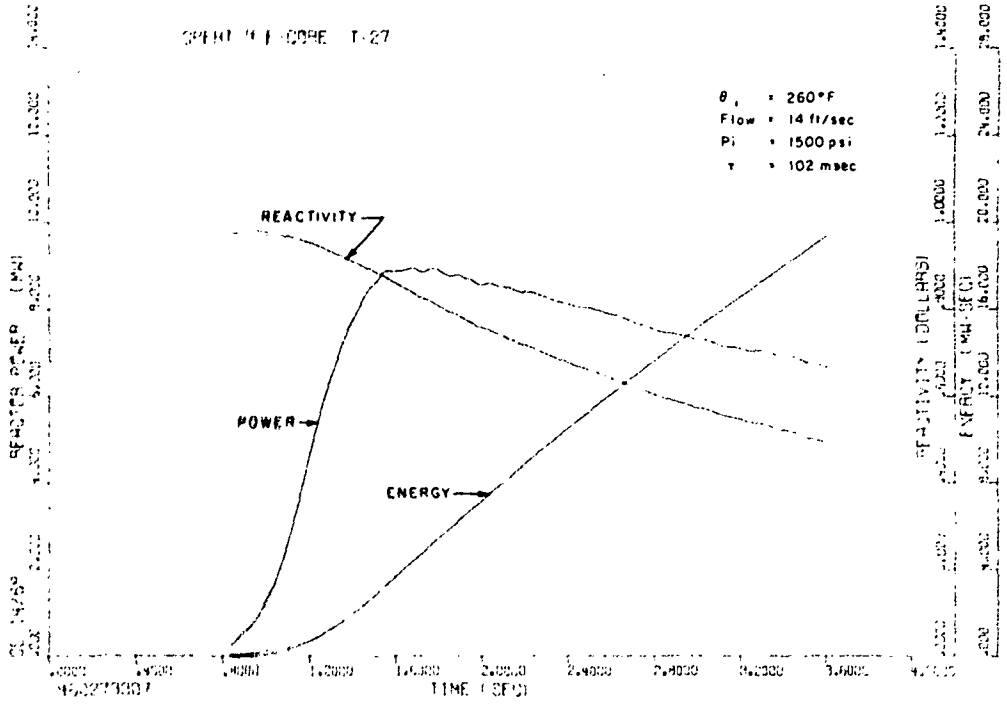

Fig. D-38 Experimental power, energy, and system reactivity for 260°F hot-startup test 27 (102 msec period, 0.98$ reactivity insertion).

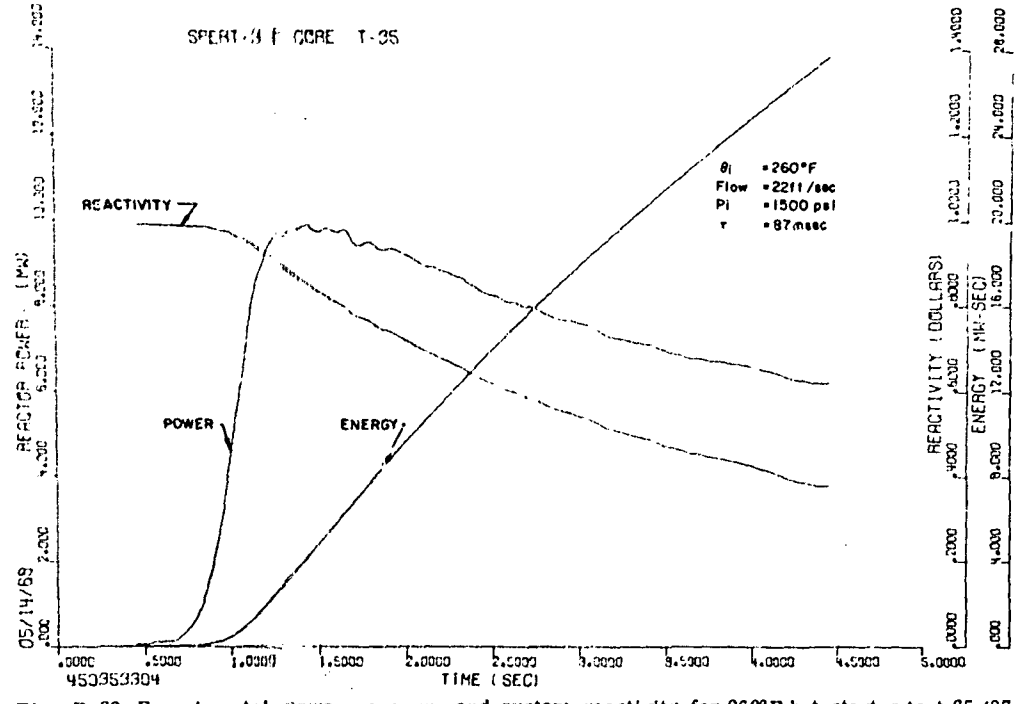

Fig. D-39 Experimental power, energy, and system reactivity for 260°F hot-startup test 35 (87 msec period, 0.99$ reactivity insertion).

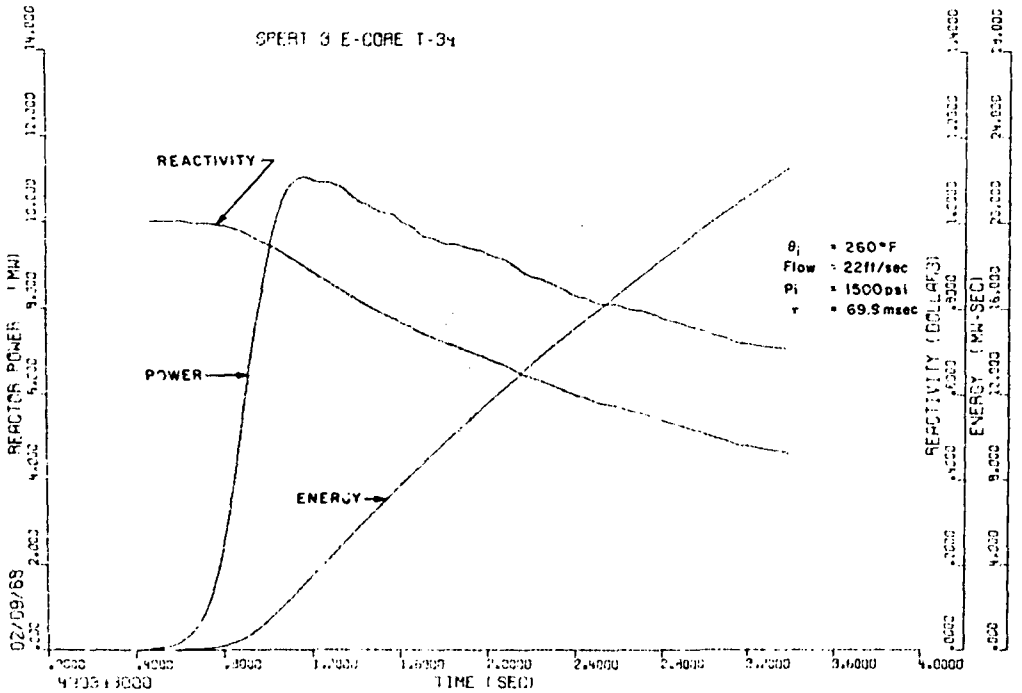

Fig. D-40 Experimental power, energy, and system reactivity for 260°F hot-startup test 34 (69.9 msec period, 1.00$ reactivity insertion).

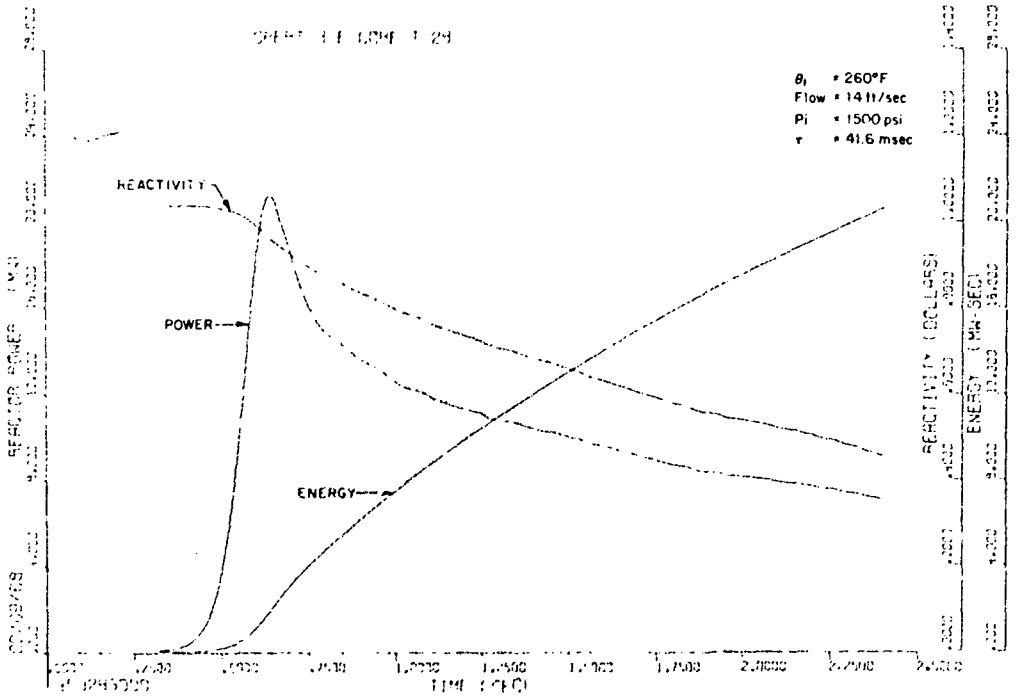

Fig. D-41 Experimental power, energy, and system reactivity for 260°F hot-startup test 28 (41.6 msec period, 1.03$ reactivity insertion).

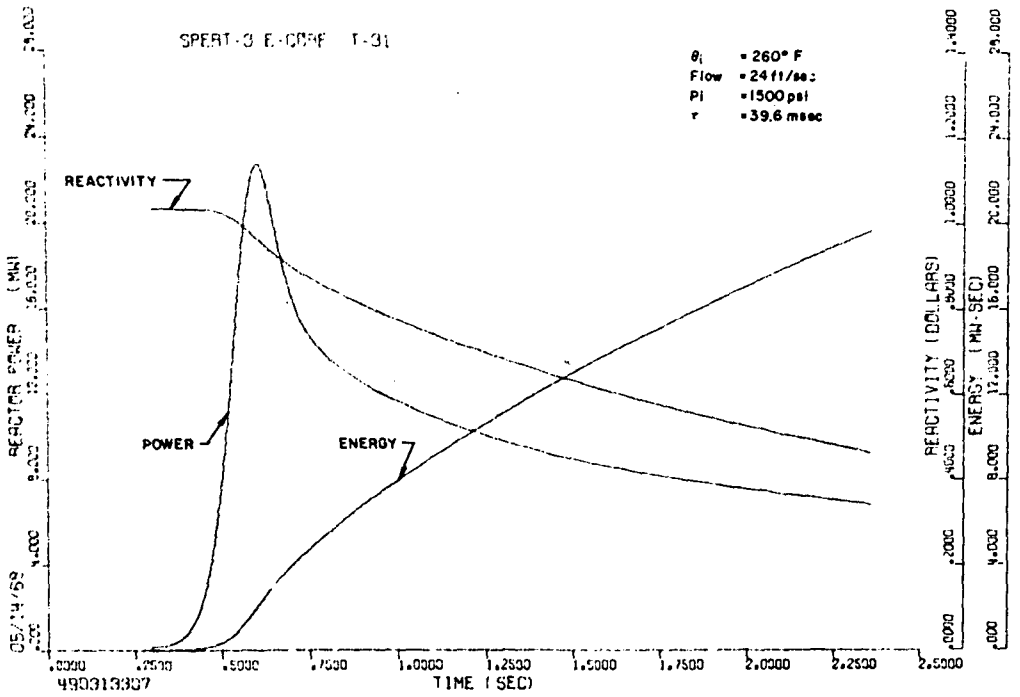

Fig. D-42 Experimental power, energy, and system reactivity for 260°F hot-startup test 31 (39.6 msec period, 1.04$ reactivity insertion).

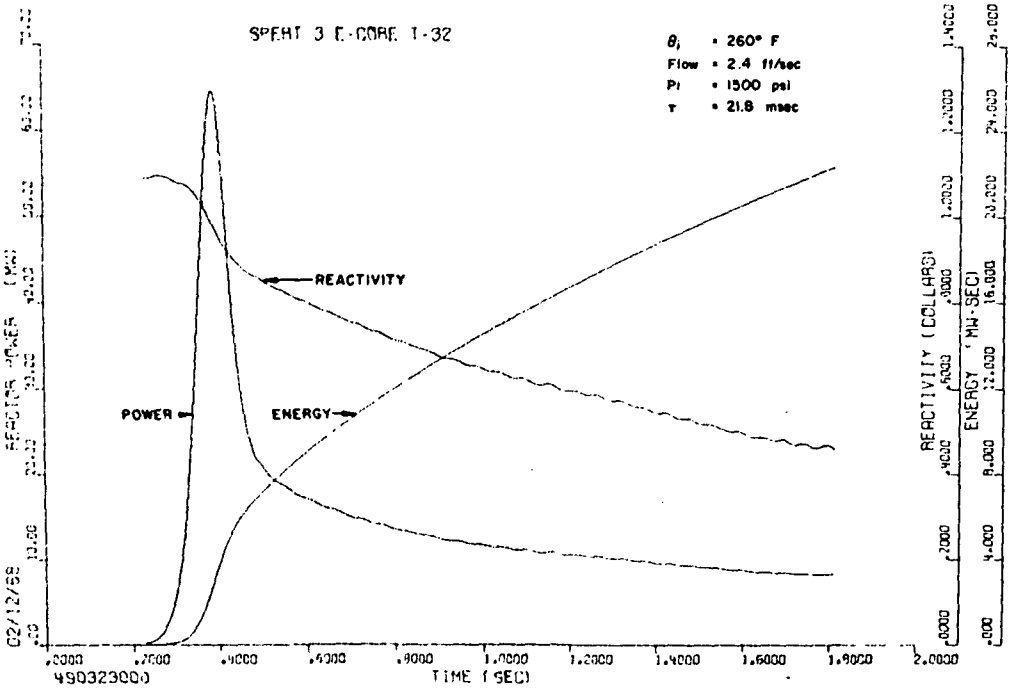

Fig. D-43 Experimental power, energy, and system reactivity for 260°F hot-startup test 32 (21.8 msec period, 1.09$ reactivity insertion).

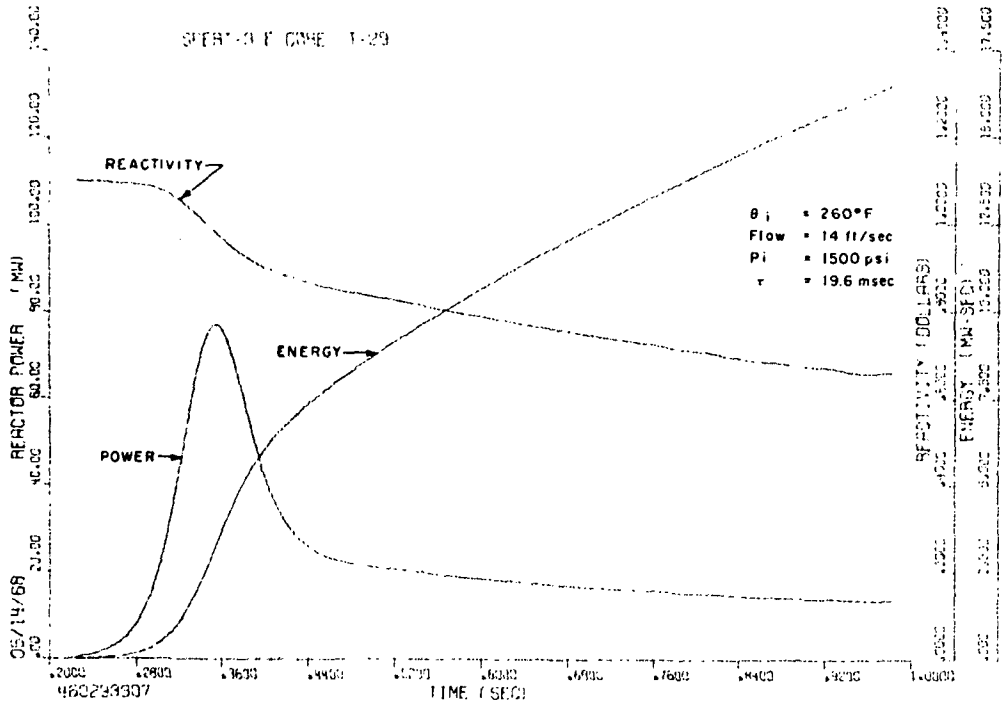

Fig. D-44 Experimental power, energy, and system reactivity for 260°F hot-startup test 29 (19.6 msec period, 1.10$ reactivity insertion).

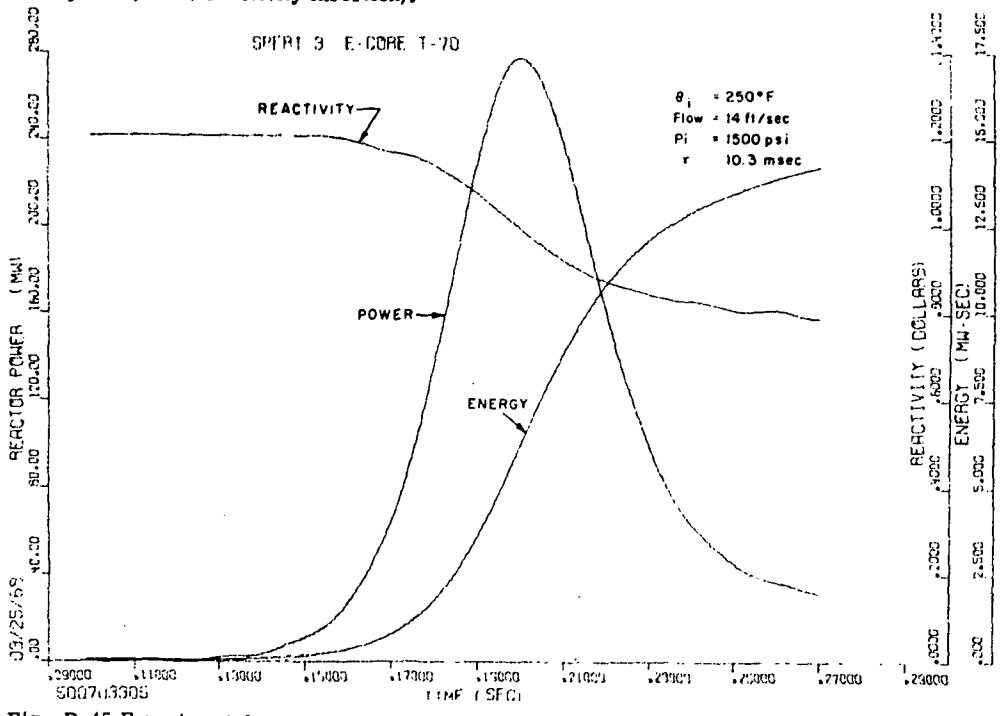

Fig. D-45 Experimental power, energy, and system reactivity for 250°F hot-startup test 70 (10.3 msec period, 1.21$ reactivity insertion).

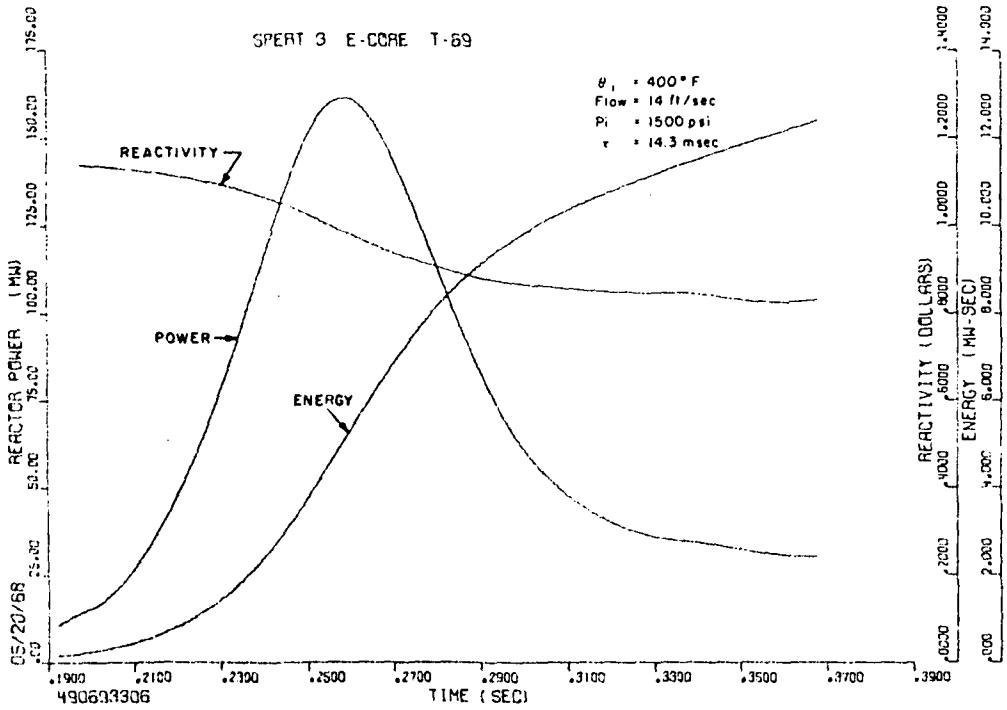

Fig. D-46 Experimental power, energy, and system reactivity for 400°F hot-startup test 69 (14.3 msec period, 1.15$ reactivity insertion).

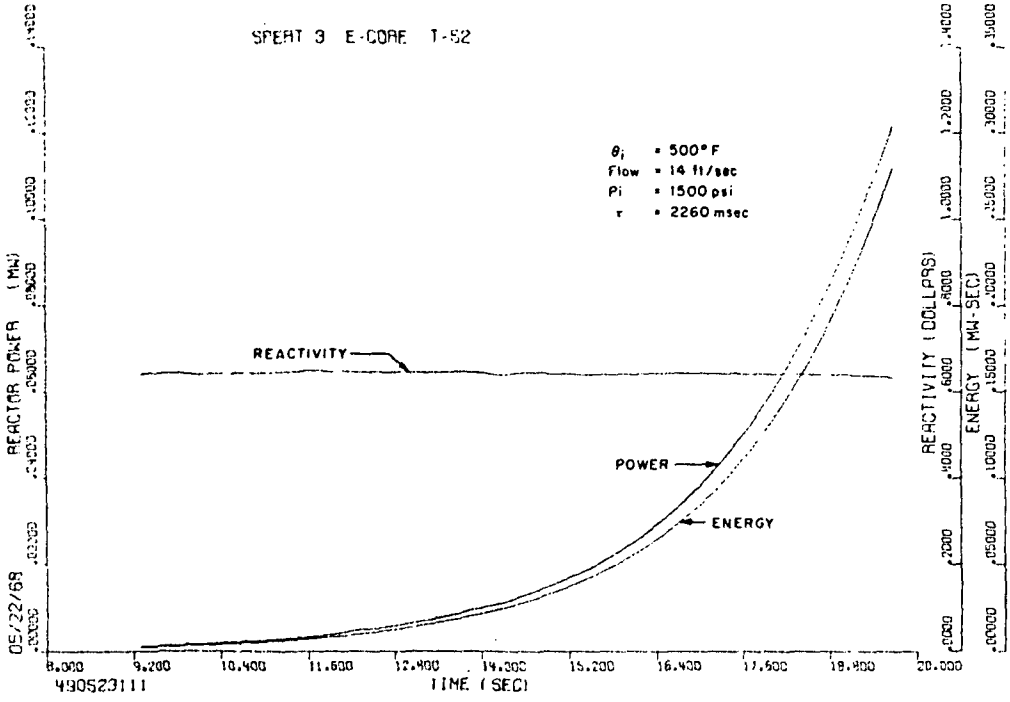

Fig. D-47 Experimental power, energy, and system reactivity for 500°F hot-startup test 52 (2260 msec period, 0.64$ reactivity insertion).

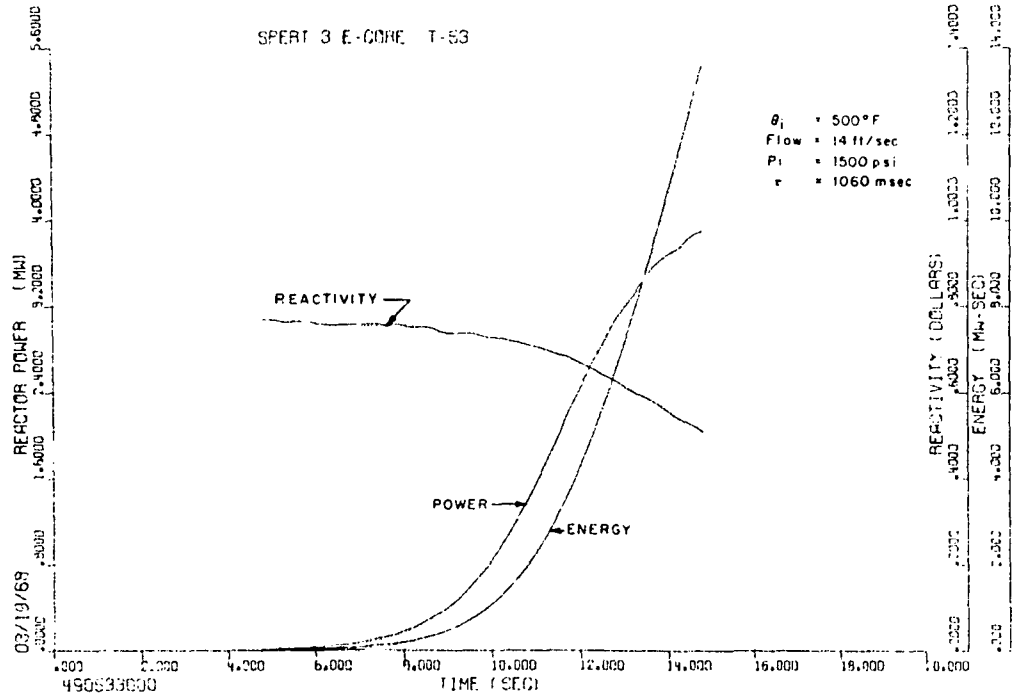

Fig. D-48 Experimental power, energy, and system reactivity for 500°F hot-startup test 53 (1060 msec period, 0.77$ reactivity insertion).

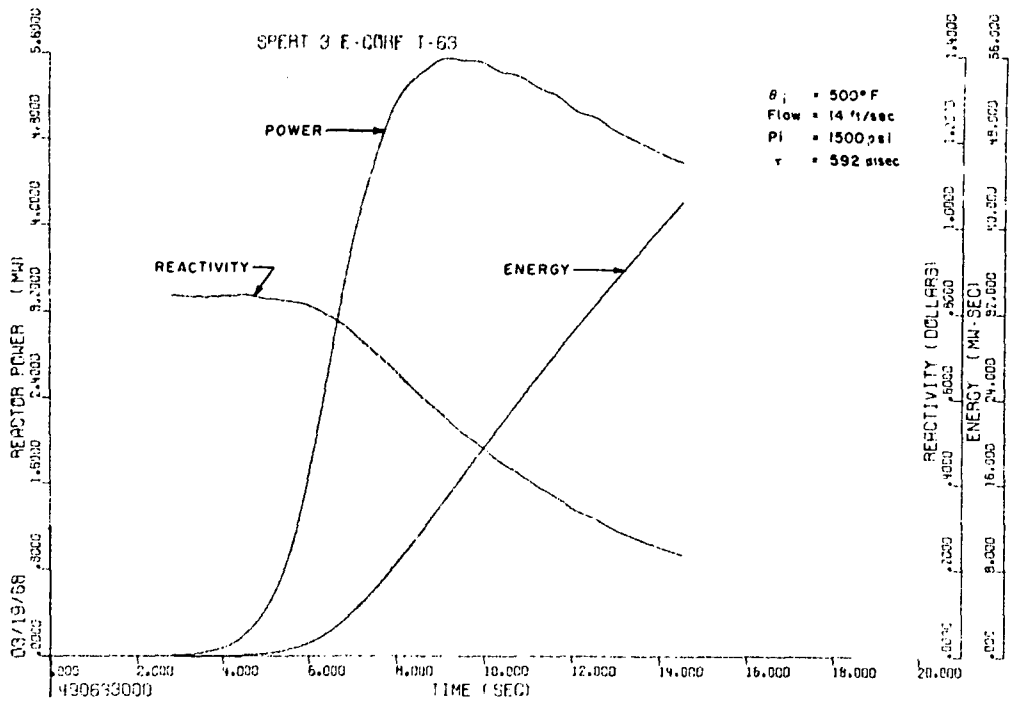

Fig. D-49 Experimental power, energy, and system reactivity for 500°F hot-startup test 63 (592 msec period, 0.84$ reactivity insertion).

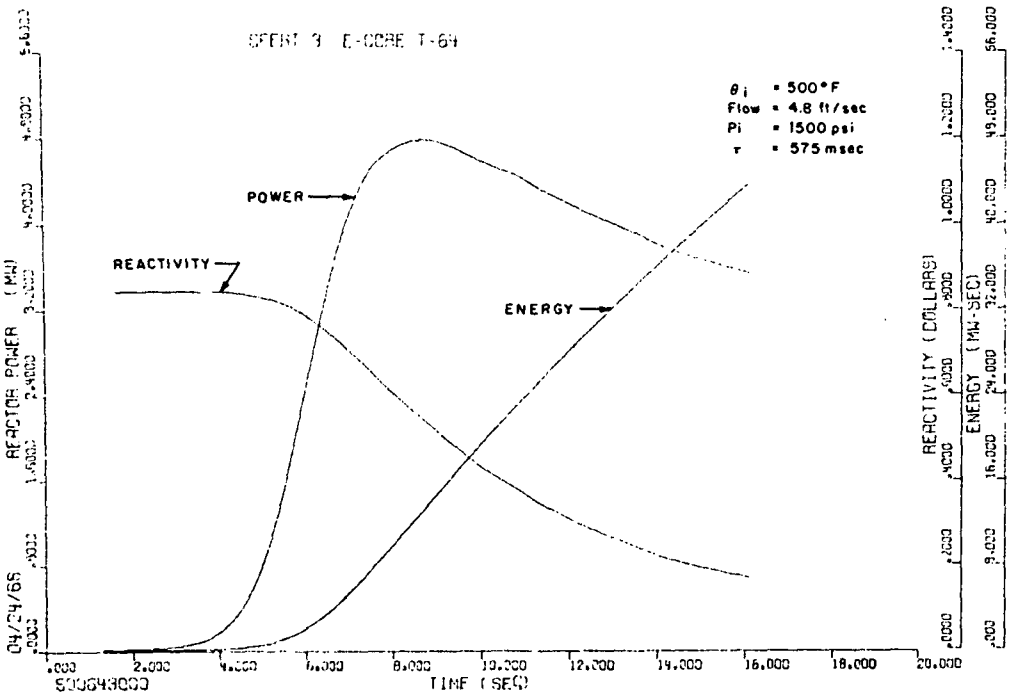

Fig. D-50 Experimental power, energy, and system reactivity for 500°F hot-startup test 64 (575 msec period, 0.82$ reactivity insertion).

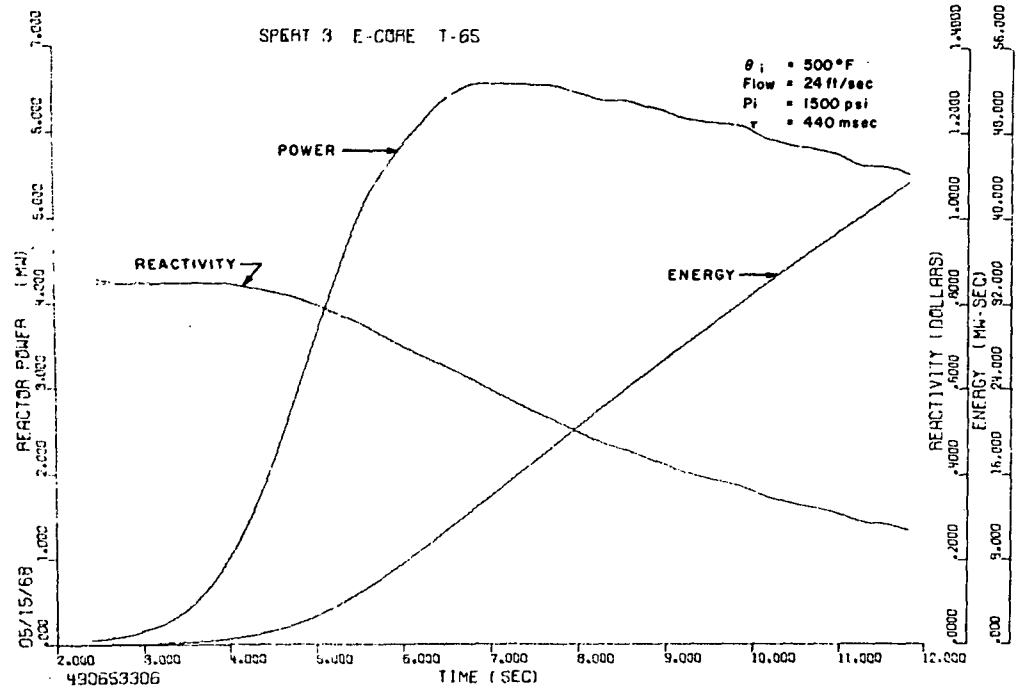

Fig. D-51 Experimental power, energy, and system reactivity for 500°F hot-startup test 65 (440 msec period, 0.87$ reactivity insertion).

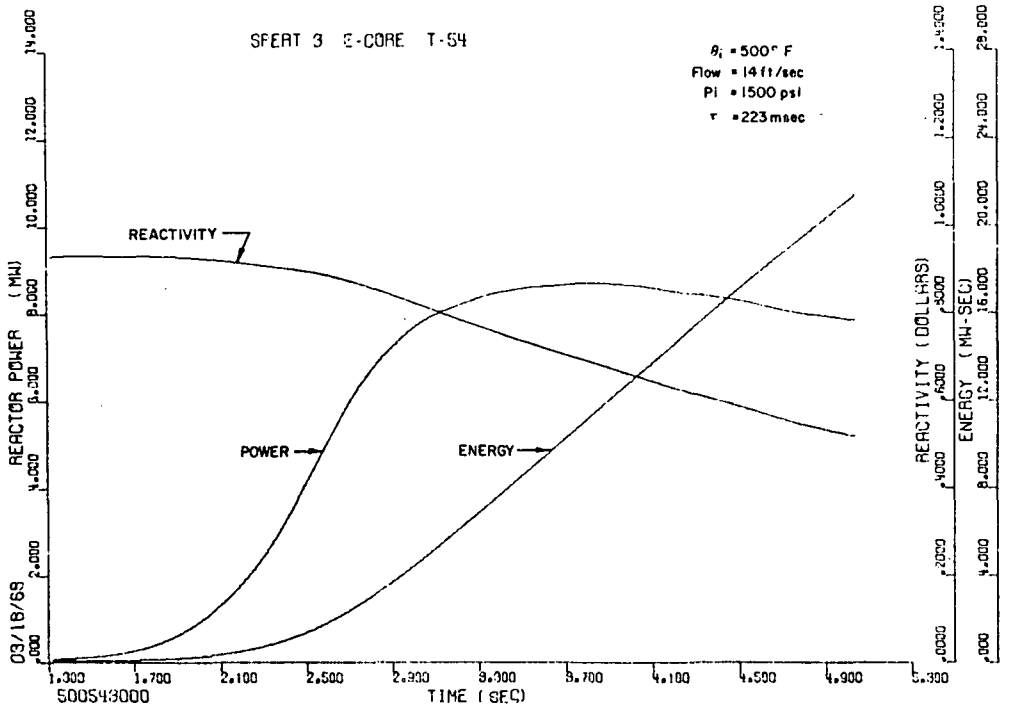

Fig. D-52 Experimental power, energy, and system reactivity for 500°F hot-startup test 54 (223 msec period, 0.93$ reactivity insertion).

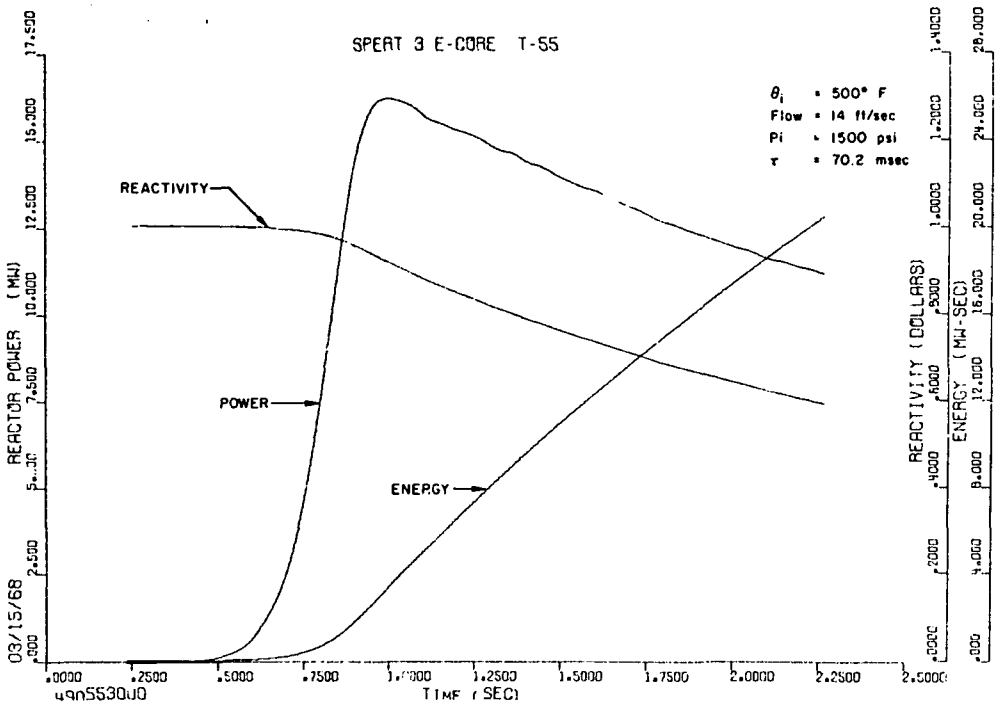

Fig. D-53 Experimental power, energy, and system reactivity for 500°F hot-startup test 55 (70.2 msec period, 1.00$ reactivity insertion).

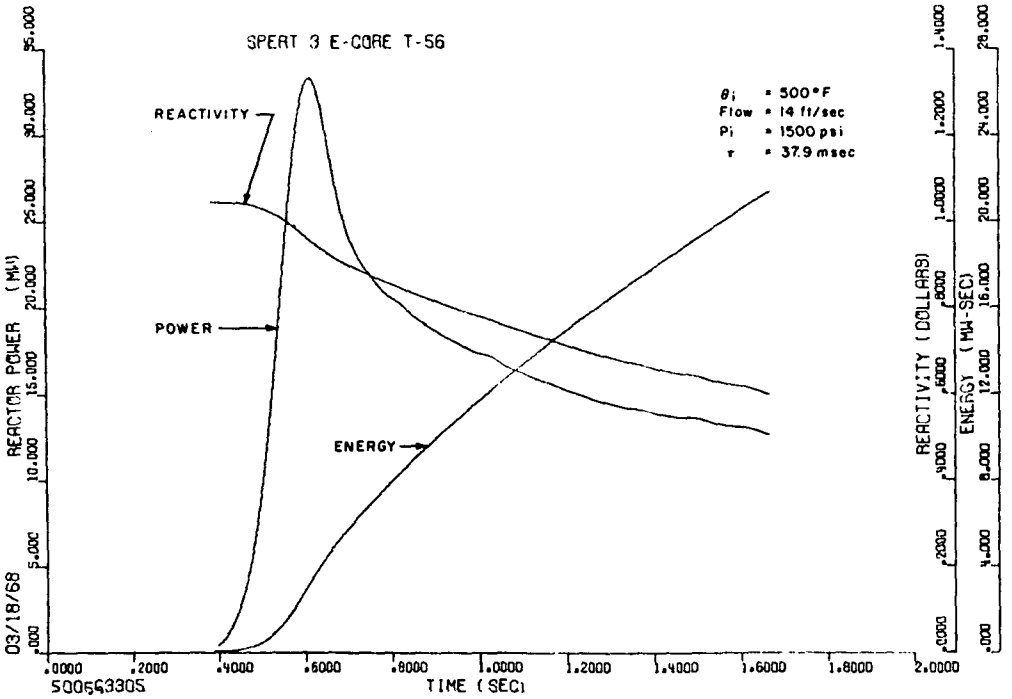

Fig. D-54 Experimental power, energy, and system reactivity for 500°F hot-startup test 56 (37.9 msec period, 1.04$ reactivity insertion).

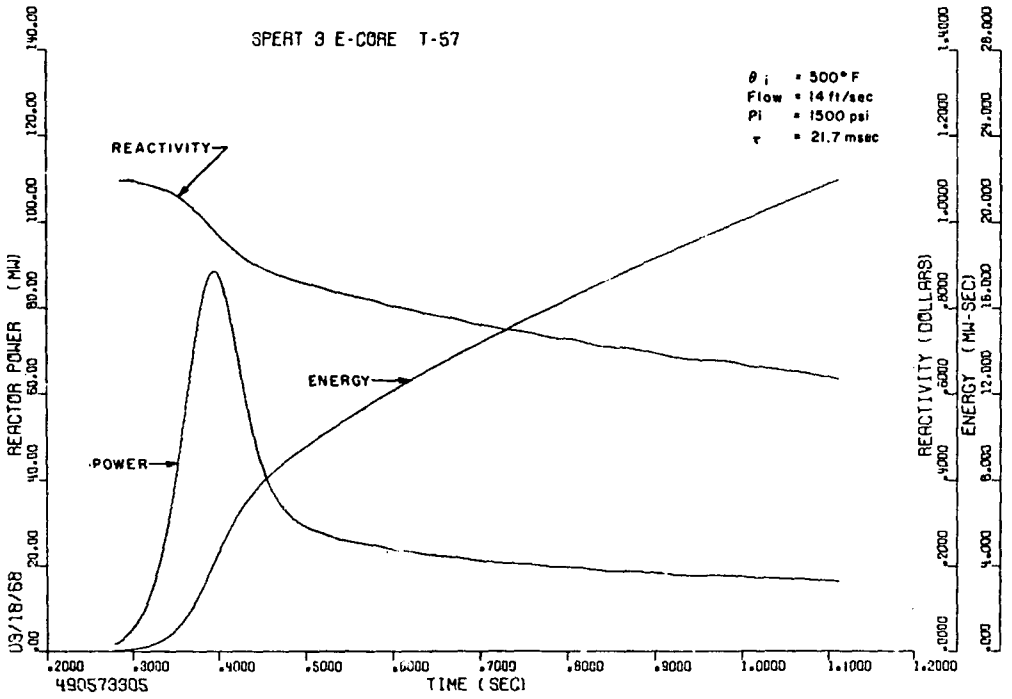

Fig. D-55 Experimental power, energy, and system reactivity for 500°F hot-startup test 57 (21.7 msec period, 1.09$ reactivity insertion).

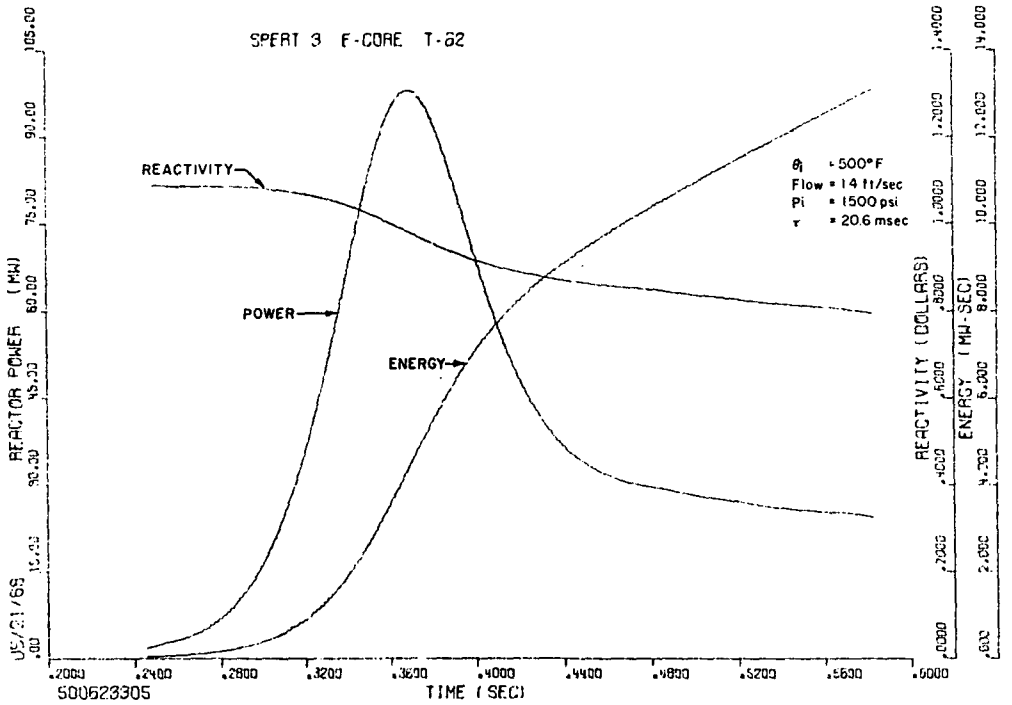

Fig. D-56 Experimental power, energy, and system reactivity for 500°F hot-startup test G2 (20.6 msec period, 1.10$ reactivity insertion).

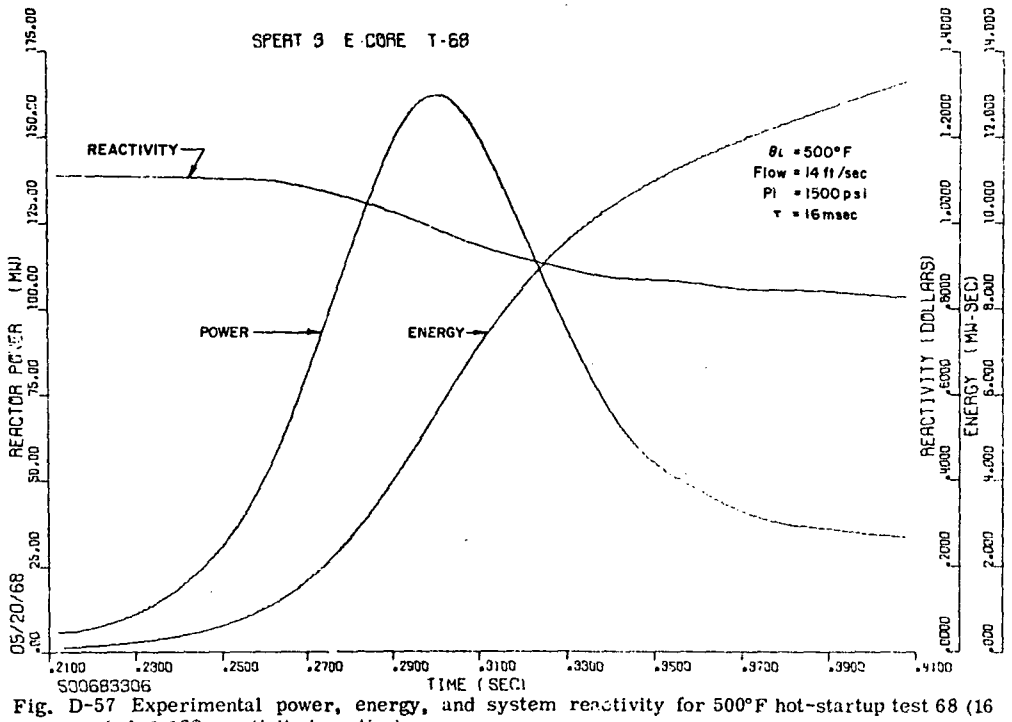

Fig. D-57 Experimental power, energy, and system reactivity for 500°F hot-startup test 68 (16 msec period, 1.13$ reactivity insertion).

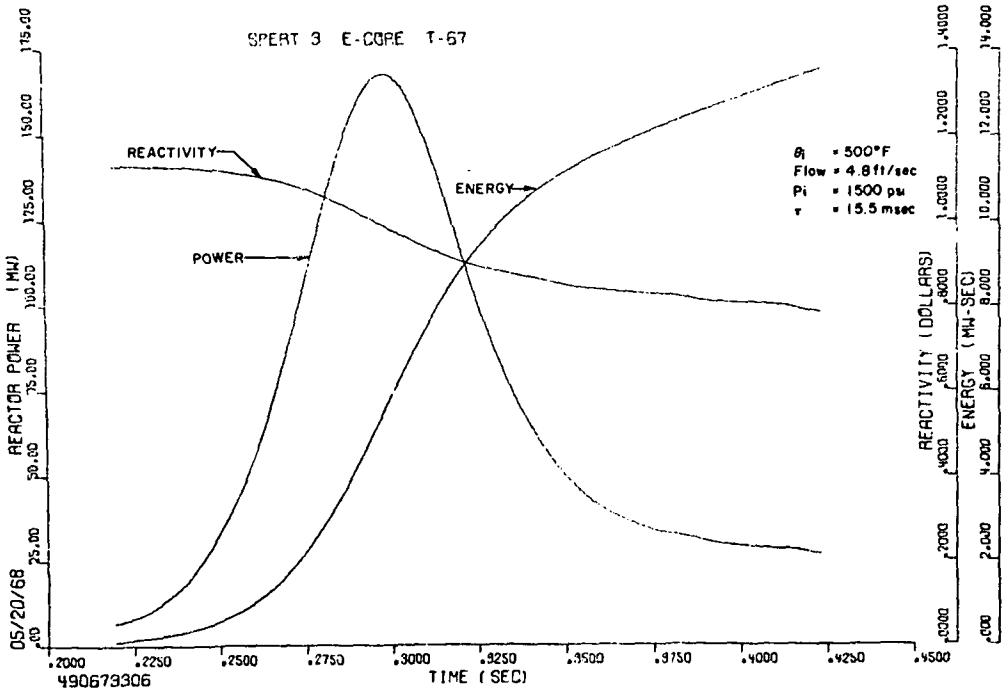

Fig. D-58 Experimental power, energy, and system reactivity for 500°F hot-startup test 67 (15.5 msec period, 1.14$ reactivity insertion).

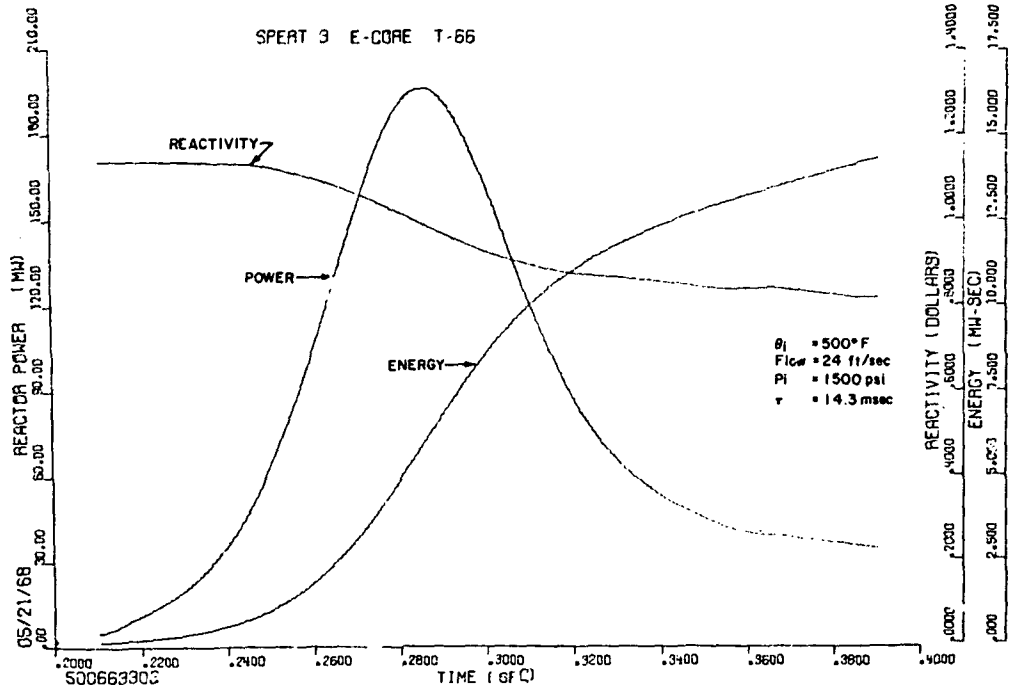

Fig. D-59 Experimental power, energy, and system reactivity for 500°F hot-startup test 66 (14.3 msec period, 1.15$ reactivity insertion).

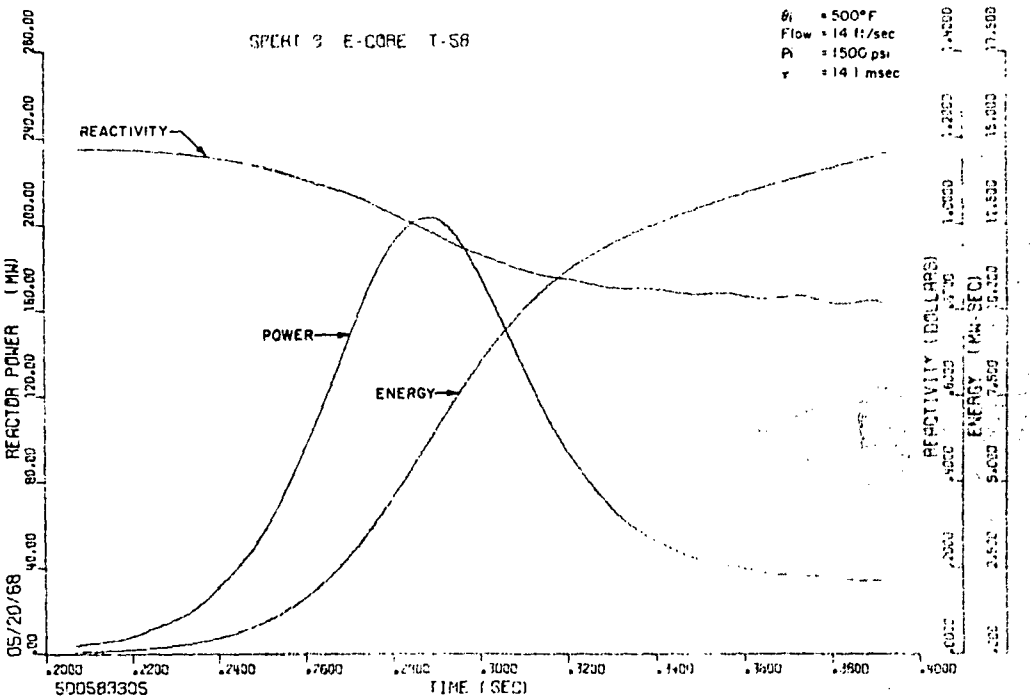

Fig. D-60 Experimental power, energy, and system reactivity for 500°F hot-startup test 58 (14.1 msec period, 1.15$ reactivity insertion).

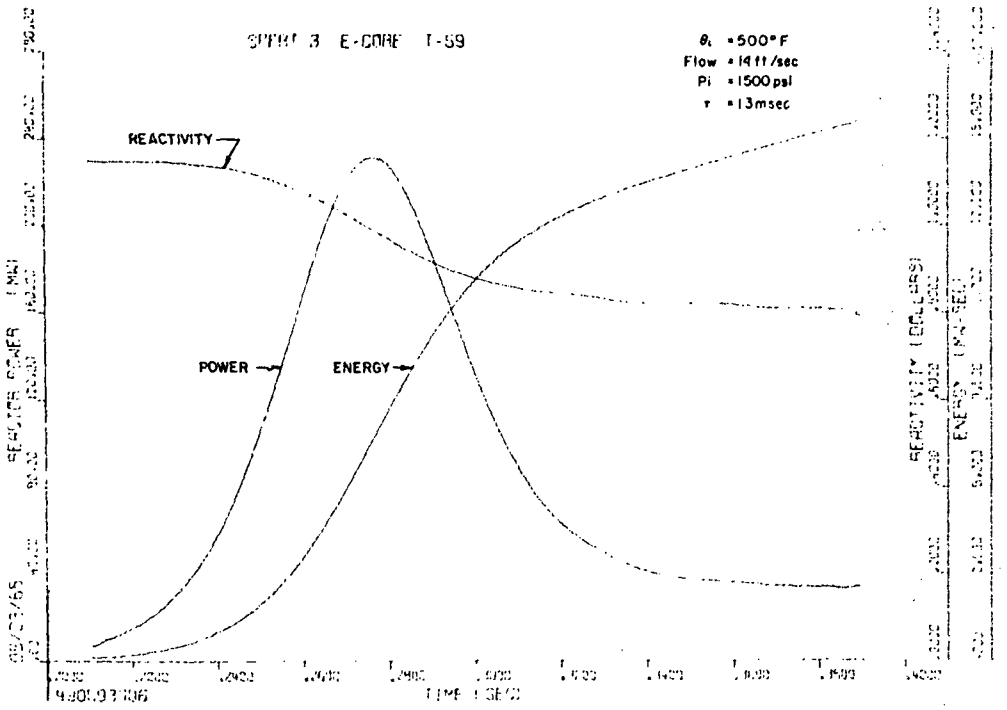

Fig. D-61 Experimental power, energy, and system reactivity for 500°F hot-startup test 59 (13 msec period, 1.17$ reactivity insertion).

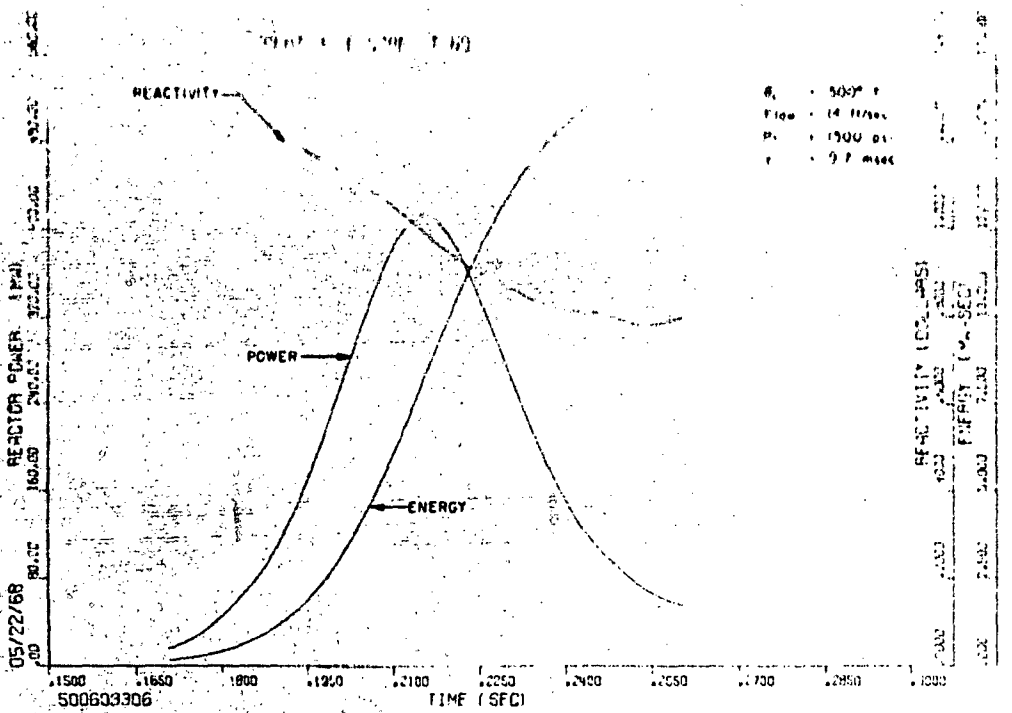

Fig. D-62 Experimental power, energy, and system reactivity for 500°F hot-startup test 60 (9.7 msec period, 1.23$ reactivity insertion).

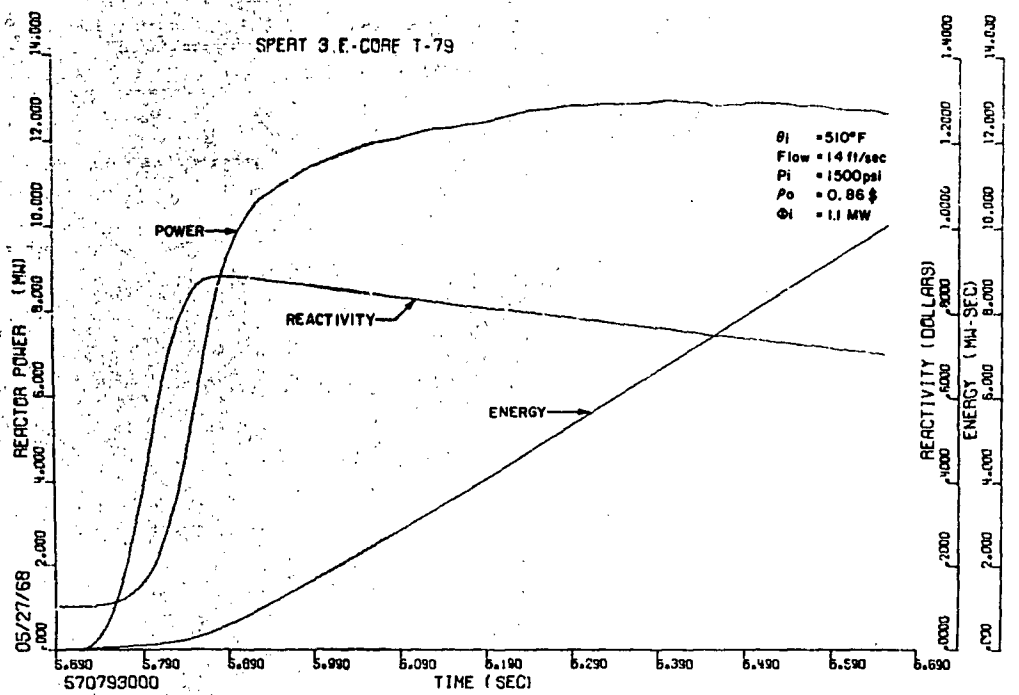

Fig. D-63 Experimental power, energy, and system reactivity for hot-standby test 79 (0.86$ reactivity insertion).

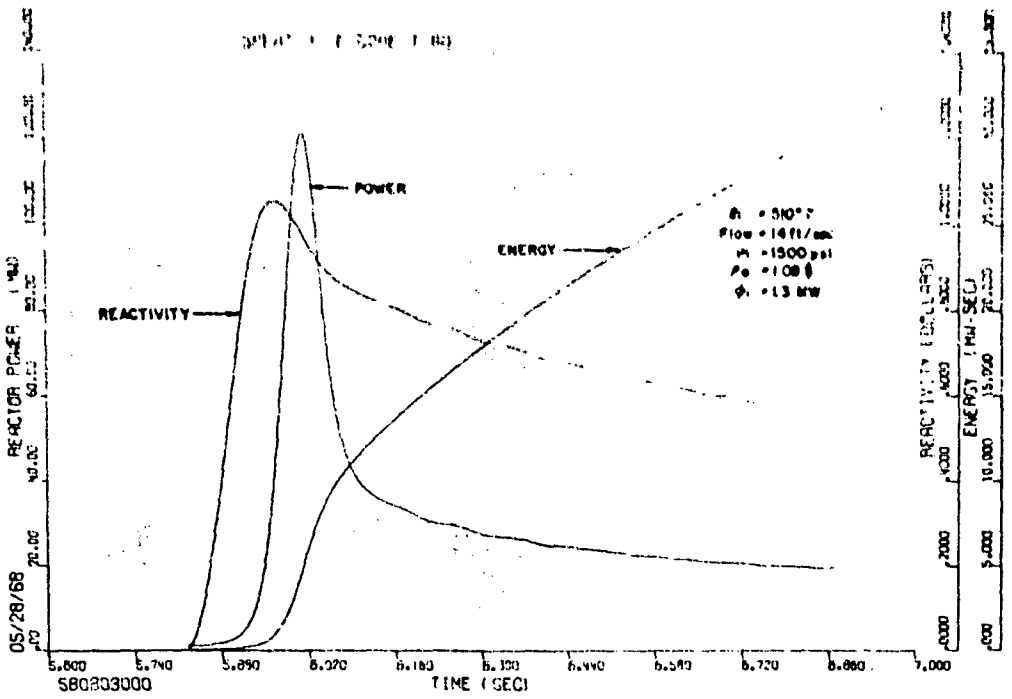

Fig. D-64 Experimental power, energy, and system reactivity for hot-standby test 80 (1.08$ reactivity insertion).

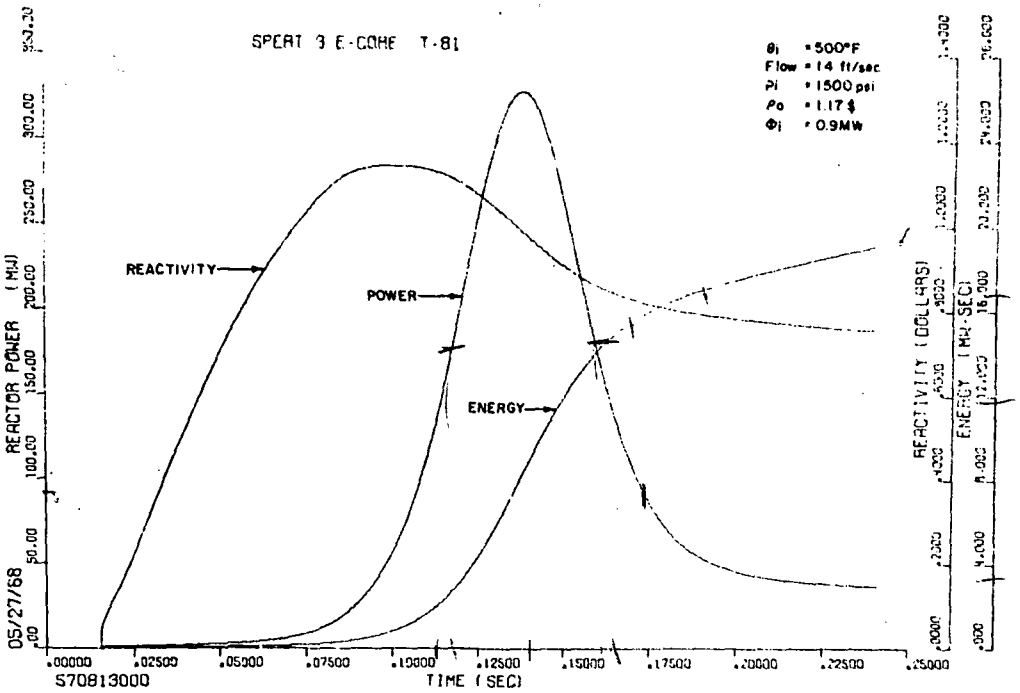

Fig. D-65 Experimental power, energy, and system reactivity for hot-standby test 81 (1.17$ reactivity insertion).

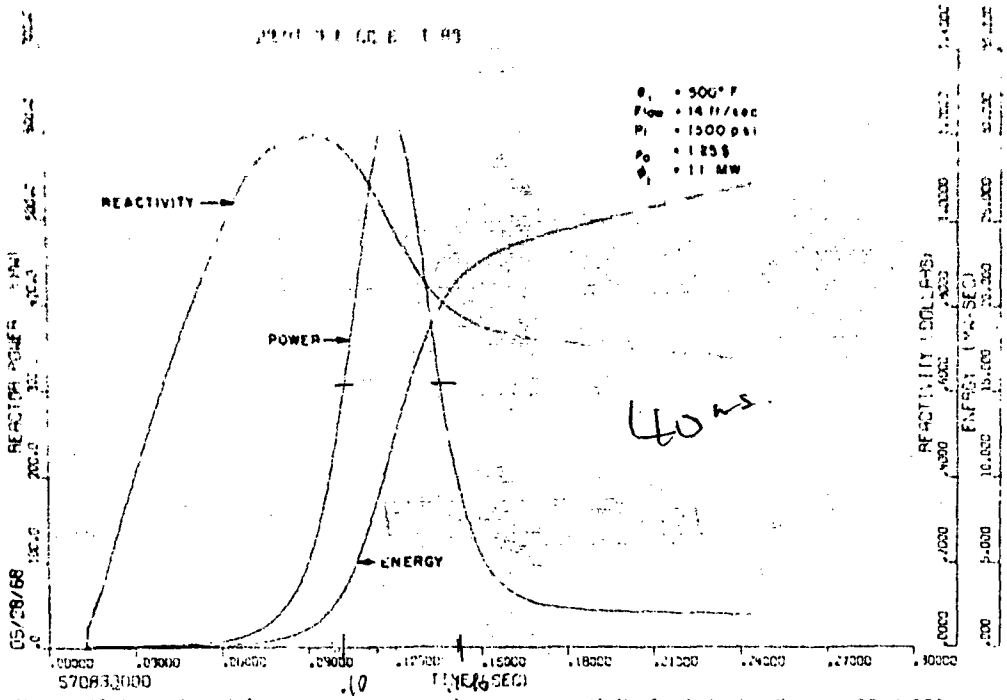

Fig. D-66 Experimental power, energy, and system reactivity for hot-standby test 83 (1.25$ reactivity insertion).

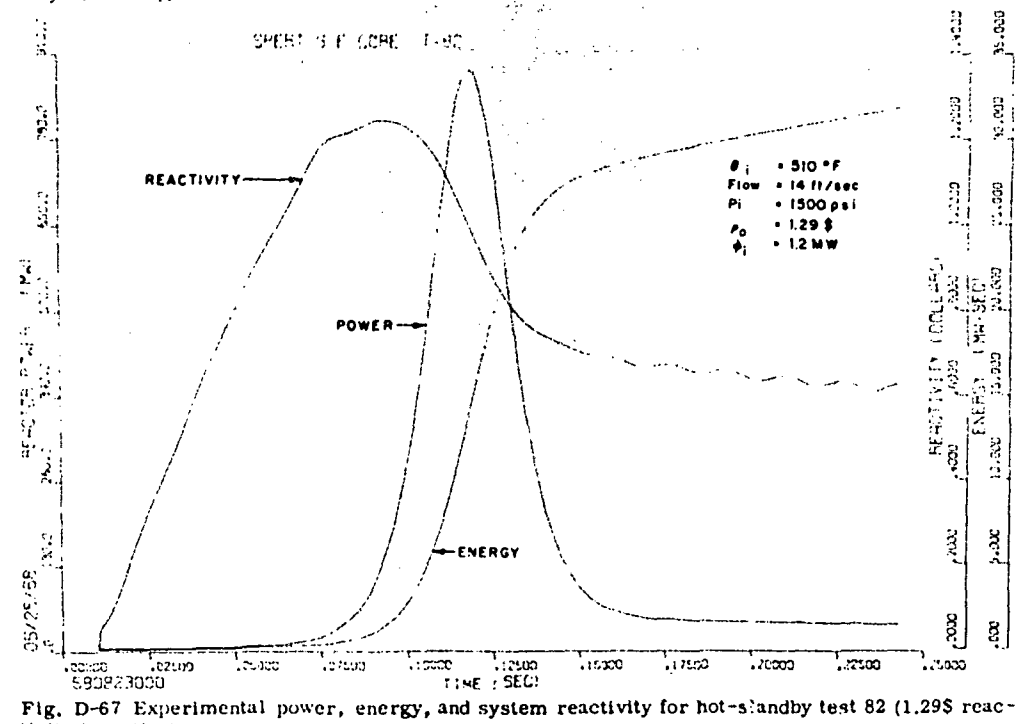

Fig. D-67 Experimental power, energy, and system reactivity for hot-standby test 82 (1.29$ reactivity insertion).

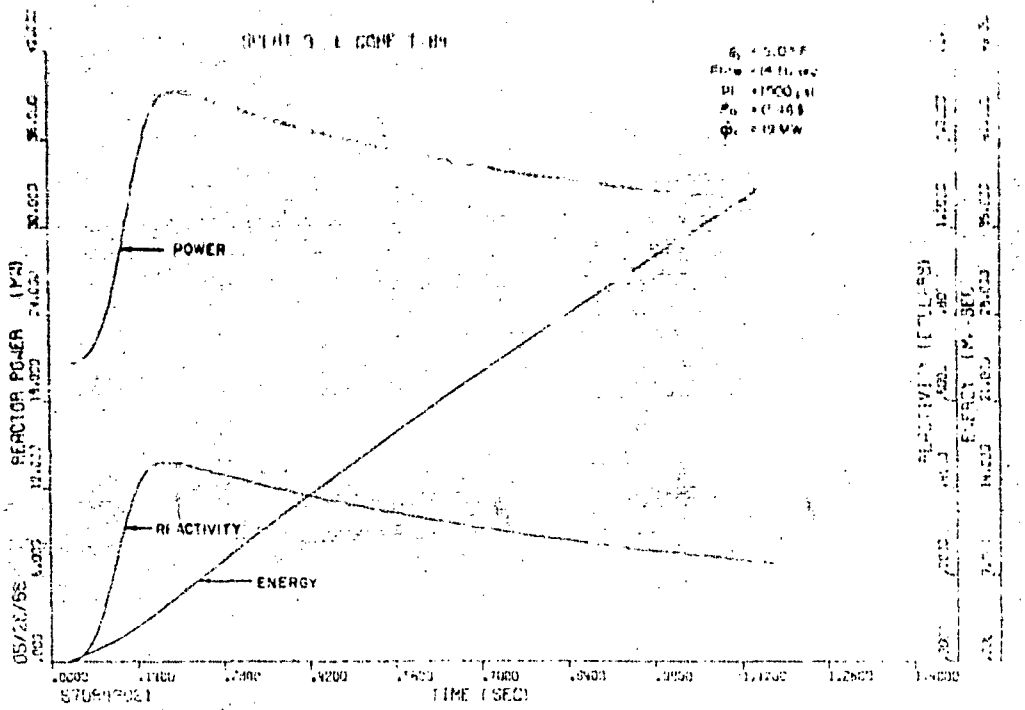

Fig. D-68 Experimental power, energy, and system reactivity for operating-power test 84 (0.46$ reactivity insertion).

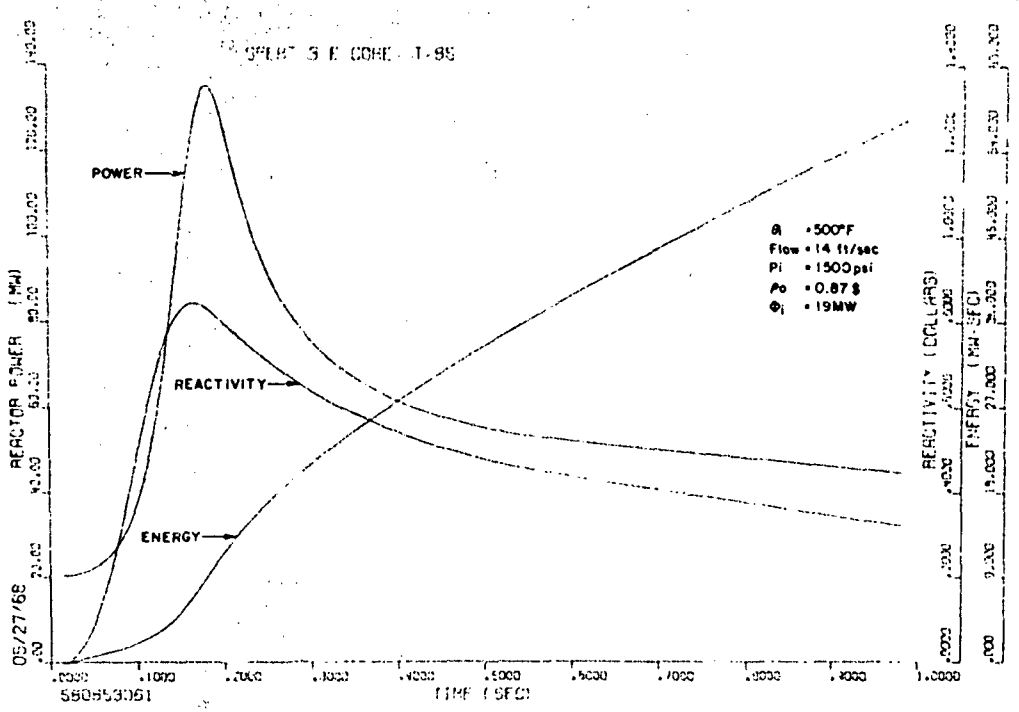

Fig. D-69 Experimental power, energy, and system reactivity for operating-power test 85 (0.87$ reactivity insertion).

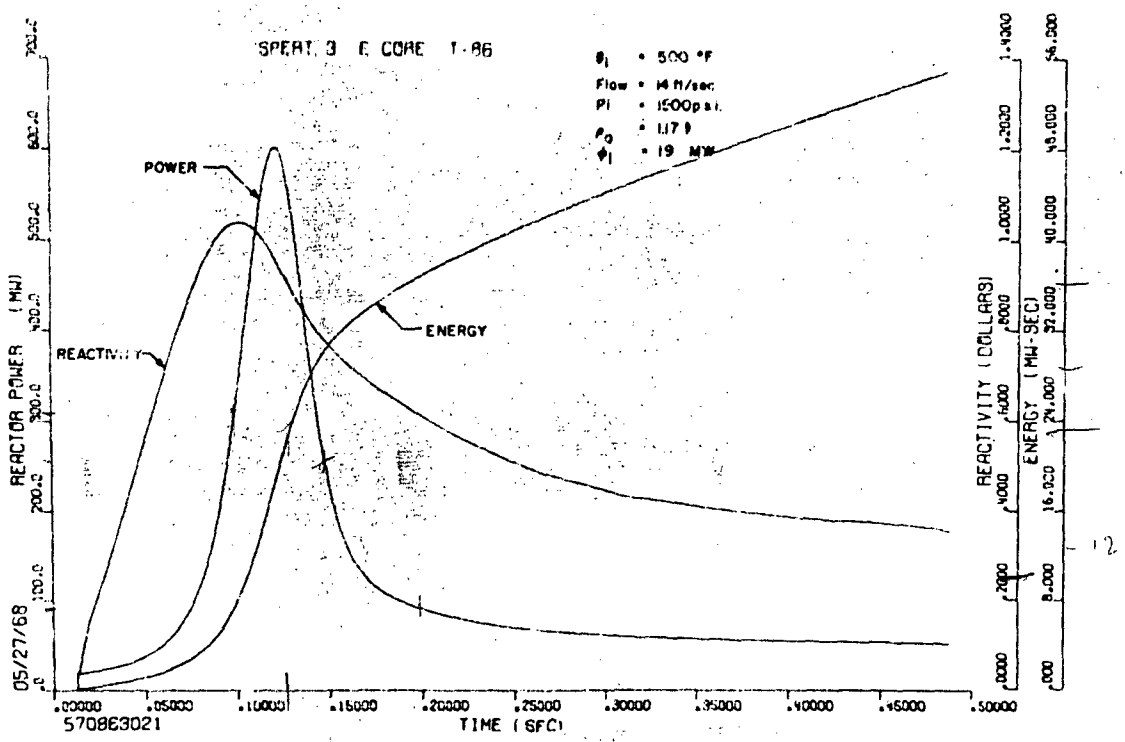

Fig. D-70 Experimental power, energy, and system reactivity for operating-power test 86 (1.17$ reactivity insertion).